To Find and to Form: Cellular Strategies for Intracellular Target Search and Higher-Order Assembly

by

Ameya P. Jalihal

A dissertation submitted in partial fulfillment
of the requirements for the degree of
Doctor of Philosophy
(Cellular and Molecular Biology)
in The University of Michigan
2021

Doctoral Committee:

Professor Nils G. Walter, Chair
Professor Sami J. Barmada
Professor Ajit P. Joglekar
Professor Mats Ljungman

Ameya P. Jalihal

ameyapj@umich.edu

ORCID iD: 0000-0003-4569-8636

© Ameya P. Jalihal 2021

DEDICATION

I dedicate this thesis to my grandparents

Prema Muttagi,

Pandurang Krishna Muttagi,

Janaki Jalihal, and

Ramachandra Anantrao Jalihal

ACKNOWLEDGEMENTS

I'm indebted to the many, many people without whom this work would not have been possible. Foremost, my deepest gratitude to Prof. Nils G Walter, for accepting me into in his lab, for all the endless opportunities he has given me as a graduate student, and for all his encouragement and support over the years. I have grown a lot as a person and a scientist during my time in his lab, and that would not have been possible without his invaluable kindness and patience.

Thank you also to my thesis committee, Prof. Sami Barmada, Prof. Mats Ljungman and Prof. Ajit Joglekar for shaping this work with lots of helpful feedback, for always making time for me and for being extremely supportive over these many years. I am grateful for their insight and presence throughout my PhD.

This work would not have been possible without my co-authors Sethuramasundaram Pitchiaya and Hui Li, without whose incredible patience, hard work, enthusiasm and unconditional support this thesis would not have been possible. I am also indebted to them. I'm also extremely grateful to Damon Hoff, whose untiring efforts keep the SMART center running.

Thank you to all the members of the Walter lab who have been wonderful colleagues, mentors and friends: Corey Custer, Laurie Heinicki, Elizabeth Cameron, Julia Widom, Chris Rohlman, Victoria Rai, Jieming Li, Alex Johnson-Buck, Adrien Chauvier, Nibedita Pal, Poorna Roy, Sujay Ray, Zi Li, Shiba Sundar, Karen Montoya, Kunal Khanna, Liuhan Dai, Guoming Gao, Saffron Little, Andreas Schmidt, Paul Lund, Robb Welty, Elizabeth Duran, Catie Scull, Javier

Cabello, and all the others who have been a part of the group. I could not have asked for a better group of people to work alongside with.

Thank you especially to Andreas Schmidt, Paul Lund and Karen Montoya, for being the best friends, companions and cheerleaders I could have asked for. This journey would not have been possible without your companionship inside and outside lab.

Thank you to everyone at CMB, but especially my cohort for being a wonderfully inspiring set of people: Hillary Miller, Brian McGrath, Lindsay Mortiz, Elaine Liu, Samantha Devenport. Special thanks to Lauren Perl, Pat Ocelnik and Margarita Bekiares whose tireless work has kept CMB running. I'm grateful to Bob Fuller, Kathy Collins, Ben Allen, Ken Cadigan, Manoj Puthenveedu and other CMB leadership for keeping the ship afloat and being outstanding figures for all of us to look up to.

Thank you to all the PIBS leadership, and especially Scott Barolo, Michelle DiMondo, Maggie Gardner and Michelle Mellis for running this monumental PhD program.

Thank you to AMS e-board members Elizabeth Gichana, Marcos Nunez, Sierra Nishizaki, Ally Cara, Sharena Rice, Nnamdi Edokobi, Clarence Pascual, Torrin McDonald, Peter Kim, Maral Budak, April Solon, Jennifer Jimenez and all the AMS members for creating a wonderfully accepting and engaged community of scholars which I'm incredibly proud of having been a part of.

The friends I made in grad school played no small part in making this thesis happen. I am indebted to the kindness, love, friendship and generosity of Natalie Warsinger-Pepe, Dominique Bouavichith, Maral Budak, Elizabeth Gichana, Saurabh Acharya, Karthik Desingh, Dhanvin Mehta, and Arushi Gupta. They have been there for me in happy times and when times have been

not-so-happy. This thesis has more of them in it than they'd think, and for that I'm very grateful. Thank you also to Dom, Justin and Tam for letting me be a part of their household and a part of their research.

I'm extremely grateful for the friendship and love of Tara Narayanan, Niveditha Ram, Sumanth Srinivasan, Abhinav Srinivasan, Amogh Jalihal, Brittany Boribong, Anand Murali, Jhui Baskar, Anirudh, Aditi Khemani, Sneha Nair and Jayadev Vijayan, and all the other dear friends who bore with me over the years with nothing but the utmost compassion.

Thank you to friends I've made on Twitter and have ended up becoming friends in real life, Shweta Ramdas, Sara Wong. Thanks also to all the friends I've made on phil-sci and science twitter but have never met in person. These conversations have been instrumental in shaping the way I think today.

Finally, thanks to my aunt and uncle Vasudha and Rajay Jain, for welcoming me into their home, for all their love and for teaching me resilience, and thanks to my parents Purnima and Devendra Jalihal, for everything.

TABLE OF CONTENTS

LIST OF FIGURES

Figure 1-3 Strategies for labeling RNA and protein components for single molecule fluorescence. **A.** Modifications are possible at various positions on RNA molecules prepared through chemical synthesis, including the 5' and 3' termini (I and II, respectively), the 2' position of the sugar (III), and various positions on the nucleobase (IV, V, and VI), among others. Modifications can include reactive chemical moieties that are used for subsequent conjugation reactions, small molecules like biotin and digoxigenin for immobilization, or direct attachment of fluorophore dyes, or even replacement of entire nucleotides by fluorophores. **B.** Example strategies for preparing fluorescently labeled RNA for in vitro studies. Fluorescent labels are shown as red stars. **C.** Example strategies for preparing fluorescently labeled protein for in vitro studies. **D.** For intracellular single molecule studies, RNA can be prepared using many of the methods suitable for in vitro work (described in B) and subsequently introduced into cells via microinjection or transfection. Alternatively, RNA transcripts can be labeled by inserting stem-loop repeat sequences that are bound by their cognate RNA binding proteins, that are expressed as fusions with intrinsically fluorescent proteins (RBP-FP). **E.** Example strategies for preparing fluorescently labeled protein for intracellular studies. In contrast to RNA, there is greater overlap between strategies for labeling protein that are suitable for in vitro and intracellular work. A small number of strategies, such as click chemistry using strained alkynes, can be applied to both RNA and proteins..... 20

Figure 1-4 Intracellular single molecule visualization A. Microinjection is an effective strategy to deliver labeled RNAs into living cells. The injected material can be imaged using various fluorescence microscopy techniques. Intracellular Single-molecule High-Resolution Localization and Counting (iSHiRLoC) uses HILO illumination to rapidly acquire images with single-molecule resolution for particle tracking. B. Injected cells are distinguished from non-injected cells by the

presence of an injection marker, a slowly diffusing, fluorescently labeled inert compound. Shown here are two cells injected into the nucleus (I) and cytosol (II) with Alexa488-labeled 100 kDa Dextran. Labeled miRNAs appear as diffusing, diffraction-limited spots upon time lapse imaging of live cells (I, inset) or as diffraction-limited spots in formaldehyde-fixed samples (II, inset). Scale bars represent 10 μm. C. I. The intensity profiles of diffraction-limited spots, recorded as pixelated point-spread functions, can be analyzed to obtain the spot centers with sub-pixel accuracy, such as by fitting the intensity profile to 2D Gaussians. II. Particle-tracking of the spot centers results in 2- or 3-dimensional diffusion trajectories. III. Displacements in successive frames yield mean-squared displacement (MSD) profiles, informing about diffusion types. D. Photobleaching analysis. Cy5 fluorophores bleach rapidly and in a step-wise manner. The number of discrete step drops in intensity is a proxy for the number of molecules in a single diffraction limited spot. Adapted with permission from Pitchiaya et al. (2012). E. Correlating the number of fluorescent spots in fixed tissue with the number of diffusion filtered trajectories yields an estimate of turnover and functionality of the labeled molecules. The open shapes represent counts of a mutant (mutant *let-7*, ml7) and artificial (*cxcr4*, cx) miRNA co-injected with mRNAs bearing complementary binding sites, and the filled shapes represent conditions where the co-injected mRNAs bore mismatched (*let-7*, l7) or no binding sites in the 3'UTR downstream of an ORF encoding *Renilla* luciferase. Adapted with permission from Pitchiaya et al. (2017)..... 27

Figure 2-1 Validation of in situ miRNA imaging system. (**A**) Representative pseudocolored and contrast-adjusted images of U2-OS cells stained for endogenous Dcp1a (green) via immunofluorescence and UGD cells expressing GFP-Dcp1a (green). Nucleus is stained with DAPI (blue). Dotted line, cell outline. Scale bar, 10 μm. (**B**) Scatter plot depicting the number of endogenous Dcp1a or GFP-Dcp1a foci in U2-OS and UGD cells respectively (n = 3, 60 cells, N.S.,

not significant based on two-tailed, unpaired Student's t-test). (**C**) Representative pseudocolored and contrast-adjusted image of UGD cells expressing GFP-Dcp1a (green) and stained for Rck (red). Nucleus is stained with DAPI (blue). Dotted line, cell outline. Scale bar, 10 μm. Orange 5.3 x 5.3 μm2 inset is zoomed out and deconvolved into individual colors. (**D**) Mean colocalization percentage of endogenous Dcp1a foci from U2-OS cells or GFP-Dcp1a from UGD cells respectively, with other PB markers. Color coded scale-bar is also depicted (n = 3, ≥ 15 cells per sample). (**E-G**) Microinjection-based titration assay. (**E**) Schematic of microinjection setup, wherein Cy5 labeled double stranded DNA (dl7-Cy5/dl7*, red) bearing the same sequence as l7-Cy5/l7* miRNA was co-microinjected along with 500 kDa FITC-Dextran (green), exclusively localizes to the cytosol. (**F**) Representative pseudocolored and contrast-adjusted images of U2-OS cells microinjected with various concentrations of dl7-Cy5/dl7*. Scale bar, 10 μm. (**G**) Plot depicting the relationship between dl7-Cy5/dl7* concentration (Conc., μM) in the microinjection solution and the number of molecules detected per cell (# Mols / Cell). Dotted line represents fitted line. Equation of fitted line and goodness of fit (R2) are also depicted. (H-K) miRNA activity assays. (**H**) Schematic of microinjection-based miRNA activity assay. (**I**) Representative pseudocolored and contrast-adjusted image of U2-OS cells expressing mCherry (mCh, red) reporter gene and GFP normalization gene (green), also containing 10 kDa cascade-blue dextran (CB-Dex, cyan) and the miRNA (Scr/Scr* - scrambled control, l7/l7* - let-7 miRNA) of interest. Scale bar, 10 μm. (**J**) Scatter plot depicting the mCh : GFP intensity ratio for various conditions (n = 3 replicates, total 30 cells; **p < 0.001 based on two-tailed, unpaired Student's t-test). Mean and s.e.m are depicted. (**K**) Luciferase reporter assays represented as the ratio of luminescence form a firefly luciferase (FL) reporter gene containing 6x let-7 MREs (FL-l7-6x) and a renilla luciferase (RL) normalization gene in U2-OS cells (n = 12 replicates, ***p < 0.0001 based on two-

tailed, unpaired Student's t-test). Mean and s.e.m are depicted. (**L-O**) Microinjection does not affect sub-cellular behavior of PBs and does not induce stress granules. Number (**L**) and diffusion constants (M) of PBs in cells that were not injected (Not Inj., NI) or injected (Inj., I). Representative pseudocolored and contrast-adjusted images of U2-OS cells stably expressing GFP-G3BP (green), a stress granule (SG) marker, and RFP-Dcp1a (red), which were not injected (NI), treated with sodium arsenite (NI + NaAsO2) or co-injected with CB-Dex (cyan) and l7-Cy5/l7* are shown in N. Scale bar, 10 μm. Quantification of the number of GFP or RFP foci per cell is shown in O. (**P**) Expected phenotype of distinct molecular species in iSHiRLoC assays. LCI, live cell imaging; FCI, fixed cell imaging. (**Q-R**) Dynamics and stoichiometry of l7-Cy5/l7* in GFP-Dcp1a expressing HeLa cells are almost identical to those in UGD cells. (Q) Distribution of l7-Cy5/l7* miRNA diffusion constants in PB and Cyt within living HeLa cells that are expressing GFP-Dcp1a. Green area on the plot depicts the range of PB diffusion constants (n = 3, 13 cells). Dotted blue line represents distribution of l7-Cy5/l7* miRNA diffusion constants within UGD cells, as in Figure 1D. (**R**) Distribution of l7-Cy5/l7* miRNA stoichiometry as monomeric (Mono, 1 photobleaching step) or multimeric (Multi, ≥ 2 photobleaching steps) complexes in PB and Cyt within fixed HeLa cells that are expressing GFP-Dcp1a (n = 4, 21 cells). Dotted blue line represents stoichiometry in UGD cells, as in Figure 2-1F..... 44

Figure 2-2 A super-resolution imaging tool for probing RNA-granule dynamics and stoichiometry. (**A**) Schematic of iSHiRLoC assay for probing miRNA-PB dynamics and colocalizations. (B and C) Representative pseudo-colored and contrast-adjusted images from live-cell imaging (**B**) and fixed cell imaging (**C**) assays of UGD cells expressing GFP-labeled PBs (green) that were microinjected with l7-Cy5/l7* miRNA (red) and imaged 2 h post injection. Scale bar, 10 μm. (**D**) Representative single-particle trajectories of PBs (green) and l7-Cy5/l7* miRNA

(red) from yellow and magenta boxes in B, representing diffusing miRNAs in PBs and in the cytoplasm (Cyt) respectively. Scale bar, 1 μm. Dotted green circle represents PB outline in the first frame of the movie. Distribution of l7-Cy5/l7* miRNA diffusion constants in PB and Cyt are also depicted. Green area on the plot depicts the range of PB diffusion constants (n = 3, 15 cells). (**E**) Zoomed-in view of orange and violet boxes in C, from fixed UGD cells. Scale bar, 2 μm. Step-wise photobleaching trajectories PB- and Cyt-localized l7-Cy5/l7* is also shown. (**F**) Distribution of l7-Cy5/l7* miRNA stoichiometry as monomeric (Mono, 1 photobleaching step) or multimeric (Multi, ≥ 2 photobleaching steps) complexes in PB and Cyt within fixed UGD cells (n = 3, 15 cells). 46

Figure 2-3 miRNAs show diverse spatiotemporal localization patterns at PB core and periphery. (**A**) Schematic and representative time-lapsed images of PBs (green) and l7-Cy5/l7* miRNAs (red) in live UGD cells. Scale bar, 1 μm. Embedded numbers in green/red overlay images (far-left and far right) represent time in seconds. Dotted green circles in red panels have been included to aid in the identification of PB boundaries. White arrow points to an individual RNA particle. Stable RNA-PB association patterns (static, dynamic and recruited) are represented in orange whereas transient ones (probe and escape) are represented in blue. nPB = number of track localizations within PBs, nCyt = number of track localizations in the cytosol. (**B**) Schematic and representative images of PBs (green) and l7-Cy5/l7* (red) representing the localization of miRNAs within shells or cores of PBs in fixed UGD cells. Scale bar, 2 μm. Dotted green and red circles represent boundaries of PBs and miRNAs respectively. Relative localization (RL) values of l7-Cy5/l7* for these representative colocalizations are embedded in the green panels. (**C**) Schematic and representative images of PBs (green) and l7-Cy5/l7* (red) representing the enrichment of miRNAs in PBs within fixed UGD cells. Dotted yellow and red circles represent PB-miRNA colocalization

photobleaching steps) complexes in PB and Cyt within fixed UGD cells (n = 3, 20 cells). (**G** and **M**) Schematic of different mRNA constructs with various 3` or 5` UTRs. Color-coded symbols for each transcript is shown and will be used to depict these respective transcripts from hereon. (H and N) Luciferase reporter assays represented as the ratio of luminescence form a firefly luciferase (FL) reporter gene and a renilla luciferase (RL) normalization gene in UGD cells. Data were normalized to the FL sample. Mean and s.e.m are represented (n = 12 replicates, ***p < 0.0001 based on two-tailed, unpaired Student's t-test). (I and O) Scatter plot representing the % of mRNA molecules that colocalize with PBs per fixed UGD cell. Each dot represents a fixed UGD cell. (J and P) Scatter plot of EI for different mRNA constructs. Each dot represents a PB in fixed UGD cells. Grey dotted line depicts an EI of one, which demarcates PB-enriched (> 1) from PB-depleted (< 1) factors. (**K** and **Q**) Relative distribution of stable and transient interactions per live UGD cell for different mRNAs. (**L** and **R**) Comparison of fast and slow mRNA-PB interaction kinetics in live UGD cells. Black line depicts acquisition window (15 s). Green-black line depicts the mean magnitude of FL-l7-6x-MS2 for the respective observable. n = 3, ≥ 15 cells per sample, NS = not significant, * p ≤ 0.01, **p ≤ 0.001 or ***p ≤ 0.0001 by two-tailed, unpaired Student's t-test. See also Figure S4. 56

Figure 2-8 Validation of in situ m/lncRNA imaging system. (**A**) Luciferase reporter assays of the appropriate mRNA constructs (n = 12). Data were normalized to FL. Mean and s.e.m are depicted (n = 12 replicates, NS = not significant or ***p < 0.0001 based on two-tailed, unpaired Student's t-test). (**B-C**) Luciferase reporter assays of the appropriate mRNA constructs treated with a control antimiR (anti-ctrl) or an anti-let7 (anti-l7) antimiR. (n = 12). Data were normalized to FL (anti-ctrl). Mean and s.e.m are depicted (n = 12 replicates, NS = not significant, **p ≤ 0.001 or ***p < 0.0001 based on two-tailed, unpaired Student's t-test). (**D** and **F**) Dwell time distribution of the

isosmotic (Iso) growth medium, hyperosmotic growth medium containing the non-ionic osmolyte Sorbitol (Sor), or rescued (Res) with isosmotic medium after Sorbitol treatment. n = 2, > 5 cells per sample. Scale bar, 10 μm. (**B**) Representative y-z projection of UGD cells (gray-scale) from 3-D imaging assay wherein the cell were treated with isotonic (150 mM Na+) medium, hypertonic (300 mM Na+) medium or rescued with isotonic medium after hypertonic treatment. n = 1, 4 cells per sample. Scale bar, 10 μm. Scatter plot of the fold change in cell volume, as normalized to the cell volume in isotonic conditions, is shown. (**C**) Representative pseudocolored images of a UGD cell (GFP, green) that was cyclically treated with isotonic (150 mM Na+) or hypertonic (300 mM Na+) medium. Scale bar, 10 μm. (**D**) Scatter plot of the fold change in foci number, as normalized to foci number in isotonic samples, associated with assay represented in C. Red line depicts exponential fit. n = 2, > 5 cells per sample. (**E**) Violin plots of diffusion constants associated with DCP1A foci, associated with assay represented in C. n = 2, > 5 cells per sample. (**F**) Bar plots of cell viability (by CellTiter-Glo assay), as normalized to isotonic samples, associated with assay represented in C. n = 3, with 3 technical replicates for each n. 109

Figure 3-6 Hyperosmotic phase separation of DCP1A is independent of cell type. Related to Figure 3-5. (**A**) Scatter plot of the number of foci per cell (top), violin plots of diffusion constants associated with DCP1A foci (bottom). Representative pseudocolored images of UGD cells (GFP, green) were treated with isosmotic (Iso) growth medium, hyperosmotic growth medium containing the non-ionic osmolyte Sucrose (Suc, 2min) or rescued (Res) with isosmotic medium (2 min) after sucrose treatment (2 min). n = 2, > 5 cells per sample. Scale bar, 10 μm. (**B**) Representative x-y (green) and y-z (gray) projection of a UGD cell from 3-D imaging assay wherein the cell was treated with isotonic (150 mM Na+) medium or hypertonic (300 mM Na+) medium. n = 1, 4 cells per sample. Scale bars, 10 μm (x and y) and 5 μm (z). (**C**) Representative pseudocolored images

Figure 3-8 Knockdown of EDC4 results in reduced expression of DCP1A. Related to Figure 3-7. (**A**) Western Blot of EDC4, DCP1A, and GAPDH after various siRNA treatment times (24, 48 and 72 hr post siRNA transfection). Bands labeled with "*" and "**" were detected by EDC4 and DCP1A antibodies respectively and either denote non-specific bands or shorter protein fragments. (**B**) Representative pseudocolored IF images of UGD cells expressing GFP-DCP1A (green), stained for EDC4 (red). Scale bar, 20 μm. Cells were either transfected with a scrambled siRNA (Scr) or siEDC4 for 48 h and then treated with isotonic (150 mM Na+, 2 min) medium or hypertonic (450 mM Na+, 2 min) medium. (**C**) Scatter plot of the average intensity of GFP (green) or EDC4 (Cy5, red) per UGD cell transfected with a scrambled siRNA (Scr) or siEDC4 in isotonic conditions. n = 2, > 20 cells per sample, *p ≤ 0.01, by two-tailed, unpaired Student's t-test. (**D**) Scatter plot of GFP-DCP1a spot number (left) and spot area (right) plotted against sum fluorescent intensity of the cell, under isotonic (blue) and hypertonic (orange) conditions. Fold change in spot numbers is relative to the lowest spot count under isotonicity. 113

Figure 3-9 High-throughput IF and GFP imaging show that several multimeric proteins of valency ≥2 generally exhibit HOPS. (**A**) Schematic of high throughput IF assay. (**B**) Representative pseudocolored IF images of U2OS cells stained for DAPI (blue, nucleus) and the appropriate protein (red). Cells were treated with isotonic (150 mM Na+) medium, hypertonic (300 mM Na+) medium, or rescued (Res) with isotonic medium after hypertonic treatment. Scale bar, 10 μm. Quantification of average number of spots per cell of the appropriate samples in panel B is shown. n = 3, > 50 cells per sample. (**C**) Heatmap representing the fold change in spot number of 108 proteins tested by high throughput IF, as normalized to isotonic conditions. "rep" denotes replicates. (**D**) Representative pseudocolored images of U2OS cells (GFP, green) transfected with the appropriate GFP-tagged construct and treated with isotonic (150 mM Na+) medium or

LIST OF TABLES

LIST OF APPENDICES

ABSTRACT

Eukaryotic RNA-protein complexes have been widely reported to form membrane-less, higher-order assemblies inside cells under a range of conditions. How these structures contribute to the regulation of intracellular biochemistry remains poorly understood. Recent biophysical studies have revealed how phase-separation, a passive, thermodynamically driven process, can explain the assembly of such structures, referred to as condensates.

This dissertation explores the relationship between macromolecular interactions that mediate the formation of dynamic condensates and the biochemical consequences of the resulting reorganization of the intracellular space. Organized into three parts, it implements and leverages new live-cell fluorescence microscopy approaches to visualize the formation of and localization of RNAs to condensates in real-time and at single-molecule resolution to address fundamental questions around intracellular biochemical regulation.

First, the dissertation explores the RNA-sequence and protein translation-dependence of RNA localization to intracellular condensates called P-bodies. This work revealed that RNAs in P-bodies localize differently to the periphery or the core of these condensates depending on their translatability, and that stable RNA localization requires specific RNA-protein interactions.

It next provides evidence for ubiquitous, proteome-wide, homomultimerization-driven phase-separation in response to osmotic volume fluctuations. These observations expand the molecular grammar of protein domains known to drive phase-separation, suggesting that a large

fraction of the proteome may be poised to undergo rapid spatial reorganization upon small perturbations in intracellular molecular crowding. Additionally, these results provide possible explanations for previously reported features of osmotic stress response, by suggesting that hyperosmolarity-induced phase-separation of CPSF6 protein might provide a mechanistic basis for the widespread loss of premRNA cleavage activity under such conditions. These observations paint a new picture of the nature of the intracellular milieu, in which the organization of the intracellular space is inextricably linked with the macromolecular sequence of its constituents, where the concentration of individual molecular species can affect both its biochemical function and spatial organization.

In the third part, the thesis discusses evidence that microRNA-induced silencing complexes may use a two-pronged strategy to search for mRNA targets inside the cell: on the one hand, transient binding and 3D search allow for rapid exploration; on the other hand, induced clustering of target mRNAs reduces the search space, such that these complexes can efficiently engage with their targets even when the concentration is limiting. Comparing the kinetics of individual

microRNA-mRNA interactions in the cell across a range of mRNAs differing in the number of microRNA binding sites suggests that binding site number, a conserved feature of mRNAs, serves to both stabilize microRNA binding and promote AGO2-dependent clustering of mRNAs.

This work refines an emerging paradigm in cell biology in which the intracellular space, far from being spatially homogeneous, is highly compartmentalized. Further, it demonstrates that such compartmentalization can be highly dynamic, and this dynamic organization is encoded by macromolecular sequence and biochemical activity. By applying single particle tracking to

understand the assembly of intracellular condensate dynamics, this work opens up new ways for studying non-equilibrium phase separation and condensate formation in cells. Studying molecular association processes at single-molecule resolution in living cells represents a significant advance in quantitative cell biology by bridging single-molecule measurements in vitro and qualitative observations in vivo. This dissertation therefore advances the study of intracellular biochemistry by describing new methods and by applying them to uncover insights into the relationship between macromolecular sequence and subcellular organization.

Chapter 1. Background and Introduction[1]

1.1. Cellular organization: spatial regulation of function

Cells, the fundamental units of life, engage in complex processes such as sensing and responding to the environment, growth and reproduction across all kingdoms of life. The biochemical reactions underlying these processes are tightly regulated in space and time. Eukaryotic cells possess multiple membrane-bound compartments called organelles that spatially segregate different biochemical processes such that molecules involved in related pathways are placed in proximity to each other to facilitate specific interactions that lead to the desired catalytic outcome, while reducing non-specific, non-productive molecular interactions. Organellar organization has been extensively studied in the context of localization of specific biological functions: genetic material is primarily stored, and gene expression is largely regulated in the nucleus; protein production and packaging occur in the endoplasmic reticulum; cellular ATP production occurs in mitochondria, and so on. The localization of enzymes and other macromolecular complexes to the appropriate organellar compartment is key to facilitating their proper function in these cases. Consequently, mis-localization of these components in the cell is

[1] The contents of this chapter have been published as:

Jalihal, A.P., Schmidt A.S., Gao G., Little S., Pitchiaya S. and Walter, N.G. Hyperosmotic phase separation: Condensates beyond inclusions, granules and organelles. (2020) JBC.

All authors contributed to writing and editing. APJ, GG and AS prepared figures.

Jalihal, A.P., Lund, P.E. and Walter, N.G. (2019) Coming together: RNAs and proteins assemble under the single molecule fluorescence microscope. In The RNA Worlds: New tools for deep exploration, pp. 451-470 (ed. T.R. Cech, J.A. Steitz & J.F. Atkins), Cold Spring Harb. Perspect. Biol. 11, a032441.

All authors contributed to writing and editing. APJ and PEL prepared figures.

frequently associated with impaired function, disease or even cell death. In general, biochemical regulation is tied tightly to spatial regulation of the biochemical components. Therefore, understanding the fundamental relationship between compartmentalization and biochemistry is of vital importance to understanding the basis of cellular function, and therefore, of life itself.

The first part of this chapter introduces a newly emerging paradigm of sub-cellular compartmentalization termed membraneless organelles, discusses how the theory of phase-separation is applied to understand the formation of these structures and provides an overview of some well-studied membraneless organelles. In the second part, it introduces specific pathways of gene regulation mediated by small RNAs, and the spatial regulation involved in these mechanisms. In the third part it describes single molecule fluorescence tools applied to the study of RNA-protein complexes that are key molecular players in such organization.

1.1.1. Membraneless organelles

In eukaryotic cells, the intracellular environment is a densely packed, highly heterogeneous environment where individual catalysts and reactants are present at low concentrations. While membrane-bound organelles have been considered paradigmatic of mechanisms that localize biochemical processes, studies from the past decades have brought increased attention to a more adaptive and dynamic strategy for intracellular spatial organization using “membraneless” organelles (MLOs). These amorphous structures are ubiquitous, are observed both in the nucleus and in the cytosol and are characterized by their lack of a lipid boundary. They are heterogeneous in composition and size, typically ranging from 0.01–10 μm, and are subjects of active study owing to their propensity to dynamically assemble and disassemble, priming the cell for rapid responses to intrinsic and extrinsic perturbations (Gomes and Shorter, 2019a; Hyman et al., 2014b; Mitrea

and Kriwacki, 2016). The prevalence of condensates in all forms of life, and the seemingly fundamental rules that govern condensate assembly suggest that these structures and mechanisms may go back to the origins of life itself (Keating, 2012; Tena-Solsona et al., 2018).

Since the early days of microscopy and cell biology, cytologists have reported observations of "lifeless bodies", "granules", "inclusions" and other membrane-less structures (Wilson, 1896, 1899). Despite being observed for over a century, they have come to be extensively studied only in the past decade, largely owing to advances in contemporary technologies that allow probing these structures at unprecedented spatiotemporal resolution, both *in vitro* and *in situ*. In addition to technical innovations, our understanding of these mesoscopic structures has been shaped by the metaphors used to describe MLOs over the years.

1.1.2. History of membraneless organelles

Membraneless structures like the nucleolus, nuclear speckles and some RNA-protein granules have been studied since the first half of the 20th century, although the earliest reports of such structures go back to the 1800s (Alberti et al., 2019). The most prominent of these structures, the nucleolus, was first described as an "organelle", in the sense of a distinct compartment with an associated function (Monty et al., 1956). Thus, the earliest descriptors to signify subcellular compartmentalization were borrowed from canonical membrane-bound organelles, and simply denoted observable organization. While this view provided a framework to understand the relationship between the structure of such compartments and their function, it did not provide a way to understand the physical origins of nucleoli.

The first decade of the 2000s saw attention turning to the function of various, newly discovered classes of membraneless structures. Structures like P-bodies, stress granules (SG), purinosomes and G-bodies were described as "granules", "compartments" or "clusters" (An et al., 2008; Anderson and Kedersha, 2006; Jin et al., 2017), terms that emphasize the appearance of such structures under the light or fluorescence microscope. These terms marked, however, a departure from "organelles" - they did not necessarily presume an associated biological function. This closely followed the first reports of the dynamic biophysical properties of these structures. Handwerger *et al.* recognized that nuclear condensates, that the authors reported to be "porous" and "sponge-like", are materially continuous with the nuclear matrix, and do not pose a barrier to diffusion, while still being compositionally distinct from the nucleoplasm (Handwerger et al., 2005). Brangwynne *et al.* noted that cytoplasmic RNA-protein (RNP) "granules are…biophysically similar to the rest of the intracellular fluid, and yet appear to represent a different "state" of cytoplasm, comprised of a locally distinct molecular ensemble" (Brangwynne, 2013). These observations broadened the study of MLOs to include the study of common principles underlying their origins, and revealed several unusual features, such as liquid-like characteristics, liquid-to-solid transitions, etc. The various contexts in which MLOs are now known to exhibit dynamic fluid properties like droplet fusion, surface tension, dripping, wetting and viscoelasticity have been reviewed elsewhere (Berry et al., 2018; Hyman and Simons, 2012).

Since the 2010s, the term "membraneless organelle", originally used to describe the nucleolus, started to be applied in a more general sense to RNA-protein granules and other "assemblies/assemblages" that show fluid-like properties (Brangwynne, 2013). This broadening of the term from one specific structure to an entire category of structures similarly marked the start

of a unification and ascension of the study of MLOs, whose biological functions were previously underappreciated and considered unrelated.

With increasing interest in phase-separation as the basis of the formation of MLOs, the introduction of the phrase “biomolecular condensates” in 2017 has helped bridge the gap between physiological in situ observations of such structures, and inquiry into their origins. The term “condensate” explicitly refers to the process of MLO formation and, in doing so, goes beyond the signifier of mere organization connoted by “droplet/membraneless organelle” to make a firmer claim about a specific mechanism of formation via phase transition (Banani et al., 2017b; Courchaine et al., 2016b). Converging on a consensus on terminology, the field has seen an increase in efforts to relate macromolecular structural and sequence features, and the nature of homo- and heterotypic intermolecular interactions that promote MLO assembly in vivo, and to study the physiological roles of such structures in development, stress response and disease (Quiroz et al., 2020).

Significant attention has been focused on the phase separation processes such as toxic protein aggregation such as those formed by β-amyloid peptide (Aβ) and tau proteins in Alzheimer’s disease, TDP-43/FUS in amyotrophic lateral sclerosis (ALS), huntingtin protein in Huntington’s disease, to name a few (Alberti and Dormann, 2019; de Oliveira et al., 2019; de Oliveira et al., 2020; Elbaum-Garfinkle, 2019a, b; Vanderweyde et al., 2013). Instead, here we provide a unifying account of intracellular phase separation in which widespread condensation across the proteome, representing the basal tendency of the intracellular environment, is co-opted to sense environmental fluctuations, or goes awry in disease.

1.1.3. Biological phase-separation is a natural tendency

A phase diagram is a graphical representation of the thermodynamics of phase separation. It depicts all possible phase states of the system in N-dimension phase space, where N is the number of parameters, called coupling constants, that determine the relative contribution of interactions to the free energy of the system compared to entropy (Goldenfeld, 1992). Key coupling constants relevant to biological phase transitions include temperature, concentration, valency and interaction strength. A critical point in this N-dimensional phase space is the threshold beyond which the differences between phases vanish and thus no phase separation is possible ("mixed"). If one coupling constant, say temperature, is fixed at or above its value at the critical point, phase separation will not occur regardless of the value of all other coupling constants. At any given temperature, the minimal concentration that causes the molecule to start forming condensates is called the saturation concentration and increasing the concentration may cause the system to enter the two-phase region ("demixed"). (Figure 1).

A biological perturbation of particular interest is change in the intracellular concentration frequently associated with altered gene expression or nucleocytoplasmic trafficking in response to a signal or a result of misregulation. Unlike these processes, hyperosmotic stress can cause much more rapid changes in effective protein concentration in the cell (Jalihal et al., 2020b). While the impact of changing concentration on phase separation is easy to study in vitro, there are important caveats regarding relating these results to intracellular concentration changes because biological perturbations often entail changes in multiple coupling constants simultaneously. Hyperosmotic compression, for instance, leads to a decrease in diffusion rates, an increase in "crowding", and possible ionic imbalances in addition to changes in effective concentrations of biomolecules

(Kedersha et al., 1999). This is similar to changes that have been reported in bacteria, yeasts and protists in response to glucose starvation, in which volume change causes a fluid-to-glass transition of the intracellular space, simultaneously impacting diffusivity as well as intracellular pH (Isom et al., 2018; Joyner et al., 2016; Munder et al., 2016). In such perturbations, the net phase transition depends on the cumulative effects of the perturbation in reshaping the phase boundaries and altering the saturation concentration (Figure 1-1A).

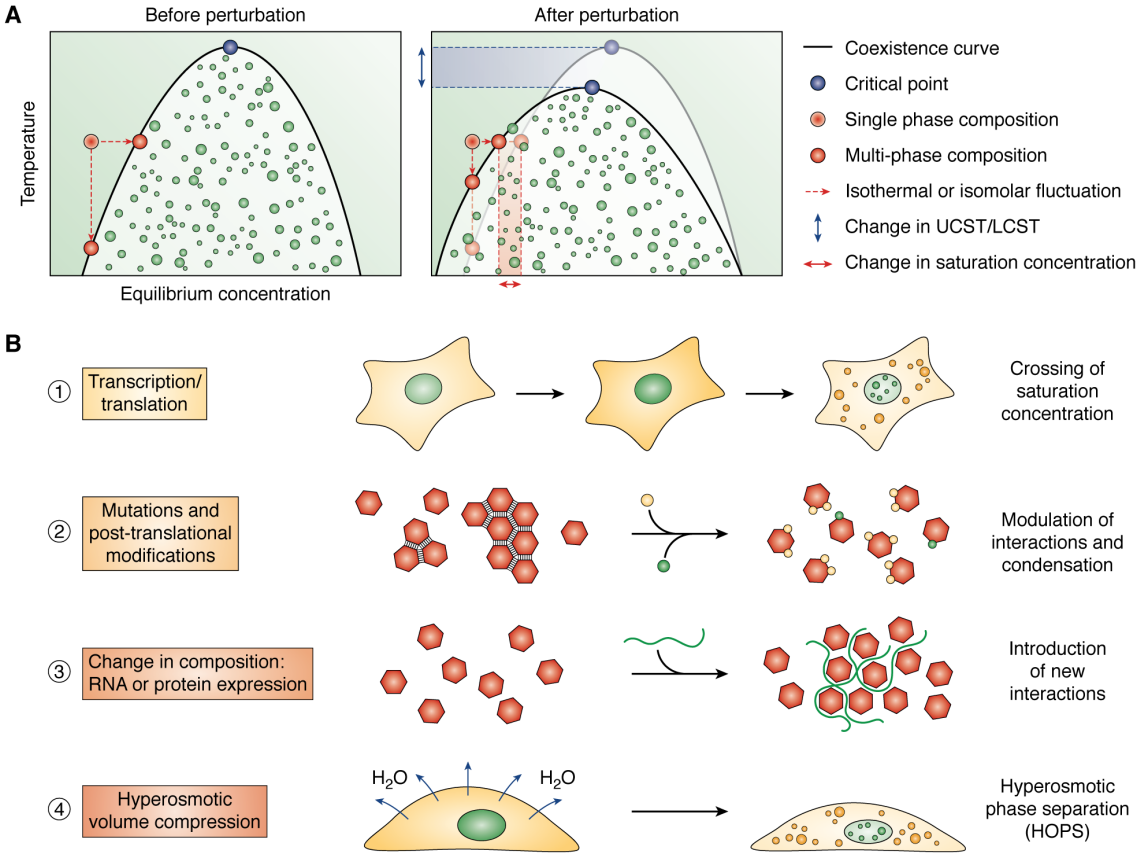

Figure 1-1 Phase separation induced by biological perturbations. **A.** A phase diagram shows the one-phase and multi-phase regions in temperature-composition space (left). Changes in temperature and concentration cause the system to transition between the single-phase region and multiphase region, shown as isothermal concentration changes or isomolar temperature changes. Biological perturbation can impact the phase diagram itself, affecting saturation concentrations and upper and/or lower critical saturation temperatures (UCST/LCST, right). **B.** 1. RNA or protein expression change their concentration until the saturation concentration is crossed. 2. Post-translational modifications such as methylation and phosphorylation or dephosphorylation alter the association strengths of the solutes and can serve as biological mechanisms to modulate condensation. 3. Changes in intracellular composition by altered

expression of RNAs or proteins can modify the phase behavior by introducing new interactions. 4. Hyperosmotic volume compression leads to a sudden jump in concentration and crowding, resulting in hyperosmotic phase separation

Extensive effort has been dedicated to elucidating the molecular features that drive intracellular phase separation (Dignon et al., 2020; Wang et al., 2018b). The most general requirement is multivalency, that allows molecules to form large assemblies via multiple inter-molecular contacts. Within protein-protein interfaces, arginine-glycine-glycine/arginine-glycine motifs (Thandapani et al., 2013), π-π (Vernon et al., 2018), cation-π, and charge-charge interactions, among others, have been shown to drive protein phase separation (Feng et al., 2019; Lin et al., 2018; Posey et al., 2018; Protter et al., 2018; Turoverov et al., 2019). These interactions stimulate the higher-order assembly of prion-like domains in protein misfolding diseases (Wang et al., 2018b), together with disordered regions and RNA-scaffolded assembly (Berry et al., 2018; Sanders et al., 2020; Yang et al., 2020). Additionally, structured protein domains are now emerging as mediators of widespread intracellular phase separation under conditions of high concentration and molecular crowding (Schmidt et al., 2020; Zhou et al., 2018).

Disrupting any of these key interactions driving phase-separation is expected to interfere with the phase-separation potential of a system. Consistent with this expectation, post-translational modifications such as phosphorylation and methylation have been found to modulate condensation responses, (Bah and Forman-Kay, 2016; Owen and Shewmaker, 2019; Rai et al., 2018). The effects of phosphorylation in particular can be dramatic, and appropriately the kinase DYRK3 that prevents condensation of splicing factors in M-phase has been referred to as a "dissolvase" (Rai et al., 2018). Similarly, SG assembly in response to various stresses depends on phosphorylation of G3BP and PABP (Kedersha et al., 2013a).

1.1.4. Phase-separation responses to environmental fluctuations

Eukaryotic cells, from yeast to human, respond to a wide variety of cell-intrinsic and -extrinsic fluctuations by condensation of proteins and RNAs (Banani et al., 2017a). The induction of P-bodies and assembly of SGs are two highly studied, and evolutionarily conserved, stress adaptation mechanisms that are triggered downstream of the integrated stress response (ISR) (Kedersha et al., 2013b). The ISR is a multistep signaling cascade activated in response to, for example, viral infection, nutrient deprivation, heat shock, oxidative and endoplasmic reticulum stress, and enhances cell survival by altering global protein translation (Pakos-Zebrucka et al., 2016). While the downstream pathways of ISR are shared, the sensor of each individual type of stress is distinct, conferring a certain degree of specificity to each stress. For instance, Pab1 (polyA binding protein) and Pub1 (polyU binding protein), two highly expressed proteins in yeast, are differentially enriched within SGs during temperature shock and pH shock respectively (Kedersha et al., 2013b; Yoo et al., 2019). Once the pathways are triggered, the pool of non-translating mRNA-protein complexes along with phosphorylation of SG component proteins participate in a network of multivalent interactions, ultimately triggering the assembly of SGs (Kedersha et al., 2013b; Riback et al., 2020; Sanders et al., 2020; Yang et al., 2020). In addition to regulating protein translation, cells suspend protein and ribosomal RNA (rRNA) metabolism by sequestering misfolded proteins and nuclear RNA-binding proteins in the nucleolus in response to impaired rRNA processing and DNA damage (Frottin et al., 2019; Latonen, 2019). Proteins that are directed to nucleoli under these conditions are thought to undergo translocation to these sites via their interactions with stress-associated non-coding RNAs.

Emerging evidence suggests that condensation responses are also involved in cell signaling cascades that aid cellular homeostasis in response to physiological cues. Condensates at cell membranes (Case et al., 2019a) and in the cytosol have been shown to regulate cell division, migration and invasion (Case et al., 2019b; Huang et al., 2019), transgenerational memory (Caudron and Barral, 2013; Majumdar et al., 2012; Si et al., 2010) and immunomodulation (Su et al., 2016) in response to a variety of morphogens and endo/para/autocrine signals. In addition to acting across a range of timescales, condensation in response to external perturbations plays a critical role in shaping the spatial organization of cells by moving RNAs and proteins into dynamic MLOs with complex organization, suggesting an intimate relationship between macromolecular sequence, intracellular organization and the extracellular environment (Al-Husini et al., 2020; Ma and Mayr, 2018; Tian et al., 2020; Trcek et al., 2020).

1.1.5. P-bodies and Stress granules

P-bodies, also called processing bodies, are RNP condensates that are enriched for non-translating mRNAs and mRNA degradation factors (Cougot et al., 2004). They are constitutively present in the eukaryotic cells, and were discovered in part by autoantigen staining from patient serum that revealed distinct cytosolic foci (Bloch et al., 2006; Eystathioy et al., 2002; Eystathioy et al., 2003). While detailed investigation of the constituents of P-bodies by immunostaining and mass spectrometry has led to the enumeration of a long list of protein components, and there is some evidence for P-bodies conferring protective phenotypes against viral infections in yeast, it remains unclear what if any general function P-bodies serve in cells (Beckham and Parker, 2008; Hubstenberger et al., 2017c; Luo et al., 2018; Noueiry et al., 2003).

SGs unlike P-bodies are not constitutively present but are induced upon heat and oxidative stress and other environmental insults. They are induced by the presence of and are enriched for non-translating mRNAs (Kedersha et al., 2002; Kedersha et al., 1999) and their formation is disrupted upon viral infections or exposure to bacterial pathogenic components (Lloyd, 2013; Reineke and Lloyd, 2013; Vonaesch et al., 2017). Thus, SG induction is associated with eIF2a phosphorylation occurring downstream of PKR activation. While PBs and SGs share many components, they contain various protein components that distinguish them from each other, prominently G3BP1. Phosphorylation causes a switch in G3BP conformation that promotes granule assembly typically 10-30 minutes after exposure to stress (Sanders et al., 2020).

1.2. Protein translation regulation

Protein translation is regulated by modulating the translation machinery or by altering the stability of mRNAs. Various mechanisms modulate the translation initiation and elongation. Prominently, phosphorylation of proteins of the cap-binding complex, and other components of the elongating ribosome is known to modulate global translation upon activation of stress response pathways or anti-growth signals (Kapp and Lorsch, 2004; Preiss and Hentze, 2003).

Dedicated mechanisms exist in eukaryotic cells to degrade mRNAs. Eukaryotic mRNAs are protected from these mechanisms by the presence of a 5' "cap", composed of a 7-methyl guanosine triphosphate (7mG) and a template independent 3' poly A "tail". The decapping complex catalyzes the removal of the 5' cap, allowing 5'-to-3' exonucleases such as XRN1 and the LSM1 complex to act upon the substrate (Blasco-Moreno et al., 2019). Likewise, the CCR4-NOT deadenylation complex can bind and remove the 3' polyA tail allowing the RNA to be degraded by 3'-to-5' exonucleases such as the nuclear exosome (Chen et al., 2002). While these

mechanisms can act on all mRNAs, non-coding RNA-based mechanisms confer specificity to specific mRNAs, and these mechanisms recruit degradation factors to target mRNAs.

1.2.1. Non-coding RNA functions

The central dogma of molecular biology as propounded by Watson and Crick is that genetic information encoded in DNA is relayed via RNA intermediates to its final functional form as a protein (Crick, 1970). In addition to its central role as a messenger, RNA has since been shown to mediate a multitude of roles beyond encoding proteins (Li and Liu, 2019; Palazzo and Lee, 2015). Indeed, the most important non-protein coding function of RNAs is to regulate and modulate the level of gene expression.

Non-coding RNAs are often conserved, vary in size and structure and are frequently found in RNA-protein complexes (Diederichs, 2014). They are known to regulate gene expression by modifying epigenetic marks on histones (long non-coding or lncRNAs), and by destabilizing mRNAs or modulating protein translation (short non-coding RNAs) (Long et al., 2017; Tsai et al., 2010). Beyond these mechanisms of gene regulation, 3'untranslated regions (3'UTRs) of mRNAs are known to spatially regulate protein translation, complex formation and localization (Ma and Mayr, 2018). This thesis focuses on RNA-dependent mechanisms that directly impact protein translation by destabilizing mRNAs.

Short RNA-mediated translation regulation mechanisms, first discovered in *C. elegans* by Craig and Mello, are understood in terms of the specific mechanisms of short-hairpin RNAs (shRNAs), small interfering RNAs (siRNAs) and microRNAs (miRNAs). These short RNAs undergo numerous processing steps after which a single 21 nucleotide strand gets incorporated

within a protein of the Argonaut (AGO) family possessing PIWI domains, and act as guides to direct the silencing RNA-protein complexes to their target RNAs. They all typically bind to the sequence-complementary regions in the 3' untranslated regions (UTRs) of mRNAs. These different small RNA-based pathways are differentiated based on their specific impact on mRNAs: siRNAs bind to 21-nt long sequence-complementary regions and stimulate AGO2's endonucleolytic activity. miRNAs guide the RNA-induced silencing complex (miRISC) via sequence complementarity to binding sites present on mRNAs, called miRNA recognition elements (MREs), and recruits mRNA degradation enzymes to the target rather than stimulating internal cleavage.

1.2.2. miRNAs, MREs and the ceRNA hypothesis

miRISC is usually present at limiting levels with respect to the transcripts it can bind to and is consequently bound to saturation under physiological expression levels. This is thought to cause binding-competition between the target transcripts, leading to the reversal of translation repression. Because miRNA targets have been shown to constitute highly connected networks, it is conceivable that changes in repression brought about by binding competition can lead to broader changes in the protein expression profile of the cell.

A miRNA can optimally bind to any sequence complementary to a 7nt "seed" region at its 5' end. Additionally, a miRNA can bind with lower affinity to sequences that possess imperfect seed-complementarity and/or complementarity to the miRNA's 3' end (Denzler et al., 2016). Any sequence that can interact with a miRNA is referred to as a miRNA recognition element or MRE. A seed-matched, 7nt MRE is expected to be found every 2400 bases in the genome, assuming equal occurrence of the four bases. However, many experimentally verified targets of miRNAs are

enriched for seed-specific MREs in their 3'UTRs, above the rate expected by random chance (Abrahante et al., 2003). Many of these are also evolutionarily conserved (Kristjánsdóttir et al., 2015). It has been speculated that additional binding sites increase the degree of translation repression by increasing probability of RISC binding although it remains unclear what specific factors influence MRE-dependent repression in cells (Mayr et al., 2007).

A typical miRNA is present at 1000-50,000 copies per cell and is close to its regime of saturation given the abundance of low- and medium-affinity MREs. Consequently, major changes in the overall number of MREs or miRNAs can independently be expected to change specific miRISC binding to target transcripts (Mukherji et al., 2011). Such changes result in "derepression" by decreased miRISC binding, and subsequent increase in translation of the previously repressed transcript. This idea of reciprocal regulation, where target transcript abundance regulates miRNA function, and vice versa has been formalized in terms of the competitive endogenous RNA (ceRNA) hypothesis. According to the hypothesis, the cellular MRE number dictates the magnitude of binding-competition to a limited miRISC pool and serves as means to modulate overall repression of translation (Seitz, 2009). Experimental evidence for such reciprocal regulation has primarily come from over-expression studies, by comparing ensemble mRNA, miRNA and protein levels before and after overexpression of MREs (Bosson et al., 2014a; Denzler et al., 2016). However, binding-competition and derepression have not been validated at the level of a single transcript. Thus, it remains unclear how transcript levels, MRE number and miRISC levels collectively contribute to establishment of repression and what concentration regimes support derepression.

1.3. Visualizing biology: Single molecule fluorescence microscopy (SMFM)

SMFM techniques are well-suited to study molecular processes that occur in multiple steps, proceed via parallel reaction pathways, show transient excursions to distinct states, and/or contain varying components, all of which are frequently true of RNA-proteins interactions (Moffitt et al., 2010; Wahl et al., 2009). The most important advantage is that these methods allow heterogeneous molecular "behaviors" to be uncovered in asynchronous populations of molecules proceeding through multiple reaction pathways at different rates (Larson et al., 2014; Lu et al., 1998). These single molecule behaviors can be scrutinized at a spatio-temporal resolution inaccessible to bulk techniques, leading to insights that can be directly compared with bulk data by post-acquisition time and ensemble averaging.

The general benefits and specifics of performing single molecule studies are beyond the scope of this chapter, but have been reviewed elsewhere (Liu et al., 2015; Roy et al., 2008; Walter et al., 2008). In this chapter, we instead will focus on the salient features of SMFM and practical considerations for its application to the study of RNPs.

A variety of SMFM approaches exist today, the exact choice of which depends largely on the study design and experimental goals. SMFM has been used to investigate numerous RNPs, including those involved in transcription, splicing, RNA modification and editing, chaperone activity, and RNA interference (Figure 2). Despite obvious differences in the underlying biology, key experimental elements common to all of these studies include illumination, a strategy for labeling the biomolecule(s) of interest, detection of fluorescence, and data analysis, as discussed below.

1.3.1. Illumination and detection

By design, SMFM approaches aim to characterize the behavior of individual molecules. However, detecting the signal from an individual molecule in the background of other molecules, potential contaminants, and instrumental noise can be challenging. Fluorescence itself facilitates distinguishing genuine signal from background as light emitted from fluorescently tagged biomolecules is red-shifted relative to the wavelength of laser light used for excitation. This spectral separation (*i.e.*, 'Stokes shift') between the excitation and emission wavelength maxima makes genuine fluorescence signal easily distinguishable from background scattering of the sample medium.

In addition to spectral isolation of the relevant signal, limiting the volume of illumination improves signal-to-noise by decreasing the contribution of out-of-focus emission. Of the illumination modalities that achieve selective volume illumination, total internal reflection fluorescence microscopy (TIRFM) is perhaps the most widely implemented (Figure 2A). In TIRFM, the excitation beam is totally internally reflected near the sample plane (Toomre, 2012). An evanescent field of excitation light is generated at the surface that extends ~100 nm into the sample. This evanescent field illuminates molecules immobilized at the imaging surface, thus minimizing background fluorescence from molecules deeper in solution. The level of background fluorescence observed in TIRFM experiments is dependent on the concentration of excess fluorescently labeled biomolecules in solution and provides good signal-to-noise up to fluorophore concentrations of ~100 nM. For RNA and proteins that interact with high affinity, this effective concentration limit does not pose a problem. However, physiologically relevant interactions often involve micromolar affinities of binding partner(s). Zero-mode waveguide (ZMW) technology

allows single molecule resolution even in solutions with high concentrations of fluorescent components (Levene et al., 2003), and have been particularly useful in studies of the ribosome (Tsai et al., 2016) (Figure 1-2B).

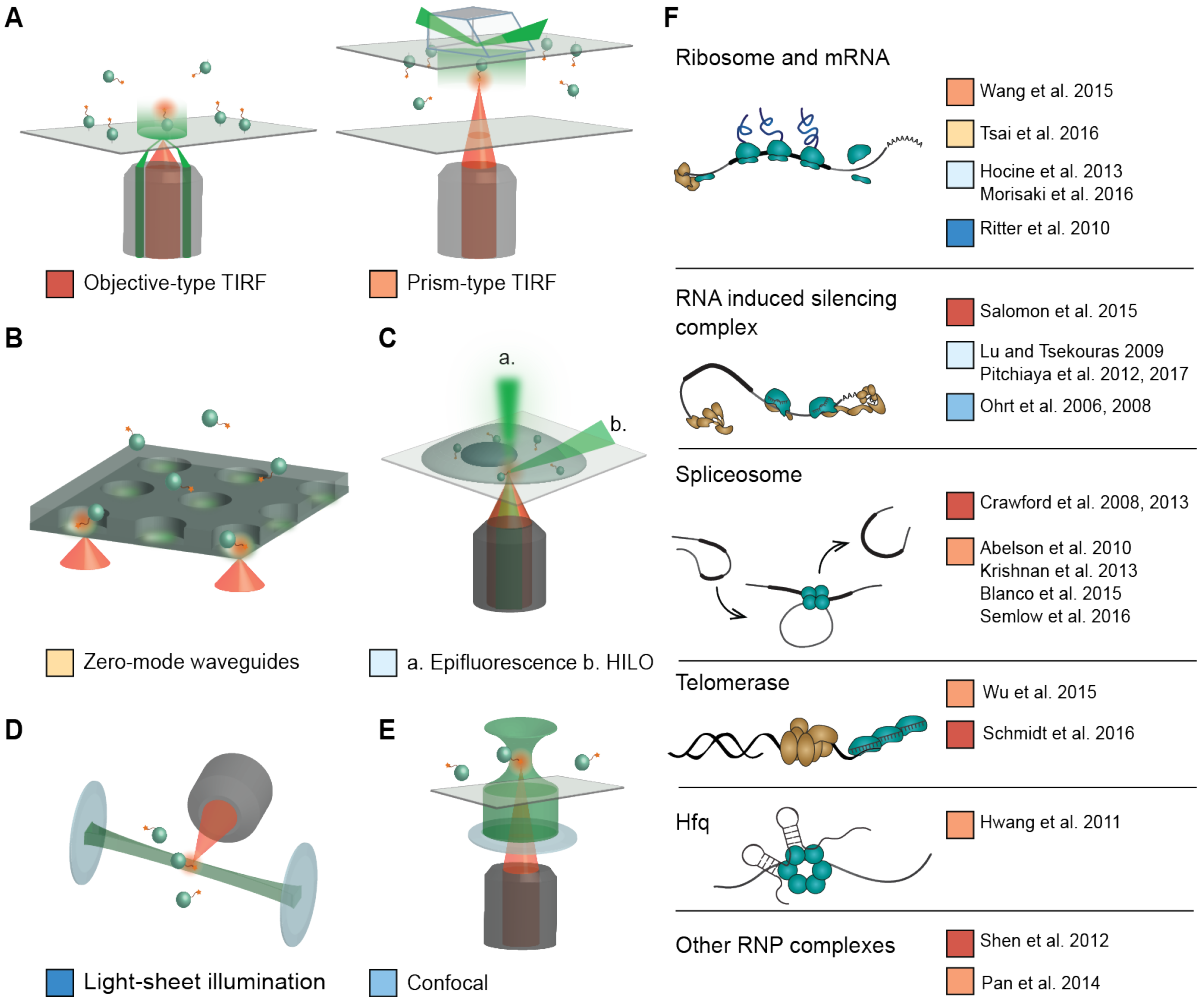

Figure 1-2. Overview of single molecule microscopies applied to study RNPs. **A.** Objective- and Prism-type TIRFM configurations **B.** Zero-mode waveguides **C.** a. Epifluorescence b. HILO illumination **D.** Light sheet microscopy **E.** Confocal illumination **F.** Selected studies on RNPs that have employed fluorescence-based single molecule methods. Colored boxes indicate the type of microscopy configuration used.

Another strategy to limit out-of-plane fluorescence by controlling the illumination area is highly inclined and laminated optical sheet (HILO) illumination (Tokunaga et al., 2008) (Figure 1-2C). In HILO microscopy, the illuminated region is thicker than it is for TIRFM (e.g., ~7 μm

for an illuminated area with a diameter of 20 μm), and contains a *z*-component, that allows for imaging of molecules that lie micrometers above the coverslip surface. These characteristics make HILO microscopy particularly suited for studying samples with three-dimensional spatial distributions, such as single molecules inside live cells. Even more sample penetration depth can be achieved by light sheet fluorescence microscopy (LSFM), where a focused sheet of light is used to illuminate only a thin section of a thick sample for single molecule detection (Ritter et al., 2010) (Figure 1-2D). Confocal microscopy uses pinholes to limit the volume in which single molecules are detected (Figure 1-2E). In addition to 2-D scanning, confocal microscopy is typically used in the context of fluorescence correlation spectroscopy (FCS) and two-color fluorescence cross-correlation spectroscopy (FCCS), in which a high-sensitivity photon-counting point detector generates time-resolved intensity measurements from the entire illuminated confocal volume (Gonzalez Bardeci et al., 2017; Liu et al., 2015).

1.3.2. Labeling proteins

For proteins, fluorophore tags may be genetically appended, as is the case with fluorescent proteins (FPs) including GFP, mCherry, and their many variants (Thorn, 2017). However, FP tags are used almost exclusively in the context of intracellular studies as their large size and unfavorable photophysical properties (e.g., propensity for blinking, low brightness) so far make them less desirable for *in vitro* single molecule studies.

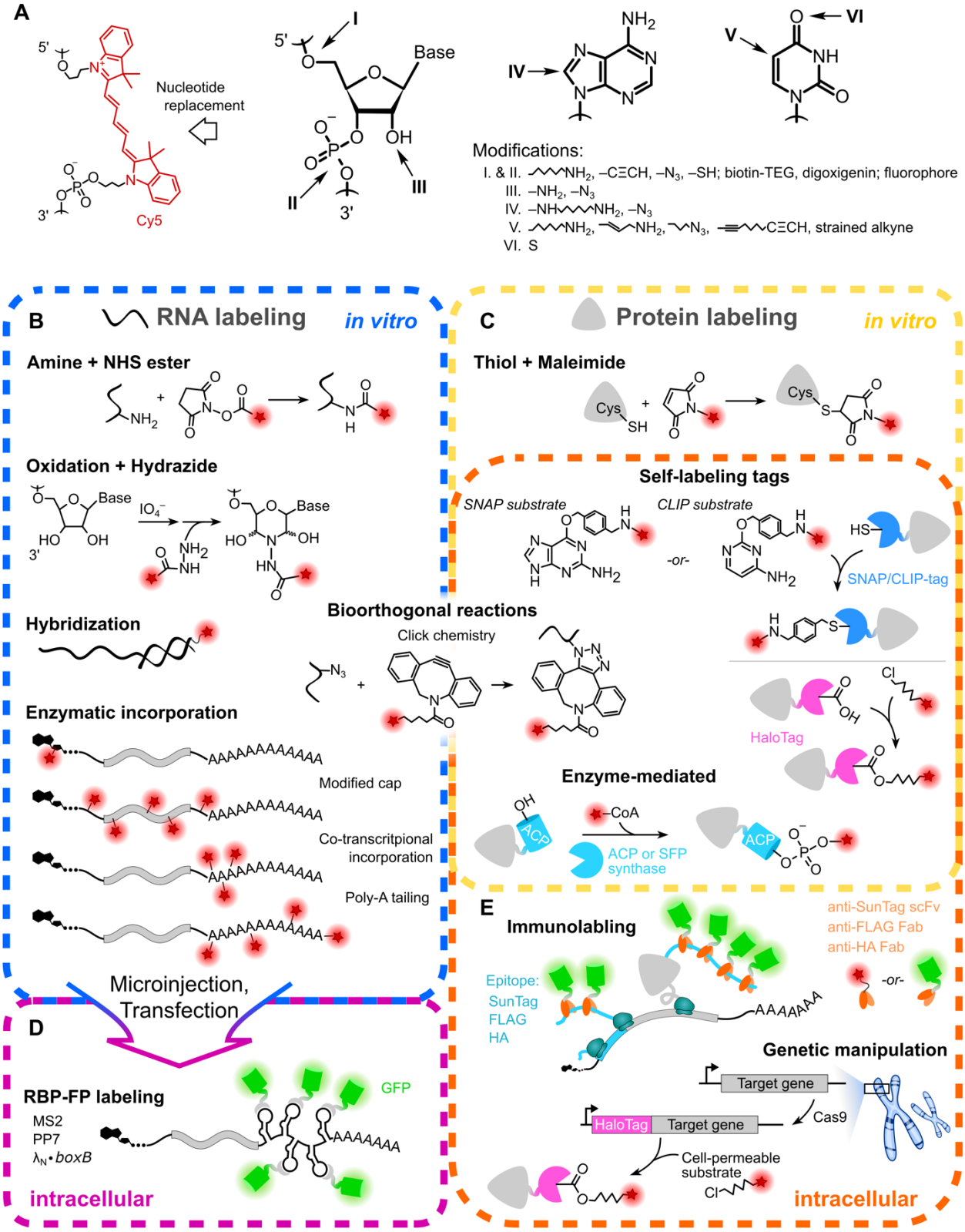
A
Nucleotide replacement
Cy5
Base
OH
Modifications:
I. & II. –NH2, –CΞCH, –N3, –SH; biotin-TEG, digoxigenin; fluorophore
III. –NH2, –N3
IV. –NH–NH2, –N3
V. –NH2, –NH2, –N3, strained alkyne
VI. S
B RNA labeling in vitro
Amine + NHS ester
Oxidation + Hydrazide
Hybridization
Enzymatic incorporation
Modified cap
Co-transcritpional incorporation
Poly-A tailing
Bioorthogonal reactions
Click chemistry
C Protein labeling in vitro
Thiol + Maleimide
Self-labeling tags
SNAP substrate
CLIP substrate
-or-
SNAP/CLIP-tag
HaloTag
Enzyme-mediated
ACP
–CoA
ACP or SFP synthase
Microinjection, Transfection
D
RBP-FP labeling
MS2
PP7
λN•boxB
GFP
intracellular
E
Immunolabling
Epitope:
SunTag
FLAG
HA
anti-SunTag scFv
anti-FLAG Fab
anti-HA Fab
-or-
Genetic manipulation
Target gene
HaloTag
Cas9
Cell-permeable substrate
intracellular

Figure 1-3 Strategies for labeling RNA and protein components for single molecule fluorescence. **A.** Modifications are possible at various positions on RNA molecules prepared through chemical synthesis, including the 5' and 3' termini (I and II, respectively), the 2' position of the sugar (III), and various positions on the nucleobase (IV, V, and VI), among others. Modifications can include reactive chemical moieties that are used for subsequent conjugation reactions, small molecules like biotin and digoxigenin for immobilization, or direct attachment of fluorophore dyes, or even replacement of entire nucleotides by fluorophores. **B.** Example strategies for preparing fluorescently labeled RNA for in vitro studies. Fluorescent labels are shown as red stars. **C.** Example strategies for preparing fluorescently labeled protein for in vitro studies. **D.** For intracellular single molecule studies, RNA can be prepared using many of the methods suitable for in vitro work (described in B) and subsequently introduced into cells via microinjection or transfection. Alternatively, RNA transcripts can be labeled by inserting stem-loop repeat sequences that are bound by their cognate RNA binding proteins, that are expressed as fusions with intrinsically fluorescent proteins (RBP-FP). **E.** Example strategies for preparing fluorescently labeled protein for intracellular studies. In contrast to RNA, there is greater overlap between strategies for labeling protein that are suitable for in vitro and intracellular work. A small number of strategies, such as click chemistry using strained alkynes, can be applied to both RNA and proteins.

The shortcomings of FPs render proteins a more challenging target for site-specific labeling compared to RNA and the options for selective conjugation chemistries for amino acids are more limited compared to nucleotides. Fluorophore-NHS-ester derivatives readily react with primary amines and so can be used to label lysine residues as well as the N-terminus. For *in vitro* studies using recombinant protein, a more conventional strategy is to use fluorophore-maleimide derivatives, that have greater selectivity for the thiol side chain of rarer cysteine residues (Figure 1-3C). This method typically requires that native cysteines be significantly less reactive (and/or accessible) than the desired labeling position. Such was the case in a study of the role of initiation factor 2 (IF2) from *E. coli*, where removal of the three native cysteines in IF2 resulted in an unstable protein, however, labeling of an additional cysteine introduced through mutagenesis in the presence of the other native cysteines still resulted in site-specific labeling (Wang et al., 2015).

Among the other methods for site-selective labeling of proteins that have been developed (Adumeau et al., 2016), the use of unnatural amino acids to incorporate reactive handles, such as those for click chemistry, is one of the more promising avenues to achieve site specificity (Lee et al., 2016; Liu and Schultz, 2010).

Purification of labeled protein from unincorporated fluorophore can be non-trivial, because proteins, being more hydrophobic than nucleic acids, have a greater propensity to bind fluorescent dyes non-specifically. The purification scheme therefore merits careful consideration. While extensive dialysis or size-exclusion chromatography may be sufficient in some cases, for others unreacted fluorophore may most robustly be removed with ion-exchange chromatography under denaturing conditions (Hickerson et al., 2005).

Protein structure data are frequently unavailable and protein folding is difficult to predict. Furthermore, the complete details of a protein's RNA binding site and other interacting partners are frequently uncharacterized or ill-defined, thus precluding the rational choice of a labeling position. Despite these gaps in knowledge, there are many cases where determining the presence or absence of a given protein is sufficient, requiring only that the protein be fluorescently labeled in a way that preserves function. However, the knowledge of a fluorophore's exact location on the three-dimensional structure of a protein is required if the protein serves as the donor or acceptor in an smFRET experiment.

A third alternative for protein labeling are self-labeling protein tags and enzyme-mediated labeling tags that are genetically encoded. These tags have been developed to allow covalent attachment of small molecule fluorescent dyes, that can be used to label proteins in live cells, in cell extracts, or to label recombinant proteins (Figure 1-3C). Of these, notable examples include the SNAP and CLIP tags, based on human O^6-alkylguanine-DNA alkyltransferase, and the engineered dehalogenase HaloTag, all of which catalyze covalent self-addition of their respective ligands (Gautier et al., 2008; Los et al., 2008; Sun et al., 2011) . A conceptually similar, albeit non-covalent, self-labeling tag is *E. coli* dihydrofolate reductase (eDHFR) (Calloway et al., 2007).

1.3.3. Labeling RNPs for intracellular visualization

One advantage of using living cells in fluorescence microscopy is the ability to genetically encode fluorophore tags in the form of FPs. The most widely adopted intracellular RNA labeling strategy has been the use of RNA-binding proteins (RBPs) fused with an FP (Tyagi 2009). This method, first demonstrated for single RNA detection by Robert Singer's group, exploits the high specificity and affinity with which RBPs such as the viral coat proteins from the MS2 or PP7 phages bind their cognate RNA stem-loop structures. Since then, this technology has been expanded to other bacteriophages, such as λN protein binding to the RNA stem-loop of the boxB gene. Labeling is achieved by inserting these stem-loop sequences into untranslated regions (usually the 3' UTR) of mRNA transcripts, that are then bound by their respective RBP fused to an FP (Figure 1-2D). Because the excess of unbound RBP-FP fusion protein creates a high fluorescence background, and because photobleaching is vastly accelerated in live cells as compared to in vitro, multiple copies of the stem-loop sequence (typically 8 to 96) are required for single molecule sensitivity. Furthermore, multiple transcript species within the same cell can be simultaneously monitored by using combinations of RBPs tagged with distinct FPs (Hocine et al. 2013).

The biggest limitation of RBP-based detection is that their cognate stem-loops are ~20 nucleotides long, that makes RBP-based methods unsuitable to study small non-coding RNAs such as miRNAs, small interfering RNAs (siRNAs), tRNAs, etc. whose function is sensitive to RNA length. Furthermore, the added molecular mass of bound RBP-FP fusion proteins can alter the diffusion properties, localization and turnover of RNPs.

Another limitation of FPs is their relatively long maturation time. For studies specifically probing protein translation, using a classical fluorescent protein to study translation rate is of limited utility because of the slow maturation of the FP (the fastest maturing GFP variants fold in ~10 minutes) relative to translation elongation (seconds to minutes for a given transcript) (Thorn 2017). However, moving the fluorescent tag to an antibody probe that can recognize a peptide epitope with specificity as it emerges from the ribosome's exit tunnel allows rapid processes such as translation elongation to be studied in real-time at single molecule resolution. Such fluorescent "immunolabeling" of proteins has been demonstrated with the SunTag epitope and "spaghetti monster" fluorescent proteins (Figure 1-3E). In these methods, single proteins are detected when multiple labeled antibody probes bind to a repeated epitope, where detection is limited by diffusion of the probes and antibody-antigen affinity (Morisaki et al. 2016; Yan et al. 2016).

The relative simplicity of working with transiently or stably transfected cell lines has led genetically-encoded FP methods for single RNP visualization to become widely accepted. We refer the reader to reviews that cover the broad applications of RBP-based mRNA detection and live cell immunolabeling for intracellular single molecule visualization (Buxbaum et al. 2015; Lyon and Stasevich 2017). An alternative approach to fluorescently label proteins uses self-modifying enzymatic tags (Figure 1-3E). Pulse labeling with a cell-permeable, fluorescent HaloTag substrate, for example, allows a sufficiently sparse set of the native proteins to be labeled. Schmidt et al. (2016) used this strategy to show that the telomerase RNP is dynamically recruited to the telomere ends of chromosomes.

An alternative RNP labeling strategy that avoids genetic modification of RNAs/proteins for intracellular detection is to covalently attach synthetic fluorophore dyes to an exogenous RNA

and subsequently deliver it into cells. For longer RNAs, click chemistry has been used to covalently attach fluorophores to modified nucleotides that are co-transcriptionally incorporated into in vitro transcribed RNA without the need for lengthy exogenous sequence motifs (compare Figure 1-3B and D). For eukaryotic mRNAs, fluorophores can be incorporated into mRNAs in the cap structure (Mamot et al. 2017), randomly incorporated throughout the transcript (Schulz and Rentmeister 2014), in the poly(A) tail, or between the 3' UTR and poly(A) tail (Custer and Walter 2017). Such covalent attachment of the fluorophore allows labeled molecules to be detected with greater sensitivity, without the background of free fluorophores that is a recurrent challenge of RBP-based RNA detection. As with RBP-mediated labeling, however, there can be functional consequences to these covalent labeling strategies—for example, random fluorophore incorporation throughout the transcript was shown to dramatically impair the coding function, and incorporation of fluorophores in the 3'UTR was shown to stabilize mRNAs (Custer and Walter 2017).

The choice of delivery method determines the types of observations that can be carried out subsequent to exogenous chemical labeling. The following section briefly surveys these methods.

1.3.4. Delivering materials for visualization in cells

The wide array of available intracellular delivery methods presents several choices for RNA and/or protein delivery (Stewart et al. 2016). They fall on a spectrum defined by, on one hand, their ability to deliver precise amounts of material to individual cells and by, on the other hand, their throughput of cells. One subset of delivery strategies aims to temporarily disrupt the cell membrane using detergents, bacterial pore-forming toxins or various physical disruption methods (bead loading, fluid shearing, electroporation, etc.), relying on diffusion of cargo along

concentration gradients and the ability of cells to reseal breaks in their cell membrane. These strategies achieve efficient cargo delivery but are not suitable for applications requiring precise dosage control. Another delivery strategy in this class involves vesicle carriers and relies on fusion of lipid vesicles with the cell membrane or natural endocytic processes, for cargo delivery. Lipid-based transfection is perhaps the most widely used strategy, however, it is unsuitable for RNA delivery for single molecule applications, as the cargo often remains trapped in endosomes and is only slowly released into the cell (Hirsch and Helm 2015), leading to the risk of artifacts and/or misinterpretation.

In contrast, methods that involve active forces, such as delivery by direct microinjection using micro-needles or nano-straws, offer more precise control over the amount of material delivered to each cell, however, they can do so only with lower throughput. Microinjection, like other membrane disruption methods, relies on the ability of cells to rapidly reseal breaks in the cell membrane (Figure 1-4) and thus can encounter problems with cell viability if improperly executed (Pitchiaya et al. 2013). The microinjector needle is a fine glass capillary used to inject femtoliters of cargo solution into each cell, allowing for precise delivery into sub-cellular compartments such as the nucleus or the cytosol. Microinjection requires only small cargo quantities compared to any other bulk delivery strategy, making it a particularly valuable and preferred tool for delivering fluorescently labeled RNP components that may be technically challenging to label and purify.

1.3.5. Single-molecule RNP visualization in living cells

The toolbox of complementary fluorescence-based approaches available today allows dynamic RNP interactions to be probed directly inside living cells. For example, fluorescence recovery after photobleaching (FRAP) and FCS both quantify diffusion of labeled molecules

(Bacia et al., 2014; McNally, 2008). The former measures the rate at which fluorophore-labeled molecules diffuse back into a small photobleached area (typically over minutes), whereas the latter measures fluorescence fluctuations in a small volume of the cell on sub-second timescales. These techniques have been used to study fluorescent molecules inside living cells for over three decades, and while they do not necessarily provide single-molecule resolution they have set the stage for intracellular SMFM.

More recently, the commercialization of photostable fluorophores, increasingly sensitive cameras, and super-resolution illumination strategies together have contributed to advances in a third technique, intracellular single particle tracking (SPT) (Shen et al., 2017). SPT bridges the capabilities of ensemble approaches such as FRAP and FCS (diffusion information) with those of *in vitro* single molecule analysis, such as colocalization (interaction) time and stepwise photobleaching analysis (for stoichiometry).

The principle behind SPT is that fluorescently labeled molecules, when present at sufficiently low densities, can be detected and tracked in time as bright, diffraction-limited "spots" using an illumination strategy such as HILO or TIRFM. The resulting trajectories represent the actual diffusive motion of the molecules and can reveal transient interactions with their local environments. Thus, intracellular SPT can be applied to study RNP reactions using cultured living cells themselves as reaction vessels, providing exquisite spatiotemporal resolution to make observations that enable both hypothesis- and discovery-driven approaches to studying the biophysical behavior of RNPs (Figure 1-4A).

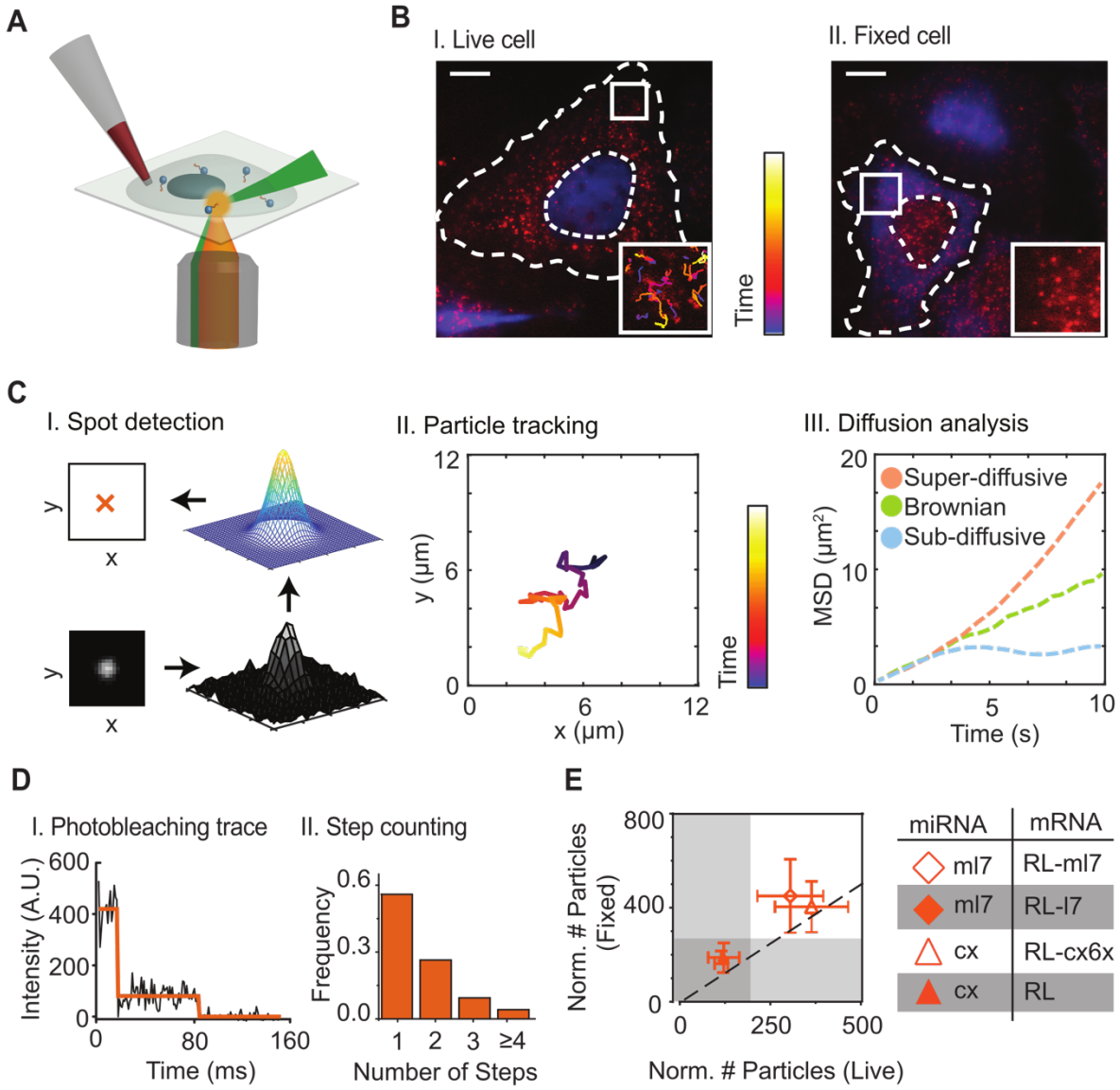

Figure 1-4 Intracellular single molecule visualization A. Microinjection is an effective strategy to deliver labeled RNAs into living cells. The injected material can be imaged using various fluorescence microscopy techniques. Intracellular Single-molecule High-Resolution Localization and Counting (iSHiRLoC) uses HILO illumination to rapidly acquire images with single-molecule resolution for particle tracking. B. Injected cells are distinguished from non-injected cells by the presence of an injection marker, a slowly diffusing, fluorescently labeled inert compound. Shown here are two cells injected into the nucleus (I) and cytosol (II) with Alexa488-labeled 100 kDa Dextran. Labeled miRNAs appear as diffusing, diffraction-limited spots upon time lapse imaging of live cells (I, inset) or as diffraction-limited spots in formaldehyde-fixed samples (II, inset). Scale bars represent 10 μm. C. I. The intensity profiles of diffraction-limited spots, recorded as pixelated point-spread functions, can be analyzed to obtain the spot centers with sub-pixel accuracy, such as by fitting the intensity profile to 2D Gaussians. II. Particle-tracking of the spot centers results in 2- or 3-dimensional diffusion trajectories. III. Displacements in successive frames yield mean-squared displacement (MSD) profiles, informing about diffusion types. D. Photobleaching analysis. Cy5 fluorophores bleach rapidly and in a step-wise manner. The number of discrete step drops in intensity is a proxy for the number of molecules in a single diffraction limited spot. Adapted with permission from Pitchiaya et al. (2012). E. Correlating the number of fluorescent spots in fixed tissue with the number of diffusion filtered trajectories yields an estimate of

turnover and functionality of the labeled molecules. The open shapes represent counts of a mutant (mutant *let-7*, ml7) and artificial (*cxcr4*, cx) miRNA co-injected with mRNAs bearing complementary binding sites, and the filled shapes represent conditions where the co-injected mRNAs bore mismatched (*let-7*, l7) or no binding sites in the 3'UTR downstream of an ORF encoding *Renilla* luciferase. Adapted with permission from Pitchiaya et al. (2017).

The following sections briefly review methods for the fluorophore labeling and intracellular macromolecule delivery needed to perform intracellular SPT.

1.3.6. Analysis and interpretation of SPT experiments

The first step for particle tracking is detection of the "spot" that represents the spatial location of a fluorescently labeled molecule of interest. The intensity levels of the brightest pixels of the spot together with the surrounding pixels approximate the point spread function (PSF) of the fluorophore(s) present on the molecule or complex. The challenge of spot detection lies in finding the center of the PSF, given the discrete pixel size and variable camera noise. A number of different algorithms exist today to perform this task (Chenouard et al. 2014) (Figure 6B). Once detected, the spots can then be tracked (i.e., temporally linked) through successive frames to yield spatiotemporal trajectories, provided the spots are sufficiently visible in the focal plane in (almost) every frame, and the particles are present at sufficiently low density for the temporal linking to be unambiguous.

From these particle trajectories, the type of motion exhibited by individual molecules can be classified into one of various types of diffusion. The most common, simple and useful tool to discriminate diffusive behaviors of single particles is the time-averaged mean-squared displacement (MSD) (Figure 6C). This plot is used to characterize the trend of the displacement of the particle at increasing time intervals. For a given trajectory, the deviation of the MSD plot from linearity is used to classify the motion as diffusive (no deviation), sub-diffusive (curved down) or super-diffusive (curved up). RNPs often exhibit complex trajectories that can be modeled

as mixtures of directed motion (such as during periods of active transport along axons) and Brownian (random) diffusion (Monnier et al. 2015). Together, such characterization can yield information regarding the molecular weight of the particle under study, and its interaction with its local environment, such as binding to and dissociation from unlabeled (and thus invisible) partners of distinct diffusivity (Knight et al. 2015).

Multicolor particle tracking can reveal even more about the intracellular milieu. By labeling molecular species using dyes with spectrally separated emission maxima, currently up to four different types of particles can be simultaneously tracked (Juette et al. 2014). The interaction between these differently labeled components can be read out as spatiotemporal colocalizations between trajectories of differently colored particles, similar to the in vitro techniques summarized in section III.2. Colocalizing trajectories can then be analyzed to characterize the kinetics and search dynamics of intracellular interactions, as has been the case for examining the intracellular search dynamics of RNP machines such as the Cas9 enzyme (Knight et al. 2015), telomerase (Schmidt et al. 2016), and miRNA-RISC (miRISC) complexes, as well as for studying the recruitment of small RNAs to sites of DNA double-strand breaks (Michelini et al. 2017).

1.4. Outline of thesis

Chapter 2 describes results regarding the molecular determinants of RNA localization to P-bodies. Chapter 3 described a novel proteome-wide phase-separation phenomenon in response to osmotic stress called hyperosmotic phase separation (HOPS). Chapter 4 provides evidence for biophysical mechanisms that promote the efficiency of miRNA-mediated target repression in mammalian cells. Chapter 5 showcases future directions and an outlook based on this body of work.

1.5. References

Abrahante, J.E., Daul, A.L., Li, M., Volk, M.L., Tennessen, J.M., Miller, E.A., and Rougvie, A.E. (2003). The Caenorhabditis elegans hunchback-like gene lin-57/hbl-1 controls developmental time and is regulated by microRNAs. Dev. Cell *4*, 625-637.

Adumeau, P., Sharma, S.K., Brent, C., and Zeglis, B.M. (2016). Site-specifically labeled immunoconjugates for molecular imaging–Part 2: Peptide tags and unnatural amino acids. Mol. Imaging Biol. *18*, 153-165.

Al-Husini, N., Tomares, D.T., Pfaffenberger, Z.J., Muthunayake, N.S., Samad, M.A., Zuo, T., Bitar, O., Aretakis, J.R., Bharmal, M.M., Gega, A.*, et al.* (2020). BR-Bodies Provide Selectively Permeable Condensates that Stimulate mRNA Decay and Prevent Release of Decay Intermediates. Mol. Cell *78*, 670-682.e678.

Alberti, S., and Dormann, D. (2019). Liquid-Liquid Phase Separation in Disease. Annu. Rev. Genet. *53*, 171-194.

Alberti, S., Gladfelter, A., and Mittag, T. (2019). Considerations and Challenges in Studying Liquid-Liquid Phase Separation and Biomolecular Condensates. Cell *176*, 419-434.

An, S., Kumar, R., Sheets, E.D., and Benkovic, S.J. (2008). Reversible compartmentalization of de novo purine biosynthetic complexes in living cells. Science *320*, 103-106.

Anderson, P., and Kedersha, N. (2006). RNA granules. J. Cell Biol. *172*, 803-808.

Bacia, K., Haustein, E., and Schwille, P. (2014). Fluorescence correlation spectroscopy: principles and applications. CSH Protocols *2014*, 709-725.

Bah, A., and Forman-Kay, J.D. (2016). Modulation of Intrinsically Disordered Protein Function by Post-translational Modifications. J. Biol. Chem. *291*, 6696-6705.

Banani, S.F., Lee, H.O., Hyman, A.A., and Rosen, M.K. (2017a). Biomolecular condensates: organizers of cellular biochemistry. Nat. Rev. Mol. Cell Biol. *18*, 285-298.

Banani, S.F., Lee, H.O., Hyman, A.A., and Rosen, M.K. (2017b). Biomolecular condensates: organizers of cellular biochemistry. Nat. Rev. Mol. Cell Biol. *18*, 285-298.

Beckham, C.J., and Parker, R. (2008). P bodies, stress granules, and viral life cycles. Cell Host Microbe *3*, 206-212.

Berry, J., Brangwynne, C.P., and Haataja, M. (2018). Physical principles of intracellular organization via active and passive phase transitions. Rep. Prog. Phys. *81*, 046601.

Blasco-Moreno, B., de Campos-Mata, L., Böttcher, R., García-Martínez, J., Jungfleisch, J., Nedialkova, D.D., Chattopadhyay, S., Gas, M.E., Oliva, B., Pérez-Ortín, J.E.*, et al.* (2019). The exonuclease Xrn1 activates transcription and translation of mRNAs encoding membrane proteins. Nat. Commun. *10*, 1298.

Bloch, D.B., Gulick, T., Bloch, K.D., and Yang, W.H. (2006). Processing body autoantibodies reconsidered. RNA *12*, 707-709.

Bosson, A.D., Zamudio, J.R., and Sharp, P.A. (2014). Endogenous miRNA and target concentrations determine susceptibility to potential ceRNA competition. Mol. Cell *56*, 347-359.

Brangwynne, C.P. (2013). Phase transitions and size scaling of membrane-less organelles. J. Cell Biol. *203*, 875-881.

Calloway, N.T., Choob, M., Sanz, A., Sheetz, M.P., Miller, L.W., and Cornish, V.W. (2007). Optimized fluorescent trimethoprim derivatives for *in vivo* protein labeling. ChemBioChem *8*, 767-774.

Case, L.B., Ditlev, J.A., and Rosen, M.K. (2019a). Regulation of Transmembrane Signaling by Phase Separation. Annu. Rev. Biophys. *48*, 465-494.

Case, L.B., Zhang, X., Ditlev, J.A., and Rosen, M.K. (2019b). Stoichiometry controls activity of phase-separated clusters of actin signaling proteins. Science *363*, 1093-1097.

Caudron, F., and Barral, Y. (2013). A super-assembly of Whi3 encodes memory of deceptive encounters by single cells during yeast courtship. Cell *155*, 1244-1257.

Chen, J., Chiang, Y.C., and Denis, C.L. (2002). CCR4, a 3'-5' poly(A) RNA and ssDNA exonuclease, is the catalytic component of the cytoplasmic deadenylase. EMBO J. *21*, 1414-1426.

Cougot, N., Babajko, S., and Séraphin, B. (2004). Cytoplasmic foci are sites of mRNA decay in human cells. J. Cell Biol. *165*, 31-40.

Courchaine, E.M., Lu, A., and Neugebauer, K.M. (2016). Droplet organelles? EMBO J. *35*, 1603-1612.

Crick, F. (1970). Central dogma of molecular biology. Nature *227*, 561-563.

de Oliveira, G.A.P., Cordeiro, Y., Silva, J.L., and Vieira, T. (2019). Liquid-liquid phase transitions and amyloid aggregation in proteins related to cancer and neurodegenerative diseases. Adv. Protein Chem. Struct. Biol. *118*, 289-331.

de Oliveira, G.A.P., Petronilho, E.C., Pedrote, M.M., Marques, M.A., Vieira, T., Cino, E.A., and Silva, J.L. (2020). The Status of p53 Oligomeric and Aggregation States in Cancer. Biomolecules *10*.

Denzler, R., McGeary, S.E., Title, A.C., Agarwal, V., Bartel, D.P., and Stoffel, M. (2016). Impact of MicroRNA Levels, Target-Site Complementarity, and Cooperativity on Competing Endogenous RNA-Regulated Gene Expression. Mol. Cell *64*, 565-579.

Diederichs, S. (2014). The four dimensions of noncoding RNA conservation. Trends Genet. *30*, 121-123.

Dignon, G.L., Best, R.B., and Mittal, J. (2020). Biomolecular Phase Separation: From Molecular Driving Forces to Macroscopic Properties. Annu. Rev. Phys. Chem. *71*, 53-75.

Elbaum-Garfinkle, S. (2019a). Matter over mind: Liquid phase separation and neurodegeneration. J. Biol. Chem. *294*, 7160-7168.

Elbaum-Garfinkle, S. (2019b). Matter over mind: Liquid phase separation and neurodegeneration. J. Biol. Chem. *294*, 7160-7168.

Eystathioy, T., Chan, E.K., Tenenbaum, S.A., Keene, J.D., Griffith, K., and Fritzler, M.J. (2002). A phosphorylated cytoplasmic autoantigen, GW182, associates with a unique population of human mRNAs within novel cytoplasmic speckles. Mol Biol Cell *13*, 1338-1351.

Eystathioy, T., Jakymiw, A., Chan, E.K., Séraphin, B., Cougot, N., and Fritzler, M.J. (2003). The GW182 protein colocalizes with mRNA degradation associated proteins hDcp1 and hLSm4 in cytoplasmic GW bodies. RNA *9*, 1171-1173.

Feng, Z., Chen, X., Wu, X., and Zhang, M. (2019). Formation of biological condensates via phase separation: Characteristics, analytical methods, and physiological implications. J. Biol. Chem. *294*, 14823-14835.

Frottin, F., Schueder, F., Tiwary, S., Gupta, R., Körner, R., Schlichthaerle, T., Cox, J., Jungmann, R., Hartl, F.U., and Hipp, M.S. (2019). The nucleolus functions as a phase-separated protein quality control compartment. Science *365*, 342-347.

Gautier, A., Juillerat, A., Heinis, C., Correa, I.R., Jr., Kindermann, M., Beaufils, F., and Johnsson, K. (2008). An engineered protein tag for multiprotein labeling in living cells. Chemistry and Biology *15*, 128-136.

Goldenfeld, N. (1992). Lectures On Phase Transitions And The Renormalization Group (Westview Press).

Gomes, E., and Shorter, J. (2019). The molecular language of membraneless organelles. J. Biol. Chem. *294*, 7115-7127.

Gonzalez Bardeci, N., Angiolini, J.F., De Rossi, M.C., Bruno, L., and Levi, V. (2017). Dynamics of intracellular processes in live-cell systems unveiled by fluorescence correlation microscopy. Int. Union Biochem. Mol. Biol. *69*, 8-15.

Handwerger, K.E., Cordero, J.A., and Gall, J.G. (2005). Cajal bodies, nucleoli, and speckles in the Xenopus oocyte nucleus have a low-density, sponge-like structure. Mol. Biol. Cell *16*, 202-211.

Hickerson, R., Majumdar, Z.K., Baucom, A., Clegg, R.M., and Noller, H.F. (2005). Measurement of internal movements within the 30 S ribosomal subunit using Förster resonance energy transfer. J. Mol. Biol. *354*, 459-472.

Huang, W.Y.C., Alvarez, S., Kondo, Y., Lee, Y.K., Chung, J.K., Lam, H.Y.M., Biswas, K.H., Kuriyan, J., and Groves, J.T. (2019). A molecular assembly phase transition and kinetic proofreading modulate Ras activation by SOS. Science *363*, 1098-1103.

Hubstenberger, A., Courel, M., Bénard, M., Souquere, S., Ernoult-Lange, M., Chouaib, R., Yi, Z., Morlot, J.B., Munier, A., Fradet, M.*, et al.* (2017). P-Body Purification Reveals the Condensation of Repressed mRNA Regulons. Mol. Cell *68*, 144-157.e145.

Hyman, A.A., and Simons, K. (2012). Cell biology. Beyond oil and water--phase transitions in cells. Science *337*, 1047-1049.

Hyman, A.A., Weber, C.A., and Jülicher, F. (2014). Liquid-liquid phase separation in biology. Annu. Rev. Cell Dev. Biol. *30*, 39-58.

Isom, D.G., Page, S.C., Collins, L.B., Kapolka, N.J., Taghon, G.J., and Dohlman, H.G. (2018). Coordinated regulation of intracellular pH by two glucose-sensing pathways in yeast. J. Biol. Chem. *293*, 2318-2329.

Jalihal, A.P., Pitchiaya, S., Xiao, L., Bawa, P., Jiang, X., Bedi, K., Parolia, A., Cieslik, M., Ljungman, M., Chinnaiyan, A.M.*, et al.* (2020). Multivalent proteins rapidly and reversibly phase-separate upon osmotic cell volume change. bioRxiv, 748293.

Jin, M., Fuller, G.G., Han, T., Yao, Y., Alessi, A.F., Freeberg, M.A., Roach, N.P., Moresco, J.J., Karnovsky, A., Baba, M.*, et al.* (2017). Glycolytic Enzymes Coalesce in G Bodies under Hypoxic Stress. Cell Rep. *20*, 895-908.

Joyner, R.P., Tang, J.H., Helenius, J., Dultz, E., Brune, C., Holt, L.J., Huet, S., Muller, D.J., and Weis, K. (2016). A glucose-starvation response regulates the diffusion of macromolecules. eLife *5*.

Kapp, L.D., and Lorsch, J.R. (2004). The molecular mechanics of eukaryotic translation. Annu. Rev. Biochem. *73*, 657-704.

Keating, C.D. (2012). Aqueous phase separation as a possible route to compartmentalization of biological molecules. Acc. Chem. Res. *45*, 2114-2124.

Kedersha, N., Chen, S., Gilks, N., Li, W., Miller, I.J., Stahl, J., and Anderson, P. (2002). Evidence that ternary complex (eIF2-GTP-tRNA(i)(Met))-deficient preinitiation complexes are core constituents of mammalian stress granules. Mol Biol Cell *13*, 195-210.

Kedersha, N., Ivanov, P., and Anderson, P. (2013a). Stress granules and cell signaling: more than just a passing phase? Trends Biochem. Sci. *38*, 494-506.

Kedersha, N., Ivanov, P., and Anderson, P. (2013b). Stress granules and cell signaling: more than just a passing phase? Trends Biochem. Sci. *38*, 494-506.

Kedersha, N.L., Gupta, M., Li, W., Miller, I., and Anderson, P. (1999). RNA-binding proteins TIA-1 and TIAR link the phosphorylation of eIF-2 alpha to the assembly of mammalian stress granules. J. Cell Biol. *147*, 1431-1442.

Kristjánsdóttir, K., Fogarty, E.A., and Grimson, A. (2015). Systematic analysis of the Hmga2 3' UTR identifies many independent regulatory sequences and a novel interaction between distal sites. RNA *21*, 1346-1360.

Larson, J.D., Rodgers, M.L., and Hoskins, A.A. (2014). Visualizing cellular machines with colocalization single molecule microscopy. Chem. Soc. Rev. *43*, 1189-1200.

Latonen, L. (2019). Phase-to-Phase With Nucleoli - Stress Responses, Protein Aggregation and Novel Roles of RNA. Front. Cell. Neurosci. *13*, 151.

Lee, T.C., Kang, M., Kim, C.H., Schultz, P.G., Chapman, E., and Deniz, A.A. (2016). Dual unnatural amino acid incorporation and click-chemistry labeling to enable single-molecule FRET studies of p97 folding. ChemBioChem *17*, 981-984.

Levene, M.J., Korlach, J., Turner, S.W., Foquet, M., Craighead, H.G., and Webb, W.W. (2003). Zero-mode waveguides for single-molecule analysis at high concentrations. Science *299*, 682-686.

Li, J., and Liu, C. (2019). Coding or Noncoding, the Converging Concepts of RNAs. Front. Genet. *10*, 496.

Lin, Y.H., Forman-Kay, J.D., and Chan, H.S. (2018). Theories for Sequence-Dependent Phase Behaviors of Biomolecular Condensates. Biochemistry *57*, 2499-2508.

Liu, C.C., and Schultz, P.G. (2010). Adding new chemistries to the genetic code. Ann. Rev. Biochem. *79*, 413-444.

Liu, Z., Lavis, L.D., and Betzig, E. (2015). Imaging live-cell dynamics and structure at the single-molecule level. Mol. Cell *58*, 644-659.

Lloyd, R.E. (2013). Regulation of stress granules and P-bodies during RNA virus infection. Wiley Interdiscip. Rev. RNA *4*, 317-331.

Long, Y., Wang, X., Youmans, D.T., and Cech, T.R. (2017). How do lncRNAs regulate transcription? Sci. Adv. *3*, eaao2110.

Los, G.V., Encell, L.P., McDougall, M.G., Hartzell, D.D., Karassina, N., Zimprich, C., Wood, M.G., Learish, R., Ohana, R.F., Urh, M.*, et al.* (2008). HaloTag: a novel protein labeling technology for cell imaging and protein analysis. ACS Chem. Biol. *3*, 373-382.

Lu, H.P., Xun, L., and Xie, X.S. (1998). Single-molecule enzymatic dynamics. Science *282*, 1877-1882.

Luo, Y., Na, Z., and Slavoff, S.A. (2018). P-Bodies: Composition, Properties, and Functions. Biochemistry *57*, 2424-2431.

Ma, W., and Mayr, C. (2018). A Membraneless Organelle Associated with the Endoplasmic Reticulum Enables 3'UTR-Mediated Protein-Protein Interactions. Cell *175*, 1492-1506.e1419.

Majumdar, A., Cesario, W.C., White-Grindley, E., Jiang, H., Ren, F., Khan, M.R., Li, L., Choi, E.M., Kannan, K., Guo, F.*, et al.* (2012). Critical role of amyloid-like oligomers of Drosophila Orb2 in the persistence of memory. Cell *148*, 515-529.

Mayr, C., Hemann, M.T., and Bartel, D.P. (2007). Disrupting the pairing between let-7 and Hmga2 enhances oncogenic transformation. Science *315*, 1576-1579.

McNally, J.G. (2008). Quantitative FRAP in analysis of molecular binding dynamics *in vivo*. Methods Cell Biol. *85*, 329-351.

Mitrea, D.M., and Kriwacki, R.W. (2016). Phase separation in biology; functional organization of a higher order. Cell Commun. Signal *14*, 1.

Moffitt, J.R., Chemla, Y.R., and Bustamante, C. (2010). Methods in statistical kinetics. Methods in Enzymology *475*, 221-257.

Monty, K.J., Litt, M., Kay, E.R., and Dounce, A.L. (1956). Isolation and properties of liver cell nucleoli. J. Biophys. Biochem. Cytol. *2*, 127-145.

Mukherji, S., Ebert, M.S., Zheng, G.X., Tsang, J.S., Sharp, P.A., and van Oudenaarden, A. (2011). MicroRNAs can generate thresholds in target gene expression. Nat. Genet. *43*, 854-859.

Munder, M.C., Midtvedt, D., Franzmann, T., Nüske, E., Otto, O., Herbig, M., Ulbricht, E., Müller, P., Taubenberger, A., Maharana, S.*, et al.* (2016). A pH-driven transition of the cytoplasm from a fluid- to a solid-like state promotes entry into dormancy. eLife *5*.

Noueiry, A.O., Diez, J., Falk, S.P., Chen, J., and Ahlquist, P. (2003). Yeast Lsm1p-7p/Pat1p deadenylation-dependent mRNA-decapping factors are required for brome mosaic virus genomic RNA translation. Mol. Cell Biol. *23*, 4094-4106.

Owen, I., and Shewmaker, F. (2019). The Role of Post-Translational Modifications in the Phase Transitions of Intrinsically Disordered Proteins. Int. J. Mol. Sci. *20*.

Pakos-Zebrucka, K., Koryga, I., Mnich, K., Ljujic, M., Samali, A., and Gorman, A.M. (2016). The integrated stress response. EMBO Rep. *17*, 1374-1395.

Palazzo, A.F., and Lee, E.S. (2015). Non-coding RNA: what is functional and what is junk? Front. Genet. *6*, 2.

Posey, A.E., Holehouse, A.S., and Pappu, R.V. (2018). Phase Separation of Intrinsically Disordered Proteins. Methods Enzymol. *611*, 1-30.

Preiss, T., and Hentze, M. (2003). Starting the protein synthesis machine: eukaryotic translation initiation. Bioessays *25*, 1201-1211.

Protter, D.S.W., Rao, B.S., Van Treeck, B., Lin, Y., Mizoue, L., Rosen, M.K., and Parker, R. (2018). Intrinsically Disordered Regions Can Contribute Promiscuous Interactions to RNP Granule Assembly. Cell Rep. *22*, 1401-1412.

Quiroz, F.G., Fiore, V.F., Levorse, J., Polak, L., Wong, E., Pasolli, H.A., and Fuchs, E. (2020). Liquid-liquid phase separation drives skin barrier formation. Science *367*.

Rai, A.K., Chen, J.X., Selbach, M., and Pelkmans, L. (2018). Kinase-controlled phase transition of membraneless organelles in mitosis. Nature *559*, 211-216.

Reineke, L.C., and Lloyd, R.E. (2013). Diversion of stress granules and P-bodies during viral infection. Virology *436*, 255-267.

Riback, J.A., Zhu, L., Ferrolino, M.C., Tolbert, M., Mitrea, D.M., Sanders, D.W., Wei, M.T., Kriwacki, R.W., and Brangwynne, C.P. (2020). Composition-dependent thermodynamics of intracellular phase separation. Nature *581*, 209-214.

Ritter, J.G., Veith, R., Veenendaal, A., Siebrasse, J.P., and Kubitscheck, U. (2010). Light sheet microscopy for single molecule tracking in living tissue. PLOS One *5*, e11639. doi: 11610.11371/journal.pone.0011639.

Roy, R., Hohng, S., and Ha, T. (2008). A practical guide to single-molecule FRET. Nat. Methods *5*, 507-516.

Sanders, D.W., Kedersha, N., Lee, D.S.W., Strom, A.R., Drake, V., Riback, J.A., Bracha, D., Eeftens, J.M., Iwanicki, A., Wang, A.*, et al.* (2020). Competing Protein-RNA Interaction Networks Control Multiphase Intracellular Organization. Cell *181*, 306-324.e328.

Schmidt, A., Gao, G., Little, S.R., Jalihal, A.P., and Walter, N.G. (2020). Following the messenger: Recent innovations in live cell single molecule fluorescence imaging. Wiley Interdiscip. Rev. RNA *11*, e1587.

Seitz, H. (2009). Redefining microRNA targets. Curr. Biol. *19*, 870-873.

Shen, H., Tauzin, L.J., Baiyasi, R., Wang, W., Moringo, N., Shuang, B., and Landes, C.F. (2017). Single particle tracking: From theory to biophysical applications. Chem. Rev. *117*, 7331-7376.

Si, K., Choi, Y.B., White-Grindley, E., Majumdar, A., and Kandel, E.R. (2010). Aplysia CPEB can form prion-like multimers in sensory neurons that contribute to long-term facilitation. Cell *140*, 421-435.

Su, X., Ditlev, J.A., Hui, E., Xing, W., Banjade, S., Okrut, J., King, D.S., Taunton, J., Rosen, M.K., and Vale, R.D. (2016). Phase separation of signaling molecules promotes T cell receptor signal transduction. Science *352*, 595-599.

Sun, X., Zhang, A., Baker, B., Sun, L., Howard, A., Buswell, J., Maurel, D., Masharina, A., Johnsson, K., Noren, C.J., *et al.* (2011). Development of SNAP-tag fluorogenic probes for wash-free fluorescence imaging. ChemBioChem *12*, 2217-2226.

Tena-Solsona, M., Wanzke, C., Riess, B., Bausch, A.R., and Boekhoven, J. (2018). Self-selection of dissipative assemblies driven by primitive chemical reaction networks. Nat. Commun. *9*, 2044.

Thandapani, P., O'Connor, T.R., Bailey, T.L., and Richard, S. (2013). Defining the RGG/RG motif. Mol. Cell *50*, 613-623.

Thorn, K. (2017). Genetically encoded fluorescent tags. Mol. Biol. Cell *28*, 848-857.

Tian, S., Curnutte, H.A., and Trcek, T. (2020). RNA Granules: A View from the RNA Perspective. Molecules *25*.

Tokunaga, M., Imamoto, N., and Sakata-Sogawa, K. (2008). Highly inclined thin illumination enables clear single-molecule imaging in cells. Nat. Methods *5*, 159-161.

Toomre, D. (2012). Cellular imaging using total internal reflection fluorescence microscopy: Theory and instrumentation. CSH Protocols *2012*, 414-424.

Trcek, T., Douglas, T.E., Grosch, M., Yin, Y., Eagle, W.V.I., Gavis, E.R., Shroff, H., Rothenberg, E., and Lehmann, R. (2020). Sequence-Independent Self-Assembly of Germ Granule mRNAs into Homotypic Clusters. Mol. Cell *78*, 941-950.e912.

Tsai, A., Puglisi, J.D., and Uemura, S. (2016). Probing the translation dynamics of ribosomes using zero-mode waveguides. Prog. Mol. Biol. Transl. Sci. *139*, 1-43.

Tsai, M.C., Manor, O., Wan, Y., Mosammaparast, N., Wang, J.K., Lan, F., Shi, Y., Segal, E., and Chang, H.Y. (2010). Long noncoding RNA as modular scaffold of histone modification complexes. Science *329*, 689-693.

Turoverov, K.K., Kuznetsova, I.M., Fonin, A.V., Darling, A.L., Zaslavsky, B.Y., and Uversky, V.N. (2019). Stochasticity of Biological Soft Matter: Emerging Concepts in Intrinsically Disordered Proteins and Biological Phase Separation. Trends Biochem. Sci. *44*, 716-728.

Vanderweyde, T., Youmans, K., Liu-Yesucevitz, L., and Wolozin, B. (2013). Role of stress granules and RNA-binding proteins in neurodegeneration: a mini-review. Gerontology *59*, 524-533.

Vernon, R.M., Chong, P.A., Tsang, B., Kim, T.H., Bah, A., Farber, P., Lin, H., and Forman-Kay, J.D. (2018). Pi-Pi contacts are an overlooked protein feature relevant to phase separation. eLife *7*.

Vonaesch, P., Sansonetti, P.J., and Schnupf, P. (2017). Immunofluorescence Analysis of Stress Granule Formation After Bacterial Challenge of Mammalian Cells. J. Vis. Exp.

Wahl, M.C., Will, C.L., and Lührmann, R. (2009). The spliceosome: design principles of a dynamic RNP machine. Cell *136*, 701-718.

Walter, N.G., Huang, C.Y., Manzo, A.J., and Sobhy, M.A. (2008). Do-it-yourself guide: How to use the modern single-molecule toolkit. Nat. Methods *5*, 475-489.

Wang, J., Caban, K., and Gonzalez, R.L., Jr. (2015). Ribosomal initiation complex-driven changes in the stability and dynamics of initiation factor 2 regulate the fidelity of translation initiation. J. Mol. Biol. *427*, 1819-1834.

Wang, J., Choi, J.M., Holehouse, A.S., Lee, H.O., Zhang, X., Jahnel, M., Maharana, S., Lemaitre, R., Pozniakovsky, A., Drechsel, D.*, et al.* (2018). A Molecular Grammar Governing the Driving Forces for Phase Separation of Prion-like RNA Binding Proteins. Cell *174*, 688-699.e616.

Wilson, E.B. (1896). The cell, in development and inheritance (The Macmillan Co.: New York).

Wilson, E.B. (1899). The structure of protoplasm. Science *10*, 33-45.

Yang, P., Mathieu, C., Kolaitis, R.M., Zhang, P., Messing, J., Yurtsever, U., Yang, Z., Wu, J., Li, Y., Pan, Q.*, et al.* (2020). G3BP1 Is a Tunable Switch that Triggers Phase Separation to Assemble Stress Granules. Cell *181*, 325-345.e328.

Yoo, H., Triandafillou, C., and Drummond, D.A. (2019). Cellular sensing by phase separation: Using the process, not just the products. J. Biol. Chem. *294*, 7151-7159.

Zhou, H.X., Nguemaha, V., Mazarakos, K., and Qin, S. (2018). Why Do Disordered and Structured Proteins Behave Differently in Phase Separation? Trends Biochem. Sci. *43*, 499-516.

Chapter 2. Dynamic Recruitment of Single RNAs to Processing Bodies Depends on RNA Functionality[2]

2.1. Abstract

Cellular RNAs often colocalize with cytoplasmic, membrane-less ribonucleoprotein (RNP) granules enriched for RNA processing enzymes, termed processing bodies (PBs). Here, we track the dynamic localization of individual miRNAs, mRNAs and long non-coding RNAs (lncRNAs) to PBs using intracellular single-molecule fluorescence microscopy. We find that unused miRNAs stably bind to PBs, whereas functional miRNAs, repressed mRNAs and lncRNAs both transiently and stably localize within either the core or periphery of PBs, albeit to different extents. Consequently, translation potential and 3' versus 5' placement of miRNA target sites significantly impact PB-localization dynamics of mRNAs. Using computational modeling and supporting experimental approaches we show that partitioning into the PB phase attenuates mRNA silencing, suggesting that physiological mRNA turnover occurs predominantly outside PBs. Our data support a PB role instead in sequestering unused miRNAs for surveillance and provides a framework for investigating the dynamic assembly of RNP granules by phase separation at single-molecule resolution.

[2] The contents of this chapter have been published as:

Pitchiaya, S., Mourao, M.D.A., Jalihal, A.P., Xiao, L., Jiang, X., Chinnaiyan, A.M., Schnell, S., and Walter, N.G. (2019). Dynamic Recruitment of Single RNAs to Processing Bodies Depends on RNA Functionality. Mol. Cell *74*, 521-533.e526.

S.P. designed and executed the study. M.D.A.M. and S.S. performed the kinetic modeling. A.P.J. performed immunofluorescence assays. L.X. and X.J. created and validated mRNA and lncRNA constructs. S.P., S.S., A.M.C. and N.G.W. conceived the study and all authors wrote the manuscript together.

2.2. Introduction

Sub-cellular, membrane-free granules have emerged as critical components of normal biology and pathophysiology (Banani et al., 2017b; Shin and Brangwynne, 2017b), owing to their key role in spatial regulation of gene expression (Martin and Ephrussi, 2009; Spector, 2006). Processing bodies (PBs) are one such class of ribonucleoprotein (RNP) granules that persist during cellular homeostasis and are enriched for RNA processing and degradation enzymes (Eulalio et al., 2007a; Parker and Sheth, 2007). These granules are observed in almost all eukaryotes, ranging from yeast to mammals, and have been implicated in multiple biological processes, including oogenesis, progression through early development, and mediation of neuroplasticity (Buchan, 2014).

More specifically, mammalian PBs have been functionally associated with storage, translational repression and/or degradation of mRNAs (Buchan, 2014; Hubstenberger et al., 2017a; Liu et al., 2005a; Schutz et al., 2017), as a result of which PBs are predominantly composed of translationally repressed messenger RNAs (mRNAs), mRNA-regulating miRNAs and, to a lesser extent, regulatory long non-coding RNAs (lncRNAs). Such a large RNP complex is hypothesized to assemble via RNA dependent phase separation (Banani et al., 2017b), wherein multiple translationally repressed RNPs are concentrated within dense foci through strong multivalent interactions and individual or oligomeric RNPs loosely interact with these dense regions to create dynamic shells (Cougot et al., 2012; Van Treeck and Parker, 2018). Consequently, PBs, as whole granules, display a wide array of dynamic behaviors (Aizer et al., 2008b), but the intra- and peri-granular RNP dynamics and RNP recruitment – processes that govern the maintenance, maturation and putative gene regulatory functions of PBs – are largely unknown. While mRNP-PB

colocalization and mRNA regulation have been shown to be tightly correlated (Buchan, 2014; Parker and Sheth, 2007), the question of whether mRNPs are degraded at microscopically visible, and thus relatively large (> 250 nm), PBs also remains unresolved.

Here, we dissect the fundamental principles governing the dynamic localization of functionally distinct classes of RNPs at phase separated PBs and unravel the functional consequence of RNA-PB colocalization. To this end, we developed methodologies to simultaneously observe single RNA molecules (miRNAs, mRNAs or lncRNAs) and individual PB foci inside both living and fixed human cells. We demonstrate that a majority of miRNAs and repressed mRNAs are stably anchored within PBs, whereas translationally active mRNAs and lncRNAs associate with PBs only transiently, suggesting a strong correlation between PB-localization and RNA class. While miRNAs and mRNAs localized at core or shells of PBs, lncRNAs were predominantly found at PB-shells. Furthermore, we find that unused (target-less) miRNAs are enriched at PB and that the 3' versus 5'terminal positioning of cis-regulatory miRNA response elements (MREs) dictates the PB localization patterns and dynamics of mRNAs. Finally, in silico modeling and experimental validation through hyperosmotic-stress induced phase separation suggest that the stochastic collision of mRNAs with freely diffusing, sub-microscopic PBs leads to more efficient mRNA regulation than their recruitment to microscopic PBs. Taken together, our observations reveal the nanoscale principles that govern the compositional complexity of mesoscale RNP granules, and a novel suggested function for PBs in accumulating target-less miRNAs for miRNA surveillance.

2.3. Results

2.3.1. Super-resolved single-molecule fluorescence microscopy probes RNA-PB interactions

To dissect the localization dynamics of RNAs at and near PBs, we created a U2-OS cell line that stably expressed GFP tagged Dcp1a, an mRNA decapping co-activator and PB marker (Aizer et al., 2008b; Hubstenberger et al., 2017a). We selected a clone (hereon termed UGD) with similar number and composition (based on colocalization with other PB markers) of Dcp1a foci as endogenously found in U2-OS cells (Figure 2-1A-D). Next, mature regulatory miRNAs, whose size (~22 nt per strand) precludes endogenous labeling strategies (Pitchiaya et al., 2014), were chemically synthesized with a fluorescent Cy5 dye at the 3'end of one of their two complementary strands, typically the guide strand. Since transfection results in the sequestration of RNA within subcellular vesicles (Cardarelli et al., 2016), we chose to deliver these miRNAs via microinjection (Figure 2-2A-C), which enables controlled delivery (Figure 2-1E-G) of physiologically relevant miRNA molecules per cell (~10-20,000 copies, i.e. $1/10^{th}$ the total number of miRNAs per cell) and defines a clear starting point for our assays by instantaneously exposing RNAs to the cellular milieu (Pitchiaya et al., 2012; Pitchiaya et al., 2013; Pitchiaya et al., 2017). We confirmed that fluorophore labeling and microinjection did not affect the gene-repressive function (Figure 2-1H-K) of let-7 miRNA (l7/l7* and l7-Cy5/l7*) (Pitchiaya et al., 2012), alter the sub-cellular abundance and behavior of PBs (Figure 2-1J-K), or induce stress granule (SG) formation (Figure 2-1L-O).

We then combined a super-registration fluorescence microscopy-based tool (Grunwald and Singer, 2010) that measures intermolecular distances of spectrally distinct fluorescent molecules with intracellular single molecule, high-resolution localization and counting

(iSHiRLoC)(Pitchiaya et al., 2012; Pitchiaya et al., 2017a; Pitchiaya et al., 2013). Consequently, we were able to visualize miRNA-PB interactions in living cells and precisely quantify miRNA stoichiometry within PBs in fixed cells (Methods, Figure 2-2A-C and Supplementary movie 1). At a spatial accuracy of 30 nm and temporal resolution of 50 ms, we can visualize large (> 400 kDa) miRNPs, such as miRISC:mRNP complexes, in living cells and all miRNPs, irrespective of RNP size, in fixed cells (Figure 2-1P) (Pitchiaya et al., 2012; Pitchiaya et al., 2017a; Pitchiaya et al., 2013). Using this new tool, we found that the tumor suppressive let-7 miRNA (l7-Cy5/l7*) diffused ~100-1,000-fold slower at PBs compared to in the cytosol (Figure 2-2G), supporting the notion that miRNAs physically dock to form higher order complexes at PBs and consistent with previous ensemble observations of miRNA accumulation at PBs (Liu et al., 2005a; Pillai et al., 2005). However, we additionally observed that PB-localized miRNAs distributed between (at least) two populations of diffusion coefficients or molecular weights. Complementarily, fixed cell analysis showed that cytoplasmic l7-Cy5/l7* miRNA were predominantly monomeric, wherein a significant minority of monomeric (~40%) and a predominant fraction of multimeric (~60%) RNA complexes (Figure 2-2H) were observed at PBs. Moreover, the PB dynamics and localization extents of l7-Cy5/l7* in GFP-Dcp1a expressing HeLa cells were almost identical to those in UGD cells (Figure 2-1Q-R), underscoring the generality of our observations across cellular systems. Our data suggest that miRNPs of diverse sizes, and perhaps composition, localize to PBs via potentially distinct mechanisms, with the possibility to yield distinct regulatory outcomes.

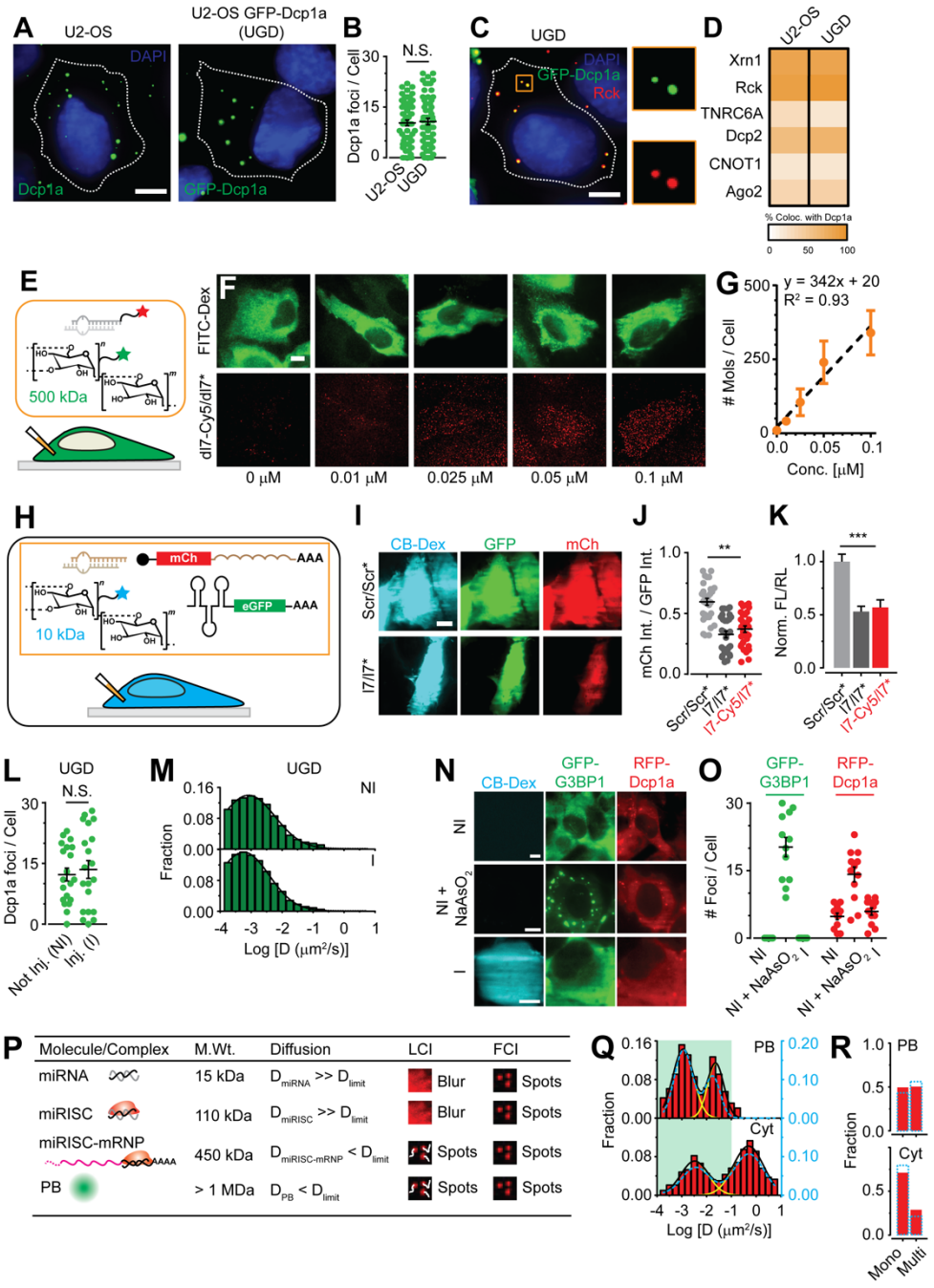

Figure 2-1 Validation of in situ miRNA imaging system. (**A**) Representative pseudocolored and contrast-adjusted images of U2-OS cells stained for endogenous Dcp1a (green) via immunofluorescence and UGD cells expressing GFP-Dcp1a (green). Nucleus is stained with DAPI (blue). Dotted line, cell outline. Scale bar, 10 µm. (**B**) Scatter plot depicting the number of endogenous Dcp1a or GFP-Dcp1a foci in U2-OS and UGD cells respectively (n = 3, 60 cells, N.S., not significant based on two-tailed, unpaired Student's t-test). (**C**) Representative pseudocolored and contrast-adjusted image of UGD cells expressing GFP-Dcp1a (green) and stained for Rck (red). Nucleus is stained with DAPI (blue). Dotted line, cell outline. Scale bar, 10 µm. Orange 5.3 x 5.3 µm2 inset is zoomed out and deconvolved into individual colors. (**D**) Mean colocalization percentage of endogenous Dcp1a foci from U2-OS cells or GFP-Dcp1a from UGD cells respectively, with other PB markers. Color coded scale-bar is also depicted (n = 3, ≥ 15 cells per sample). (**E-G**) Microinjection-based titration assay. (**E**) Schematic of microinjection setup, wherein Cy5 labeled

double stranded DNA (dl7-Cy5/dl7*, red) bearing the same sequence as l7-Cy5/l7* miRNA was co-microinjected along with 500 kDa FITC-Dextran (green), exclusively localizes to the cytosol. (**F**) Representative pseudocolored and contrast-adjusted images of U2-OS cells microinjected with various concentrations of dl7-Cy5/dl7*. Scale bar, 10 µm. (**G**) Plot depicting the relationship between dl7-Cy5/dl7* concentration (Conc., µM) in the microinjection solution and the number of molecules detected per cell (# Mols / Cell). Dotted line represents fitted line. Equation of fitted line and goodness of fit (R2) are also depicted. (H-K) miRNA activity assays. (**H**) Schematic of microinjection-based miRNA activity assay. (**I**) Representative pseudocolored and contrast-adjusted image of U2-OS cells expressing mCherry (mCh, red) reporter gene and GFP normalization gene (green), also containing 10 kDa cascade-blue dextran (CB-Dex, cyan) and the miRNA (Scr/Scr* - scrambled control, l7/l7* - let-7 miRNA) of interest. Scale bar, 10 µm. (**J**) Scatter plot depicting the mCh : GFP intensity ratio for various conditions (n = 3 replicates, total 30 cells; **p < 0.001 based on two-tailed, unpaired Student's t-test). Mean and s.e.m are depicted. (**K**) Luciferase reporter assays represented as the ratio of luminescence form a firefly luciferase (FL) reporter gene containing 6x let-7 MREs (FL-l7-6x) and a renilla luciferase (RL) normalization gene in U2-OS cells (n = 12 replicates, ***p < 0.0001 based on two-tailed, unpaired Student's t-test). Mean and s.e.m are depicted. (**L-O**) Microinjection does not affect sub-cellular behavior of PBs and does not induce stress granules. Number (**L**) and diffusion constants (M) of PBs in cells that were not injected (Not Inj., NI) or injected (Inj., I). Representative pseudocolored and contrast-adjusted images of U2-OS cells stably expressing GFP-G3BP (green), a stress granule (SG) marker, and RFP-Dcp1a (red), which were not injected (NI), treated with sodium arsenite (NI + NaAsO2) or co-injected with CB-Dex (cyan) and l7-Cy5/l7* are shown in N. Scale bar, 10 µm. Quantification of the number of GFP or RFP foci per cell is shown in O. (**P**) Expected phenotype of distinct molecular species in iSHiRLoC assays. LCI, live cell imaging; FCI, fixed cell imaging. (**Q-R**) Dynamics and stoichiometry of l7-Cy5/l7* in GFP-Dcp1a expressing HeLa cells are almost identical to those in UGD cells. (Q) Distribution of l7-Cy5/l7* miRNA diffusion constants in PB and Cyt within living HeLa cells that are expressing GFP-Dcp1a. Green area on the plot depicts the range of PB diffusion constants (n = 3, 13 cells). Dotted blue line represents distribution of l7-Cy5/l7* miRNA diffusion constants within UGD cells, as in Figure 1D. (**R**) Distribution of l7-Cy5/l7* miRNA stoichiometry as monomeric (Mono, 1 photobleaching step) or multimeric (Multi, ≥ 2 photobleaching steps) complexes in PB and Cyt within fixed HeLa cells that are expressing GFP-Dcp1a (n = 4, 21 cells). Dotted blue line represents stoichiometry in UGD cells, as in Figure 2-1F.

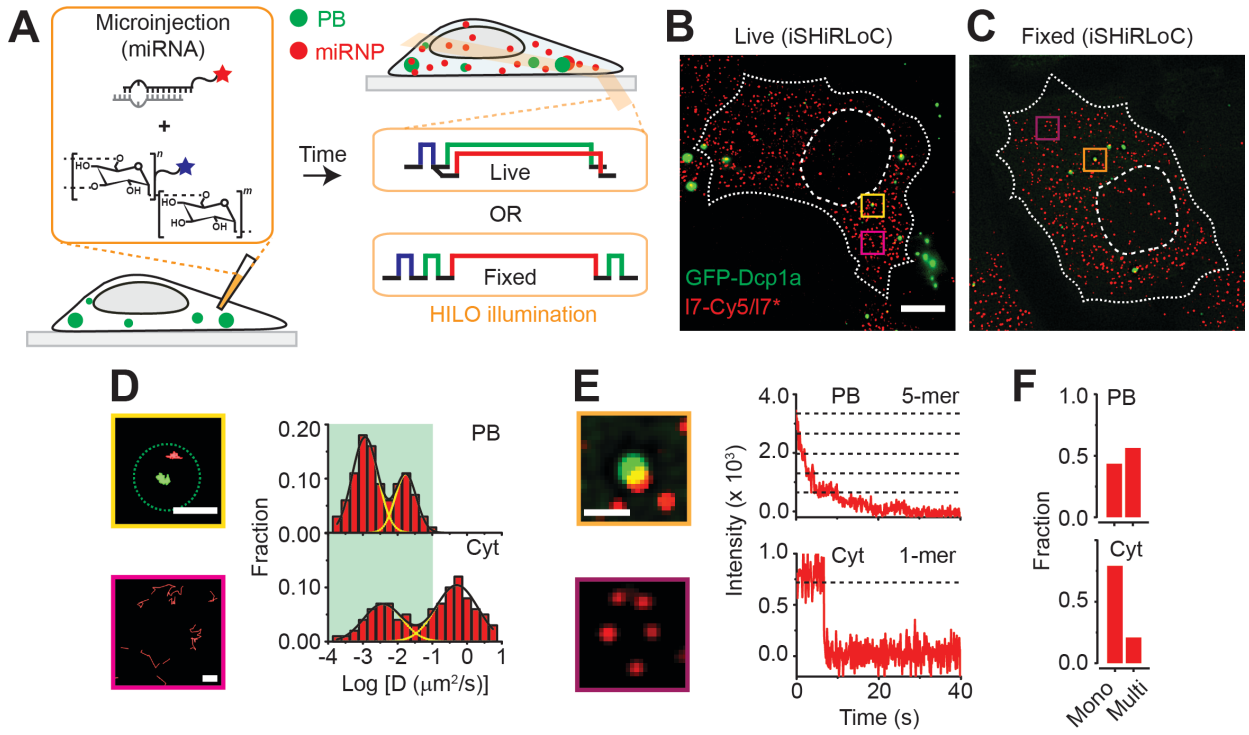

Figure 2-2 A super-resolution imaging tool for probing RNA-granule dynamics and stoichiometry. (**A**) Schematic of iSHiRLoC assay for probing miRNA-PB dynamics and colocalizations. (B and C) Representative pseudo-colored and contrast-adjusted images from live-cell imaging (**B**) and fixed cell imaging (**C**) assays of UGD cells expressing GFP-labeled PBs (green) that were microinjected with l7-Cy5/l7* miRNA (red) and imaged 2 h post injection. Scale bar, 10 µm. (**D**) Representative single-particle trajectories of PBs (green) and l7-Cy5/l7* miRNA (red) from yellow and magenta boxes in B, representing diffusing miRNAs in PBs and in the cytoplasm (Cyt) respectively. Scale bar, 1 µm. Dotted green circle represents PB outline in the first frame of the movie. Distribution of l7-Cy5/l7* miRNA diffusion constants in PB and Cyt are also depicted. Green area on the plot depicts the range of PB diffusion constants (n = 3, 15 cells). (**E**) Zoomed-in view of orange and violet boxes in C, from fixed UGD cells. Scale bar, 2 µm. Step-wise photobleaching trajectories PB- and Cyt-localized l7-Cy5/l7* is also shown. (**F**) Distribution of l7-Cy5/l7* miRNA stoichiometry as monomeric (Mono, 1 photobleaching step) or multimeric (Multi, ≥ 2 photobleaching steps) complexes in PB and Cyt within fixed UGD cells (n = 3, 15 cells).

2.3.2. miRNAs stably or transiently localize at the core or periphery of PBs

We next sought to understand whether the observed diverse miRNP diffusion and assembly states at PBs are based on the type of miRNA-PB interaction. To this end, we first inspected individual trajectories of PB-localized l7-Cy5/l7* in live cells to discover diversities in the kinetics and modalities of miRNA-PB interactions. We identified five distinct types RNA-PB interactions, each of which could be classified by a unique combination of diffusion coefficient (D), photobleaching corrected dwell time (T) and percentage of an RNA track colocalizing with a PB (P) (Figure 2-3A, 2-4A and Supplementary movie 2): 1) RNAs stably anchoring at PBs (D = 0.0001 – 0.1 $\mu m^2/s$, T ≥ 15 s, P = 100%, Supplementary movie 2); 2) RNAs displaying significant dynamics within PBs (D = 0.001 – 0.1 $\mu m^2/s$, T ≥15 s, P = 100%, Supplementary movie 2); 3) RNAs entering PBs from the cytosol (D = 0.0001 – 0.01 $\mu m^2/s$, T = 7.9 ± 0.7 s, P = 52 – 89%, Supplementary movie 2); 4) RNAs transiently probing PBs (D = 0.0001 – 1 $\mu m^2/s$, T = 0.9 ± 0.1 s, P = 3 – 72%, Supplementary movie 2); and 5) RNAs exiting a PB into the cytosol (D = 0.0001 – 1 $\mu m^2/s$, T = 0.8 ± 0.1 s, P = 7 – 83%, Supplementary movie 2). The first three and latter two interaction types depict what we refer to as stable and transient RNA-PB localizations, respectively. These data suggest that the diffusion rate and dwell times of miRNPs defines the type

of interaction with PBs. Next, we quantified the relative localization of PB-resident proteins or a few control proteins with respect to GFP-Dcp1a (Figure 2-4B). Using this intra-granular localization atlas as a template, we spatially mapped the localization of miRNPs with reference to PB boundaries and found that miRNAs localized near the core or the periphery/shell of PBs in fixed cells (Figure 2-3B). We then performed ratiometric quantification of core- or shell-localized immunofluorescence (IF) signal at PBs and the adjacent cytosol (Figure 2-4C), which yields similar information as the average percentage of IF signal within PBs per cell but also accounts for any heterogeneities between PBs within the same cell, and created a small compendia of proteins that were either enriched (> 1) or depleted (< 1) from PBs (Figure 2-4C). Combining this new quantification tool with single-molecule counting, we discovered that miRNAs were either clustered (enriched within PBs compared to the adjacent cytosol) or dispersed at PBs (Figure 2-3C). As a control, we also probed dl7-Cy5/dl7*, a control DNA oligonucleotide of the same sequence as let-7 miRNA, but incompetent for RNA silencing. In contrast to l7-Cy5/l7*, and as expected, we found that dl7-Cy5/dl7* neither localized to nor was enriched at/near PBs (Figure 2-3D). Taken together, these findings unravel a potentially tight relationship between miRNP composition and type of miRNP-PB interaction, and the requirement for small double-stranded (ds) oligonucleotides to assemble into large RNPs to stably interact with PBs.

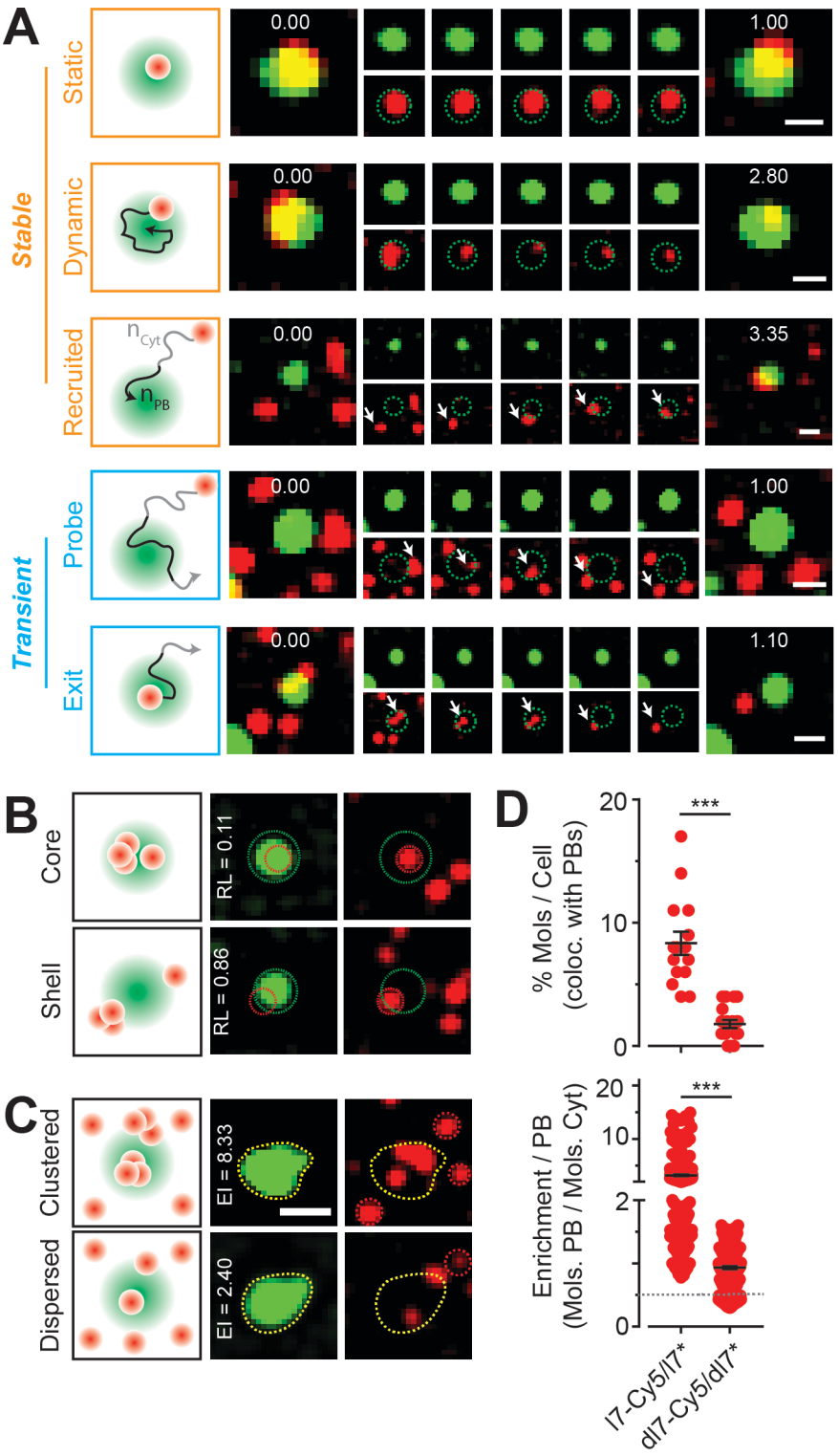

Figure 2-3 miRNAs show diverse spatiotemporal localization patterns at PB core and periphery. (**A**) Schematic and representative time-lapsed images of PBs (green) and l7-Cy5/l7* miRNAs (red) in live UGD cells. Scale bar, 1 µm. Embedded numbers in green/red overlay images (far-left and far right) represent time in seconds. Dotted green circles in red panels have been included to aid in the identification of PB boundaries. White arrow points to an individual

RNA particle. Stable RNA-PB association patterns (static, dynamic and recruited) are represented in orange whereas transient ones (probe and escape) are represented in blue. nPB = number of track localizations within PBs, nCyt = number of track localizations in the cytosol. (**B**) Schematic and representative images of PBs (green) and l7-Cy5/l7* (red) representing the localization of miRNAs within shells or cores of PBs in fixed UGD cells. Scale bar, 2 µm. Dotted green and red circles represent boundaries of PBs and miRNAs respectively. Relative localization (RL) values of l7-Cy5/l7* for these representative colocalizations are embedded in the green panels. (**C**) Schematic and representative images of PBs (green) and l7-Cy5/l7* (red) representing the enrichment of miRNAs in PBs within fixed UGD cells. Dotted yellow and red circles represent PB-miRNA colocalization and cytoplasmic miRNAs respectively. Enrichment of l7-Cy5/l7* per PB (EI) for these representative colocalizations are embedded in the green panels. Images are scaled as in B. (**D**) Scatter plot representing the % of RNA or DNA molecules that colocalize with PBs per fixed UGD cell (top). Each dot represents a cell. Scatter plot of enrichment of molecules per PB (below) is also shown. Each dot represents an individual PB in fixed UGD cells. n = 3, > 15 cells, ***p ≤ 0.0001 by two-tailed, unpaired Student's t-test. Grey dotted line depicts an EI of one, which demarcates PB-enriched (> 1) from PB-depleted (< 1) factors. See also Figure S2.

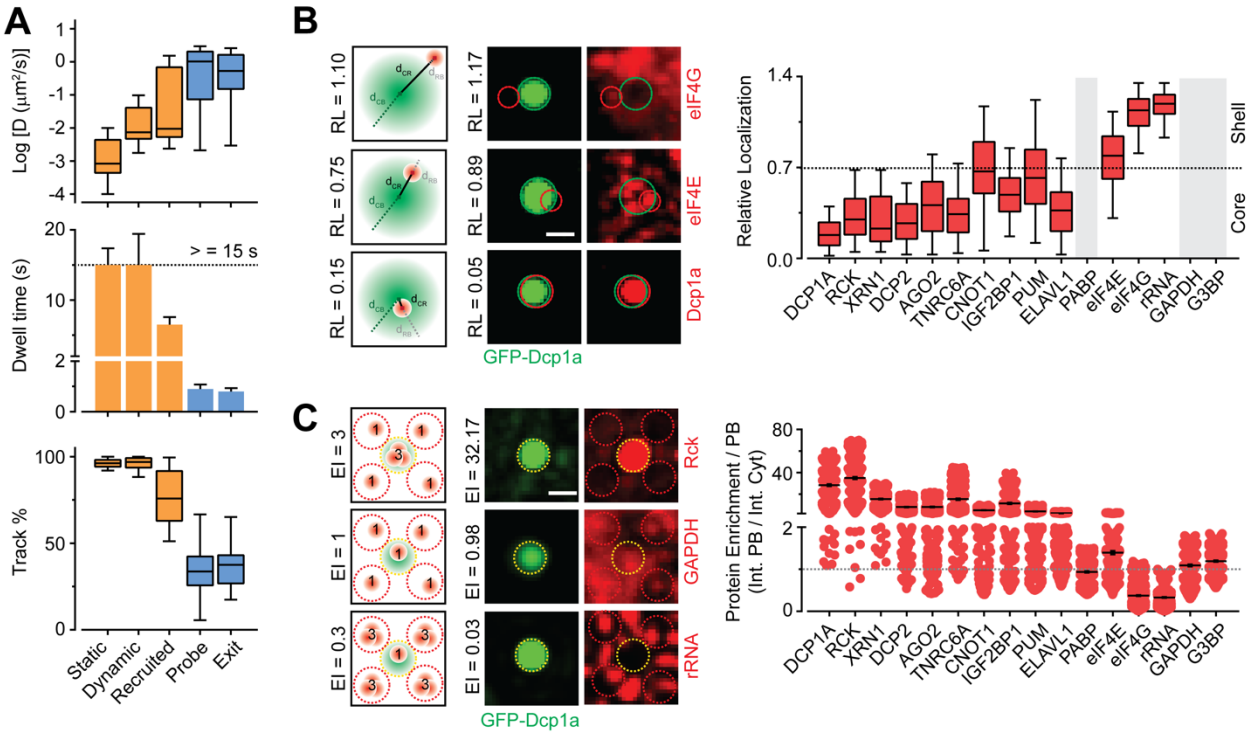

Figure 2-4 Characterization of miRNA-PB interaction modes and localization patterns (Related to Figure 2). (**A**) Distribution of diffusion constants (top), Dwell time statistics (middle) and distribution of the percentage of track length colocalizing with PB (bottom) for each RNA-PB interaction type. Dotted black line represents duration of acquisition. Photobleaching corrected dwell times that were greater than acquisition window were rounded to the acquisition time span (n = 3, 15 cells). (**B**) Schematic (left) of relative localization (RL) calculation. dCR = distance of RNA centroid from PB centroid, dRB = distance of RNA centroid from PB boundary, dCB = distance of PB centroid from PB boundary. Representative pseudoclored and contrast-adjusted regions of UGD cells (middle) with GFP-Dcp1a (green), stained for eIF4G, eIF4E or Dcp1a (red). Green and red dotted circles represent boundaries of PBs and Rck particles respectively. Scale bar, 2 µm. Relative localization values of top and bottom panels are represented within the images. Distribution of protein localization relative to GFP-Dcp1a, which were used to define PB center and boundary (n = 3, ≥ 15 cells per sample). Black dotted line represents the RL limit for core localizations. Grey boxes denotes the protein factors which were evenly dispersed across the entire cytosol and consequently did not have any detectable features (local maxima) for RL calculations. (**C**) Schematic (left) of enrichment index (EI) calculation. Representative pseudoclored and contrast-adjusted regions of UGD cells (middle) with GFP-Dcp1a (green), stained for Rck, GAPDH or rRNA (red,). Yellow and red dotted circles represent PB-localized and cytoplasmic signal

respectively. Scale bar, 2 μm. EI of top and bottom panels are represented within the images. Scatter plot of EI (right) for IF signal at PBs. Each dot represents an individual PB colocalization event (n = 3, ≥ 15 cells per sample). Grey dotted line depicts an EI of one, which demarcates PB-enriched (> 1) from PB-depleted (< 1) factors.

2.3.3. mRNA-targeting and target-free miRNAs are both enriched at PBs but display distinct PB localization dynamics

Based on our observations that a functionally repressive l7-Cy5/l7* miRNA dynamically localized to PBs via diverse modes (Figure 2-3), we hypothesized that the regulatory potential of miRNAs impacts their PB localization. To test this hypothesis, we compared the PB-localization of functional l7-Cy5/l7* with l7/l7*-Cy5, let-7 miRNA Cy5-labeled on the passenger instead of the guide strand, where the passenger strand has very few endogenous targets and is at least 8-fold less stable than the guide strand, and with ml7-Cy5/ml7*, a seed-sequence mutated let-7 miRNA variant that cannot bind endogenous let-7 targets and is at least 4-fold less stable than let-7 miRNA (Figure 2-5A) (Pitchiaya et al., 2017a). Strikingly, the fractional extents of PB localization and enrichment were significant and similar for l7-Cy5/l7*, l7/l7*-Cy5 and ml7-Cy5/l7* (Figure 2-5B-C). Similar trends (Figure 2-6A-C) were observed for all other small dsRNAs, namely an oncogenic miRNA miR-21 (m21-Cy5/m21*), an artificial miRNA cxcr4 (cx-Cy5/cx*) and scrambled control dsRNA (Scr-Cy5/Scr*). Considering that each of these dsRNAs have distinct regulatory potential and intracellular stability (Pitchiaya et al., 2017a), our data strongly suggest that miRNA functionality is not necessary for PB localization. However, ml7-Cy5/ml7*, l7/l7*-Cy5, cx-Cy5/cx* and Scr-Cy5/Scr* rarely displayed any transient interactions (Figure 2-5D and Figure 2-6D), but instead exhibited monophasic dwell time distributions, residing in PBs for ≥ 15 s (Figure 2-5D and 2-6), significantly different from the PB-dynamics of l7-Cy5/l7* and m21-Cy5/m21*. These observations suggest that transient PB interactions of a miRNA are correlated with its ability to target mRNAs, whereas unused (target-less) miRNAs are more stably recruited

to PBs. Further corroborating this notion, we found that, upon co-microinjecting its cognate (RL-ml7-2x) mRNA, the mRNA-targeting ml7-Cy5/ml7* exhibited a substantial 5-fold increase in the fraction of transient interactions, resulting in a biphasic dwell time distribution with T_{fast} = 0.7 s and T_{slow} = 13.2 s (Figure 2-5E-F and 2-6C-D). Taken together, our results are consistent with PBs stably capturing target-less, non-coding miRNAs for surveillance, and suggest that instead transient PB interactions are dominant for functional miRNAs engaging mRNA targets.

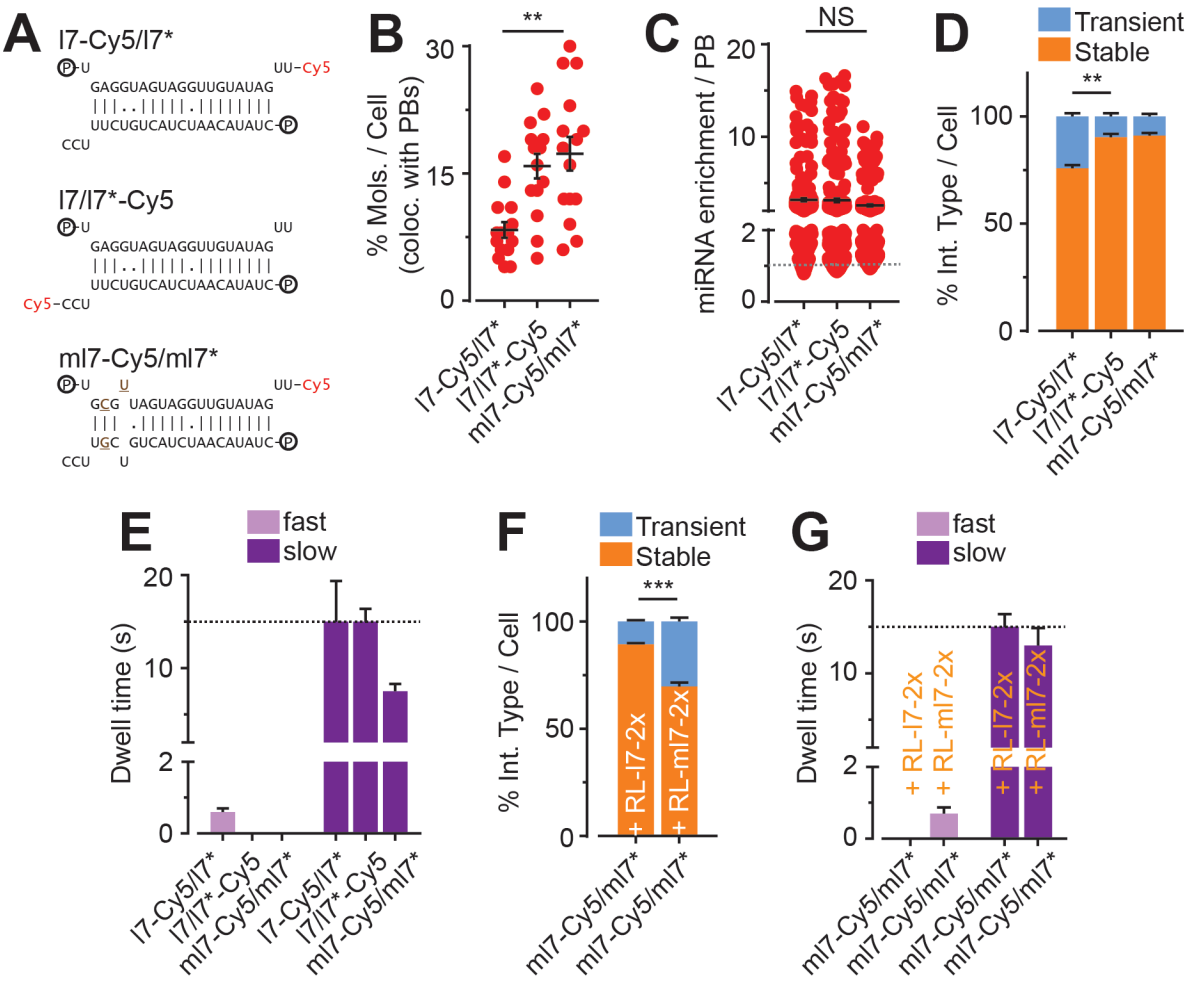

Figure 2-5 miRNA functionality influences miRNA-PB interaction kinetics. (**A**) Schematic of miRNAs used. P, lines and dots represent 5` phosphate, Watson-crick base pairing and wobble pairing respectively. (**B**) Scatter plot representing the % of RNA or DNA molecules that colocalize with PBs per fixed UGD cell. Each dot represents a cell. (**C**) Scatter plot of EI for different constructs. Each dot represents an individual PB in fixed UGD cells. Grey dotted line depicts an EI of one, which demarcates PB-enriched (> 1) from PB-depleted (< 1) factors. (**D**) Relative distribution of stable and transient interactions per live UGD cell for different miRNAs. (**E**) Comparison of fast and

slow miRNA-PB interaction kinetics in live UGD cells. (**F**) Relative distribution of stable and transient interactions per live UGD cell for ml7-Cy5/ml7* RNAs co-injected with a seed mismatched (RL-l7-2x) or seed matched (RL-ml7-2x) mRNA target. (**G**) Comparison of fast and slow ml7-Cy5/ml7*-PB interaction kinetics in the presence of a seed mismatched (RL-l7-2x) or seed matched (RL-ml7-2x) mRNA target in live UGD cells. n = 3, 15 cells per sample, NS = not significant, **p ≤ 0.001 or ***p ≤ 0.0001 by two-tailed, unpaired Student's t-test. See also Figure S3.

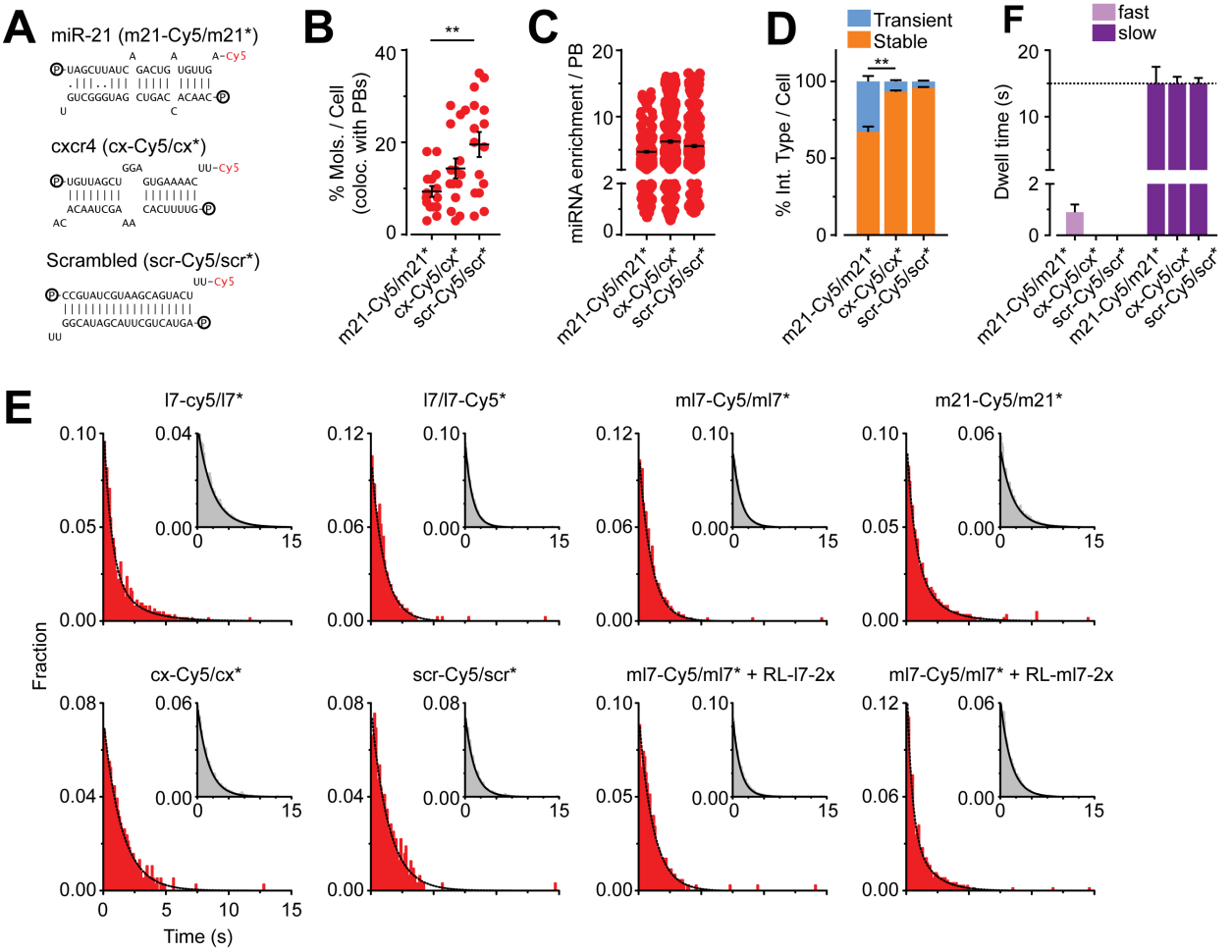

Figure 2-6 PB-localization and interaction kinetics of different miRNAs, in the presence or absence of cognate targets (Related to Figure 3). (**A**) Schematic of additional miRNAs used. P, lines and dots represent 5` phosphate, Watson-crick base pairing and wobble pairing respectively. (**B**) Scatter plot representing the % of miRNA molecules that colocalize with PBs per fixed UGD cell. Each dot represents a cell. (**C**) Scatter plot of EI for different constructs. Each dot represents an individual miRNA-PB colocalization event in fixed UGD cells. (**D**) Relative distribution of stable and transient interactions per live UGD cell for different miRNAs. (**E**) Dwell time distribution of all miRNAs at PBs in live UGD cells. Black line depicts single or double exponential fit. Inset, dwell time distribution of miRNAs inside cells, prior to photobleaching. Black line depicts single exponential fit. (**F**) Comparison of fast and slow miRNA-PB interaction kinetics for the additional miRNAs in live UGD cells. (n ≥ 3; ≥ 15 cells, **p ≤ 0.001 by two-tailed, unpaired Student's t-test.).

2.3.4. miRNA-targeted mRNAs localize to PBs depending on 3` versus 5` terminal positioning of MREs

Next, we probed whether miRNAs and their cognate mRNA targets displayed similar dynamics and localization patterns at PBs. mRNAs were endogenously expressed and tagged via a modified version of the widely used MS2-MCP labeling system (Fusco et al., 2003), wherein a total of up to ~1,000 Halo-MCP bound MS2-RNA molecules were visualized per living cell upon covalently coupling the Halo tag with the cell-permeable fluorescent dye JF646 (Figure 4A-B and Supplementary movie 3) (Grimm et al., 2015). mRNAs in fixed cells were instead visualized by standard single-molecule fluorescence *in situ* hybridization (smFISH, Figure 2-7A and 2-7C) (Raj et al., 2008). We created an MS2-MCP tagged construct bearing the firefly luciferase (FL) coding sequence (CDS) and an artificial 3`untranslated region (3`UTR) bearing six tandem miRNA response elements (MREs) for the tumor suppressive let-7 miRNA (l7-6x). Upon performing live and fixed cell imaging respectively, we found that that the mobility and assembly of FL-l7-6x-MS2 mRNA was similar to its cognate l7-Cy5/l7* miRNA (Figure 2-2 and 2-7A-F), strongly supporting the notion that a miRISC-mRNP complex interacts with PBs. As a control, we created an MS2-tagged FL gene with ml7-6x, a 3`UTR composed of six tandem mutant MREs ml7/ml7* that are not targeted by endogenous let-7 (Figure 2-7G).

Considering that MRE-containing mRNAs are repressed, irrespective of whether the MREs are in the 3` or 5` UTR of the mRNA (Lytle et al., 2007), we created additional control constructs with either l7-6x or ml7-6x in the 5`UTR of the MS2-tagged FL gene, termed l7-6x-FL-MS2 and ml7-6x-FL-MS2 respectively (Figure 2-7G). As expected, ensemble activity assays showed that all MS2-tagged constructs were translated and regulated much like their untagged

counterpart (Figure 2-8A-B). FL-ml7-6x-MS2 and ml7-6x-FL-MS2 were expressed to much higher extents (Figure 2-7H) than the let-7-MRE containing FL-l7-6x-MS2 and l7-6x-FL-MS2, which both were similarly repressed by let-7 miRNA (Figure 2-7H and 2-8C), thus corroborating prior reports that MREs embedded in either the 3` or 5`UTR are functional. However, the fractional extents of localization and enrichment of l7-6x-FL-MS2 at PBs were similar to those of the non-targeted FL-ml7-6x-MS2 and ml7-6x-FL-MS2, and significantly (at least 5-fold) lower than those of FL-l7-6x-MS2 (Figure 2-7I-J). Still, l7-6x-FL-MS2, FL-ml7-6x-MS2 and ml7-6x-FL-MS2, much like FL-l7-6x-MS2, interacted transiently with PBs and displayed biphasic interaction kinetics (Figure 2-7K-L and 2-8D). While the "fast" phase for l7-6x-FL-MS2, FL-ml7-6x-MS2 and ml7-6x-FL-MS2 (spanning ~0.5, 0.7 and 0.6 s, respectively) was similar to that of FL-l7-6x-MS2 (0.9 s), the "slow" phase for these constructs was ~3-fold faster than that of FL-l7-6x-MS2 (4.2 s, 3.7 and 2.5 s, respectively, compared to 15 s, Figure 2-7K), indicating a significant difference in behavior upon targeting the 3` versus 5`UTR. Similarly, a minority of l7-6x-FL-MS2, FL-ml7-6x-MS2 and ml7-6x-FL-MS2 particles did not photobleach and resided in PBs for the entire duration of acquisition (~ 15 s), with the number of such occurrences ~3-fold lower than for FL-l7-6x-MS2 (Figure 2-8E). Not only do these observations strongly support the notion that miRNAs and their cognate mRNA targets display generally similar PB localization kinetics and patterns, consistent with the hypothesis that they interact, but they uniquely demonstrate that 3`UTR versus 5`UTR positioning of MREs distinctly impacts PB colocalization in that only 3`UTR targeting leads to the most stable PB interactions. We posit that distinct aspects of translation are blocked when miRNAs engage the 3`UTR versus 5`UTR, resulting in compositionally distinct mRNPs that differentially recruit them to PBs.

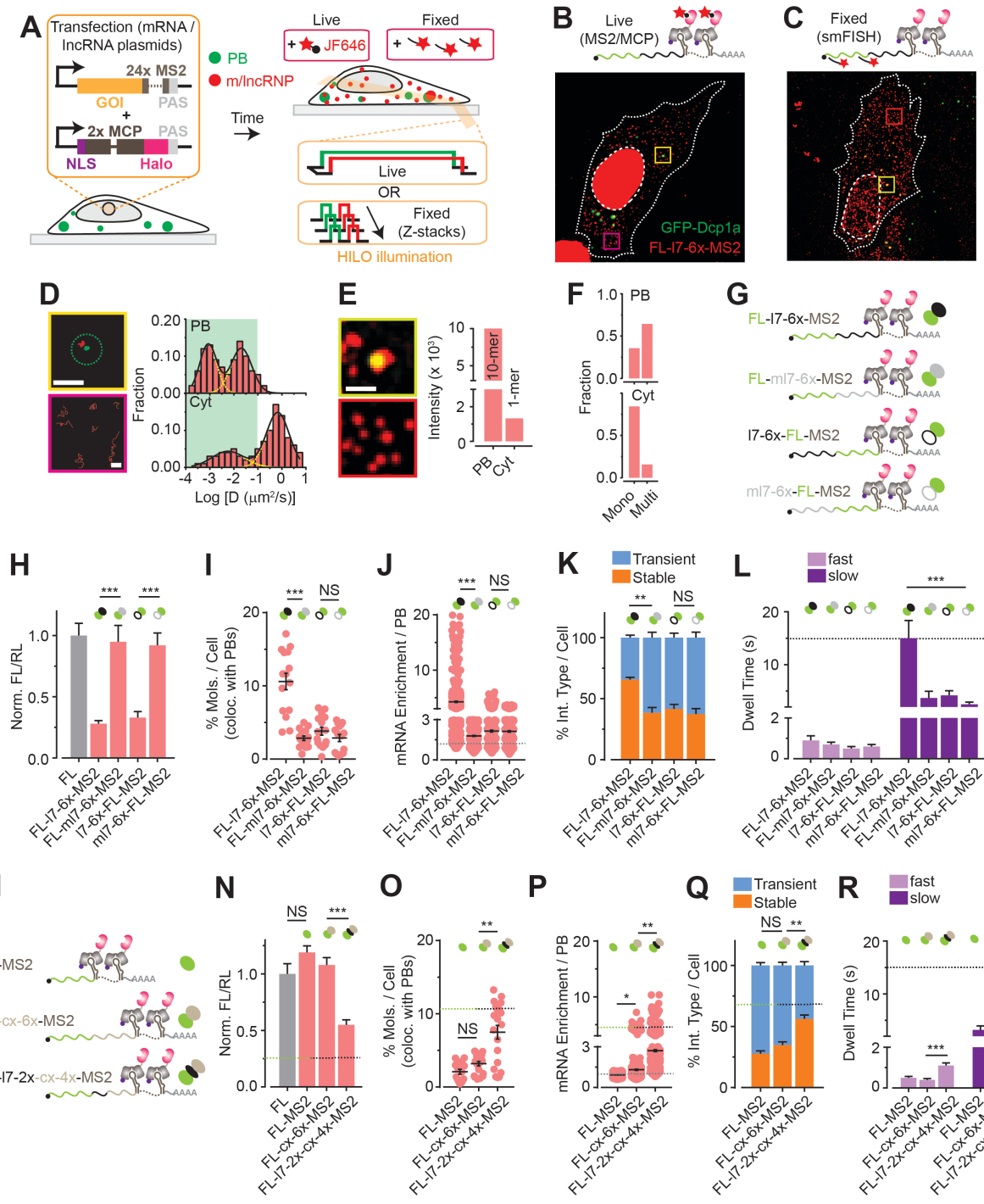
A
Transfection (mRNA / lncRNA plasmids)
24x MS2
GOI
PAS
+
2x MCP
PAS
NLS
Halo
PB
m/lncRNP
Time
Live
Fixed
JF646
Live
OR
Fixed (Z-stacks)
HILO illumination
B
Live (MS2/MCP)
GFP-Dcp1a
FL-I7-6x-MS2
C
Fixed (smFISH)
D
PB
Cyt
Fraction
Log [D (μm²/s)]
E
Intensity (x 10³)
10-mer
1-mer
PB
Cyt
F
PB
Cyt
Fraction
Mono
Multi
G
FL-I7-6x-MS2
FL-ml7-6x-MS2
I7-6x-FL-MS2
ml7-6x-FL-MS2
H
Norm. FL/RL
I
% Mols. / Cell (coloc. with PBs)
J
mRNA Enrichment / PB
K
Transient
Stable
% Int. Type / Cell
L
fast
slow
Dwell Time (s)
FL
FL-I7-6x-MS2
FL-ml7-6x-MS2
I7-6x-FL-MS2
ml7-6x-FL-MS2
M
FL-MS2
FL-cx-6x-MS2
FL-I7-2x-cx-4x-MS2
N
Norm. FL/RL
O
% Mols. / Cell (coloc. with PBs)
P
mRNA Enrichment / PB
Q
Transient
Stable
% Int. Type / Cell
R
fast
slow
Dwell Time (s)
FL-MS2
FL-cx-6x-MS2
FL-I7-2x-cx-4x-MS2

Figure 2-7 mRNAs localize to PBs depending on 3` versus 5` terminal positioning of MREs and translation potential. (**A**) Schematic of assay for probing mRNA-PB dynamics and colocalizations. (B and C) Representative pseudo-colored and contrast-adjusted images from live-cell imaging (**B**) and fixed cell imaging (**C**) assays of UGD cells expressing GFP-labeled PBs (green) and MCP tagged FL-l7-6x-MS2 mRNAs (red). Scale bar, 10 μm. (**D**) Representative single-particle trajectories of PBs (green) and FL-l7-6x-MS2 mRNAs (red) from yellow and magenta boxes in B, representing diffusing mRNAs in PBs and in the cytoplasm (Cyt) respectively. Scale bar, 1 μm. Dotted green circle represents PB outline in the first frame of the movie. Distribution of FL-l7-6x-MS2 mRNAs diffusion constants in PB and Cyt are also depicted. Green area on the plot depicts the range of PB diffusion constants (n = 3, 20 cells). (**E**) Zoomed-in view of orange and violet boxes in C, from fixed UGD cells. Scale bar, 2 μm. Intensity measurements of PB- and Cyt-localized FL-l7-6x-MS2 mRNAs is also shown. (**F**) Distribution of FL-l7-6x-MS2 mRNAs stoichiometry as monomeric (Mono, 1 photobleaching step) or multimeric (Multi, ≥ 2 photobleaching steps) complexes in PB and Cyt within fixed UGD cells (n = 3, 20 cells). (**G** and **M**) Schematic of different mRNA constructs with various 3` or 5` UTRs. Color-coded symbols for each transcript is shown and will be used to depict these respective transcripts from hereon. (H and N) Luciferase reporter assays represented as the ratio of luminescence form a firefly luciferase (FL) reporter gene and a renilla luciferase (RL) normalization gene in UGD cells. Data were normalized to the FL sample. Mean and s.e.m are represented (n = 12 replicates, ***$p < 0.0001$ based on two-tailed, unpaired Student's t-test). (I and O) Scatter plot representing the % of mRNA molecules that colocalize with PBs per fixed UGD cell. Each dot represents a fixed UGD cell. (J and P) Scatter plot of EI for different mRNA constructs. Each dot represents a PB in fixed UGD cells. Grey dotted line depicts an EI of one, which demarcates PB-enriched (> 1) from PB-depleted (< 1) factors. (**K** and **Q**) Relative distribution of stable and transient interactions per live UGD cell for different mRNAs. (**L** and **R**) Comparison of fast and slow mRNA-PB interaction kinetics in live UGD cells. Black line depicts acquisition window (15 s). Green-black line depicts the mean magnitude of FL-l7-6x-MS2 for the respective observable. n = 3, ≥ 15 cells per sample, NS = not significant, * $p \leq 0.01$, **$p \leq 0.001$ or ***$p \leq 0.0001$ by two-tailed, unpaired Student's t-test. See also Figure S4.

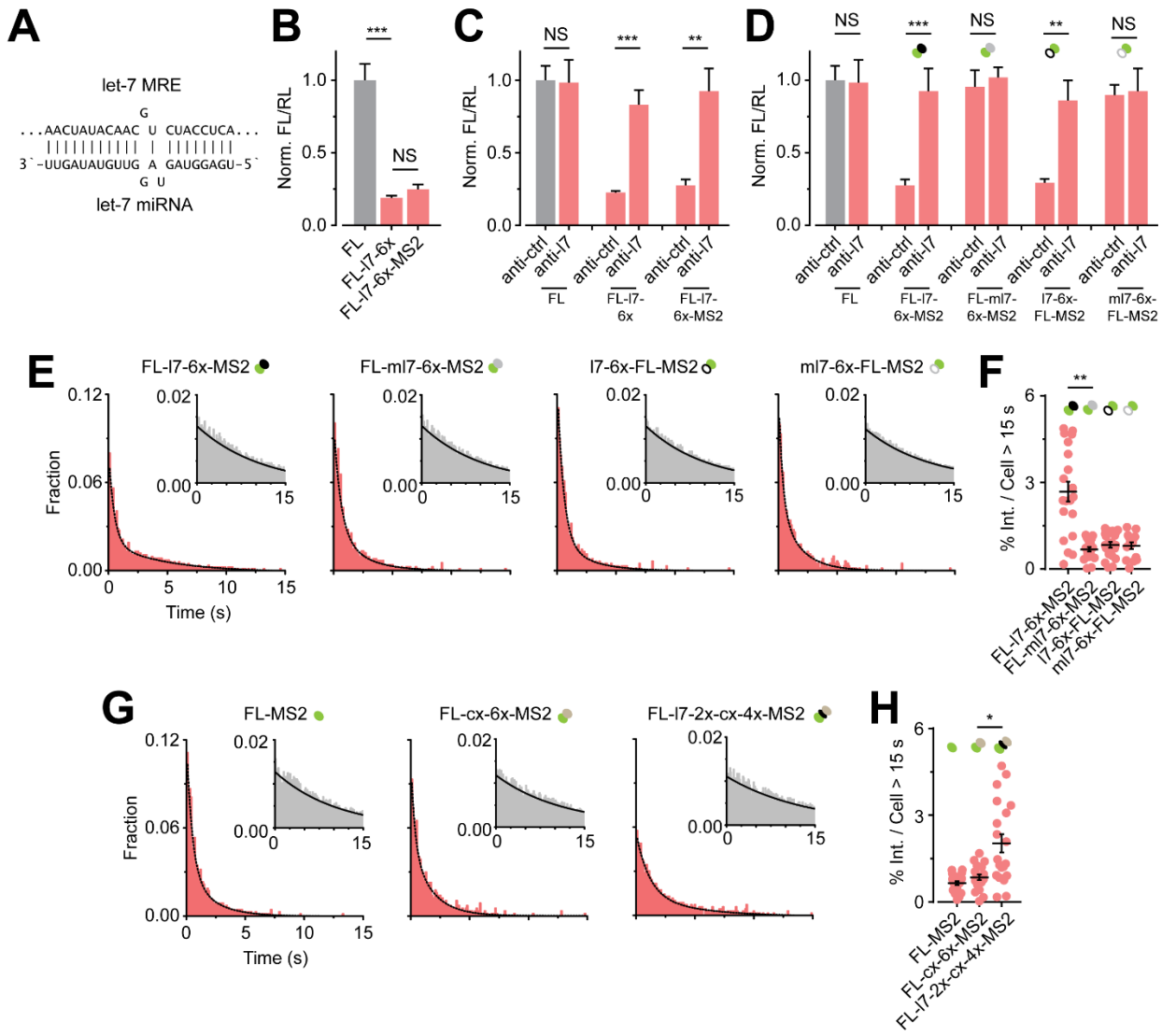

Figure 2-8 Validation of in situ m/lncRNA imaging system. (**A**) Luciferase reporter assays of the appropriate mRNA constructs (n = 12). Data were normalized to FL. Mean and s.e.m are depicted (n = 12 replicates, NS = not significant or ***p < 0.0001 based on two-tailed, unpaired Student's t-test). (**B-C**) Luciferase reporter assays of the appropriate mRNA constructs treated with a control antimiR (anti-ctrl) or an anti-let7 (anti-l7) antimiR. (n = 12). Data were normalized to FL (anti-ctrl). Mean and s.e.m are depicted (n = 12 replicates, NS = not significant, **p ≤ 0.001 or ***p < 0.0001 based on two-tailed, unpaired Student's t-test). (**D** and **F**) Dwell time distribution of the appropriate mRNA constructs at PBs. Black line depicts double exponential fit Inset, dwell time distribution of mRNAs inside cells, prior to photobleaching. Black line depicts single exponential fit. (**E** and **G**) Scatter plot representing % of mRNA-PB interactions that last for the entire duration of imaging (15 s), without photobleaching, per live UGD cell. n = 3, ≥ 15 cells per sample, **p < 0.001 based on two-tailed, unpaired Student's t-test.

2.3.5. mRNA-PB interactions depend on translation potential

Given that translationally unrepressed mutant FL-ml7-6x-MS2 and translationally repressed FL-l7-6x-MS2 mRNAs displayed distinct PB-dynamics and localization patterns

(Figure 2-7), we hypothesized that the translation potential of an mRNA inversely correlates with PB localization. To test this hypothesis, we compared the PB localization dynamics of the let-7 regulated FL-l7-6x-MS2 mRNA (Figure 2-7) with those of FL-MS2 (lacking the regulatory 3`UTR), FL-l7-2x-cx-4x-MS2 (carrying a 3`UTR with two tandem MREs targetable by endogenous let-7 and four MREs for a non-endogenous cxcr4 miRNA) and FL-CX-6x-MS2 (carrying a 3`UTR with six tandem MREs for cxcr4 miRNA) (Figure 2-7M). Notably, protein expression of FL-MS2 and FL-cx-6x-MS2 was significantly higher (~2.7 fold) than FL-l7-2x-cx-4x-MS2, which in turn was higher (~2.2-fold) than FL-l7-6x-MS2 (Figure 2-7N). Consistent with our hypothesis, the fractional extents of localization and enrichment of FL-MS2 and FL-cx-6x-MS2 were significantly (at least 2.8 fold or 5-fold) lower than those of FL-l7-2x-cx-4x-MS2 or FL-l7-6x-MS2 (Figure 2-7G-H). Additionally, the interaction modalities and "slow" phase kinetics of FL-MS2 and FL-cx-6x-MS2 were distinct from FL-l7-2x-cx-4x-MS2 and FL-l7-6x-MS2, with the former set of constructs displaying at least ~2.5-fold more transient interactions and ~3-fold shorter dwell times at PBs (Figure 2-7I-J) compared to the latter set. A significant minority of FL-MS2 and FL-cx-6x-MS2 particles resided in PBs for the entire duration of acquisition (~15 s), potentially representing mRNAs that are currently translation inactive, but the number of such occurrences was ~2.9-fold and ~4.5-fold lower than those for FL-l7-2x-CX-4x-MS2 and FL-l7-6x-MS2 (Figure 2-8F), respectively. These observations strongly support the notion that actively translating mRNAs rarely localize to PBs, and conversely that the propensity for PB-localization increases with extent of mRNA repression.

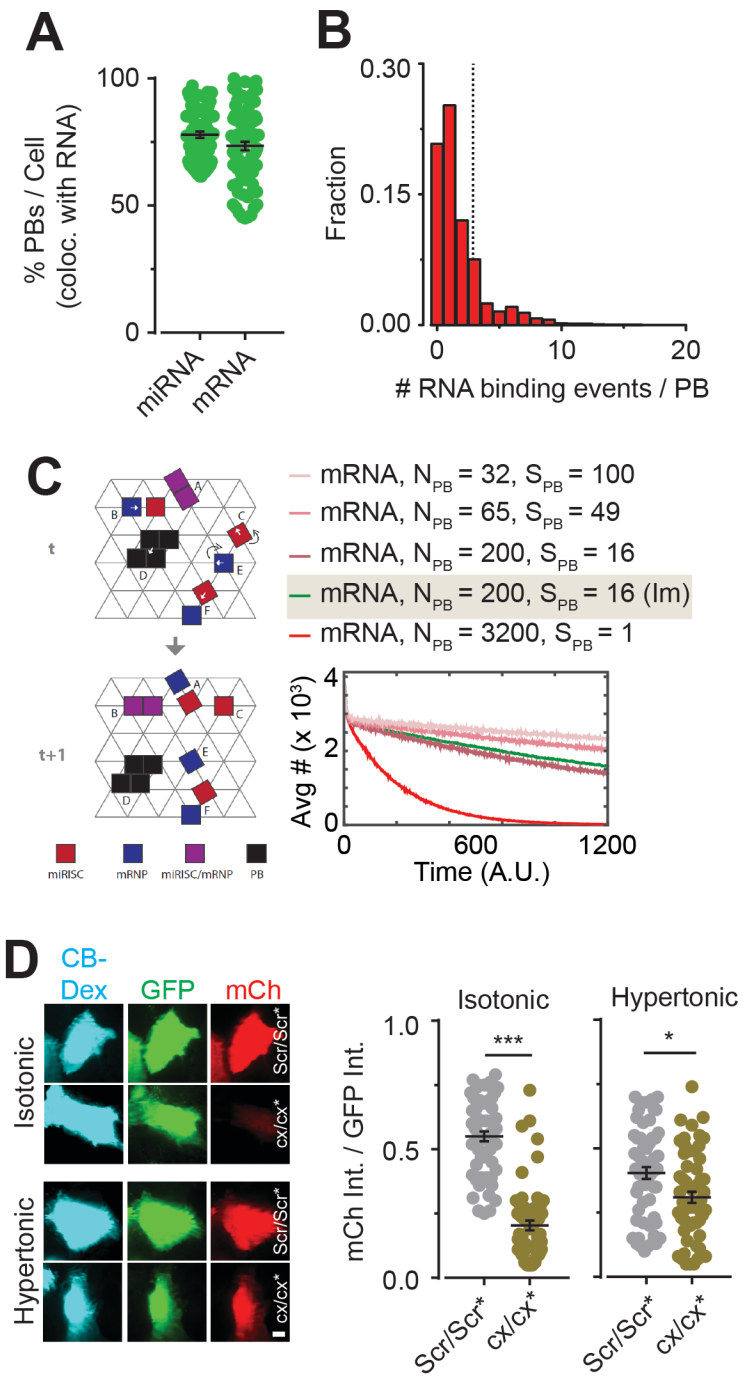

Figure 2-9 A majority of microscopically visible PBs associate with mRNAs, but mRNAs are more effectively degraded with a larger number of smaller, microscopically-invisible PBs. (**A**) Scatter plot representing the % PBs that colocalize with RNAs, per fixed UGD cell (n = 3, ≥ 15 cells per sample). (**B**) Frequency distribution of the number of times an individual PB encounters an RNA in live UGD cells (n = 3, 155 cells, 2102 PBs). Dotted line represents the average number of RNA encounters per PB after correcting for photobleaching. (**C**) Schematic (left) of in silico kinetic modeling of RNA-PB interactions and RNA decay. Changes in the abundance of mRNA over the timescale of the simulation is also depicted (right). Im (highlighted text) represents simulations in which PBs were immobile, whereas PBs were mobile in all other conditions. (**D**) Experimental validation of simulations using microinjection-based miRNA activity assay. Left, representative images of U2-OS cells treated with isotonic or hypertonic (300 mM Na+)

medium and co-injected with CB-Dextran, GFP mRNA,mCh mRNA with MREs for cxcr4 (cx/cx*) miRNA and either a scrambled, control siRNA (Scr/Scr*) or cx/cx*. Images were acquired 4 h after injection. Right, scatter plot representing the ratio of mCh : GFP intensity at various injection and treatment conditions. Each dot represents a U2-OS cell (n = 3, 60 cells for each sample).

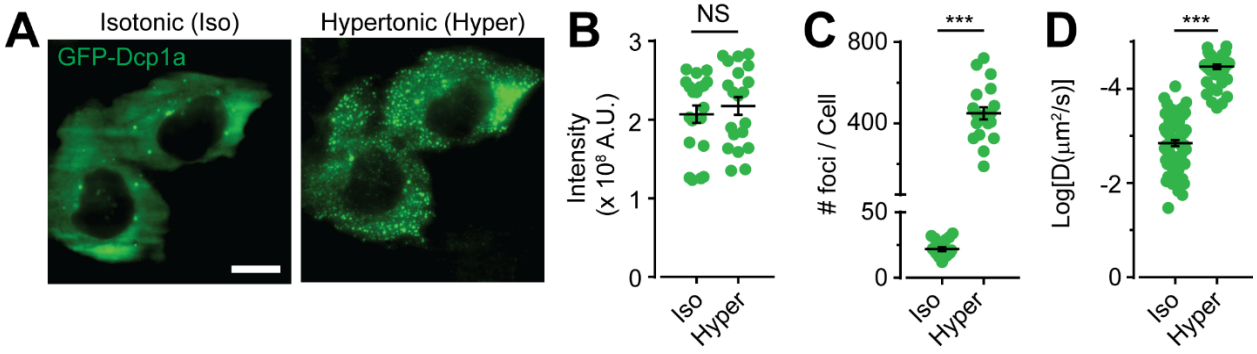

Figure 2-10 Characterization of cells treated with hyper-osmotic medium (Related to Figure 5). (**A**) Representative pseudocolored images of UGD cells treated with isotonic or hypertonic media. GFP-Dcp1a, green. Scale bar, 10 μm. (**B-D**) Scatter plot of the intensity per cell (**B**), number of GFP foci per cell (**C**) and diffusion coefficients of PBs (**D**) under each treatment condition. n = 3, 20 cells per sample, NS = not significant or ***p < 0.00)1 based on two-tailed, unpaired Student's t-test.

2.3.6. miRNA-targeted mRNA turnover predominantly occurs outside of PBs

We find that almost all visible PBs colocalize with miRNA or mRNA molecules, irrespective of relative RNA enrichment (Figure 2-9A), and a single PB associates with at least 3 labeled RNA molecules within our timeframe of imaging (Figure 2-9B). Considering this frequent encounter of mi/mRNAs and PBs, that miRNA-mediated translational repression would eventually lead to RNA decay (Djuranovic et al., 2012) and that PBs are enriched for mRNA degradation enzymes (Hubstenberger et al., 2017a; Parker and Sheth, 2007), we sought to test whether PBs are designated sites of RNA decay responsible for the bulk of cellular mRNA turnover. While fluorescence microscopy can visualize large PBs (> 50 nm), it does not capture smaller functional complexes of RNA decay enzymes. We therefore kinetically modeled (Mourao et al., 2014) the mRNA degradation activity of microscopically visible and invisible PBs computationally (Figure

2-9C). We specifically tested miRNA-mediated mRNA decay, largely due its cellular prevalence and prior reports on miRNA programmed mRNA localization to PBs; however, our method is extendable to other decay processes. We devised a basic set of reactions, each with predefined rates, whereby the interaction of miRISC with mRNPs activates PB-mediated mRNA degradation. Upon computing the copy number of each of these molecular species as they diffused across the lattice through time, we found that mRNA degradation was most efficient when there was a large number of small, mobile PBs (Figure 2-9C). That is, while degradation is possible within large, microscopically visible PBs, the process is most efficient when degradation factors, perhaps individual molecules, are unconstrained in the cell, thus presenting a large surface area for capturing repressed mRNAs.

To test our *in silico* predictions experimentally, we resorted to modulating PB number and size via hyperosmotic stress, a method that has been proven to increase PB number in yeast (Huch and Nissan, 2017a). We confirmed that hyperosmotic treatment of UGD cells results in a high number of immobile GFP-Dcp1a foci (Figure 2-10A-D), which form due to local association of previously mobile, microscopically-unresolved GFP-Dcp1a proteins, an aspect that is efficiently recapitulated by our *in silico* kinetic modeling approach (Figure 5C, “Im”). Microinjection-based miRNA activity assays (Figure 2-1E) in U2-OS cells suggested that, as predicted, miRNA-mediated gene repression is alleviated when PBs are aggregated upon subjection of cells to hyperosmotic stress (Figure 2-9D). Taken together, our data predict that mRNA degradation is primarily mediated by degradation enzymes rendered more efficient by freely diffusing in the cytosol, relegating PBs to degrading only a small fraction of repressed mRNAs.

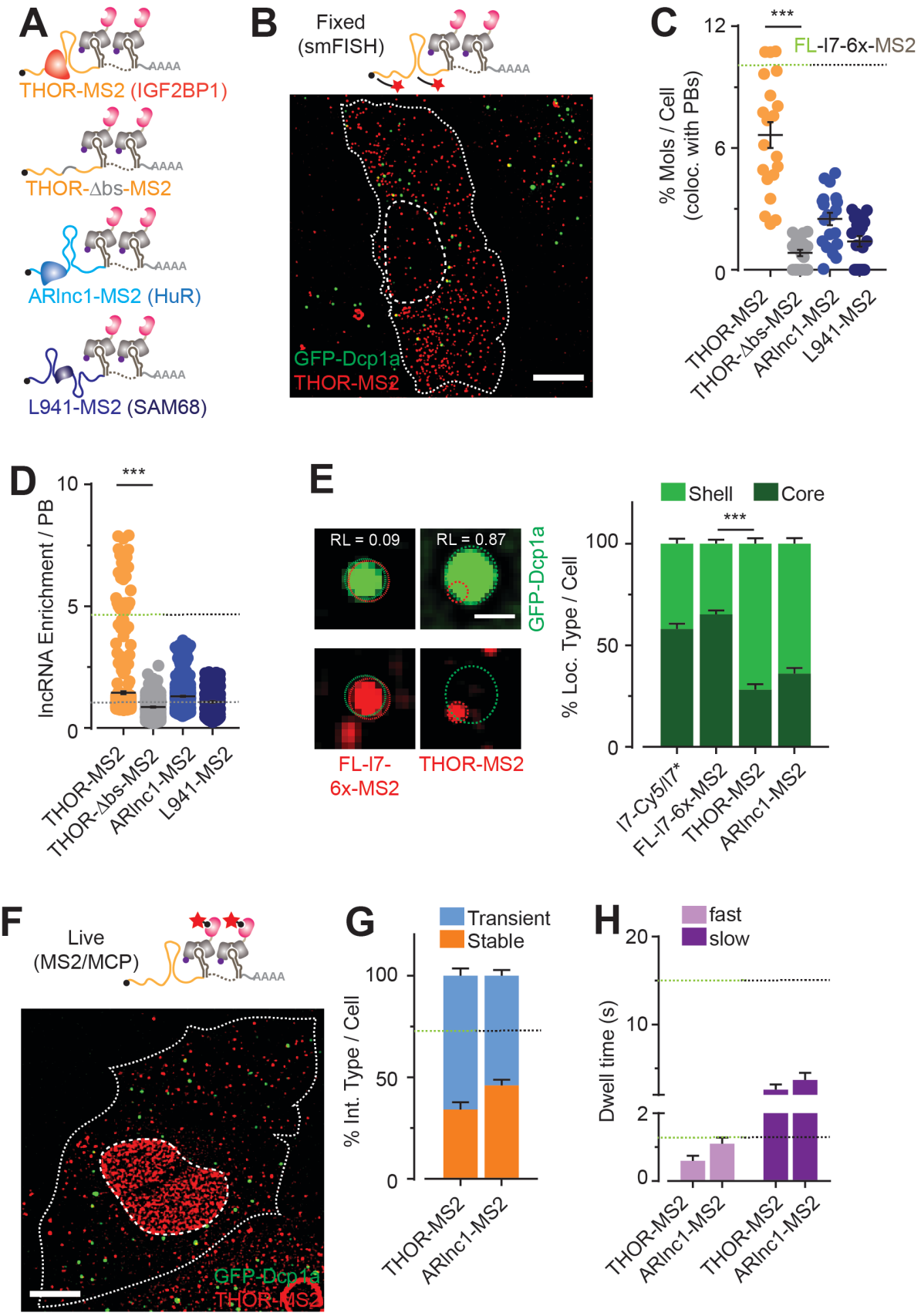
A
THOR-MS2 (IGF2BP1)
THOR-Δbs-MS2
ARlnc1-MS2 (HuR)
L941-MS2 (SAM68)
AAAA
B
Fixed
(smFISH)
GFP-Dcp1a
THOR-MS2
C
***
FL-I7-6x-MS2
% Mols / Cell
(coloc. with PBs)
12
6
0
THOR-MS2
THOR-Δbs-MS2
ARlnc1-MS2
L941-MS2
D
***
lncRNA Enrichment / PB
10
5
0
THOR-MS2
THOR-Δbs-MS2
ARlnc1-MS2
L941-MS2
E
RL = 0.09
RL = 0.87
GFP-Dcp1a
FL-I7-
6x-MS2
THOR-MS2
Shell
Core
***
% Loc. Type / Cell
100
50
0
I7-Cy5/I7*
FL-I7-6x-MS2
THOR-MS2
ARlnc1-MS2
F
Live
(MS2/MCP)
GFP-Dcp1a
THOR-MS2
G
Transient
Stable
% Int. Type / Cell
100
50
0
THOR-MS2
ARlnc1-MS2
H
fast
slow
Dwell time (s)
20
10
2
0
THOR-MS2
ARlnc1-MS2
THOR-MS2
ARlnc1-MS2

Figure 2-11 lncRNAs transiently interact with PB peripheries. (**A**) Schematic of different lncRNA constructs bound by their respective interacting protein partner. (**B**) Representative pseudocolored and contrast-adjusted images of fixed a UGD cell expressing GFP-Dcp1a (green) and stained for THOR-MS2 via smFISH (red). Dotted line, cell and nuclear outline. Scale bar, 10 μm. (**C**) Scatter plot representing the percentage of lncRNA molecules per cell that colocalize with PBs. Each dot is a cell. (**D**) Scatter plot for the enrichment of lncRNAs at PBs. Each dot is a PB. Grey dotted line depicts an EI of one, which demarcates PB-enriched (> 1) from PB-depleted (< 1) factors. (**E**) Representative pseudoclored and contrast-adjusted regions of fixed UGD cells with GFP-Dcp1a (green), stained for FL-l7-6x-MS2 mRNA or THOR-MS2 lncRNA via smFISH (red). Green and red dotted circles represent boundaries of PBs and THOR-MS2 respectively. Scale bar, 2 μm. Relative localization value is represented within the image. (**F**) Representative pseudocolored and contrast-adjusted images of a live UGD cells expressing GFP-Dcp1a (green) and THOR-MS2 (red). Dotted line, cell and nuclear outline. Scale bar, 10 μm. (**G**) Relative distribution of stable and transient interactions per live UGD cell for. (**H**) Comparison of fast and slow interaction kinetics in in live UGD cells. Green-black line depicts the mean magnitude of FL-l7-6x-MS2 for the respective observable. n = 3, ≥ 15 cells per sample, NS = not significant, * $p \leq 0.01$, ** $p \leq 0.001$ or *** $p \leq 0.0001$ by two-tailed, unpaired Student's t-test. See also Figure S6.

Figure 2-12 lncRNA construct validation and kinetics (Related to Figure 6). (**A**) Relative expression of the appropriate lncRNA constructs transfected into UGD cells as measured by RT-qPCR and normalized to mock. (**B**) Cell growth as measured by ATP abundance in UGD cells transfected with the appropriate lncRNA construct (**C**) Relative expression of MYC in UGD cells transfected with lncRNA constructs, as measured by RT-qPCR and normalized to mock. Mean and s.e.m are depicted for A-C. n = 3 replicates, ** $p < 0.0001$ based on two-tailed, unpaired Student's t-test. (**D**) Distribution of THOR-MS2 lncRNA diffusion constants in PB and Cyt within live UGD cells. (**E**) Distribution of THOR-MS2 lncRNA stoichiometry as monomeric or multimeric complexes in PB and Cyt within fixed UGD cells.

(**F**) Dwell time distribution of all lncRNAs at PBs in live UGD cells. Black line depicts single or double exponential fit. Inset, dwell time distribution of lncRNAs inside cells, prior to photobleaching. Black line depicts single exponential fit. n = 3, 20 cells.

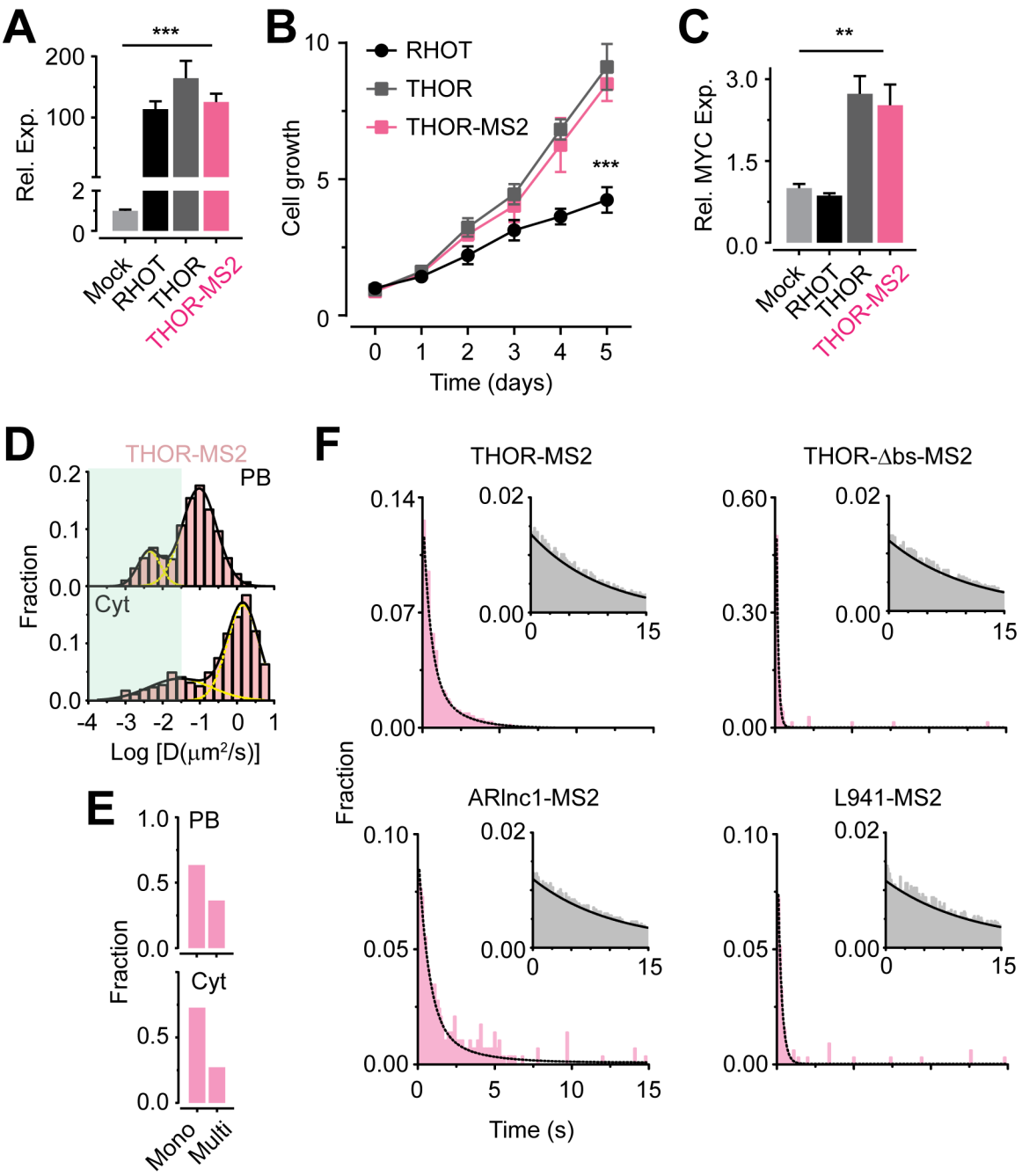

2.3.7. lncRNA-PB interactions are distinct from those of regulatory miRNAs and repressed mRNAs

Having discovered the importance of translation versus translational repression in mRNA-PB colocalization behavior, we hypothesized that lncRNAs that sparsely interact with the

translational machinery must localize to PBs via mechanisms distinct from those involving miRNAs and mRNAs. To address this hypothesis, we chose as model the nucleo-cytoplasmic lncRNA THOR (Figure 2-11A) that binds PB-enriched IGF2BP1 protein (Hubstenberger et al., 2017a). We confirmed that THOR-MS2 still mediates the oncogenic phenotype of the unmodified lncRNA (Hosono et al., 2017) as evident by it promoting cell growth and stimulating oncogene expression (Figure 2-12A-C). We then performed live cell imaging assays (Supplementary movie 4) and found that that THOR-MS2 molecules, on an average, diffused faster than miRNAs or mRNAs that we imaged, but distributed between at least two populations of diffusion constants at PBs, much like the other RNAs (Figure 2-12D). Fixed cell imaging showed that the stoichiometry of THOR at PBs was marginally higher than that found in the cytosol (Figure 2-11B and 2-12E). While the fractional extent of RNA-PB colocalization did not significantly differ between mRNAs on the one hand and lncRNAs on the other (Figure 2-11C-D), we found significant differences in the localization patterns and interaction kinetics between mi/mRNAs and THOR-MS2 lncRNAs (Figure 2-11). In particular, THOR-MS2 frequently localized to the shell of PBs, whereas l7-Cy5/l7* miRNA or FL-l7-6x-MS2 mRNA, ~2.5-5-fold more PB-enriched than THOR-MS2, predominantly localized near PB cores (Figure 2-11E). We also observed that a THOR version lacking IGF2BP1 binding sites (THOR-Δbs-MS2) only rarely localized to or interacted with PBs (Figure 2-11C-D), indicating that THOR-PB interactions are mediated by IGF2BP1. Moreover, THOR-MS2 displayed ~2-3-fold more transient PB interactions than FL-l7-6x-MS2 mRNA (Figure 2-11F-G). Although the dwell time distributions were bi-phasic for both (Figure S5C and S6F), l7-Cy5/l7* miRNA or FL-l7-6x-MS2 mRNA (T_{fast} = 0.6 s and $T_{slow} \geq 15$ s) resided at PBs for a significantly longer time than THOR-MS2 (T_{fast} = 0.6 s and T_{slow} = 2.9 s, Figure 2-11B and 2-12B). We further found that oncogenic lncRNA ARlnc1 (Zhang et al., 2018), known to bind PB-

enriched HuR (Hubstenberger et al., 2017a), displayed similar PB-localization kinetics and patterns as THOR (Figure 2-11 and 2-12F); whereas oncogenic LINC00941 (L941) (Shukla et al., 2017), a lncRNA that lacks consensus binding motifs for PB-enriched proteins (Hubstenberger et al., 2017a), only rarely localized to PBs and displayed mono-phasic interaction kinetics, much like THOR-Δbs-MS2 (Figure 2-11 and 2-12F). Together, these data support our hypothesis that regulatory miRNAs and miRNA-regulated mRNAs are stably captured by PBs; by contrast, regulatory, non-translating lncRNAs that bind PB-localizing protein factors only transiently associate with PBs. These specific, yet transient lncRNA-PB interactions are often missed in ensemble assays that largely rely on the enrichment of stable, high-affinity interactions, likely leading to the relative dearth of lncRNAs observed in the transcriptome of PB cores (Hubstenberger et al., 2017a).

2.4. Discussion

Previous reports have provided exquisite static snapshots of RNA and protein colocalization with PBs (Cougot et al., 2012; Horvathova et al., 2017; Kedersha and Anderson, 2007; Liu et al., 2005a), but could not assess the dynamics of the underlying recruitment processes. Others have provided valuable information regarding the dynamics of PB movement and the bulk exchange of proteins or mRNAs between PBs and the cytosol, but could not extract mechanistic information about the recruitment of biomolecules to PBs (Aizer et al., 2008b; Aizer et al., 2014; Kedersha et al., 2008; Leung et al., 2006). Using single-molecule live-cell imaging we here uniquely demonstrate that miRNAs, mRNAs and lncRNAs dynamically localize to PB either stably or transiently (Figures 2-2 and 2-3). Having dissected the molecular anatomy of PBs (Figure 2-4), we find that stable anchoring at PBs is concordant with snapshots that visually portray RNA

accumulation within PB "cores", whereas more mobile localizations and transient interactions are more likely to depict the localization of RNAs in PB "shells". In agreement with our data on mi/m/lncRNA-PB interactions during cellular homeostasis, recent reports (Moon et al., 2019; Wilbertz et al., 2019) have complementarily shown that mRNAs associate both stably and transiently with both stress granules (SGs) and PBs during the integrated stress response. The dwell times annotated as stable (~250 s) or transient (~10 s) in these reports are akin to particles in our datasets that dwell at PBs for the entire duration of acquisition (> 15 s) and for ~3-5 s, respectively. We have found an additional, highly dynamic interaction mode that lasts ~ 1 s, which potentially represents a relatively rapid PB-probing step. Based on the dwell times of THOR-Δbs-MS2 and L941-MS2 (~0.1-0.3 s, Figure 2-12F and Table 2-3), which seldom localize to PBs, it is unlikely that the dynamic interaction mode (~1 s) is an artifact of coincidental interaction/co-localization of RNAs with PBs. Upon RNP remodeling, these rapid encounters may transition into longer spans of granule probing or stable docking of RNAs to granules.

Elucidation of the PB-core transcriptome (Hubstenberger et al., 2017a) has suggested that certain miRNAs, lncRNAs and repressed mRNAs are enriched in PBs, yet it is unclear whether the principles governing PB enrichment for these major classes of transcripts are similar or different. Strikingly, we found that miRNAs, mRNAs and lncRNAs have distinct PB localization signatures, which appear correlated with the distinct functionalities of these transcripts and the diversity in the types of RNPs they form (Figure 2-5). Based on our data, we propose a model that assigns PB localization patterns to specific RNA forms and functionalities (Figure 2-13). Stably anchored and PB-enriched miRNAs are predominantly dysfunctional – they do not have many mRNA targets and localize to PBs in their unbound or miRISC-bound (single-stranded or double-stranded) forms (Figure 2-7). Functional miRNAs, more likely to reside in RISC-mRNA

complexes, display this behavior only in their minority and, when anchored, preferably localize within PB cores.

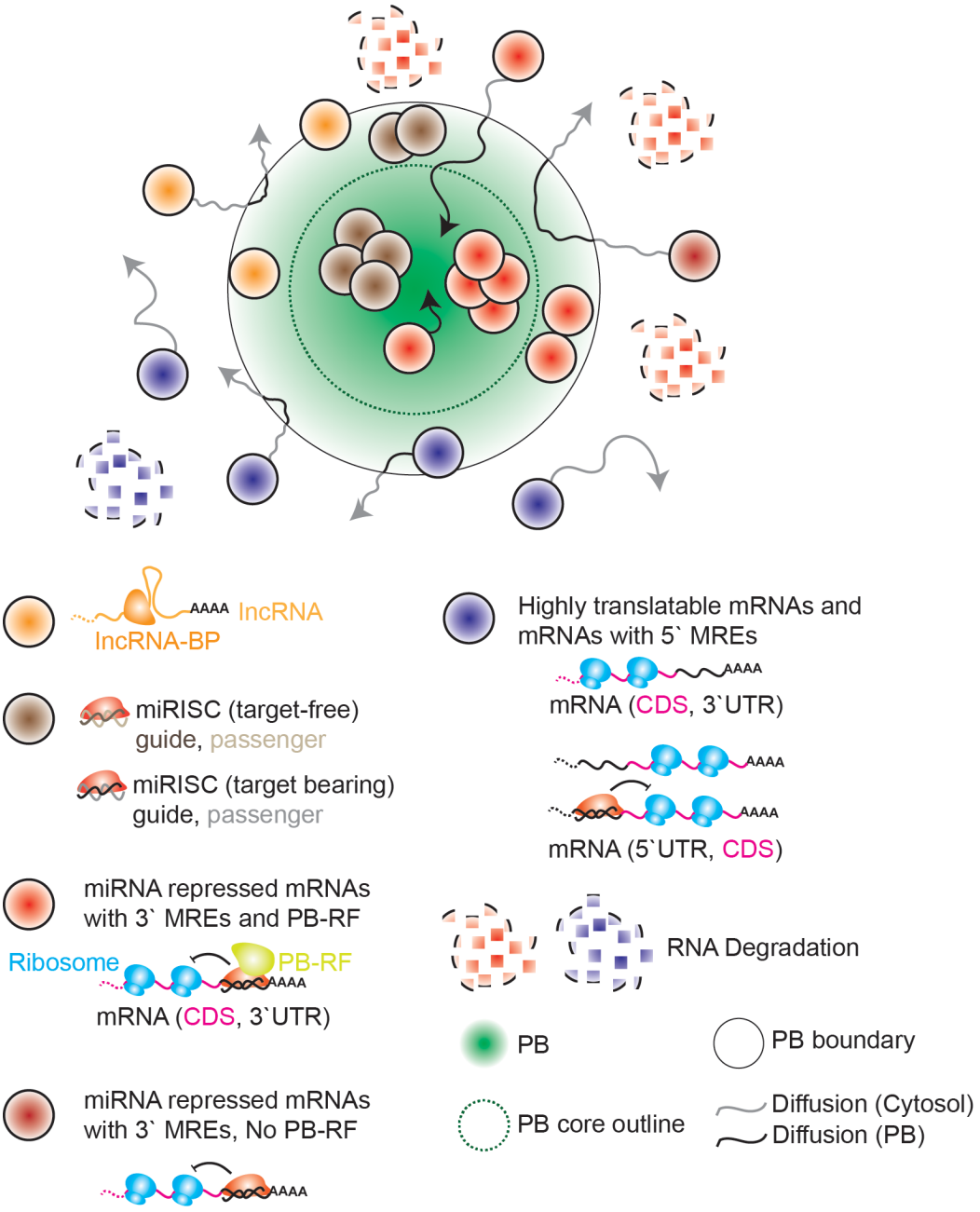

Figure 2-13 Resulting model for the dynamic recruitment of specific RNAs to PBs. RNAs dynamically associate with PB core or shell based on functionality. Target-free miRNAs, mRNA-targeting miRNAs and miRNA-targeted mRNAs with 3`UTR MREs are stably enriched within either cores or shells of PBs. The presence of a PB recruitment factor (PB-RF) may influence the dynamics and enrichment extent of miRNA-targeted mRNAs at PBs. lncRNAs transiently-yet-specifically associate with PB shells when the lncRNA binding protein (lncRNA-BP) is a PB enriched

factor or is a PB-RF. Other lncRNAs, translating mRNAs and miRNA-targeted mRNAs with 5`UTR MREs transiently associate with PB shells, or are excluded from PBs. A majority of nuclease mediated RNA degradation occurs outside of PBs.

These data are consistent with prior reports that both strands of both target-less and target-containing siRNAs localize to PBs (Jakymiw et al., 2005). We posit that, by contrast, transient associations at PB peripheries represent miRISC-mRNA complexes that do not yet have bound an important recruiting protein, such as GW182 or LAMP1 (Moon et al., 2019; Wilbertz et al., 2019), that is required for PB association. Conversely, highly translatable mRNAs that are not associated with miRNAs, while transiently associating peripherally, are not enriched at PBs. Based on recent reports (Moon et al., 2019; Wilbertz et al., 2019) and our data (Figures 2-3, 2-5) we predict that non-translating mRNAs and translationally repressed mRNAs bearing MREs in their 3`UTR stably associate with PB cores, while only the latter are enriched at PBs. Furthermore, we find that miRNA-repressed mRNAs with MREs in the 5`UTR (Figure 2-10A-B) are not enriched at and only transiently associate with PBs, probably also due to the lack of a PB-recruitment factor bound to these RNPs (Figure 2-9). Prior reports have demonstrated that MREs in the 5' UTR cause translational repression downstream of translation initiation sites (Lytle et al., 2007), potentially resulting in polysome bound non-translating mRNAs, which consequently cannot enter ribosome excluded PB cores (Parker and Sheth, 2007). By contrast, MREs in the 3'UTR typically result in inhibition of translation initiation, leading to non-translating mRNAs that are also free of ribosomes, which can then enter PB cores. Taken together, our data suggest that different modes of miRNA-mediated mRNA repression favor different types of PB localization.

THOR, ARlnc1 and LNC00941 are recently discovered, oncogenic lncRNAs with distinct protein interactomes and functions. First, THOR is a highly conserved testis-specific lncRNA that is up-regulated in a broad range of human cancers and found to work in concert with IGF2BP1

(Hosono et al., 2017), a PB-enriched protein (Hubstenberger et al., 2017a) that stabilizes transcripts via CRD (coding region instability determinant)-mediated mRNA stabilization (Weidensdorfer et al., 2009). Second, ARlnc1 is a lineage-specific lncRNA that collaborates with the PB-enriched protein HuR to enhance the stability of transcripts bound via an RNA-RNA interaction (Zhang et al., 2018). Third, LINC00941 (L941) is a lncRNA that is highly expressed in lung cancer (Shukla et al., 2017), that does not have consensus sequences for binding PB-resident proteins (data not shown). Based on our data, we propose that THOR, ARlnc1 and LINC00941 all assemble into slowly diffusing (D = 0.0001 – 0.1 $\mu m^2/s$, Figure 2-12D) RNPs, which we posit correlate with their functions (Hosono et al., 2017). The frequent, transient associations of THOR and ARlnc1 with PBs may be linked to the regulatory role of these lncRNAs, wherein one can envision: 1) the lncRNAs depositing regulated mRNAs for storage at PBs; or 2) the lncRNAs instead selecting PB-stored mRNAs for reintroduction into the translating cytoplasmic pool. Of note, we rarely observed any stable anchoring or significant enrichment of THOR, ARlnc1 or LINC00941 at PBs, which suggests that the mere inability of an RNA to be translated is not a sole prerequisite for stable PB association and enrichment. Moreover, the mere ability of THOR and ARlnc1 to bind RNA-stabilizing proteins (IGF2BP1 and HuR respectively) may preclude stable, long lasting interactions with PBs that are enriched for RNA destabilizing factors. However, the relative contribution of stabilizing/destabilizing RBPs on PB-recruitment of mRNAs is yet to be determined and will clearly identify the molecular driving forces of RNP recruitment into phase separated granules and their subsequent regulation at these sites. Finally, our data also supports the notion that ncRNA-PB interactions are dependent on the size, as reported for SGs (Khong et al., 2017b), and class of the regulatory ncRNA (Figure 2-11).

More broadly, our molecular observations of colocalizations of varying dynamics are consistent with phase transition principles that recently have been recognized to govern the assembly of large membrane-free granules (Protter and Parker, 2016; Shin and Brangwynne, 2017b). Static, core-localized and enriched RNPs may serve as nucleating factors for large PBs, whereas dynamic, shell-localized and dispersed colocalizations may occur when the interfaces of the RNP, PB and surrounding cytoplasm are similar, as in a Neumann's triangle observed in Cajal bodies attached to B-snurposomes (Shin and Brangwynne, 2017b). Transient colocalizations may represent cases where the smaller RNP and PB come in close proximity, but the interfacial surface tension is too high for the two to fuse, presumably due to the absence of an appropriate PB-recruitment factor on the RNP.

Although there is general agreement on the phase-separation assembly principles of PBs and other RNA granules, the functions of these granules are still a topic of intense debate. Some reports have suggested that PBs may have stress dependent RNA decay or storage roles (Aizer et al., 2014), whereas others have suggested that PBs are sites of RNA storage, but not decay (Eulalio et al., 2007b; Horvathova et al., 2017; Stalder and Muhlemann, 2009; Tutucci et al., 2017). Notably, all previous studies have examined only microscopically visible PBs. Our computational simulations, which considered PBs both large and small, together with subsequent experiments using hyperosmotic stress to induce PB aggregation, suggest that microscopically visible PBs cannot account for the bulk of cellular mRNA decay (Figure 2-11). Our data instead suggest that fundamental principles of physical chemistry hold true for mRNA regulation processes within the complex cellular environment, in that the entropic gain from the larger degree of freedom and surface area of freely diffusing decay components dominates, an aspect that warrants additional lines of investigation. In addition to storing repressed mRNAs, our work unveils an additional

housekeeping role for PBs in storing or possibly degrading unused miRNAs for their surveillance. Super-resolved fluorescence microscopy thus is shown to provide a powerful approach for mechanistically probing the dynamic assembly of RNP granules by phase separation at single-molecule resolution.

2.5. Methods

Cell lines HeLa (CCl-2, ATCC) and U2-OS (HTB-96, ATCC) cells were propagated in DMEM (GIBCO, #11995) and McCoy's 5A (GIBCO, # 16600) basal media respectively supplemented with 10% FBS (GIBCO, # 16000). HeLa or U2-OS cells stably expressing GFP- Dcp1a (UGD) was created by transfecting U2-OS cells with pEGFP-Dcp1a and selecting for stable clones by G418 selection. UGD cells were grown in the abovementioned medium supplemented with 100 µg/mL G418 (Thermo-Fisher, # 10131027). All medium typically contained 1x Penicillin-Streptomycin (GIBCO, #15140). U2-OS cells stably expressing GFP-G3BP and RFP-Dcp1a (UGG-RD, gift from Nancy Kedersha) were propagated in McCoy's 5A (GIBCO, # 16600) basal media supplemented with 10% FBS (GIBCO, # 16000). Phenol-red free McCoy's 5A (GE-Amersham, # SH3027001) supplemented with 1% FBS was used for seeding and cells for imaging experiments. For hyperosmotic shock, cells were treated with the above media supplemented with 10 x PBS such that the final sodium concentration was 300 mM. Plasmid transfections for MS2-MCP imaging and cell growth assays were achieved using Fugene HD (Promega, # E2311). Cotransfection of plasmids with oligos was achieved using lipofectamine 2000 (Thermo-Fisher, # 11668027). For inducing stress granules (SGs), growth media of UGG-RD cells were supplemented with 0.5mM Sodium Arsenite ($NaAsO_2$) for 1 h. All cell lines were subjected to biweekly mycoplasma contamination and, HeLa and U2-OS cells were genotyped.

DNA, RNA and LNA oligonucleotides All DNA and RNA oligonucleotides used for iSHiRLoC experiments and reverse transcription, followed by quantitative polymerase chain reaction (RT-qPCR) were obtained from IDT. Oligonucleotides contained a 5` Phosphate (P) and, in the case of fluorophore labeled oligonucleotides, a Cy5 dye at the 3`end. Dyes were attached after oligonucleotide synthesis to a 3`amino group on a C6 carbon linker and were HPLC purified by the vendor. Guide and passenger strands were heat-annealed in a 1:1.1 ratio to achieve 10 µM stock solutions and were frozen until further use. Negative control siRNA (Scr/Scr*) was purchased as ready-to-use duplex samples from Ambion respectively. Six tandem let-7 (l7-6x) miRNA response elements (MREs) or mutant l7-6x (ml7-6x) MREs were purchased as gene blocks from IDT. AntimiR LNA oligos were purchased from Exiqon. Oligonucleotide and gene block sequences are listed in Table S1.

Plasmids pEGFP-Dcp1a was constructed by ligating PCR amplified (using Pfu ultra polymerase, Agilent, # 600380) EGFP ORF (from pEGFP-C1, Clontech) into pmRFP1-hDcp1a (gift from Nancy Kedersha, Brigham Women‘s hospital) within the AgeI and XhoI restriction enzyme (RE) sites. This replaces mRFP1 with EGFP in the plasmid. pEF6-mCh and pEF6-mCh-cx-6x construction was previously described previously (Pitchiaya et al., 2017). pEF6-mCh-l7-6x plasmid was constructed by ligating l7-6x gene block within NotI and XbaI sites of pEF6-mCh plasmid. Plasmids pRL-TK-let7-A, pRL-TK-let7-B, pRL-TK-cxcr4-6x, phage-ubc-nls-ha-2xmcp-HALO (a gift from Phil Sharp, Addgene plasmid # 11324, #11325, # 11308 and # 64540) and pmiR-GLO (pmG, Promega, # E1330) were purchased. pmG-MS2, encoding the firefly luciferase (FL) gene followed by 24 MS2 stem loops (FL-MS2), was created in two steps. First, the coding sequence (CDS) of IF2 was PCR amplified and ligated into the SbfI and NotI RE site of pmG, to create pmG-IF2. MS2 stem loops from pSL-MS2_24x (a gift from Robert Singer, Addgene

plasmid # 31865) were then cloned into the EcoRI (introduced by above PCR)-NotI restriction enzyme sites pmG-IF2, to generate pmG-MS2. Clones containing the MS2 stem loops were created in SURE2 bacterial cells (Stratagene) to minimize recombination of the MS2 repeats with the bacterial genome. pmG-l7-6x-MS2 and pmG-ml7-6x-MS2 encoding FL-l7-6x-MS2 and FL-ml7-6x-MS2 respectively were constructed by ligating the l7-6x or ml7-6x gene blocks within the XhoI RE site in pmG-MS2. l7-6x-pmG and ml7-6x-pmG encoding l7-6x-FL and ml7-6x-FL respectively were created by ligating the synthesized I7-6x or ml7-6x fragment within the Esp3I and BbsI in pmG, between the human phosphoglycerate kinase promoter and FL CDS. l7-6x-pmG-MS2 and ml7-6x-pmG-MS2 encoding l7-6x-FL-MS2 and ml7-6x-FL-MS2 respectively were created using 24x MS2 stem loops from pMG-MS2 into EcoRI and NotI sites of l7-6x-pmG and ml7-6x-pmG. pmG-I7-2x-cx-4x was constructed by ligating the synthesized I7-2x-cx-4x fragment within the XhoI and EcoRI in pmG. pmG-I7-2x-cx-4x-MS2 was constructed by ligating 24x MS2 stem loops from pMG-MS2 into EcoRI and NotI sites of pmG-I7-2x-cx-4x. pmG-cx-6x-MS2 constructed by ligating 24x MS2 stem loops from pMG-MS2 into XhoI and NotI sites of pmG-cx-6x (Pitchiaya et al, 2017). pLenti6-THOR and pLenti6-RHOT (antisense of THOR) were constructed as described (Hosono et al., 2017). plenti6-THOR-MS2 was constructed by ligating 24x MS2 stem loops from pmG-MS2 into EcoRI and NotI sites of pLenti6-THOR. pCDH-ARlnc1-MS2 was constructed by ligating 24x MS2 stem loops from pMG-MS2 into XhoI and NotI sites of pCDH-ARlnc1 (Zhang et al. 2018). pCDH-LINC00941 was constructed by cloning LINC00941 into BstBt and BamHI sites of pCDH. pCDH- LINC00941-MS2 was then then constructed by ligating 24x MS2 stem loops from pMG-MS2 into XhoI and NotI sites of pCDH- LINC00941.

mRNA synthesis pRL-TK-cx6x, pRL-TK-let7-A and pRL-TK-let7-B were linearized with NotI to generate RL-cx6x RL-l7-2x and RL-ml7-2x mRNAs respectively. pEF6-mCh-cx6x and pEF6-

mCh-l7-6x were linearized with XbaI to generate mCh-cx6x and mCh-l7-6x mRNA respectively. The pCFE-GFP plasmid (Thermo Scientific) was directly used in the in vitro transcription reactions to generate the GFP mRNA. The linearized plasmids were extracted with phenol and chloroform and subsequently ethanol precipitated. In vitro transcriptions were performed using the MegaScript T7 kit (Thermo-Fisher, # AM1334) according to manufacturer's protocol. Transcription reactions were then DNase treated (turbo DNase supplied with kit) and the respective RNAs were purified by sequential gel-filtration chromatography (Nap-5 followed by Nap-10, GE healthcare, # 17085301 and #17085401 respectively) and ethanol precipitation. The RNAs were 5'capped (ScriptCap™ m7G Capping System, CELLSCRIPT, # C-SCCE0625) and polyadenylated (A-Plus™ Poly(A) Polymerase Tailing Kit, CELLSCRIPT, # C-PAP5104H) and were further purified by sequential gel-filtration chromatography and ethanol precipitation. The length of the polyA tails was estimated based on electrophoretic mobility on a 1.2% formaldehyde agarose gel.

Luciferase reporter assays 100 µL of 10, 000 -20, 000 cells were seeded per well of a 96 well plate in antibiotics-free medium. Transfection conditions and luminescence readouts are as described previously (Pitchiaya et al., 2012; Pitchiaya et al., 2013; Pitchiaya et al., 2017). Briefly, cells were transfected with 60 ng of the indicated plasmid, 10 nM of the indicated dsRNA, and when appropriate 30 nM anti-ctrl or anti-l7 antimiRs, 0.4 µL of Lipofectamine 2000 (Invitrogen) and 50 µL of OptiMEM (GIBCO). 6 h after transfection the growth medium was replaced with fresh medium. 24 h after transfection, medium was replaced with phenol red-free McCoy's 5A. Dual luciferase assays were performed using the Dual-Glo luciferase assay reagents (Promega, # E2920) as per the manufacturer's protocol and luminescence was detected using a Genios Pro (Tecan) plate reader.

RT-qPCR Cells were harvested and total RNA from cells were isolated using QIAzol Lysis reagent (Qiagen) and the miRNeasy kit (Qiagen) with DNase digestion according to the manufacturer's instructions. cDNA was synthesized using Superscript III (Invitrogen) and random primers (Invitrogen). Relative RNA levels determined by qRT-PCR were measured on an Applied Biosystems 7900HT Real-Time PCR System, using Power SYBR Green MasterMix (Applied Biosystems). Expression was quantified by $2^{\Delta Ct}$ method, wherein Myc expression was first normalized to that of GAPDH and then this normalized expression was further normalized to Mock treatment.

Cell growth assays 100 µL of 10, 000 -20, 000 cells were seeded per well of a 96 well plate in antibiotics-free medium and were transfected every 24 h with the appropriate plasmid construct using Fugene HD (Promega, # E2311). Cell growth and viability was measured as an end point measurement for each time point using the Cell-titer GLO assay (Promega, # G7570) based on manufacturer's instructions.

Microinjection Cells grown on DeltaT dishes (Bioptechs, # 0420042105C) were microinjected as described (Pitchiaya et al., 2012; Pitchiaya et al., 2013, Pitchiaya et al., 2017). Briefly, injection solutions contained the appropriate miRNA at 1 µM concentration, 1x PBS and 0.5 mg/mL of 10 kDa cascade blue-conjugated dextran (CB-Dex, Thermo-Fisher, # D1976). For microinjection based titration assays solution with 0 – 0.1 µM, 1x PBS and 0.1 mg/mL of 500 kDa cascade blue-conjugated dextran (FITC-Dex, Thermo-Fisher, # D7136). For microinjection-based miRNA activity assay, mRNAs were added at a stoichiometric amount based on the number of miRNA binding sites, for instance, 0.16 µM of RL-cx6x mRNA, bearing 6 cxcr4 binding sites, was added along with 1 µM cxcr4 miRNA. Solutions were filtered through a 0.45 µm Ultrafree-MC filter

(Millipore, # UFC30HV00) and then centrifuged at 16,000 x g for 15min at 4 °C immediately before injection. The solution was loaded into a femtotip (Eppendorf, # E5242952008). Injections were performed using a Femtojet pump (Eppendorf) and an Injectman (Eppendorf) mounted to the microscope. Microinjections were performed at 100 hPa injection pressure for 0.5 s with 20 hPa compensation pressure. This pressure translates to a volume of 0.02 pL and 10,000-20,000 miRNA molecules.

Single-molecule fluorescence *in situ* hybridization smFISH was performed as described (Hosono et al., 2017). Briefly, cells were grown on 8-well chambered coverglasses (Thermo-Fisher, # 155383PK), formaldehyde fixed and permeablized overnight at 4ºC using 70% ethanol. Cells were rehydrated in a solution containing 10% formamide and 2 × SSC for 5 min and then treated with 100 nM fluorescence in situ hybridization probes (LGC-Biosearch) for 16 h in 2 × SSC containing 10% dextran sulfate, 2 mM vanadyl-ribonucleoside complex, 0.02% RNAse-free BSA, 1 μg μl−1 E. coli transfer RNA and 10% formamide at 37 °C. After hybridization, cells were washed twice for 30 min at 37 °C using a wash buffer (10% formamide in 2 × SSC). Cells were then mounted in solution containing 10 mM Tris/HCl pH 7.5, 2 × SSC, 2 mM trolox, 50 μM protocatechiuc acid and 50 nM protocatechuate dehydrogenase. Mounts were overlaid with mineral oil and samples were imaged immediately. Sequences of Q670 labeled probes against the FL gene are listed in Table S1 and probes against THOR and ARlnc1 were previously described (Hosono et al., 2017 and Zhang et al., 2018).

Immunofluorescence Cells were grown on 8-well chambered coverglasses (Thermo-Fisher, # 155383PK), formaldehyde fixed and permeablized using 0.5% Triton-X100 (Sigma, T8787-100ML) in 1x PBS at room temperature (RT) for 10 min. Cells were then treated with blocking

buffer containing 5% normal goat serum (Jackson Immunoresearch, 005-000-121), 0.1% Tween-20 (Sigma, P9416-50ML) in 1x PBS at RT for 1 h. Primary antibodies (pA) were diluted in blocking buffer to appropriate concentrations and cells were treated with pA at RT for 1 h. Following three washes with the blocking buffer for 5 min each, cells were treated with secondary antibodies (sA) diluted in blocking buffer to appropriate concentrations. Following two washes with the blocking buffer and two washes with 1x PBS for 5 min each, cells were mounted in solution containing 10 mM Tris/HCl pH 7.5, 2 × SSC, 2 mM trolox, 50 µM protocatechiuc acid and 50 nM protocatechuate dehydrogenase. Mounts were overlaid with mineral oil and samples were imaged immediately.

Microscopy Highly inclined laminated optical sheet (HILO) imaging was performed as described (Pitchiaya et al., 2012; Pitchiaya et al., 2013, Pitchiaya et al., 2017) using a cell-TIRF system based on an Olympus IX81 microscope equipped with a 60x 1.49 NA oil-immersion objective (Olympus), as well as 405 nm (Coherent ©, 100 mW at source, ~65 µW for imaging CB-Dex), 488 nm (Coherent ©, 100 mW at source, ~1.2 mW for imaging GFP), 561 nm (Coherent ©, 100 mW at source, ~50 µW for imaging mCh) and 640 nm (Coherent ©, 100 mW at source, 13.5 mW for imaging Cy5) solid-state lasers. Quad-band filter cubes consisting of z405/488/532/640rpc or z405/488/561/640rpc dichroic filters (Chroma) and z405/488/532/640m or z405/488/561/640m emission filters (Chroma) were used to filter fluorescence of the appropriate fluorophores from incident light. Emission from individual fluorophores was detected sequentially on an EMCCD camera (Andor IXon Ultra) for fixed cell imaging. For multicolour live-cell imaging, the emitted light was split onto two different EMCCDs using a single beamsplitter within a filter adapter (TuCam, Andor). Emission filters were placed just prior to each camera to minimize fluorescence bleed-through. For simultaneous detection of GFP and Cy5, a filter set with a 585dxcru dichroic

that splits fluorescence into et525/50m and et705/100m emission filters respectively was placed in the Tucam adapter. For live cell imaging of MS2-MCP constructs, UGD cells on Delta T dishes were treated with 100 nM JF646- Halo ligand (a kind gift from Luke Lavis) for 30 min in growth medium without phenol red (Grimm et al., 2015). After the treatment, cells were washed three times in media and placed back in the incubator for 30 min, prior to imaging.

Image analysis The two cameras used for simultaneous acquisition of GFP and Cy5 fluorescence in live cells were first registered as described (Churchman et al., 2005). Registration was achieved by imaging 0.1 µm tetraspeck beads (Thermo-Fisher, # T7279), whose emission is similar to both GFP and Cy5, before or after imaging of live cells. The registration matrix was then applied to GFP and Cy5 images for accurate tracking of PBs and RNAs respectively. Single particle tracking was performed as described (Pitchiaya et al., 2012; Pitchiaya et al., 2013) with some minor modifications. Briefly, particle tracking analysis was performed in Imaris (Bitplane) using tracks that spanned at least four video frames and all tracks were fit to a Brownian diffusion model to extract diffusion coefficients. PB boundaries were detected using a local contrast/threshold approach in Image J and Imaris. An RNA particle was identified as colocalizing with a PB when the centroid of the RNA is at or within the boundary of a PB. The use of finite observation windows to measure the dwell times introduces a systematic bias in the observed dwell times. This was corrected for by measuring the aggregate time for Cy5 photobleaching (T_{phb}) and subtracting its reciprocal this from the reciprocal of the observed dwell time (T_{obs}) along with the reciprocal of the observation window (T_w), as described by $T_{actual} = 1 / ((1/ T_{obs}) - (1/ T_{phb}) - (1/ T_w))$, as described (Rueda et al., 2004). Dwell times of all transcripts are summarized in Table S2. Percentage of track colocalizing with PBs (track %) was calculated as $n_{PB} / (n_{PB} + n_{Cyt})$, where n_{PB} = number of track localizations within PBs, n_{Cyt} = number of track localizations in the cytosol and depicted in Figure

2. This measure, in addition to visual inspection of individual tracks were used to objectively define trajectory "phenotypes" as stable or transient.

Step-wise photobleaching analysis of fluorophore labeled miRNAs and intensity analysis of smFISH particles in fixed cells were done using custom written Lab-view codes and ImageJ macros that can be shared upon request, as described (Pitchiaya et al., 2012; Hosono et al., 2017). To overcome statistical biases of co-incidental colocalizations introduced merely by RNA abundance, we calculated the accumulation of RNA within PBs via an enrichment index (EI) – a ratio of the number of RNA molecules in PB to those outside of PBs (Figure 2 and S2). An E.I. of > 1 suggests that the RNA accumulates at PB, whereas the opposite is true if the E.I. is ≤ 1. We also calculated the percentage of RNA or protein signal within PBs per cell by calculating the ratio between the cumulative abundance of signal within PBs divided by the total signal within the cell. Mean abundance / cell of all transcripts are provided in Table S3. Relative localization (RL) of RNAs within PBs was calculated as $d_{CR} / (d_{RB} + d_{CB})$, where d_{CR} = distance of RNA centroid from PB centroid, d_{RB} = distance of RNA centroid from PB boundary, d_{CB} = distance of PB centroid from PB boundary and depicted in Figure S2. The centroid and boundary of PBs were obtained via a modest variation of the local/adaptive-threshold method previously described (Simonson et al., 2010).

mCh and GFP signal from microinjection-based miRNA activity assay were extracted and analyzed as described (Pitchiaya et al., 2012; Pitchiaya et al., 2017). Briefly, mCh and GFP intensity threshold were set (Huang threshold in image J) to automatically identify cell boundary. Background intensity, outside of cell boundary, was subtracted from mCh and GFP signal to extract the corrected intensity, whose ratio was calculated on a per cell basis.

***In silico* kinetic modeling** The fundamental theory and basic methodology of modeling, including the lattice gas automata algorithm are as described (Mourao et al., 2014). Our simulation platform allows for the specification of a variable number of elementary reactions. Unless otherwise stated, the results presented here were obtained using two different reactions:

$$miRISC + mRNP \underset{k_{-1}}{\overset{k_1}{\rightleftarrows}} \text{miRISC/mRNP} \quad (1)$$

$$miRISC/mRNP + \text{PB} \underset{k_{-2}}{\overset{k_2}{\rightleftarrows}} \text{miRISC/mRNP/PB} \xrightarrow{k_3} PB + miRISC \quad (2)$$

The reaction in (2) represents a catalytic event. The rate coefficients k_i are modeled as reaction probabilities. For example, in (1) k_1 is modeled by the probability that a miRISC and an mRNP molecule will react to form complex miRISC/mRNP, given that they have collided. Unless otherwise stated, the probability of a forward reaction (on the basis of the rate coefficients k_1 and k_2) is set to 1 and the probability of a reverse reaction (on the basis of the rate coefficients k_{-1} and k_{-2}) is set to 0.1. The probability of a catalytic reaction (on the basis of the rate coefficient k_3) is set to 0.1. Note that the forward reaction rates (e.g., k_1) may remain constant over time, in agreement with the law of mass action, or decay over time for diffusion-limited reactions, when the time required for any two reactants to interact increases with the level of obstruction to diffusion. In the latter case, it can be shown that $\log(k_1)$ decays linearly at long times in a logarithmic time scale, as described (Mourao et al., 2014).

Each simulation begins with all particles randomly placed on a 2D lattice of size 200x200 lattice points with cyclic boundary conditions. Particles can be initialized with different sizes, provided that they are square, i.e., each initial particle can only occupy x2 positions, x being at

least 1. Our platform allows for the creation of initial aggregates of a particular number and size. With the restriction mentioned above, we modulate the number and size of P-body particles within an aggregate with the assumption that all P-body particles within an aggregate have the same size. Each aggregate of P-bodies is created in two main steps. In the first step occurs, we insert the first molecule of the aggregate in the lattice. This first molecule is placed in a random position in the lattice. In the second step, we randomly select an adjacent neighborhood of a random P-body in the existing aggregate as a destination for the new P-body. The addition of P-bodies to an aggregate follows the reaction:

$$PB + N_1\ PB \longrightarrow (N_1 + 1)\ \mathrm{PB} \tag{3}$$

where N_1 corresponds to the number of P-bodies in the existing aggregate. This is done iteratively until the pre-determined aggregated size is achieved. Every particle is randomly initialized with a given orientation and direction of rotation. There are six possible orientations, corresponding to the coordinate number of a triangular lattice. The direction of rotation is always clockwise (CW) or counterclockwise (CCW). Note that, although the particle's movement is independent of its orientation, reactant particles will only associate if their orientations are complementary.

Quantification and statistical analysis Graphpad-Prizm and Origin were used for statistical analysis and plotting. For pairwise comparisons, p-values were calculated based on non-parametric unpaired t-tests with Kolmogorov-Smirnov test. For comparisons involving more than 2 samples, one-way-ANOVA tests were used with Geisser-Greenhouse correction

2.6. Acknowledgements

We thank T.C. Custer and M. Denies for technical assistance. We thank N. Kedersha, D. Bartel and R. Singer for generous gifts of plasmids containing GFP-Dcp1a, the 3`UTR of HMGA2 and the MS2 system of plasmids respectively. We thank L. Lavis for providing JF646 dye. We thank V. Krishnan for inputs on the manuscript. This work was supported by National Institutes of Health (NIH) R01 grant GM081025 and a University of Michigan Comprehensive Cancer Center/Biointerfaces Institute Research Grant to N.G.W., whereas A.J. is supported by the NIH Cellular and Molecular Biology Training Grant T32-GM007315. A.M.C. is supported by the Prostate Cancer Foundation, by the Howard Hughes Medical Institute and is an American Cancer Society Research Professor. S.P. was supported by an AACR-Bayer Prostate Cancer Research Fellowship (16-40-44-PITC). L.X. was supported by a US Department of Defense Postdoctoral Fellowship (W81XWH-16-1-0195). We also acknowledge NSF MRI-ID grant DBI-0959823 to N.G.W. for seeding the Single Molecule Analysis in Real-Time (SMART) Center whose Single Particle Tracker TIRFM equipment was used for much of this study

Table 2-1 List of reagents and resources referenced in Chapter 2.

REAGENT or RESOURCE	SOURCE	IDENTIFIER
Antibodies		
Rabbit-anti-Dcp1a	Sigma	HPA013202
Rabbit-anti-Dcp2	Thermo	PIPA5-34455
Rabbit-anti-PUM	Abcam	EPR3795
Rabbit-anti-ELAVL1	Sigma	07-1735
Rabbit-anti-PABP	Abcam	ab21060
Rabbit-anti-eIF4E	Abcam	ab1126
Rabbit-anti-eIF4G	Sigma	07-1800
mouse-anti-rRNA	Novus Biologicals	NB100-662SS
Rabbit-anti-GAPDH	Cell signaling technol.	2118S
Rabbit-anti-Xrn1	Bethyl labs	A300-443A
Rabbit-anti-DDX6	Bethyl labs	A300-460A
Mouse-anti-GW182	Abcam	Ab70522
Rabbit-anti-Ago2	Sigma	07-590
Mouse-anti-G3BP	BD Transduction labs	611126
Rabbit-anti-CNOT1	Proteintech	14276-1-AP
Goat-anti-rabbit-Cy5	Jackson Immunolabs	111-175-144
Goat-anti-mouse-Cy5	Jackson Immunolabs	115-175-146
Chemicals, Peptides, and Recombinant Proteins		
JF646-HaloTag ligand	Lab of Luke Lavis,	N/A
Sodium Arsenite	Sigma	S7400-100G
Critical Commercial Assays		
MegaScript T7	Thermo-Fisher	AM1334
ScriptCap™ m7G Capping System	CELLSCRIPT	C-SCCE0625
A-Plus™ Poly(A) Polymerase Tailing Kit	CELLSCRIPT	C-PAP5104H
Fugene HD	Promega	E2311
Lipofectamine 2000	Thermo-Fisher	11668027
CellTiter-Glo® Luminescent Cell Viability Assay	Promega	G7570
Dual-Glo Luciferase Assay System	Promega	E2920
Deposited Data		
Unprocessed image files used to prepare the images	Mendeley Data	http://dx.doi.org/10.17632/65t29ys57x.1
Experimental Models: Cell Lines		
Human: U2-OS	ATCC	HTB-96
Human: HeLa	ATCC	CCL-2
Human: HeLa stably expressing GFP-Dcp1a	This work	N/A
Human: U2-OS stably expressing GFP-Dcp1a	This work	N/A
Human: U2-OS stably expressing GFP-G3BP and RFP-Dcp1a	Nancy Kedersha	N/A
Oligonucleotides		
Labeled microRNAs for injection see Table S1	This work	N/A

Primers and gene blocks for cloning see Table 2-2	This work	N/A
Recombinant DNA		
pRL-TK-cx6x	Lab of Phil Sharp	Addgene: 11324
pRL-TK-let7-A	Lab of Phil Sharp	Addgene: 11325
pRL-TK-let7-B	Lab of Phil Sharp	Addgene: 11308
pEF6-mCh-cx6x	Pitchiaya *et al.*, 2017	N/A
pEF6-mCh-l7-6x	Pitchiaya *et al.*, 2017	N/A
pEGFP-C1	Clontech	Discontinued
pmRFP1-hDcp1a	Nancy Kedersha	N/A
phage-ubc-nls-ha-2xmcp-HALO	Lab of Phil Sharp	Addgene: 64540
pmiR-GLO	Promega	E1330
pSL-MS2_24x	Lab of Robert Singer	Addgene: 31865
pmG-MS2	This work	N/A
pmG-l7-6x	This work	N/A
pmG-l7-6x-MS2	This work	N/A
pmG-ml7-6x	This work	N/A
pmG-ml7-6x-MS2	This work	N/A
pmG-cx-6x	Pitchiaya *et al.*, 2017	N/A
pmG-cx-6x-MS2	This work	N/A
l7-6x-pmG	This work	N/A
l7-6x-pmG-MS2	This work	N/A
ml7-6x-pmG	This work	N/A
ml7-6x-pmG-MS2	This work	N/A
pmG-l7-2x-cx-4x	This work	N/A
pmG-l7-2x-cx-4x-MS2	This work	N/A
pLenti6-THOR	Hosono *et al.*, 2017	N/A
pLenti6-RHOT	Hosono *et al.*, 2017	N/A
pLenti6-THOR-MS2	This work	N/A
pCDH-THOR-ΔIGF2BP1	This work	N/A
pCDH-THOR-ΔIGF2BP1-MS2	This work	N/A
pCDH-ARLNC1	Zhang *et al.*, 2018	N/A
pCDH-ARLNC1-MS2	This work	N/A
pCDH-LINC00941	This work	N/A
pCDH-LINC00941-MS2	This work	N/A
Software and Algorithms		
MATLAB 8.3	The Mathworks Inc.	R2014a
Prizm 7.04	GraphPad	Prizm 7.04
Origin 2018	OriginLab	Origin 2018
Imaris 9.1.0	Bitplane AG	Imaris 9.1.0
Fiji	ImageJ/NIH	Fiji
Custom MATLAB routines	This work	N/A
Custom Image J macros	This work	N/A
Bacterial and viral strains		
E.coli SURE2 Supercompetent Cells	Agilent	200152

Table 2-2 Sequences of olignonucleotides.

Name	DNA/ RNA	Sequence
l7	RNA	P-UGAGGUAGUAGGUUGUAUAGUU-X
l7*	RNA	P-CUAUACAAUCUACUGUCUUUCC-X
dl7	DNA	P-TGAGGTAGTAGGTTGTATAGTT-X
dl7*	DNA	P-CTATACAATCTACTGTCTTTCC-X
ml7	RNA	P-UGCGUUAGUAGGUUGUAUAGUU-X
ml7*	RNA	P-CUAUACAAUCUACUGUCGUUCC-X
m21	RNA	P-UAGCUUAUCAGACUGAUGUUGA-X
m21*	RNA	P-CAACACCAGUCGAUGGGCUGU-X
cx	RNA	P-UGUUAGCUGGAGUGAAAACUU-X
cx*	RNA	P-GUUUUCACAAAGCUAACACA-X
Scr	RNA	P-CCGUAUCGUAAGCAGUACUUU-X
Scr*	RNA	P-AGUACUGCUUACGAUACGGUU-X
GAPDH	DNA	F: CCATCACCATCTTCCAGGAGCGA R: GGTGGTGAAGACGCCAGTGGA
Myc	DNA	F: GCTCGTCTCAGAGAAGCTGG R: GCTCAGATCCTGCAGGTACAA
Anti-ctrl	LNA	TAACACGTCTATACGCCCA
Anti-l7	LNA	ACTATACAACCTACTACCTC
l7-6x	DNA	F:atcgccgtgtaattctagttgtttAACTATACAAGGACTACCTCACCGGA ACTATACAATGACTACCTCACCGGAACTATACAAGGACTAC CTCACCGGAACTATACAATGACTACCTCACCGGAACTATAC AAGGACTACCTCACCGGAACTATACAATGACTACCTCACCG Gaaacgagctcgctagcctcgagtct R:agactcgaggctagcgagctcgtttCCGGTGAGGTAGTCATTGTATAGTT CCGGTGAGGTAGTCCTTGTATAGTTCCGGTGAGGTAGTCATT GTATAGTTCCGGTGAGGTAGTCCTTGTATAGTTCCGGTGAG GTAGTCATTGTATAGTTCCGGTGAGGTAGTCCTTGTATAGTT aaacaactagaattacacggcgatc
ml7-6x		F:gatcgccgtgtaattctagttgtttAACTATACAAGGACTAACGCACCGG AACTATACAATGACTAACGCACCGGAACTATACAAGGACTA ACGCACCGGAACTATACAATGACTAACGCACCGGAACTATA CAAGGACTAACGCACCGGAACTATACAATGACTAACGCACC GGaaacgagctcgctagcctcgagtct

		R:agactcgaggctagcgagctcgtttCCGGTGCGTTAGTCATTGTATAGTT CCGGTGCGTTAGTCCTTGTATAGTTCCGGTGCGTTAGTCATT GTATAGTTCCGGTGCGTTAGTCCTTGTATAGTTCCGGTGCGT TAGTCATTGTATAGTTCCGGTGCGTTAGTCCTTGTATAGTTaa acaactagaattacacggcgatc
L7-2x-cx-4x	DNA	F:gggaattcAACTATACAAGGACTACCTCAccggAACTATACAAG GACTACCTCAccggaagttttcacaaagctaacaCCGGaagttttcacaaagctaacac cggaagttttcacaaagctaacaggcggccgc R:gcggccgcctgttagctttgtgaaaacttccggtgttagctttgtgaaaacttCCGGtgttagctt tgtgaaaacttccggTGAGGTAGTCCTTGTATAGTTccggTGAGGTAGT CCTTGTATAGTTgaattccc
FL-Q670 (smFISH)	DNA	TCTTCGAGTGGGTAGAATGG TAGCGCTTCATGGCTTTGTG CGTCGGTAAAGGCGATGGTG GTAATGTCCACCTCGATATG CGAACGCTCATCTCGAAGTA ATAGCGCTTCATAGCTTCTG GATCCGATGGTTTGTATTCA AAGCTATTCTCGCTGCACAC CCAACACGGGCATGAAGAAC ACAGCCACACCGATGAACAG TTGTAGATGTCGTTAGCTGG CCTTTCTTGCTCACGAATAC TTGCACGTTGAGGATCTTTT TGGTAGTCGGTCTTGCTATC AGGTGTACATGCTTTGGAAG GGTGGCAAATGGGAAGTCAC CACGAAGTCGTACTCGTTGA ATGATCAGGGCGATGGTTTT CAATCCGGTACTGCCACTAC TGAATCGGACACAAGCGGTG ATGATCTGGTTGCCGAAGAT TGAAATGGCACCACGCTGAG AGCGTGGTGAACATGCCGAA AAAGCCGCAGATCAAGTAGC AAGCGGTACATGAGCACGAC AAGCTGCGCAAGAATAGCTC GCAGGGCAGATTGAATCTTA GAAGCTAAATAGTGTGGGCA TACTTGTCGATGAGAGTGCT ATCTCGTGCAAGTTGCTTAG CTGGTAGGTGGAAGCGTTTG

L941-Q670 (smFISH)	DNA	TTGTTTCTGTCAGGCCGTAG CTTCGGGGGTGATCAGAATG CACCTTAGCCTCGAAGAAGG GTTCACACCCAGTGTCTTAC TTAACGTAGCCGCTCATGAT GTCGATGAGAGCGTTTGTAG CGGTCCACGATGAAGAAGTG CTTGTATTTGATCAGGCTCT ACATAGTCCACGATCTCCTT AGCTTCTTGGCGGTTGTAAC CTCGTCCACGAACACAACAC TGAGAATCTCGCGGATCTTG GACTGACTTCAGCCACGTC CATAATGCTGCCGAGGAGC CATCCGGCTCTCAGAAGTG TCTGGACCTGGCTCCAAG CTGAGAGGAGCCAGGATGG CGCAGTTCAGAGAAGGCTA TGTGGACCCGGGAGAAAAG CCGGAGCGGTGGGAACTG AAATCGCGGCGCACTGGG ACTCTGGGGCTTGGACAC TGGGGGTTGGTCTCAGAG GAAGGCAGGAAGTCTGTGC CTTTAGACACTTCTCGAGGG GTTGTTTGGCTATCAACTGT GCTTCTTTCATAATCAGTCA CTGATTCTTGATACCAGTCT GCTGAATGGTCAATGTCTGG GTCTTTGTGCTGAATGTTCA ATTCTGTGGGACTCTTCTGG TTTTCTCTGAATAGTTTCCC TTTGTATTGTCAGTATGCCT GTCCACTACGTTAGAAGGAT AAGATGGATACATGCTCCAG TTGTGAAAGTGATCTCTGCT CAATTCAAATCAAGAGCCCA TGGATAGAGGGCTCATTACA GAATCCAGTCAATTCGCAGA GGCAGCAAGAATGAGAGTTG AAGCATAGTTGGTCCATTGA AGTGGTTATCATGTTATCCT

P: 5` Phosphate, X: 3` hydroxyl or C6 linker + Cy3 or C6 linker + Cy5

Table 2-3 Summary of dwell time quantifications from exponential fits.

Construct	RNA	S/D*	T_1 (s)	T_2 (s)	T_{phb} (s)	T_w (s)
l7-Cy5/l7*	miRNA	D	0.5 ± 0.1	1.9 ± 0.6	2.3 ± 0.1	15
l7/l7*-Cy5	miRNA	S	-	1.1 ± 0.1	1.3 ± 0.1	15
ml7-Cy5/ml7*	miRNA	S	-	1.0 ± 0.2	1.3 ± 0.3	15
m21-Cy5/m21*	miRNA	D	0.6 ± 0.2	1.8 ± 0.3	2.1 ± 0.3	15
cx-Cy5/cx*	miRNA	S		1.5 ± 0.2	1.8 ± 0.1	15
scr-Cy5/scr*	miRNA	S		1.3 ± 0.1	1.5 ± 0.1	15
ml7-Cy5/ml7* + RL-l7-2x	miRNA+ mRNA	S	-	1.1 ± 0.2	1.3 ± 0.2	15
ml7-Cy5/ml7* + RL-ml7-2x	miRNA+ mRNA	D	0.4 ± 0.1	1.5 ± 0.2	1.7 ± 0.2	15
FL-l7-6x-MS2	mRNA	D	0.8 ± 0.1	4.9 ± 1.1	10.5 ± 1.7	15
FL-ml7-6x-MS2	mRNA	D	0.6 ± 0.2	2.3 ± 0.7	10.5 ± 1.7	15
l7-6x-FL-MS2	mRNA	D	0.5 ± 0.1	2.5 ± 0.5	10.4 ± 1.2	15
ml7-6x-FL-MS2	mRNA	D	0.6 ± 0.1	1.8 ± 0.3	10.9 ± 1.6	15
FL- MS2	mRNA	D	0.5 ± 0.1	2.1 ± 0.5	10.6 ± 2.0	15
FL-cx-6x-MS2	mRNA	D	0.4 ± 0.2	2.2 ± 0.1	11.4 ± 1.6	15
FL-l7-2x-cx-6x-MS2	mRNA	D	1.1 ± 0.3	4.8 ± 0.2	13.7 ± 2.1	15
THOR-MS2	lncRNA	D	0.4 ± 0.1	2.1 ± 0.6	9.6 ± 1.1	15
THOR-Δbs-MS2	lncRNA	S	0.1 ± 0.1		9.6 ± 1.1	15
ARlnc1-MS2	lncRNA	D	0.9 ± 0.2	2.3 ± 0.4	10.4 ± 1.4	15
L941-MS2	lncRNA	S	0.2± 0.1	-	11.2 ± 2.3	15

*Single exponential fit equation (S):

$y = y_0 + A_1.e^{(-x/T1)}$; At x = 0, $y = y_0 + A_1$

Double exponential fit equation (D):

$y = y_0 + A_1.e^{(-x/T1)} + A_2.e^{(-x/T2)}$; At x = 0, $y = y_0 + A_1 + A_2$

$T_1 = T_{fast}$; $T2 = T_{slow}$; T_{phb} = Photobleaching time; T_w = Acquisition window

Table 2-4 Summary of the number of cells, PBs / cell and RNAs / cell probed in this study

RNA class	Name	Length	Live cell imaging				Fixed cell imaging	
			# Cells	# PB / Cell	# particles / Cell	# Cells	# PBs / Cell	# RNAs / Cell
miRNAs	l7-Cy5/l7*	22 nt	20	16	280	20	15	440
	l7/l7*-Cy5	22 nt	15	16	98	15	14	208
	ml7-Cy5/ml7*	22 nt	15	18	116	15	21	221
	ml7-Cy5/ml7* + RL-l7-2x	22 nt + ~1.2 kb	15	21	126	15	24	256
	ml7-Cy5/ml7* + RL-ml7-2x	22 nt + ~1.2 kb	15	17	254	15	18	381
	m21-Cy5/m21*	22 nt	15	23	232	20	20	372
	cx-Cy5/cx*	21 nt	15	23	128	20	21	225
	scr-Cy5/scr*	21 nt	15	27	65	20	26	193
mRNAs	FL-MS2	~3.2 kb	20	14	311	20	12	398
	FL-cx-6x-MS2	~3.4 kb	20	16	298	20	18	312
	FL-l7-2x-cx-6x-MS2	~3.4 kb	20	21	152	20	23	148
	FL-l7-6x-MS2	~3.4 kb	20	20	108	20	29	151
	FL-ml7-6x-MS2	~3.4 kb	20	11	247	20	12	219
	l7-6x-FL-MS2	~3.4 kb	20	14	113	20	13	108
	ml7-6x-FL-MS2	~3.4 kb	20	18	204	20	19	243
lncRNAs	THOR-MS2	~ 2.3 kb	20	22	141	20	23	203
	THOR-Δbs-MS2	~ 2.1 kb	30	21	122	15	22	102
	ARlnc1-MS2	~4.2 kb	20	18	195	15	21	275
	L941-MS2	~3.4 kb	30	17	228	15	17	208

2.7. References

Aizer, A., Brody, Y., Ler, L.W., Sonenberg, N., Singer, R.H., and Shav-Tal, Y. (2008). The dynamics of mammalian P body transport, assembly, and disassembly in vivo. Mol Biol Cell *19*, 4154-4166.

Aizer, A., Kalo, A., Kafri, P., Shraga, A., Ben-Yishay, R., Jacob, A., Kinor, N., and Shav-Tal, Y. (2014). Quantifying mRNA targeting to P-bodies in living human cells reveals their dual role in mRNA decay and storage. Journal of cell science *127*, 4443-4456.

Banani, S.F., Lee, H.O., Hyman, A.A., and Rosen, M.K. (2017). Biomolecular condensates: organizers of cellular biochemistry. Nat Rev Mol Cell Biol *18*, 285-298.

Buchan, J.R. (2014). mRNP granules. Assembly, function, and connections with disease. RNA biology *11*, 1019-1030.

Cougot, N., Cavalier, A., Thomas, D., and Gillet, R. (2012). The dual organization of P-bodies revealed by immunoelectron microscopy and electron tomography. Journal of molecular biology *420*, 17-28.

Djuranovic, S., Nahvi, A., and Green, R. (2012). miRNA-mediated gene silencing by translational repression followed by mRNA deadenylation and decay. Science *336*, 237-240.

Eulalio, A., Behm-Ansmant, I., and Izaurralde, E. (2007a). P bodies: at the crossroads of post-transcriptional pathways. Nature reviews Molecular cell biology *8*, 9-22.

Eulalio, A., Behm-Ansmant, I., Schweizer, D., and Izaurralde, E. (2007b). P-body formation is a consequence, not the cause, of RNA-mediated gene silencing. Molecular and cellular biology *27*, 3970-3981.

Fusco, D., Accornero, N., Lavoie, B., Shenoy, S.M., Blanchard, J.M., Singer, R.H., and Bertrand, E. (2003). Single mRNA molecules demonstrate probabilistic movement in living mammalian cells. Current biology : CB *13*, 161-167.

Grimm, J.B., English, B.P., Chen, J., Slaughter, J.P., Zhang, Z., Revyakin, A., Patel, R., Macklin, J.J., Normanno, D., Singer, R.H.*, et al.* (2015). A general method to improve fluorophores for live-cell and single-molecule microscopy. Nature methods *12*, 244-250, 243 p following 250.

Grunwald, D., and Singer, R.H. (2010). In vivo imaging of labelled endogenous beta-actin mRNA during nucleocytoplasmic transport. Nature *467*, 604-607.

Horvathova, I., Voigt, F., Kotrys, A.V., Zhan, Y., Artus-Revel, C.G., Eglinger, J., Stadler, M.B., Giorgetti, L., and Chao, J.A. (2017). The Dynamics of mRNA Turnover Revealed by Single-Molecule Imaging in Single Cells. Molecular cell *68*, 615-625 e619.

Hosono, Y., Niknafs, Y.S., Prensner, J.R., Iyer, M.K., Dhanasekaran, S.M., Mehra, R., Pitchiaya, S., Tien, J., Escara-Wilke, J., Poliakov, A.*, et al.* (2017). Oncogenic Role of THOR, a Conserved Cancer/Testis Long Non-coding RNA. Cell *171*, 1559-1572 e1520.

Hubstenberger, A., Courel, M., Benard, M., Souquere, S., Ernoult-Lange, M., Chouaib, R., Yi, Z., Morlot, J.B., Munier, A., Fradet, M.*, et al.* (2017). P-Body Purification Reveals the Condensation of Repressed mRNA Regulons. Molecular cell *68*, 144-157 e145.

Huch, S., and Nissan, T. (2017). An mRNA decapping mutant deficient in P body assembly limits mRNA stabilization in response to osmotic stress. Scientific reports *7*, 44395.

Jakymiw, A., Lian, S., Eystathioy, T., Li, S., Satoh, M., Hamel, J.C., Fritzler, M.J., and Chan, E.K. (2005). Disruption of GW bodies impairs mammalian RNA interference. Nature cell biology *7*, 1267-1274.

Kedersha, N., and Anderson, P. (2007). Mammalian stress granules and processing bodies. Methods in enzymology *431*, 61-81.

Kedersha, N., Tisdale, S., Hickman, T., and Anderson, P. (2008). Real-time and quantitative imaging of mammalian stress granules and processing bodies. Methods in enzymology *448*, 521-552.

Khong, A., Matheny, T., Jain, S., Mitchell, S.F., Wheeler, J.R., and Parker, R. (2017). The Stress Granule Transcriptome Reveals Principles of mRNA Accumulation in Stress Granules. Molecular cell *68*, 808-820 e805.

Leung, A.K., Calabrese, J.M., and Sharp, P.A. (2006). Quantitative analysis of Argonaute protein reveals microRNA-dependent localization to stress granules. Proceedings of the National Academy of Sciences of the United States of America *103*, 18125-18130.

Liu, J., Valencia-Sanchez, M.A., Hannon, G.J., and Parker, R. (2005). MicroRNA-dependent localization of targeted mRNAs to mammalian P-bodies. Nature cell biology *7*, 719-723.

Lytle, J.R., Yario, T.A., and Steitz, J.A. (2007). Target mRNAs are repressed as efficiently by microRNA-binding sites in the 5' UTR as in the 3' UTR. Proceedings of the National Academy of Sciences of the United States of America *104*, 9667-9672.

Martin, K.C., and Ephrussi, A. (2009). mRNA localization: gene expression in the spatial dimension. Cell *136*, 719-730.

Moon, S.L., Morisaki, T., Khong, A., Lyon, K., Parker, R., and Stasevich, T.J. (2019). Multicolour single-molecule tracking of mRNA interactions with RNP granules. Nature cell biology.

Mourao, M., Kreitman, D., and Schnell, S. (2014). Unravelling the impact of obstacles in diffusion and kinetics of an enzyme catalysed reaction. Physical chemistry chemical physics : PCCP *16*, 4492-4503.

Parker, R., and Sheth, U. (2007). P bodies and the control of mRNA translation and degradation. Molecular cell *25*, 635-646.

Pillai, R.S., Bhattacharyya, S.N., Artus, C.G., Zoller, T., Cougot, N., Basyuk, E., Bertrand, E., and Filipowicz, W. (2005). Inhibition of translational initiation by Let-7 MicroRNA in human cells. Science *309*, 1573-1576.

Pitchiaya, S., Androsavich, J.R., and Walter, N.G. (2012). Intracellular single molecule microscopy reveals two kinetically distinct pathways for microRNA assembly. EMBO reports *13*, 709-715.

Pitchiaya, S., Heinicke, L.A., Park, J.I., Cameron, E.L., and Walter, N.G. (2017). Resolving Subcellular miRNA Trafficking and Turnover at Single-Molecule Resolution. Cell reports *19*, 630-642.

Pitchiaya, S., Krishnan, V., Custer, T.C., and Walter, N.G. (2013). Dissecting non-coding RNA mechanisms in cellulo by Single-molecule High-Resolution Localization and Counting. Methods *63*, 188-199.

Protter, D.S., and Parker, R. (2016). Principles and Properties of Stress Granules. Trends in cell biology *26*, 668-679.

Raj, A., van den Bogaard, P., Rifkin, S.A., van Oudenaarden, A., and Tyagi, S. (2008). Imaging individual mRNA molecules using multiple singly labeled probes. Nature methods *5*, 877-879.

Rueda, D., Bokinsky, G., Rhodes, M.M., Rust, M.J., Zhuang, X., and Walter, N.G. (2004). Single-molecule enzymology of RNA: essential functional groups impact catalysis from a distance. Proceedings of the National Academy of Sciences of the United States of America *101*, 10066-10071.

Schutz, S., Noldeke, E.R., and Sprangers, R. (2017). A synergistic network of interactions promotes the formation of in vitro processing bodies and protects mRNA against decapping. Nucleic acids research *45*, 6911-6922.

Shin, Y., and Brangwynne, C.P. (2017). Liquid phase condensation in cell physiology and disease. Science *357*.

Shukla, S., Evans, J.R., Malik, R., Feng, F.Y., Dhanasekaran, S.M., Cao, X., Chen, G., Beer, D.G., Jiang, H., and Chinnaiyan, A.M. (2017). Development of a RNA-Seq Based Prognostic Signature in Lung Adenocarcinoma. Journal of the National Cancer Institute *109*.

Simonson, P.D., Deberg, H.A., Ge, P., Alexander, J.K., Jeyifous, O., Green, W.N., and Selvin, P.R. (2010). Counting bungarotoxin binding sites of nicotinic acetylcholine receptors in mammalian cells with high signal/noise ratios. Biophysical journal *99*, L81-83.

Spector, D.L. (2006). SnapShot: Cellular bodies. Cell *127*, 1071.

Stalder, L., and Muhlemann, O. (2009). Processing bodies are not required for mammalian nonsense-mediated mRNA decay. Rna *15*, 1265-1273.

Tutucci, E., Vera, M., Biswas, J., Garcia, J., Parker, R., and Singer, R.H. (2017). An improved MS2 system for accurate reporting of the mRNA life cycle. Nature methods.

Van Treeck, B., and Parker, R. (2018). Emerging Roles for Intermolecular RNA-RNA Interactions in RNP Assemblies. Cell *174*, 791-802.

Weidensdorfer, D., Stohr, N., Baude, A., Lederer, M., Kohn, M., Schierhorn, A., Buchmeier, S., Wahle, E., and Huttelmaier, S. (2009). Control of c-myc mRNA stability by IGF2BP1-associated cytoplasmic RNPs. Rna *15*, 104-115.

Wilbertz, J.H., Voigt, F., Horvathova, I., Roth, G., Zhan, Y., and Chao, J.A. (2019). Single-Molecule Imaging of mRNA Localization and Regulation during the Integrated Stress Response. Molecular cell.

Zhang, Y., Pitchiaya, S., Cieslik, M., Niknafs, Y.S., Tien, J.C., Hosono, Y., Iyer, M.K., Yazdani, S., Subramaniam, S., Shukla, S.K.*, et al.* (2018). Analysis of the androgen receptor-regulated lncRNA landscape identifies a role for ARLNC1 in prostate cancer progression. Nature genetics *50*, 814-824.

Chapter 3. Multivalent Proteins Rapidly and Reversibly Phase-Separate Upon Osmotic Cell Volume Change[3]

3.1. Abstract

Processing bodies (PBs) and stress granules (SGs) are prominent examples of sub-cellular, membrane-less granules that phase-separate under physiological and stressed conditions, respectively. We observe that the trimeric PB protein DCP1A rapidly (within ~10 s) phase-separates in mammalian cells during hyperosmotic stress and dissolves upon isosmotic rescue (over ~100 s) with minimal impact on cell viability even after multiple cycles of osmotic perturbation. Strikingly, this rapid intracellular hyperosmotic phase separation (HOPS) correlates with the degree of cell volume compression, distinct from SG assembly, and is exhibited broadly by homo-multimeric (valency ≥ 2) proteins across several cell types. Notably, HOPS leads to nuclear sequestration of pre-mRNA cleavage factor component CPSF6, rationalizing hyperosmolarity-induced global impairment of transcription termination. Together, our data suggest that the multimeric proteome rapidly responds to changes in hydration and molecular

[3] The contents of this chapter have been published as:

Jalihal, A.P.*, Xiao, L., Bawa, P., Jiang, X., Bedi, K., Cieslik, M., Ljungman, M., Chinnaiyan, A.M., Pitchiaya, S.* and Walter, N.G. Multivalent proteins rapidly and reversibly phase-separate upon osmotic cell volume change. (2020) Mol. Cell. Vol.79, Issue 6, 978 - 990.e5

A.P.J. performed all live-cell imaging experiments. S.P. and X.J. performed all fixed cell assays and phenotypic analyses. L.X. constructed several plasmids. P.B., K.B., M.C. and M.L. performed and analyzed the sequencing assays. A.P.J., S.P., A.M.C. and N.G.W. designed the study. A.P.J. S.P., and N.G.W. and wrote the manuscript, and all authors provided feedback on the manuscript.

*denoted equal contributing first authors.

crowding, revealing an unexpected mode of globally programmed phase separation and sequestration that adapts the cell to volume change.

3.2. Introduction

Membrane-less condensates, often referred to as membrane-less organelles (MLOs), represent sub-cellular sites within the cytosol or nucleus of mammalian cells, wherein key processes such as transcription, translation, post-transcriptional gene regulation, and metabolism are altered compared to the nucleoplasmic or cytoplasmic bulk (Banani et al., 2017a; Spector, 2006). Mis-regulation of MLOs and the *de novo* condensation of mutated proteins into MLOs have been strongly associated with altered gene regulation (Berchtold et al., 2018) and severe pathologies such as amyotrophic lateral sclerosis (ALS) (Banani et al., 2017a; Patel et al., 2015; Shin and Brangwynne, 2017a). Therefore, understanding the cellular mechanisms by which these structures assemble should yield insights critical for both cellular physiology and disease (Alberti, 2017; Hyman et al., 2014a; Toretsky and Wright, 2014).

MLOs are hypothesized to arise from the phase separation of dispersed multivalent biomolecules under specific conditions of pH, temperature, and concentration (Boeynaems et al., 2018; Hyman et al., 2014a; Shin and Brangwynne, 2017a). Extensive evaluation of this notion *in vitro* has defined the molecular features required to form MLOs (Hyman et al., 2014a; Shin and Brangwynne, 2017a; Wang et al., 2018a), especially in the context of homotypic or heterotypic interactions of low complexity domain (LCD) containing proteins and RNAs, and has yielded an ever-expanding list of cellular components that can spontaneously phase-separate in the test tube. Yet, the significance of the propensity of these biomolecules to phase-separate under the physiological conditions of their native intracellular environment, where molecular crowding is

dominant, is poorly understood (Alberti et al., 2019). While it is possible to alter crowding within the test tube via the addition of synthetic macromolecules (Alberti et al., 2019), the nature and extent of crowding in the cellular context is quite different (Daher et al., 2018a; Walter, 2019) and dynamically changes with the cellular state. For example, cell volume adjustments occur during processes critical to both cellular homeostasis and pathology, including the cell cycle (Tzur et al., 2009; Zlotek-Zlotkiewicz et al., 2015) as well as upon cell adhesion and migration (Guo et al., 2017; Watkins and Sontheimer, 2011). Changes in cell volume and molecular crowding, frequently encountered by cells of the kidney, liver, and gut (Lang et al., 1998), are even more rapid and dramatic during osmotic perturbation (Guo et al., 2017; Hersen et al., 2008; Miermont et al., 2013). How cells respond to rapid and frequent volume perturbations with seemingly minimal impact on their viability and whether the resulting dynamic changes in macromolecular crowding affect intracellular phase separation remain unknown.

Processing bodies (PBs) are an example of gene regulatory MLOs that are constitutively present in eukaryotic cells under physiological conditions and concentrations (Anderson and Kedersha, 2009). Their intracellular copy number has been shown to be modulated not only during the cell cycle (Aizer et al., 2013), but also upon prolonged (minutes to hours) hypertonic or hyperosmotic stress (Huch and Nissan, 2017b), which can lead to nephritic and vascular pathologies (Brocker et al., 2012). Much like other environmental stressors (e.g., heat shock, oxidative stress, metabolite deprivation), prolonged hyperosmotic stress also triggers the integrated stress response (ISR) and the formation of a type of gene-regulatory MLOs called stress granules (SGs) (Anderson and Kedersha, 2009). While both PBs and SGs are thought to assemble via a conceptually similar mechanism involving multivalent interactions between non-translating mRNAs and LCD-bearing RNA binding proteins (Van Treeck and Parker, 2018), they are

compositionally distinct (Hubstenberger et al., 2017b; Jain et al., 2016; Khong et al., 2017a). Whether components of PBs and SGs are affected differentially by distinct stresses is largely unknown. Given that hyperosmotic stress rapidly (seconds to minutes) imparts cell volume change (Guo et al., 2017; Hersen et al., 2008; Miermont et al., 2013), it is also unclear whether the ISR, and consequently SGs, can be induced at this time scale. Finally, the observation that PBs are similarly regulated by the cell cycle and hypertonic stress (Aizer et al., 2013; Huch and Nissan, 2017b) raises the question of whether PB regulation and cell volume change may be connected.

Here we investigate the role of macromolecular crowding and cell volume change on the intracellular phase separation of proteins using osmotic perturbations. We observe that DCP1A, a marker of PBs and component of the mRNA decapping machinery, rapidly (within ~10 s) undergoes cytosolic phase separation in response to hypertonic stress and that these condensates dissolve over ~100 s upon return to isotonic media. This hyperosmotic phase separation (HOPS) can be cycled multiple times with minimal impact on cell viability, and is caused by changes in cellular water content and molecular crowding since its extent is directly proportional to the osmotic compression of the cell. We further find that HOPS is induced by DCP1A's homo-trimerization domain and observed across a variety of cell types. Strikingly, most multimeric proteins tested with a valency of at least 2 (i.e., forming trimers and higher order multimers, but not dimers and monomers) undergo HOPS, strongly suggesting that rapid changes in hydration and molecular crowding are sensed by a significant fraction of the proteome and may lead to pleiotropic effects. Notably, G3BP and polyA RNA, as markers of SGs, do not undergo HOPS (as characterized by condensation within ~10 s), suggesting distinct intracellular phase separation phenomena of proteins with multivalent interactions and with LCDs. HOPS of multimeric Cleavage and Polyadenylation Specific Factor 6 (CPSF6) within the cell's nucleus is correlated

with widespread impairment of transcription termination, possibly due to sequestration of this component of the pre-mRNA cleavage factor Im complex from a subset of transcription end sites (TES). Our findings suggest that HOPS is a heretofore-underappreciated fundamental cellular driver of protein phase separation that rapidly senses changes in cell volume with profound impact on cellular homeostasis.

3.3. Results

3.3.1. Changes in extracellular tonicity induce rapid and reversible intracellular phase separation of DCP1A, but not SG markers

In a previous study (Pitchiaya et al., 2019a), we observed that osmotic stress leads to phase separation of DCP1A, a non-catalytic protein component of the eukaryotic decapping complex and conserved PB marker (Anderson and Kedersha, 2009). To study the intracellular kinetics of PB and SG formation in response to stress more broadly, we subjected U2OS cells to osmotic and oxidative stressors, and performed fixed-cell protein immunofluorescence (IF) or combined IF and RNA fluorescent *in situ* hybridization (RNA-FISH) before and after the stressors (Figure 3-1). Under isotonic conditions (150 mM Na^+), DCP1A localized to ~10-30 foci (each ranging ~300-800 nm in diameter) per cell, whereas G3BP protein and polyA RNA, as markers of SGs (Patel et al., 2015), were dispersed throughout the cytosol (Figure 3-1A and 3-2A). Upon a short (2 min) hypertonic (300 mM Na^+) shock, DCP1A, but neither G3BP nor polyA RNA, formed ~200-300 foci per cell that were smaller (200-300 nm) than the pre-existing foci (Figures 3-1A and 3-2A). No significant change was observed even after prolonged (60 min) hypertonic treatment. At this later time point, both G3BP and polyA RNA showed significant focus formation (~100-200 foci per cell, 200-300 nm in diameter; Figure 3-1A and 3-2A), thus in line with previous observations

(Bounedjah et al., 2012). By contrast, after 2 min of treatment with sodium arsenite to induce oxidative stress, DCP1A foci were unchanged in number and diameter from those observed in unstressed cells, and G3BP and polyA RNA were still dispersed throughout the cytosol (Figures 3-1B and 3-2B). The number of DCP1A foci only marginally increased (~25-40 foci per cell, 300-800 nm in diameter) in response to prolonged (60 min) arsenite stress, with a concomitant small increase in G3BP and polyA RNA foci (~10-30 per cell, 400-1100 nm in diameter, Figures 1B and 3-2B). These data suggest that DCP1A and G3BP/polyA RNA, when visualized in their physiological contexts, assemble into microscopically detectable foci at distinct rates and extents in response to osmotic and oxidative stressors.

Next, we tested whether the increased focus number could be rescued (Res) by first subjecting cells to stress and subsequently recovering them in regular, isotonic growth medium (Figures 3-1C-D and 3-2C-D). We observed that hypertonicity induced DCP1A foci rapidly disappeared, within 2 min, irrespective of the duration of the stress (Figure 3-1C). While a significant fraction of the G3BP and polyA RNA foci also rapidly disappeared (within 2 min), the kinetics of complete recovery to the baseline (i.e., pre-treatment) focus number differed from those of DCP1A (Figure 3-1C and 3-2C). By comparison, DCP1A, G3BP, and polyA RNA foci induced by arsenite stress did not disappear even after 60 min of rescue (Figure 3-1D and 3-2D). These data suggest that DCP1A and G3BP/polyA RNA foci show differences in the kinetics of both assembly and disassembly, and that the rapid phase separation of DCP1A in response to altered tonicity is distinct from SG formation.

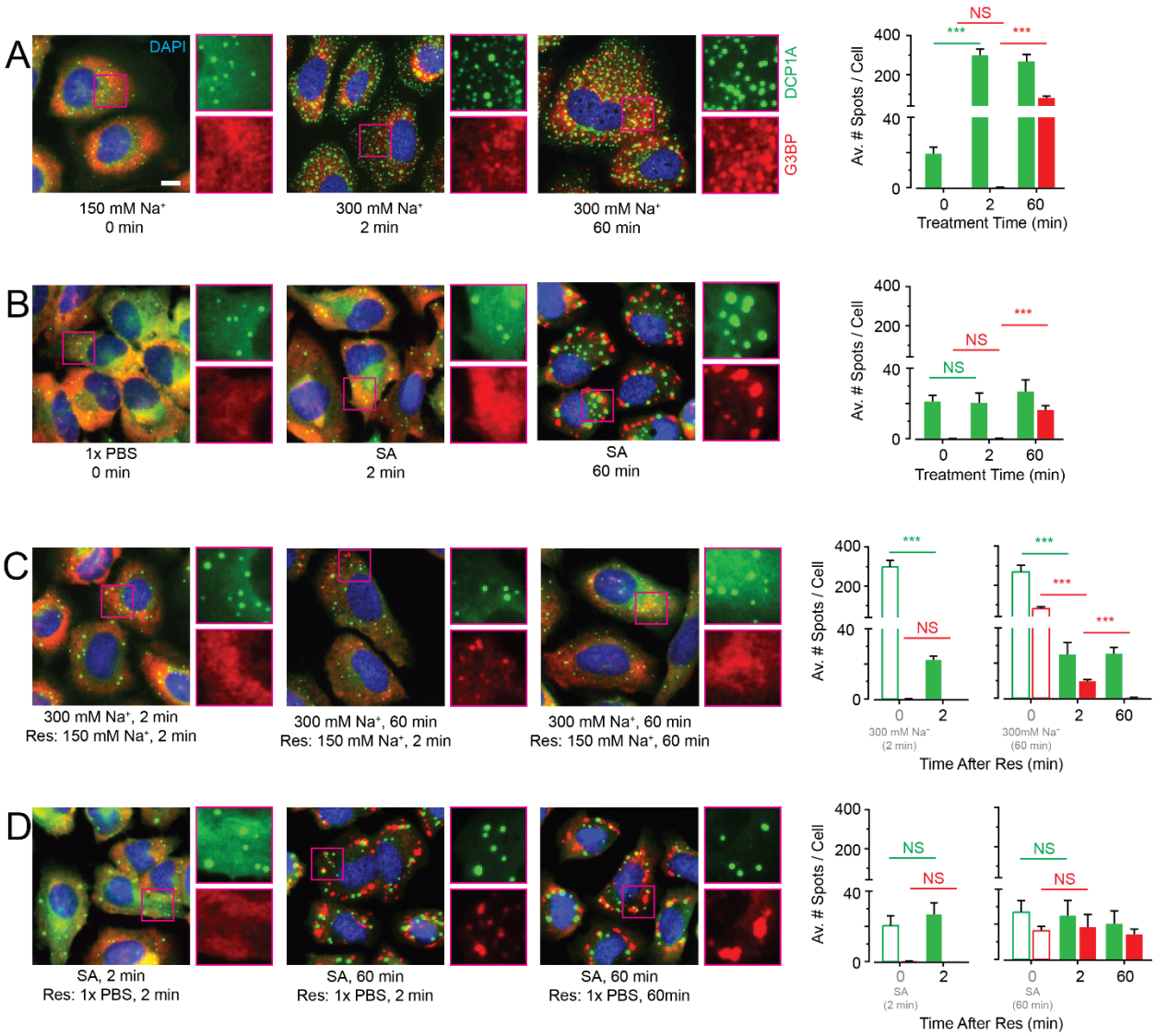

Figure 3-1 Extent and kinetics of DCP1A phase separation during hypertonic stress are distinct from those of SG markers G3BP and polyA RNA. (**A-D**) Representative pseudocolored immunofluorescence (IF) images of U2OS cells stained for DAPI (blue), DCP1A (green) or G3BP (red) and the corresponding quantification of average number of spots per cell. Scale bar, 10 µm. (**A**) Cells were treated with isotonic (150 mM Na+) medium or hypertonic (300 mM Na+) medium for the appropriate time points. (**B**) Cells were mock treated with 1x PBS or treated with 0.5 mM arsenite for the appropriate time points. (**C**) Cells were first treated with hypertonic media (300 mM Na+) for the appropriate time points and then rescued with isotonic (150 mM Na+) media for various durations. Bars with green and red outline depict data points from panel A. (**D**) Cells were first treated with 0.5 mM arsenite for the appropriate time points and then rescued with medium containing 1x PBS for various durations. Bars with green and red outline depict data points from panel B. n = 3, > 60 cells, ***p ≤ 0.0001, N.S. denotes non-significance by two-tailed, unpaired Student's t-test.

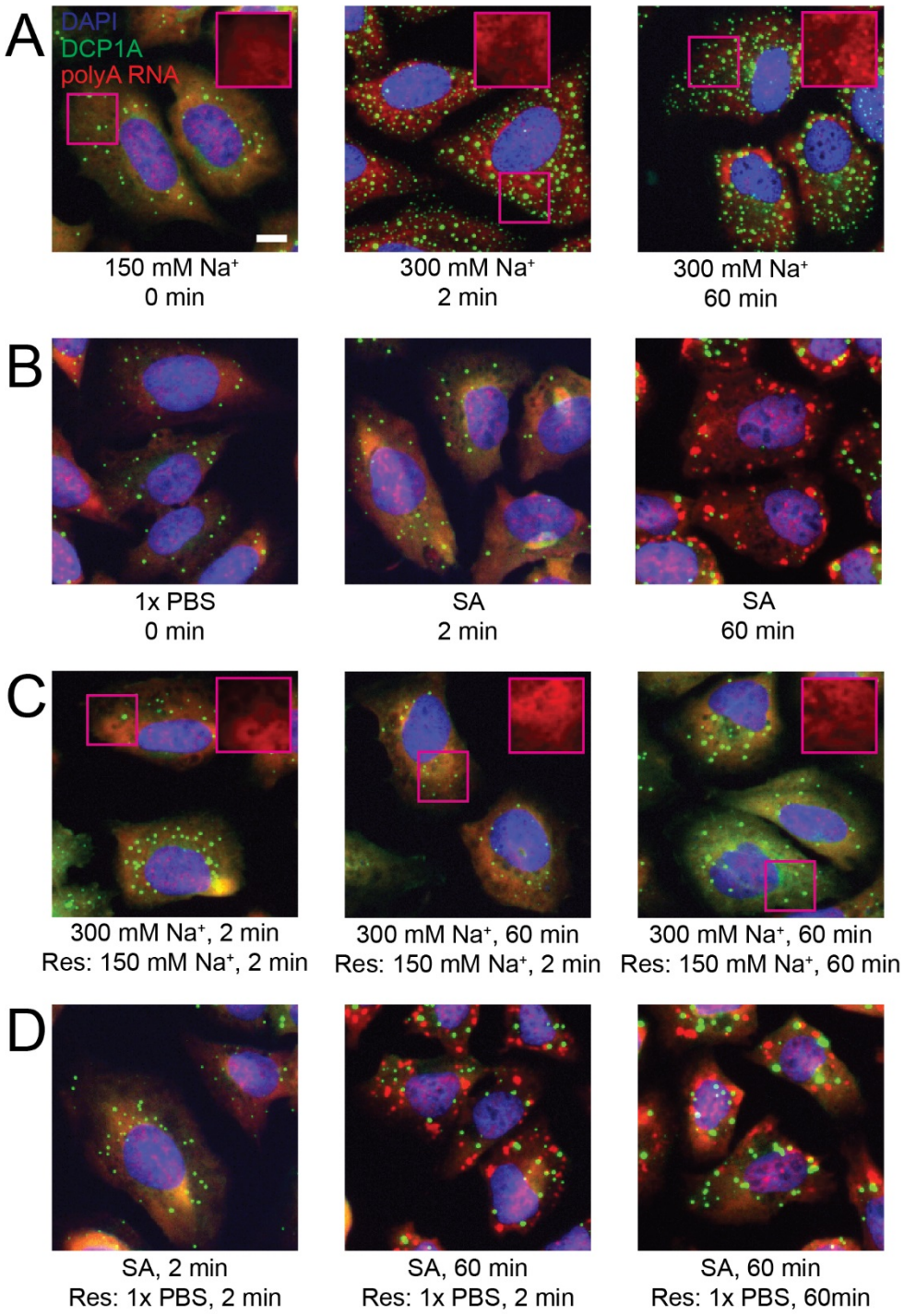

Figure 3-2 Extent and kinetics of DCP1A foci formation are distinct from that of polyA RNA during hypertonic stress. Related to Figure 3-1. (**A-D**) Representative pseudocolored, combined IF – RNA-FISH images of U2-OS cells stained for DAPI (blue), DCP1A (green), or polyA RNA (red). Scale bar, 10 μm. (**A**) Cells were treated with isotonic (150 mM Na+) or hypertonic (300 mM Na+) medium for the appropriate time points. (**B**) Cells were mock treated with 1x PBS or treated with 0.5 mM SA for the appropriate time points. (**C**) Cells were first treated with hypertonic (300 mM Na+) media for the appropriate time points and then rescued with isotonic (150 mM Na+) media for various durations. (**D**) Cells were first treated with 0.5 mM SA for the appropriate time points and then rescued with medium containing 1x PBS for various durations.

3.3.2. Hypertonicity rapidly induces the formation of immobile DCP1A condensates in live cells

Since fixed-cell experiments revealed that the rapid phase separation of DCP1A condensates was distinct from SG formation over minutes/hours, we decided to probe the sub-cellular dynamics at greater temporal resolution. To this end, we subjected the previously developed UGD cell line (a U2OS cell line that stably expresses GFP-DCP1A; (Pitchiaya et al., 2019a) to a systematic set of hypertonic conditions. We chose this cell line because it contains a similar number of DCP1A foci as the parental U2OS cells, and each of these foci compositionally resembles endogenous PBs (Liu et al., 2005b). As a control, we first confirmed in transiently transfected U2OS cells that DCP1A rapidly and reversibly forms "condensates" (Banani et al., 2017a) irrespective of the fluorescence tag to which it is fused (GFP, mCherry, Halo, or CLIP; Figure 3-4A). We noted that the condensation and rescue of SNAP tagged DCP1A were distinct from the other tags (Figure 3-3A), raising the possibility that the nature of tagging might interfere with phase separation. Next, live cell imaging of UGD cells subjected to a cycle of isotonic conditions, brief hypertonic stress, and isotonic rescue recapitulated the rapid and reversible nature of DCP1A phase separation (Figure 3-1). Furthermore, imaging of UGD cells at various levels of tonicity (150 mM to 450 mM Na^+) showed that the number of GFP-DCP1a condensates per cell rapidly and monotonically increases with the salt concentration (Figure 3-4A); however, the mobility of the condensates, as measured by their diffusion constants, decreases. Within the time frame of treatment, typically 1-3 min, the cells remained viable across all concentrations of Na^+ and survived 225 mM Na^+ for up to 24 h (Figure 3-4B).

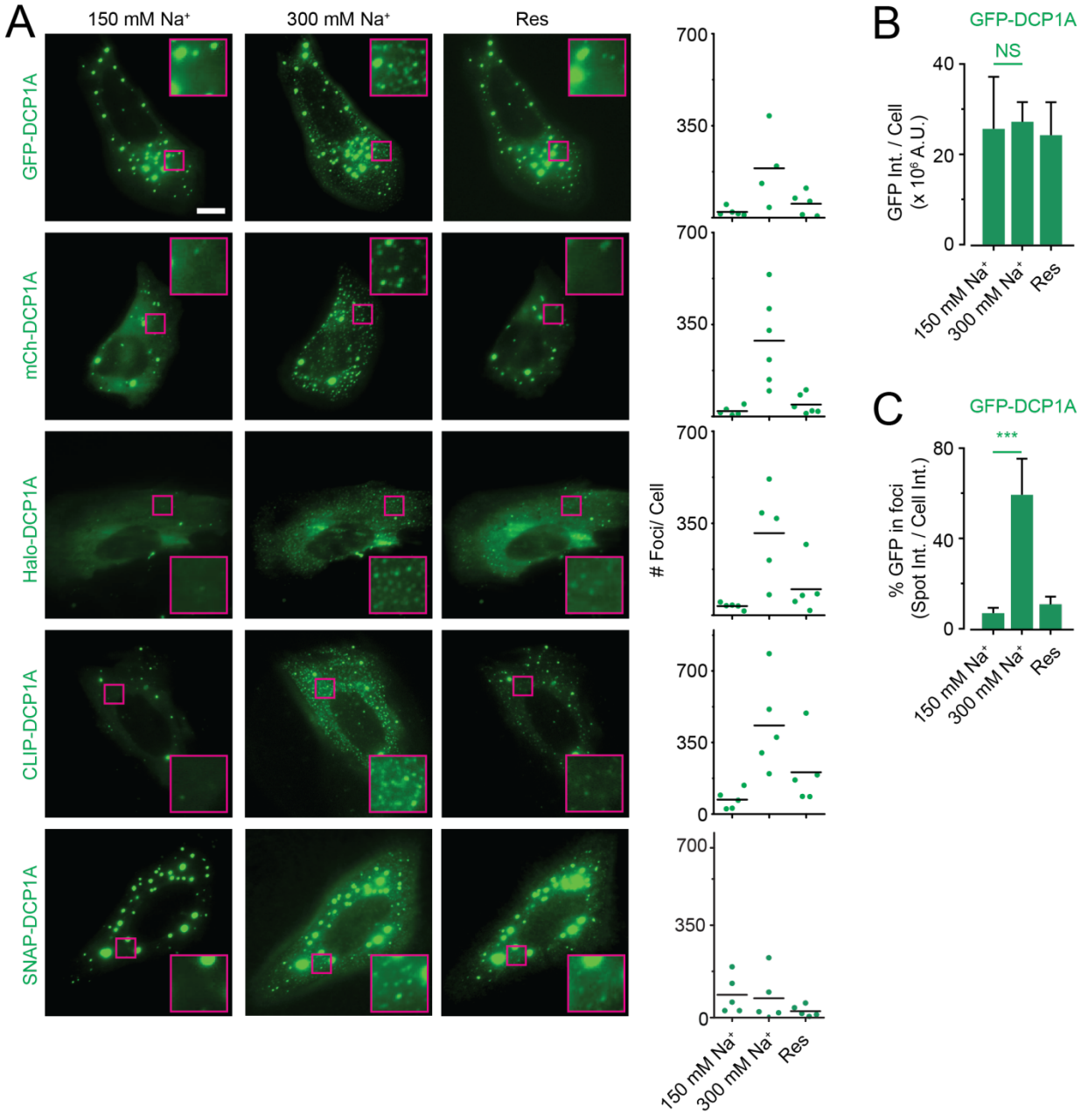

Figure 3-3 Tags do not interfere with the ability of DCP1A to rapidly and reversibly form condensates in living U2-OS cells. Related to Figure 3-3. (**A**) Representative pseudocolored images of U2-OS cells expressing DCP1A fused to different types of fluorescent or fluorogenic tags (green). Cells were treated with isotonic (150 mM Na+, 2 min) medium, hypertonic (300 mM Na+, 2 min) medium, or rescued with isotonic medium (2 min) after hypertonic treatment (2 min). Scale bar, 10 μm. Scatter plot of the number of foci per cell for each treatment condition is also shown. n = 2, > 5 cells per sample. (**B**) Average GFP intensity per UGD cell at various treatment and rescue conditions. n = 5, 300 cells per sample. (**C**) Percentage of GFP intensity within foci in UGD cells at various treatment and rescue conditions. n = 5, 300 cells per sample.

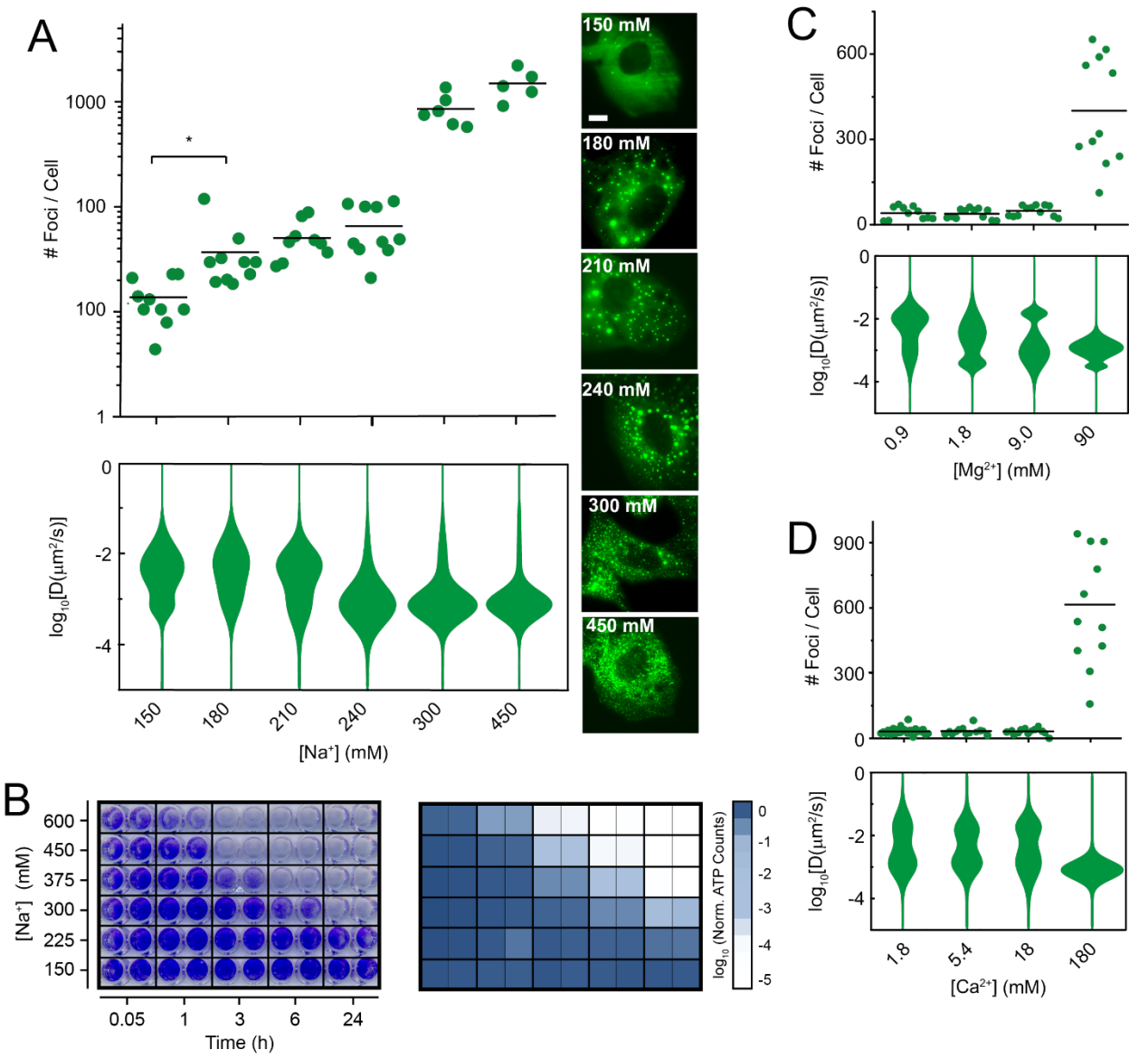

Figure 3-4 Physicochemical and phenotypic characterization of DCP1A phase separation during hypertonic stress. (**A**) Scatter plot of the number of foci per cell (top), violin plots of diffusion constants associated with DCP1A foci (bottom) and representative pseudocolored images of UGD cells (GFP, green) treated with growth medium containing various concentrations of Na+. n = 2, > 5 cells per sample, *p ≤ 0.01 by two-tailed, unpaired Student's t-test. (**B**) Representative images of 96-well plate probed for cell viability by crystal violet staining (left) or cell-titer glo assay (right) across various Na+ concentrations and multiple time points. n = 3, with technical replicates for each n. (**C** and **D**) Scatter plot of the number of foci per cell (top) and violin plots of diffusion constants associated with DCP1A foci (bottom) within UGD cells treated with growth medium containing various levels if Mg2+ (**C**) or Ca2+ (**D**). n = 3, > 5 cells per sample.

Considering that many cellular processes depend on Mg^{2+} and Ca^{2+}, we next examined whether DCP1A condensation was affected by increased concentration of these divalent metal ions

in the growth medium. Both Mg^{2+} and Ca^{2+} induced GFP-DCP1A condensation only upon 100-fold increase over isotonic concentrations (Figure 3-4C, D), which corresponded to a significant increase in osmolarity to near double the osmolarity of isotonic growth medium (~600 mOsm/L). These data suggest that DCP1A condensation occurs independently of the type of ion. Moreover, the rapid change in foci number generally occurs without a concomitant change in the total GFP fluorescence of the cell (Figure 3-3C), indicating that the GFP-DCP1A condensation is a direct response of the existing cellular protein to osmotic perturbation rather than an indirect response of protein expression or cellular signaling.

3.3.3. DCP1A phase separation is modulated by osmotic cell volume change

To distinguish between the possibilities that DCP1a condensation is a result of an increase in either specifically ionic or general osmotic concentration, we examined the sub-cellular effects of two non-ionic osmolytes, sucrose and sorbitol. Subjecting UGD cells to 300 mOsm/L of either of these osmolytes supplemented to regular growth media again resulted in the formation of immobile DCP1A condensates; however, cells recovered quickly when reversing to isosmotic medium (Figures 3-5A and 3-6A). These observations strongly suggest that DCP1A condensates form in response to osmotic shock rather than changes in ionic strength only.

Since hyperosmolarity is a state of increased extracellular osmotic pressure and causes cellular volume reduction by compensatory exosmosis (i.e., water loss), we hypothesized that DCP1A foci formation is the result of osmotic cellular compression causing an increase in intracellular molecular crowding (Guo et al., 2017; Miermont et al., 2013). To test this hypothesis, we estimated volume changes of UGD cells in hyperosmotic medium using DiI staining (Sukenik

et al., 2018) and 3-dimensional (3-D) imaging (Figures 3-5B and 3-6B). We found that cell height, as a proxy for cell volume, rapidly (within ~1 min) and monotonically decreased over the increasing range of tested osmotic conditions with a concomitant increase in the number of DCP1A foci. The cell height recovered partially on the same time scale upon reverting to isotonic medium, and the effect of these changes on DCP1a foci were independent of cell lineage (Figure 3-6C). Together, our data support a direct link between molecular crowding and GFP-DCP1A condensation.

Since DCP1A exhibits rapid and reversible condensation dependent on the degree of osmotic cell volume change, and since mammalian cells repeatedly experience such osmotic perturbations, we examined the response of UGD cells to cycling osmotic volume change (Figure 3C, D). To this end, UGD cells were treated for 1 min with hypertonic medium and allowed to recover for 30 min, and this treatment regimen was repeated. Quantification of the number and diffusion constants of foci across the treatment regimen showed that the time-scales of DCP1A focus assembly (~10 s) and disassembly (~100 s), as well as changes in focus mobility, were highly similar across all cycles and occurred with minimal impact on cell viability (Figure 3-5C-F). We henceforth refer to this phenomenon of cytosolic DCP1A condensation as intracellular hyperosmotic phase separation (HOPS) and posit that it is a cellular adaptation to osmolarity-induced changes in molecular crowding.

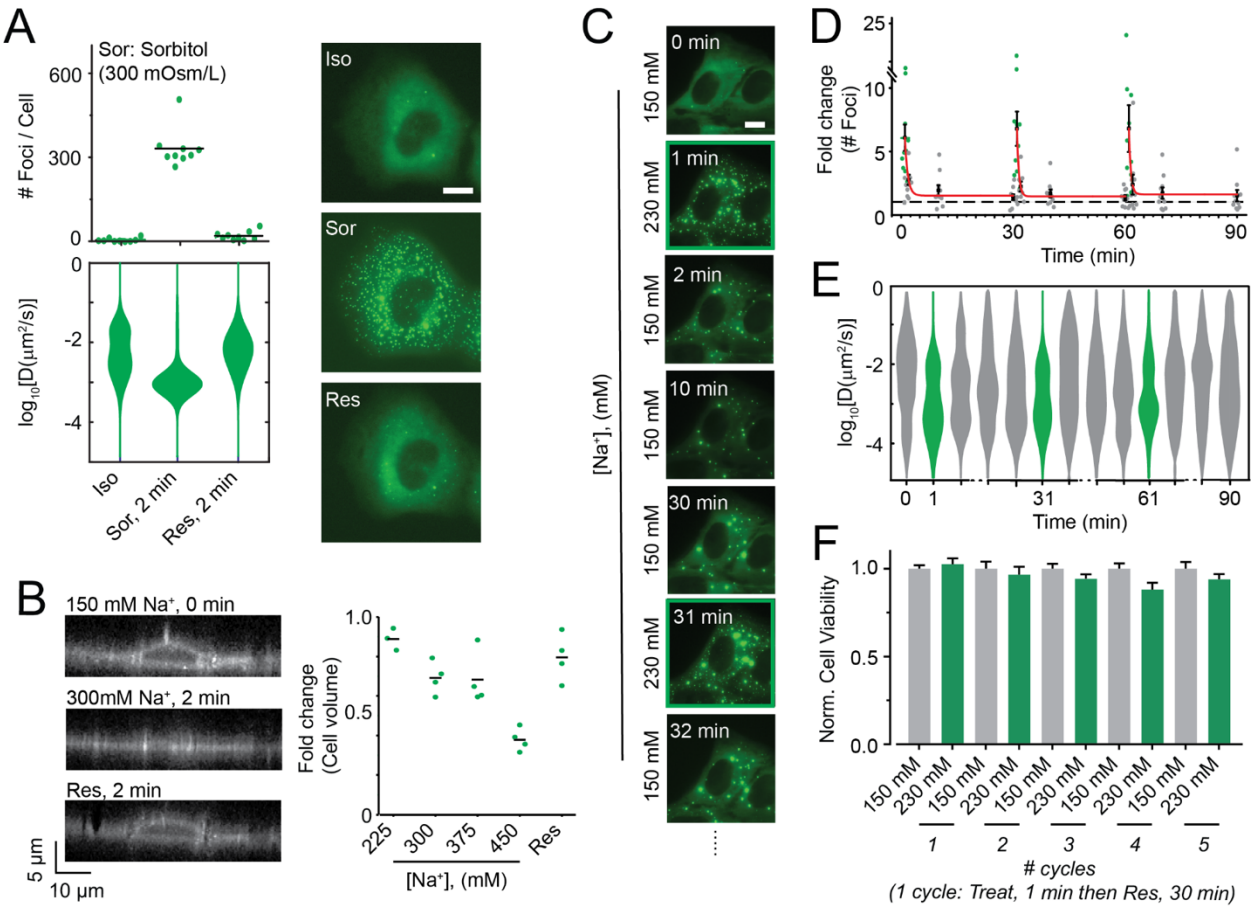

Figure 3-5 Hyperosmotic compression mediates DCP1A phase separation. (**A**) Scatter plot of the number of foci per cell (top), violin plots of diffusion constants associated with DCP1A foci (bottom) and representative pseudocolored images of UGD cells (GFP, green) treated with isosmotic (Iso) growth medium, hyperosmotic growth medium containing the non-ionic osmolyte Sorbitol (Sor), or rescued (Res) with isosmotic medium after Sorbitol treatment. n = 2, > 5 cells per sample. Scale bar, 10 μm. (**B**) Representative y-z projection of UGD cells (gray-scale) from 3-D imaging assay wherein the cell were treated with isotonic (150 mM Na+) medium, hypertonic (300 mM Na+) medium or rescued with isotonic medium after hypertonic treatment. n = 1, 4 cells per sample. Scale bar, 10 μm. Scatter plot of the fold change in cell volume, as normalized to the cell volume in isotonic conditions, is shown. (**C**) Representative pseudocolored images of a UGD cell (GFP, green) that was cyclically treated with isotonic (150 mM Na+) or hypertonic (300 mM Na+) medium. Scale bar, 10 μm. (**D**) Scatter plot of the fold change in foci number, as normalized to foci number in isotonic samples, associated with assay represented in C. Red line depicts exponential fit. n = 2, > 5 cells per sample. (**E**) Violin plots of diffusion constants associated with DCP1A foci, associated with assay represented in C. n = 2, > 5 cells per sample. (**F**) Bar plots of cell viability (by CellTiter-Glo assay), as normalized to isotonic samples, associated with assay represented in C. n = 3, with 3 technical replicates for each n.

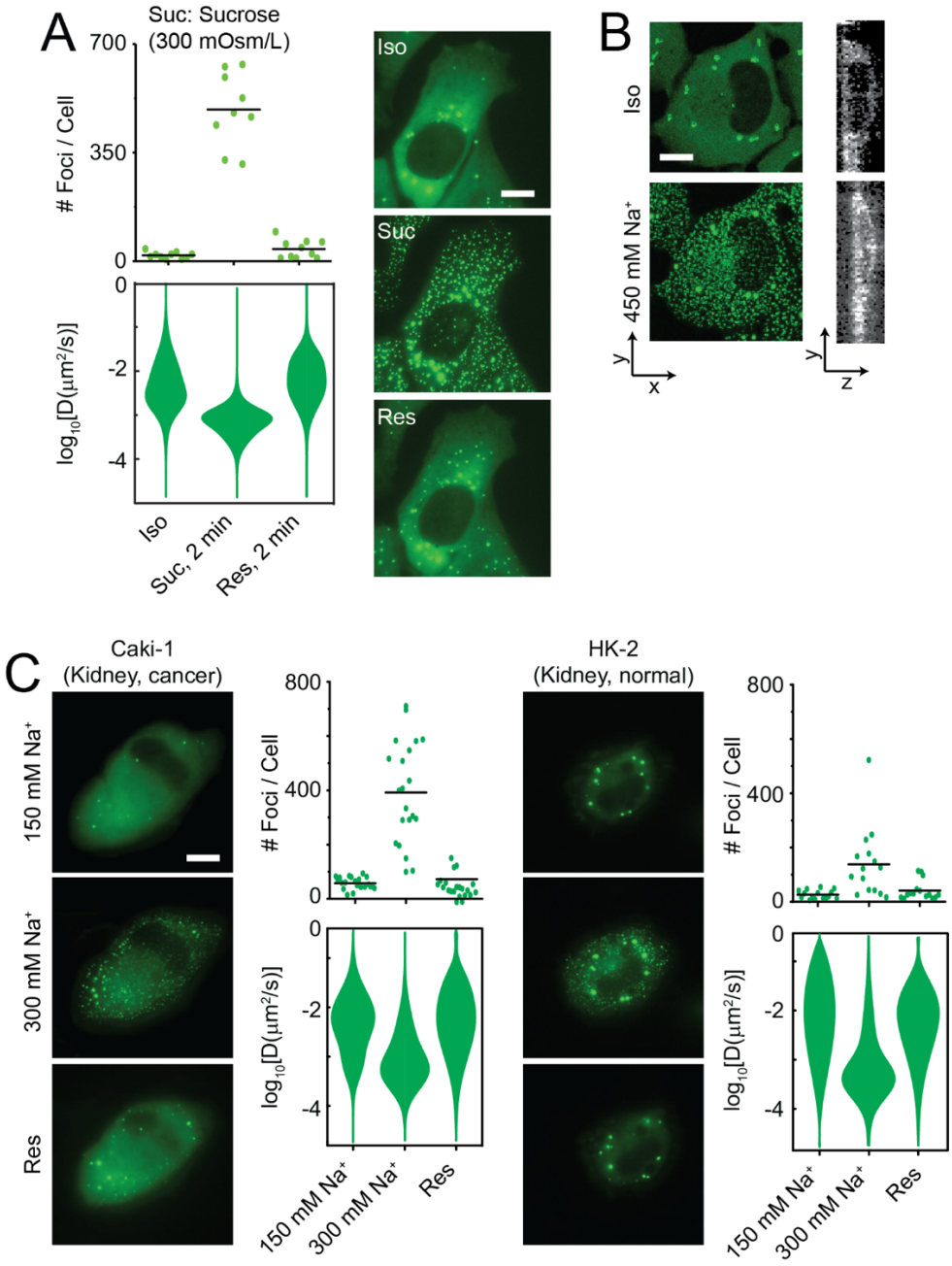

Figure 3-6 Hyperosmotic phase separation of DCP1A is independent of cell type. Related to Figure 3-5. (**A**) Scatter plot of the number of foci per cell (top), violin plots of diffusion constants associated with DCP1A foci (bottom). Representative pseudocolored images of UGD cells (GFP, green) were treated with isosmotic (Iso) growth medium, hyperosmotic growth medium containing the non-ionic osmolyte Sucrose (Suc, 2min) or rescued (Res) with isosmotic medium (2 min) after sucrose treatment (2 min). n = 2, > 5 cells per sample. Scale bar, 10 μm. (**B**) Representative x-y (green) and y-z (gray) projection of a UGD cell from 3-D imaging assay wherein the cell was treated with isotonic (150 mM Na+) medium or hypertonic (300 mM Na+) medium. n = 1, 4 cells per sample. Scale bars, 10 μm (x and y) and 5 μm (z). (**C**) Representative pseudocolored images of Caki-1 or HK-2 cells expressing GFP-DCP1A (green). Cells were treated with isotonic (150 mM Na+, 2 min) medium, hypertonic (300 mM Na+, 2 min) medium or rescued with isotonic medium (2 min) after hypertonic treatment (2 min). Scale bar, 10 μm. Scatter plot of the number of foci

per cell (top) and violin plots of diffusion constants associated with DCP1A foci (bottom) for each treatment condition for Caki-1 or HK-2 cells are also shown. n = 2, > 5 cells per sample.

3.3.4. HOPS of DCP1A depends on its trimerization domain and post-translational modification status

Macromolecular phase separation is widely thought to be driven by multivalent protein-protein and protein-nucleic acid interactions mediated by specific side chain interactions and structures (Guo and Shorter, 2015). To investigate the underlying molecular basis of DCP1A condensation, we first tested the dependence of HOPS on different DCP1A domains. While DCP1A does not contain any annotated nucleic acid binding domains, it contains two prominent protein interaction domains, an N-terminal EVH1 domain that interacts with the mRNA decapping protein DCP2, a C-terminal trimerization domain that interacts with EDC3/4, and a scaffolding protein of the decapping complex (Aizer et al., 2013). GFP-tagged truncation constructs of DCP1A's N-terminal domain (NTD) or C-terminal domain (CTD) were transiently transfected into U2OS cells. Upon exposing these cells to hyperosmotic shock, we observed that the CTD showed rapid and reversible condensation similar to the full-length protein. In contrast, a truncation mutant containing the NTD did not show detectable foci upon hyperosmotic shock (Figure 3-7A-B). As the CTD mediates both DCP1a trimerization and EDC4 interaction, we tested whether EDC4 is responsible for HOPS of DCP1A to narrow down the basis of condensation. Compared to a scrambled (Scr) silencing RNA (siRNA) control, knockdown of EDC4 by siEDC4 resulted in reduced expression (~2-fold) of GFP-DCP1A (Figure 3-8A-C) and larger GFP-DCP1A foci under isotonic conditions (Figure 3-7C-D), but did not prevent HOPS of DCP1A. In fact, the slight reduction in HOPS of DCP1A is consistent with the ~2-fold reduced cytosolic availability of DCP1A via reduced expression and enhanced localization within large foci. Consistent with these findings, we found that the intracellular condensation of DCP1A was correlated with its

cellular abundance (Figure 3-8D). These data strongly suggest that DCP1A homo-trimerization is a major driver of its HOP

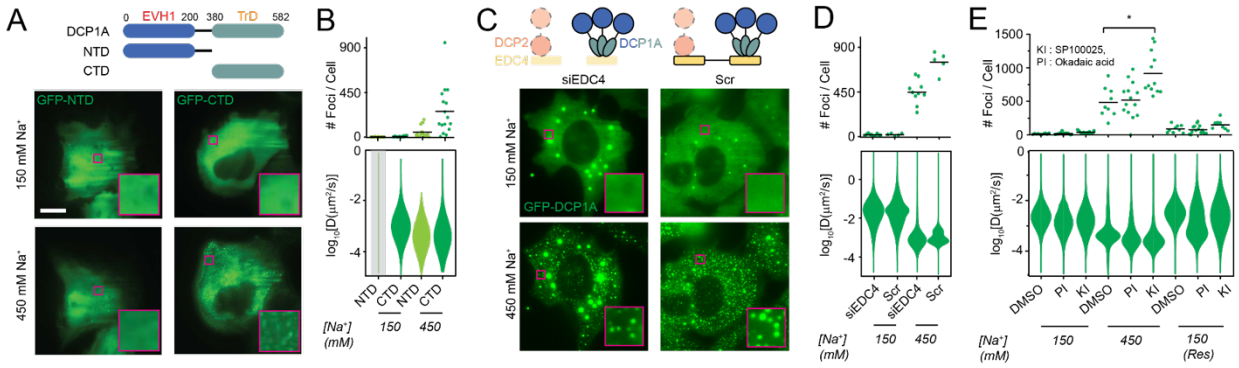

Figure 3-7 HOPS of DCP1A is dependent on its trimerization domain and modulated by PTMs, but not its interaction with EDC4. (**A**) Schematic of full length DCP1A, NTD, or CTD constructs (top, not to scale). EVH1 domain, trimerization domain, and the amino acid numbers are marked. Representative pseudocolored images of U2OS cells (GFP, green) transfected with GFP-NTD or GFP-CTD that were treated with isotonic (150 mM Na+) or hypertonic (300 mM Na+) medium (bottom). Scale bar, 10 µm. (**B**) Scatter plot of the number of foci per cell (top) and violin plots of diffusion constants associated with DCP1A foci (bottom) imaged in panel A. n = 3, > 5 cells per sample. (**C**) Schematic of DCP1A, DCP2 and EDC4 in the decapping complex (top, not to scale) in siEDC4 or Scr treatment conditions. Representative pseudocolored images of siEDC4 or Scr siRNA treated UGD cells (GFP, green) treated with isotonic (150 mM Na+) or hypertonic (300 mM Na+) medium (bottom). Scaled as in panel A. (**D**) Scatter plot of the number of foci per cell (top) and violin plots of DCP1A diffusion constants (bottom), associated with assay represented in C. n = 3, > 5 cells per sample. (**E**) Scatter plot of the number of foci per cell (top) and violin plots of DCP1A diffusion constants (bottom) within UGD cells that were pre-treated treated with DMSO, KI, or PI, and imaged in isotonic (150 mM Na+) medium, hypertonic (300 mM Na+) medium, or rescued (Res) with isotonic medium after hypertonic treatment. n = 3, > 5 cells per sample.

Previous reports have suggested that PB formation can be modulated by post-translational modification (PTM), as accompanying cell cycle progression (Aizer et al., 2008a). We reasoned that if change in phosphorylation status would influence PB assembly and disassembly during the cell cycle, such modifications should also modify the protein's response to molecular crowding. We stimulated global changes in phosphorylation using either a general phosphatase inhibitor (PI), okadaic acid, or the c-Jun N-terminal kinase inhibitor (KI), SP600125, on UGD cells. While the PI did not significantly alter HOPS of GFP-DCP1A compared to a DMSO treated control, the KI significantly increased the number of newly formed immobile condensates (Figure 3-7E).

Additionally, PI treatment mediated a significant reduction in the mobility of DCP1A condensates even after rescuing the cells with isotonic media (Figure 3-7E). Together, these observations suggest that PTM modulates HOPS of proteins, likely by altering surface charges that protein-protein interactions depend on.

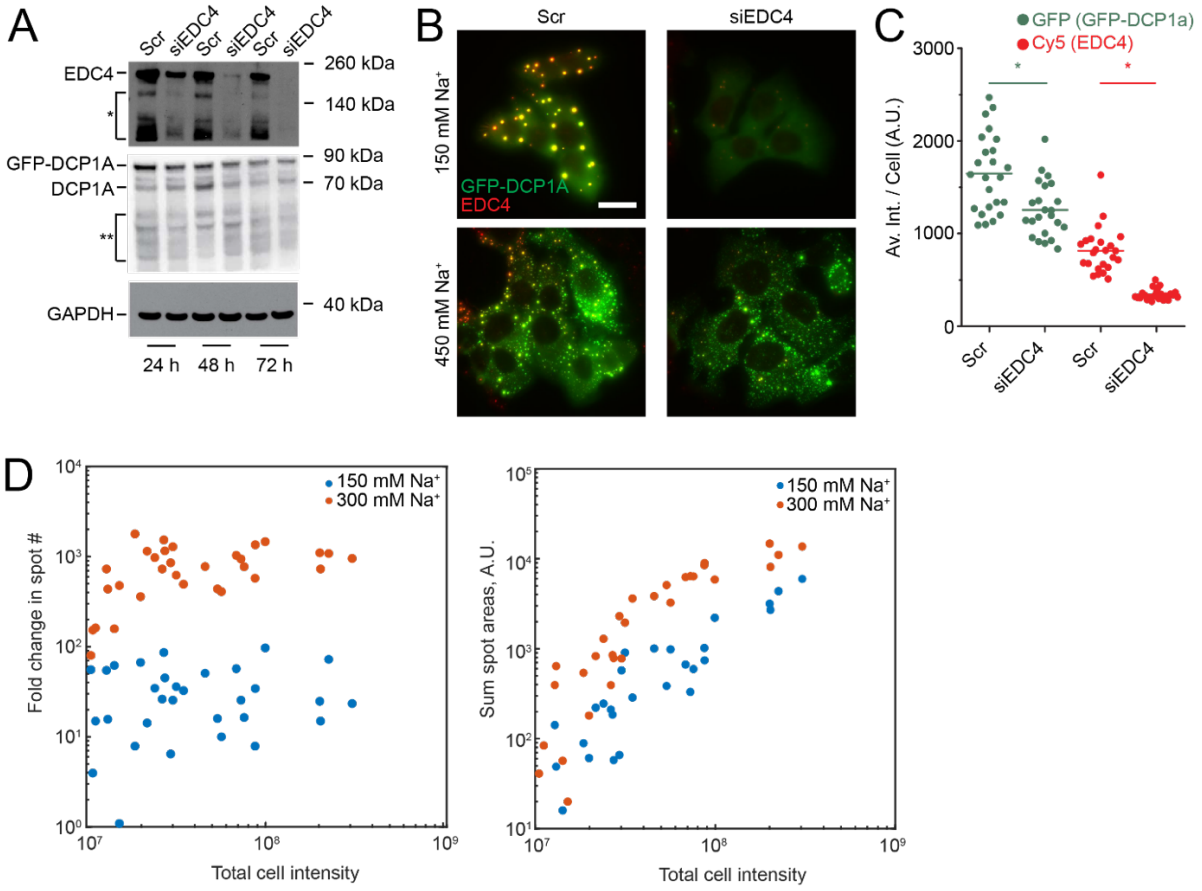

Figure 3-8 Knockdown of EDC4 results in reduced expression of DCP1A. Related to Figure 3-7. (**A**) Western Blot of EDC4, DCP1A, and GAPDH after various siRNA treatment times (24, 48 and 72 hr post siRNA transfection). Bands labeled with "*" and "**" were detected by EDC4 and DCP1A antibodies respectively and either denote non-specific bands or shorter protein fragments. (**B**) Representative pseudocolored IF images of UGD cells expressing GFP-DCP1A (green), stained for EDC4 (red). Scale bar, 20 µm. Cells were either transfected with a scrambled siRNA (Scr) or siEDC4 for 48 h and then treated with isotonic (150 mM Na+, 2 min) medium or hypertonic (450 mM Na+, 2 min) medium. (**C**) Scatter plot of the average intensity of GFP (green) or EDC4 (Cy5, red) per UGD cell transfected with a scrambled siRNA (Scr) or siEDC4 in isotonic conditions. n = 2, > 20 cells per sample, *$p \leq 0.01$, by two-tailed, unpaired Student's t-test. (**D**) Scatter plot of GFP-DCP1a spot number (left) and spot area (right) plotted against sum fluorescent intensity of the cell, under isotonic (blue) and hypertonic (orange) conditions. Fold change in spot numbers is relative to the lowest spot count under isotonicity.

3.3.5. Multimeric proteins with a valency of at least 2 generally exhibit HOPS

Considering that the minimally required structural determinant of HOPS of DCP1A is only its trimerization domain (Figure 3-7), we reasoned that other self-interacting proteins with multimerization domains might also exhibit HOPS. To test this hypothesis, we performed an unbiased high-throughput IF analysis of ~108 endogenous proteins in U2OS and UGD cells subjected to transient osmotic stress (Figure 3-9A-C). Since antibodies may exhibit cross-reactivity and impaired access to some proteins in osmotically compressed cells, we complemented high-throughput IF analysis by imaging osmotically perturbed U2OS cells transiently transfected with GFP-tagged proteins (Figure 3-9D, 3-10D and Methods). A combined analysis of both assays showed that monomeric proteins (e.g., GFP), dimeric proteins (e.g., TP53, AKT), and several proteins without annotated multimerization domains (e.g., PARP13) did not exhibit HOPS. By contrast, almost all multimeric proteins with a self-interaction valence of ≥2 (i.e. trimers and other higher-order multimers, including LCD bearing proteins such as DCP1A, HSF1, PKM2, PAICS, FUS, and TDP43), as well as several proteins with no known multimerization domain (e.g. ERp72) exhibited HOPS (Figure 3-9B-D)**.** In some cases**,** we observed the disappearance of foci upon hyperosmotic shock, which rapidly reformed upon isotonic rescue (e.g., CDK12; Figure 3-9B, C). These observations support the hypothesis that multimeric proteins with a self-interaction valency of 2 or more generally undergo HOPS. Overall, our data suggest that the sub-cellular distribution of a significant fraction of the cellular proteome, 16% of which is annotated to be self-interacting (Perez-Bercoff et al., 2010), appears to be altered by osmotic compression. Our findings thus support a widespread and pervasive impact of HOPS on subcellular organization.

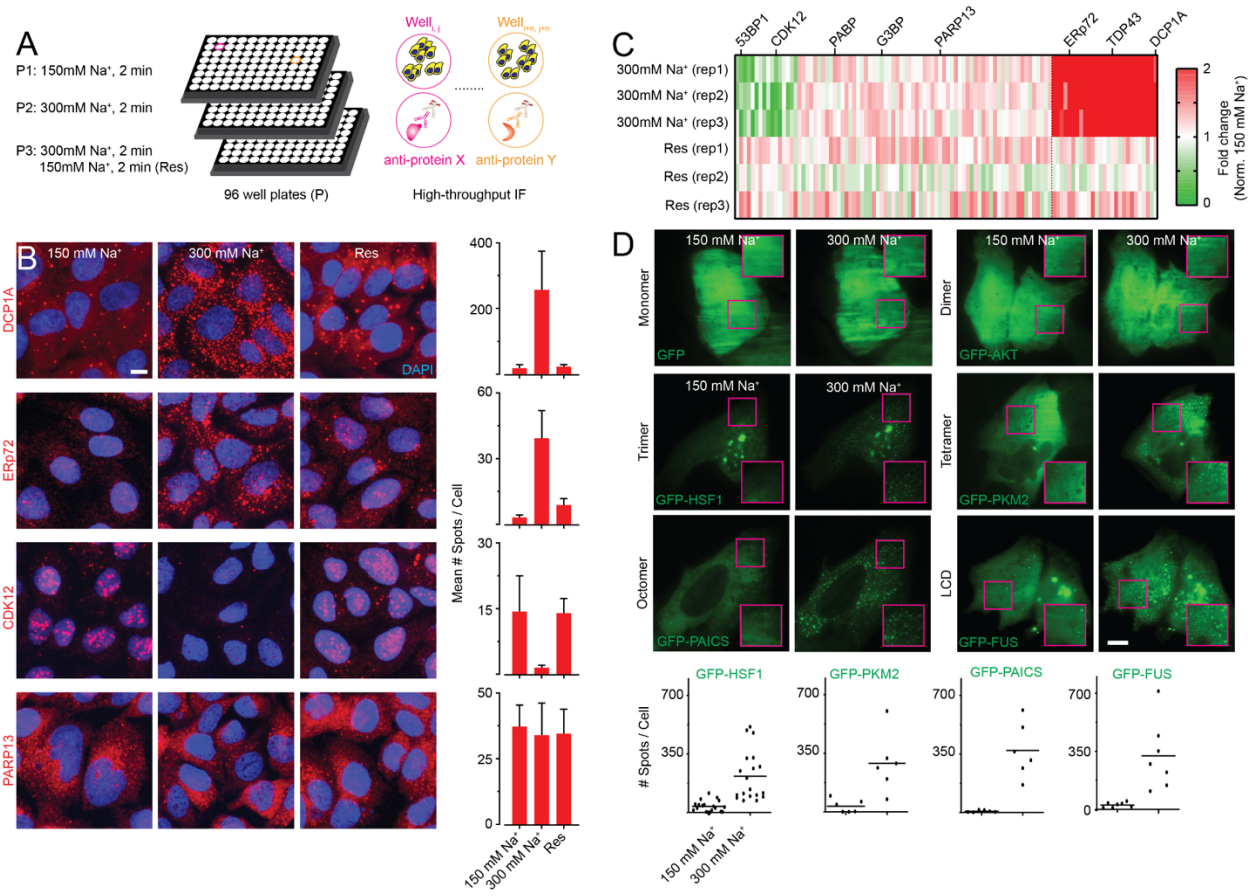

Figure 3-9 High-throughput IF and GFP imaging show that several multimeric proteins of valency ≥2 generally exhibit HOPS. (**A**) Schematic of high throughput IF assay. (**B**) Representative pseudocolored IF images of U2OS cells stained for DAPI (blue, nucleus) and the appropriate protein (red). Cells were treated with isotonic (150 mM Na+) medium, hypertonic (300 mM Na+) medium, or rescued (Res) with isotonic medium after hypertonic treatment. Scale bar, 10 µm. Quantification of average number of spots per cell of the appropriate samples in panel B is shown. n = 3, > 50 cells per sample. (**C**) Heatmap representing the fold change in spot number of 108 proteins tested by high throughput IF, as normalized to isotonic conditions. "rep" denotes replicates. (**D**) Representative pseudocolored images of U2OS cells (GFP, green) transfected with the appropriate GFP-tagged construct and treated with isotonic (150 mM Na+) medium or hypertonic (300 mM Na+) medium. Scaled as in panel A. Inset depicts a zoomed-in area corresponding to a 15 x 15 µm2 magenta box. Scatter plot of the number of foci per cell for each construct is shown. n = 2, > 5 cells per sample.

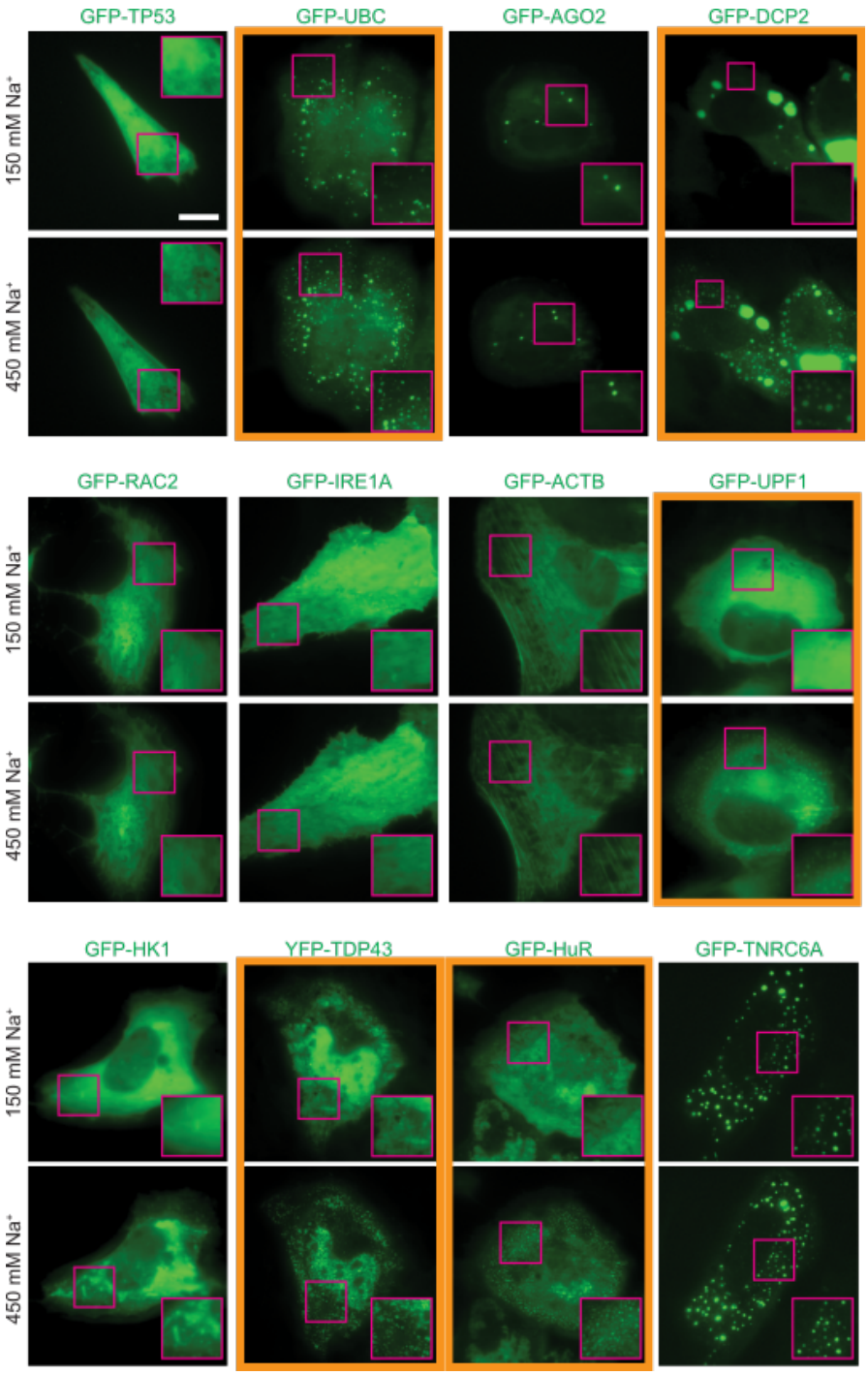

Figure 3-10 GFP imaging of several proteins transiently expressed in U2OS cells. Related to Figure 3-9. Representative pseudocolored images of U2OS cells (GFP, green) transfected with the appropriate GFP-tagged construct and treated with isotonic (150 mM Na+) medium or hypertonic (300 mM Na+) medium for 2 min. Scale bar, 10 µm. Inset depicts a zoomed-in area corresponding to a 15 x 15 µm2 magenta box. Constructs that exhibit HOPS are highlighted in orange.

3.3.6. HOPS of CPSF6 is correlated with hyperosmolarity-induced impairment of transcription termination

Hyperosmotic stress has been shown to impair transcription termination in certain cellular lineages, leading to continued transcription of regions downstream of annotated genes, and to be mediated by the impaired function of cleavage and polyadenylation factors (CPSFs) (Vilborg et al., 2015). To assess how hyperosmolarity affects the nascent transcriptome, which was expected to be highly sensitive to termination defects, in our osteosarcoma lineage, we performed nascent state RNA sequencing of nascent transcripts by 5-bromouridine metabolic labeling and sequencing (Bru-seq) and BruChase-seq after 30 min of hyperosmotic stress (Paulsen et al., 2014). We found that, indeed, the read density of sequences downstream of transcription end sites (TES) was significantly higher in the hypertonic samples than under isotonic conditions (Figures 3-11A, B and 3-12A). Performing steady-state RNA-seq of UGD cells subjected to prolonged (4 h) osmotic perturbations revealed that hyperosmotic stress also had a pervasive long-term effect that, strikingly, was reversed upon rescuing cells from hypertonic shock with isotonic medium (Figures 3-12B, C).

Finally, we asked whether impaired cleavage, polyadenylation, and HOPS of multimeric proteins may be related. Strikingly, CPSF6, a structural component of the CPSF complex (Elkon et al., 2013), underwent rapid HOPS in the nucleus (Figure 3-11C). Such condensates may sequester CPSF6 away from chromatin, thereby suggesting a possible mechanism for the functional impairment of CPSFs under hyperosmotic stress conditions (Figure 3-11D).

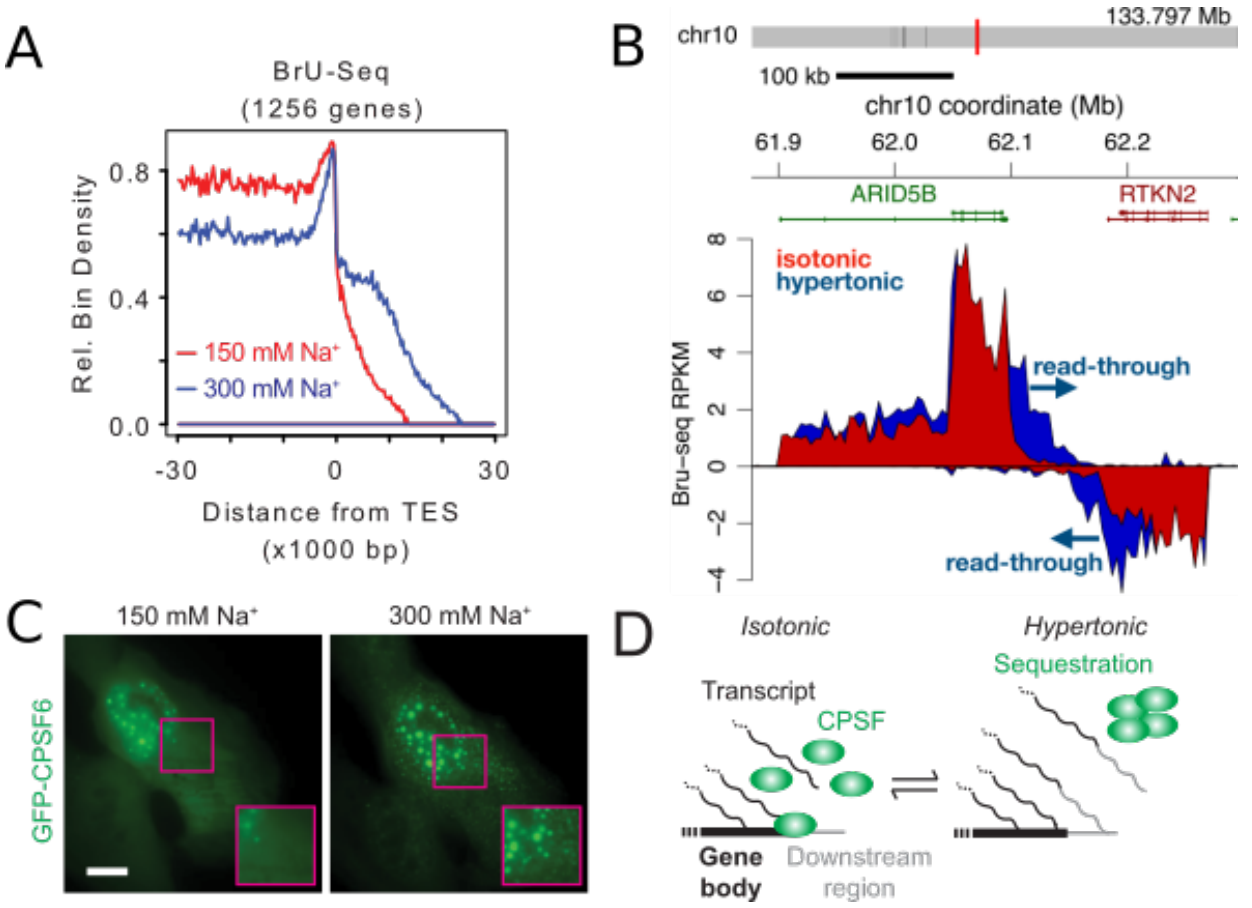

Figure 3-11 HOPS of CPSF6 is correlated with impaired transcription termination. (**A**) Aggregate nascent RNA Bru-Seq enrichment profile across TESs. Relative bin density of ~1256 genes expressed >0.5 RPKM and >30 kb long showing an ~10 kb average extension of reads past the TES following exposure to hypertonic conditions for 30 min. Samples were prepared from cells treated with isotonic (150 mM Na+, red) or hypertonic (300 mM Na+, blue) medium for 30 min. (**B**) Bru-seq tracks across the ARID5B and RTKN2 genes showing transcriptional read-through of the TES. (**C**) Representative pseudocolored images of a U2OS cell transfected with GFP-CPSF6 (green) incubated with isotonic (150 mM Na+, red) medium and then treated with hypertonic (300 mM Na+, blue) medium for 1 min. Scale bar, 10 μm. (**D**) Model that explains the transcript read-through phenotype.

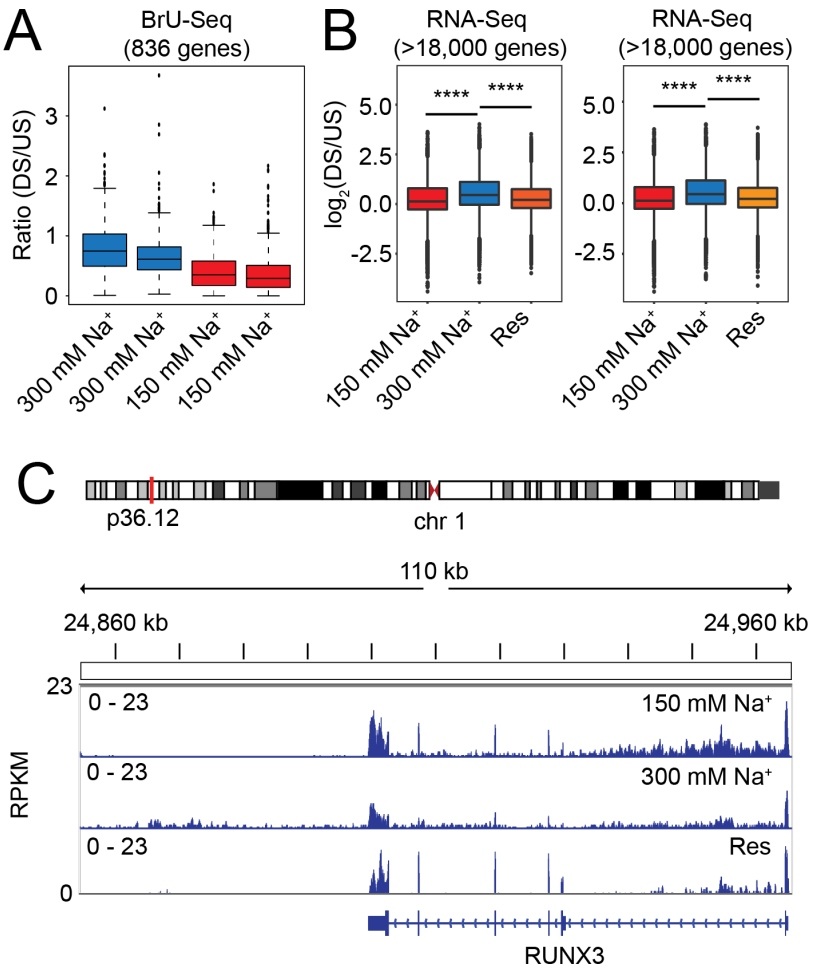

Figure 3-12 Hyperosmolarity-induced transcript read-through can be concordantly measured with RNAseq and BruSeq. Related to Figure 3-11. (**A**) Ratio between read counts downstream (DS) and read-counts upstream (US) of TES for 836 genes assayed by BrU-Seq for each replicate. Cells were treated with isotonic (150 mM Na+, 30 min) or hypertonic (300 mM Na+, 30 min) mediums prior to sequencing. (**B**) DS:US ratio of > 18,000 genes that show transcript read-through in RNA-Seq assays. Cells were treated with isotonic (150 mM Na+, 4 h) medium, or hypertonic (300 mM Na+, 4 h) medium, or rescued (Res) with isotonic medium (4 h) after hypertonic treatment (4 h) prior to sequencing. (**C**) RNA-seq tracks of the RUNX3 locus under isotonic (150 mM Na+, 4 h) medium, hypertonic (300 mM Na+, 4 h) medium, or rescued (Res) with isotonic medium (4 h) after hypertonic treatment (4 h) prior to sequencing.

3.4. Discussion

In this study, we report a multiscale (i.e., cellular, subcellular, and molecular) characterization of a seemingly widespread intracellular phase separation phenomenon in response to hyperosmotic stress, here termed HOPS (Figure 3-13). We find that a significant fraction of the multimeric proteome undergoes rapid and reversible intracellular redistribution into phase-

separated condensates during osmotic cell volume change. Empirically, proteins with a self-interaction valency of ≥2 exhibit HOPS in response to changes in cell volume, and these changes are in turn intricately linked with altered hydration and molecular crowding during hyperosmotic stress.

3.4.1. Exosmosis leads to protein concentration increase, molecular dehydration, and HOPS

Intracellular water expelled upon hyperosmotic compression (i.e. exosmosis) is thought to originate from both "free" water molecules that constitute the bulk of the cell and water molecules bound to cellular solutes and involved in macromolecular solvation (Ball, 2017). On the one hand, the loss of free water upon exosmosis leads to cell volume loss and a concomitant increase in cellular concentration that will shift the monomer-multimer equilibrium of a protein towards multimerization, which may be facilitated by depletion attraction (Marenduzzo et al., 2006). On the other hand, the loss of bound water will result in decreased protein hydration, which may lead to protein precipitation by increasing the surface exposure of hydrophobic regions (Muschol and Rosenberger, 1997). Rehydration rapidly replenishes both types of water molecules to shift the monomer-multimer equilibrium back towards the solvated monomer, dissolving the condensate.

It is thought that hydrophobic patches found in homo-multimeric proteins can spontaneously interact upon hydration loss or "dewetting" (Jensen et al., 2003; Liu et al., 2005b), whereas the phase separation driven by LCDs and RNAs is posited to involve larger interaction networks (Wang et al., 2018a); this differences, thus, lead to two distinct mechanisms with different condensation rates. The high speed and high reversibility of HOPS of multimeric proteins appear most consistently with the former mechanism wherein the rapid condensation leads to large,

amorphous assemblies (Figure 3-13). Just like in protein folding, the cost in translational and polypeptide chain entropy upon condensation into such large, slowly diffusing aggregates is expected to be slightly more than compensated by the enthalpic gain of hydrophobic patch association.

3.4.2. The features and functional consequences of widespread intracellular HOPS

We observe that increasing the intracellular crowding ~2-fold (based on the up to ~2-fold change in cell height) leads to the formation of a large number of DCP1a condensates with greatly reduced mobility; further, cellular volume recovery readily reverses both the condensation and decreased mobility (Figures 3-4, 5). Additionally, we find that the cellular concentration of the protein monomer affects the size and number of condensates (Figure 3-8D). The latter observation implies that, under low protein concentration conditions, our ability to identify proteins undergoing HOPS may be limited by our fluorescence microscope's resolution. A conservative estimate, based on cytoplasmic redistribution of GFP signal into hyperosmotic condensates (Figure 3-3B, C), suggests that we can detect 10-mers and any higher-order condensates. This level of sensitivity has allowed us to use IF to curate a high-confidence list of endogenous proteins that do and do not undergo HOPS (Figure 3-9). Thus, we can define the protein features that govern HOPS, primarily the requirement for a homo-multimerization domain of valency ≥2 that is common among cellular proteins.

It is becoming increasingly clear that excluded volume effects mediated by molecular crowding affect macromolecular structure, protein stability, enzyme activity and nucleo-cytoplasmic organization (Daher et al., 2018a; Delarue et al., 2018; Hancock, 2004; Minton, 2001;

Sukenik et al., 2018). Previous work has noted the potential for phase separation to dynamically buffer the intracellular protein concentration (Alberti et al., 2019). More directly, we find that the structural pre-mRNA cleavage and polyadenylation factor CPSF6 (Elkon et al., 2013) undergoes nuclear HOPS, which we observe to be correlated with transcriptome-wide functional impairment of transcription termination (Figure 3-11).

3.4.3. HOPS may serve as a rapid cellular sensor of volume compression

The rapid time scales of hyperosmotic cell volume compression, volume recovery under isotonicity, and cell viability after multiple osmotic cycles (Figures 3-4, 5) that we observe concur with prior reports on cell volume changes (Guo et al., 2017; Hersen et al., 2008; Miermont et al., 2013). Our data, which indicate that even a 20% reduction in cell volume by osmotic compression can mediate HOPS, reinforce evidence of the high sensitivity of the multimeric proteome towards volume changes. Our findings are consistent with the notion that the eukaryotic proteome is delicately balanced near the threshold of phase separation (Walter and Brooks, 1995; Wilson, 1899). In fact, it stands to reason that the interaction energies and concentrations of homo-multimeric proteins may have evolved to facilitate rapid crossing of their individual phase separation thresholds if, and only if, cellular conditions demand.

Notably, our HOPS-associated cell volume changes are comparable to the rapid volume changes – also a result of exosmosis – occurring during cell adhesion and migration through confined spaces (Guo et al., 2017; Watkins and Sontheimer, 2011), as well as those associated with the cell cycle (Tzur et al., 2009). Incidentally, homeostatic processes that may be expected to suppress phase separation, such as PTMs and allosteric effects by metabolically compatible

osmolytes, operate over the time scales (minutes to hours) of the cell cycle. Consistent with this expectation, we find that the loss of phosphorylation enhances the extent of HOPS (Figure 3-7).

Perhaps the most striking aspect of HOPS is its rapid onset, which is faster than the speed of canonical stress responses (Wheeler et al., 2016). This feature is similar to recent reports of rapid nuclear condensation of DEAD-box RNA helicase DDX4 in response to environmental stress (Nott et al., 2015), and of transcriptional co-activator YAP in response to hyperosmotic stress (Cai et al., 2018). Notably, prolonged exposure to hyperosmotic conditions, similar to other environmental stressors, triggers the ISR and subsequent assembly of SGs, often localized adjacently to pre-formed DCP1A condensates or PBs (Figure 3-1) (Kedersha et al., 2005). These observations support a model whereby phase-separated PB components and, possibly, other homo-multimeric proteins serve as "first responders" of osmotic compression, anchoring and gatekeeping SG assembly and the subsequent stress response. Such early volume sensors may be critical for suspending cellular biochemistry until an appropriate protective or corrective action has been initiated. This escalating response may be critical since osmotic changes in the environment are unpredictable and can rapidly fluctuate yet have widespread implications in an array of physiological and disease contexts. For instance, cells in the renal medulla frequently and rapidly experience high salt concentrations resulting in up to four-times the osmolarity of serum during urine production (Lang et al., 1998). Extreme dehydration can lead to hypernatremia, a state of serum hyperosmolarity characterized by elevated Na^+ levels exceeding 145 mM and is associated with pervasive physiological dysfunction (Nilsson and Sunnerhagen, 2011). During such prolonged stress, initiation of the ISR may then lead to long-term adaptation. For instance, long-lasting condensates of the protein WNK1, which notably also is a homo-multimer, have been observed in viable kidneys of mice raised on high-K^+ diets (Boyd-Shiwarski et al., 2018a).

Both rapid and prolonged HOPS are reversible (Figure 3-1) and can mediate widespread effects, including impairment of transcription termination (Figure 3-11) (Vilborg et al., 2015), YAP-programmed transcription initiation (Cai et al., 2018), inhibition of ribosomal translocation (Wu et al., 2019), and modulation of RNA silencing (Pitchiaya et al., 2019a). While other mechanisms may be also at play, protein sequestration away from the site of their function provides a straightforward biophysical explanation for many of these effects (Figure 3-11). In fact, such a mechanism may also explain the defects in transcription termination observed in cells exposed to prolonged heat shock (Cardiello et al., 2018), suggesting that protein sequestration might be a common mechanism across multiple stress responses. Future studies will help better understand the connection between MLO formation and protective cellular mechanisms heralded here.

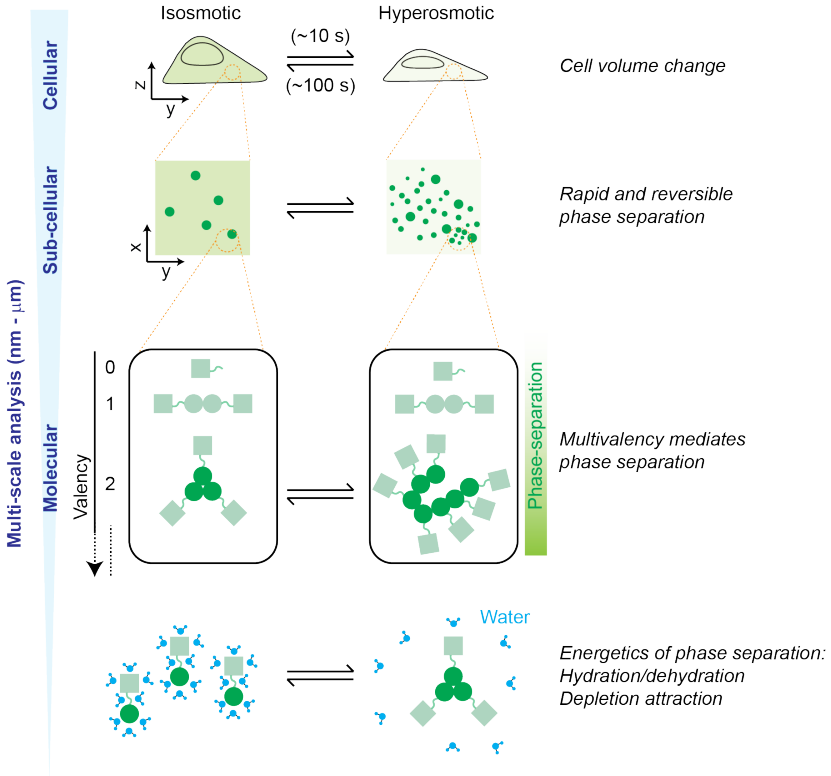

Figure 3-13 Model of the multiscale features of HOPS. Our multi-scale analysis has shown that HOPS of multimeric proteins is mediated by the concerted changes in cell volume, macromolecular crowding, and hydration.

3.4.4. Methods

DNA and RNA oligonucleotides. DNA oligonucleotide with 30 consecutive T's (Oligo-dT36-Cy5) contained a Cy5 dye at the 3' end and was purchased from IDT. Dyes were attached after oligonucleotide synthesis to a 3' amino group on a C6 carbon linker and were HPLC purified by the vendor. Negative control siRNA (Scr, Ambion negative control siRNA 1) and siRNA against EDC4 (siEDC4, siRNA targeting EDC4 SMARTPool) were purchased as ready-to-use duplexes from Thermo-Fisher and Dharmacon respectively.

Plasmids. Most plasmids were purchased from Addgene or were shared by independent labs. GFP-tagged proteins candidates were selected based on gene ontology annotation containing terms "identical protein binding" (GO:0042802), "protein homotrimerization" (GO:0070207),

"protein trimerization" (GO:0070206), "protein dimerization" (GO:0046983) and "protein tetramerization" (GO:0051262) and independently verified for their self-interacting ability by the tool SLIPPER (http://lidong.ncpsb.org/slipper/index_1.html). The resulting pools of proteins were selected to cover a range of valences. The proteins tested in each class are: monomeric, p53; dimeric, AKT, Rac2; trimeric, HSF1; tetrameric, PKM2; octomeric, PAICS; IDR-containing: FUS, TDP-43. pcDH-Halo-DCP1a, pcDH-SNAP-DCP1a, pcDH-GFP-DCP1a, pcDH-mCherry-DCP1a, and pcDH-CLIP-DCP1a were constructed by first sub-cloning the DCP1A open-reading frame (ORF) from pEGFP-DCP1A into the pcDH backbone to generate pcDH-DCP1A. The ORFs of Halo, SNAP, GFP, mCherry and CLIP were PCR amplified from pFN21A (Promega), pSNAPf (NEB), pEGFP-C1 (Clontech), pEF1a-mCherry (Clontech), and pCLIPf (NEB), respectively. These amplicons were then sub-cloned into the pcDH-DCP1A backbone to generate the appropriate plasmids.

Cell culture. U2OS and U2OS-GFP-DCP1a (UGD) cells were propagated in McCoy's 5A medium supplemented with 10% fetal bovine serum and Penicillin-Streptomycin (GIBCO, #15140). UGD cells were kept under positive selection with 100 µg/mL G418. Hypertonic medium was prepared by supplementing regular growth medium with 10x PBS such that the appropriate sodium concentration was achieved. Isotonic medium was prepared by mock supplementing regular growth medium with 1x PBS, whose volumes matched that of 10x PBS in hypertonic medium. Oxidative stress was induced by treating cells with 0.5 mM sodium arsenite (SA). Hyperosmotic medium with sucrose or sorbitol were prepared by directly dissolving the appropriate reagent to achieve 300mOsm/L (300 mM). Plasmid transfections for GFP imaging were achieved using Fugene HD (Promega, # E2311) as per the manufacturer's protocol. UGD cells were transfected with siRNAs using Lipofectamine RNAimax (Thermo-Fisher, # 13778030)

as per the manufacturer's protocol. For live cell imaging of Halo-DCP1A, CLIP-DCP1A, and SNAP-DCP1A, cells were treated with 100 nM of the appropriate ligand for 30 min in growth medium without phenol-red. After the treatment, cells were washed three times in phenol-red free medium and placed back in the incubator for 30 min, prior to imaging. For live cell imaging, cells were imaged in phenol-red free medium containing 1% FBS and the appropriate tonicity.

For DCP1A expression time course data (Figure S4D), U2OS cells were transfected with pGFP-DCP1A using Fugene HD. Transfected cells were imaged at 12, 24, 36, 48 and 72 hours after transfection to allow the expression level of the protein to build up. Cells were images under isotonic and hypertonic conditions at each time point to cover about 2-orders of magnitude of total GFP fluorescence intensity.

Cell viability assays. 100 μL of 10, 000 -20, 000 cells were seeded per well of a 96 well white bottom plate or 96 well transparent plate in regular growth medium. 24 h after seeding, cells were treated with appropriate isotonic or hypertonic medium. Cell growth and viability were measured on the 96 well white bottom plate as an end point measurement for each time point and/or treatment using the Cell-titer GLO assay (Promega, # G7570) based on manufacturer's instructions. 96 well transparent plates were fixed with 100% methanol at RT for 10 min, stained with crystal violet (0.5% in 20% methanol) for 20 min at RT, washed with water and photographed.

Immunofluorescence. Cells were grown on 8 well chambered coverglasses (Thermo-Fisher, # 155383PK), washed with PBS, formaldehyde fixed and permeablized using 0.5% Triton-X100 (Sigma, T8787-100ML) in 1x PBS at room temperature (RT) for 10 min. It is important that the tonicity of the wash buffer and fixative matched that of the cell medium. Cells were then treated with blocking buffer containing 5% normal goat serum (Jackson Immunoresearch, 005-000-121),

0.1% Tween-20 (Sigma, P9416-50ML) in 1x PBS at RT for 1 h. Primary antibodies (pA) were diluted in blocking buffer to appropriate concentrations and cells were treated with pA at RT for 1 h. Following three washes with the blocking buffer for 5 min each, cells were treated with secondary antibodies (sA) diluted in blocking buffer to appropriate concentrations. Then, following two washes with the blocking buffer and two washes with 1x PBS for 5 min each, cells were mounted in solution containing 10 mM Tris/HCl pH 7.5, 2 × SSC, 2 mM trolox, 50 μM protocatechiuc acid, and 50 nM protocatechuate dehydrogenase. Mounts were overlaid with mineral oil and samples were imaged immediately.

Combined IF and RNA fluorescence *in situ* hybridization. Following the final 1x PBS washes in the abovementioned IF protocol, cells were formaldehyde fixed and permeablized overnight at 4 ºC using 70% ethanol. Cells were rehydrated in a solution containing 10% formamide and 2 × SSC for 5 min and then treated with 100 nM Oligo-dT30-Cy5 (IDT) for 16 h in 2 × SSC containing 10% dextran sulfate, 2 mM vanadyl-ribonucleoside complex, 0.02% RNAse-free BSA, 1 μg μl−1 E. coli transfer RNA and 10% formamide at 37 °C. After hybridization, cells were washed twice for 30 min at 37 °C using a wash buffer (10% formamide in 2 × SSC). Cells were then mounted in solution containing 10 mM Tris/HCl pH 7.5, 2 × SSC, 2 mM trolox, 50 μM protocatechiuc acid, and 50 nM protocatechuate dehydrogenase. Mounts were overlaid with mineral oil and samples were imaged immediately.

Microscopy. Highly inclined laminated optical sheet (HILO) imaging was performed as described (Pitchiaya et al., 2012; Pitchiaya et al., 2013, Pitchiaya et al., 2017, Pitchiaya et al., 2019) using a cell-TIRF system based on an Olympus IX81 microscope equipped with a 60x 1.49 NA oil-immersion objective (Olympus), as well as 405 nm (Coherent ©, 100 mW at source, ~65

μW for imaging CB-Dex), 488 nm (Coherent ©, 100 mW at source, ~1.2 mW for imaging GFP), 561 nm (Coherent ©, 100 mW at source, ~50 μW for imaging mCh) and 640 nm (Coherent ©, 100 mW at source, 13.5 mW for imaging Cy5) solid-state lasers. Quad-band filter cubes consisting of z405/488/532/640rpc or z405/488/561/640rpc dichroic filters (Chroma) and z405/488/532/640m or z405/488/561/640m emission filters (Chroma) were used to filter fluorescence of the appropriate fluorophores from incident light. Emission from individual fluorophores was detected sequentially on an EMCCD camera (Andor IXon Ultra) for fixed cell imaging. For live cell imaging cells were seeded on Delta T dishes (Bioptechs, 04200417C) and imaged on a Bioptechs temperature control module (Bioptechs, 0420-4). High-throughput IF was performed on the same microscope using a 60x 0.9 NA air objective. The multi-well scanning mode in Metamorph®, the acquisition software, was used to control a motorized stage (MS-2000, Applied Scientific Instrumentation Inc.).

Image Analysis. For measuring the average GFP signal per cell, GFP intensity thresholds were set (Huang threshold in image J) to automatically identify cell boundaries. Background intensity, outside of cell boundaries, was subtracted from GFP signal to extract the background corrected GFP intensity within cells. The corrected intensity was then divided by the total number of thresholded (Huang threshold in image J) DAPI stained nuclei to extract the average GFP intensity per cell. For measuring the percentage of GFP signal within foci, images were first thresholded (percentage threshold in image J) to create masks of foci and the GFP intensity within this mask was calculated. Background corrected foci intensity was then divided by the background corrected GFP intensity within cells. Average number of foci per cell in IF images were identified using the find maxima function in image J. Briefly, a 5-pixel radius rolling ball was used to subtract the background from images, which were subsequently convolved with a 5x5 pixel kernel and a

2-pixel radius Gaussian blur function. These image processing steps enhanced the definition of a spot that were easy to identify with the find maxima function. The noise tolerance (or threshold value) in the find maxima function was maintained across samples that were compared. The total number of spots was then divided by the number of nuclei to calculate the mean spots per cell. Imaris was used for single particle tracking. Custom Matlab scripts were used to extract diffusion rates of the trajectories by fitting the mean squared displacement ($< r^2 >$) over the first five observation time windows to a line and extracting the slope. Diffusion rates (D) were then calculated as per the 2-D diffusion equation from

$$< r^2 > = 4 * D * t$$

The obtained logarithm of the obtained diffusion values was plotted as histograms in Origin which were then visualized as violin plots using custom scripts in Matlab. Final figures were assembled in Illustrator.

RNAseq and Bru-seq. For steady-state RNAseq, UGD cells were grown in 10 cm dishes, treated with the appropriate medium (isotonic, 150 mM Na^+ or hypertonic, 300 mM Na^+) and cells were harvested by scraping in RIPA buffer (Thermo-Fisher, PI89900). Total RNA was then extracted with QIAGEN RNeasy midi kit (Cat. No. 75144). RNA integrity was assessed using an Agilent Bioanalyzer. Each sample was sequenced in duplicated using the Illumina HiSeq 2000 (with a 100-nt read length). Strand-specific paired-end reads were then inspected for sequencing and data quality (for example, insert size, sequencing adaptor contamination, rRNA content, sequencing error rate). Libraries passing quality control were trimmed of sequencing adaptors and aligned to the human reference genome, GRCh38. Sample were demultiplexed into paired-end reads using Illumina's bcl2fastq conversion software v2.20. Reads were mapped onto hg38 human

reference genome using TopHat2. First the reference genome was indexed using bowtie2-build. Paired end reads were then aligned to the reference genome using TopHat2 with strand-specificity and allowing only for the best match for each read. Aligned file was used to calculate strand specific read count for each gene using bedtools multicov with -s option. A known genes gtf file downloaded from UCSC was used to calculate read count. Two additional bed files were created for each gene representing 10kb upstream and 10kb downstream of the TSS. For each gene, read count was calculated for its upstream and downstream region as well with strand-specificity. To estimate an RNA read-through event, we calculated the ratio of read count for 10kb downstream of TSS to 10kb upstream of TSS after normalizing it for gene expression and sequencing depth. A box plot was plotted for this normalized ratio for the three samples using R software and ggplot2 package. Evaluation of significance was performed using the student's t-test. The aligned bam file of the sample was converted into bigwig format using deepTools bamcoverage. The resultant bigwig file was uploaded onto IGV for viewing of the RNA read-through event.

For Bru-seq, UGD cells were grown on T75 flasks to >80% confluency. Flasks were washed once with fresh medium before bromouridine (BrU) treatment. BrU solution was diluted to a final concentration of 2 mM in McCoy's 5A medium containing 2% FBS containing 145 mM (isotonic) or 300 mM (hypertonic) monovalents. Cells were incubated in the appropriate bromouridine-containing media for 30 minutes. Cells treated with hypertonic media were allowed to recover in isotonic media for 30 minutes or 6 h in isotonic media before they were harvested. Nascent transcript libraries for Bru- and Bru-Chase seq were performed and sequenced as described (Paulsen et al, 2014).

Data from both RNAseq and Bru-seq were analyzed as follows. We identified the transcription end sites (TES) of genes by GENCODE annotation and defined a 10 kb region upstream (US) and downstream (DS) of each TES, especially for genes that did not have any neighboring gene DS within the 10 kb distance. We then computed reads per kilobase million (rpkm) values for these US and DS bins and computed a DS/US ratio.

Statistical analysis. Graphpad-Prizm and Origin were used for statistical analysis and plotting. For pairwise comparisons, p-values were calculated based on non-parametric unpaired t-tests with a Kolmogorov-Smirnov test. For comparisons involving more than 2 samples, one-way-ANOVA tests were used with a Geisser-Greenhouse correction.

Table 3-1 List of antibodies used in Chapter 3.

REAGENT or RESOURCE	SOURCE	IDENTIFIER
Rabbit anti DCP1A polyclonal	Bethyl	A303-591A
Mouse anti EDC4 monoclonal	Santa Cruz	sc-374211
Rabbit anti EDC4 polyclonal	Abcam	ab72408
Recombinant Anti-METTL3 antibody [EPR18810]	Abcam	ab195352
Recombinant Anti-RENT1/hUPF1 antibody [EPR4681]	Abcam	ab109363
Recombinant Anti-Nkx3.1 antibody [EPR16653]	Abcam	ab196020
Recombinant Anti-TDP43 antibody [EPR5810]	Abcam	ab109535
Recombinant Anti-FXR1 antibody [EPR7932]	Abcam	ab129089
Recombinant Anti-CPSF6 antibody [EPR12898]	Abcam	ab175237
Anti-PABP antibody	Abcam	ab21060
Anti-TIA1 antibody - C-terminal	Abcam	ab40693
Recombinant Anti-POT1 antibody [EPR6319]	Abcam	ab124784
Anti-RPS20 antibody produced in rabbit	Abcam	SAB4502698
Anti-Proteasome 20S alpha + beta antibody	Abcam	ab22673
Anti-SNF5/SMARCB1 antibody - ChIP Grade	Abcam	ab12167
Recombinant Anti-Telomerase reverse transcriptase antibody [Y182]	Abcam	ab32020
Anti-RNA polymerase II CTD repeat YSPTSPS (phospho S2) antibody - ChIP Grade	Abcam	ab5095
Recombinant Anti-ERG antibody [EPR3864]	Abcam	ab92513
Anti-EDC4 (N-terminal) antibody produced in rabbit	Sigma	SAB4200114
CNOT1 Antibody	Proteintech	14276-I-AP

Vimentin (D21H3) XP® Rabbit mAb	Cell signaling technol.	5741S
LC3A/B (D3U4C) XP® Rabbit mAb	Cell signaling technol.	12741S
Argonaute 2 (C34C6) Rabbit mAb	Cell signaling technol.	2897S
HIF-1α (D1S7W) XP® Rabbit mAb	Cell signaling technol.	36169S
Anti-eIF4G Antibody	Sigma	07-1800
MOV10 Antibody	Proteintech	10370-I-AP
CBP80 antibody [N1N2], N-term	Gene tech	GTX114570
Anti-RNA helicase A Abs	Vaxron	PA-001
TRF-2 Antibody	Novus biologicals	NB110-57130SS
Anti-IGF2BP3 (IMP3) (Human/Mouse) pAb	MBL	RN009P
c-Fos (9F6) Rabbit mAb	Cell signaling technol.	2250S
JunB (C37F9) Rabbit mAb	Cell signaling technol.	3753S
Anti-DUT antibody produced in rabbit	Atlas antibodies	HPA054422
ANTI-CDK12 antibody produced in rabbit	Sigma / atlas	HPA008038
DCP2 Polyclonal Antibody	Thermo	PA5-34455
GAPDH (14C10) Rabbit mAb	Cell signaling technol.	2118S
Anti-PAICS antibody produced in rabbit	Sigma / atlas	HPA035895
Anti-SORD antibody produced in rabbit	Sigma / atlas	HPA040260
β-Actin (13E5) Rabbit mAb	Cell signaling technol.	4970T
Hexokinase I (C35C4) Rabbit mAb	Cell signaling technol.	2024T
TIAR (D32D3) XP® Rabbit mAb	Cell signaling technol.	8509T
YB1 (D299) Antibody	Cell signaling technol.	4202S
YY1 (D5D9Z) Rabbit mAb	Cell signaling technol.	46395S
YAP (D8H1X) XP® Rabbit mAb	Cell signaling technol.	14074T
PFKL antibody [C1C3]	Gene tech	GTX105697
Monoclonal ANTI-FLAG® M2 antibody produced in mouse	Sigma	F1804
PKM2 (D78A4) XP® Rabbit mAb	Cell signaling technol.	4053T
hnRNP A1 (D21H11) Rabbit mAb	Cell signaling technol.	8443S
Estrogen Receptor α (D6R2W) Rabbit mAb	Cell signaling technol.	13258S
Anti-TARBP2 antibody produced in rabbit	Sigma	AV40512-100UL
Akt Antibody	Cell signaling technol.	9272S
Recombinant Anti-Cyclin A2 antibody [Y193]	Abcam	ab32386
Pan-Cadherin Antibody	Cell signaling technol.	4068S
ZC3HAV1 Polyclonal Antibody	Invitrogen	PA5-31650
Antibody against N6-methyladenosine modifications of RNA and DNA	synaptic systems	m6a-202003
METTL14 Antibody	Novus biologicals	NBP1-81392
Anti-ALKBH5 antibody produced in rabbit	Sigma / atlas	HPA007196
Anti-Dicer antibody [13D6] - ChIP Grade (ab14601)	Abcam	ab14601
HPRT Antibody (5F11A7)	Novus biologicals	NBP2-37245
LAMP1 (D4O1S) Mouse mAb #15665	Cell signaling technol.	15665S
Anti-CFTR antibody [CF3] (ab2784)	Abcam	ab2784
E-Cadherin (4A2) Mouse mAb #14472	Cell signaling technol.	14472S
Monoclonal Anti-IRX5 antibody produced in mouse	Sigma	WH0010265M1
Anti-GW182 antibody [4B6] - P/GW Body Marker (ab70522)	Abcam	ab70522
Human/Mouse/Rat Muscle Phosphofructokinase/PFKM Antibody	R&D systems	MAB7687
Monoclonal Anti-ALDOA antibody produced in mouse	Sigma	WH0000226M1
PCNA (PC10) Mouse mAb #2586	Cell signaling technol.	2586T

Purified Mouse Anti-Ki-67	BD	550609
α-Tubulin (DM1A) Mouse mAb #3873	Cell signaling technol.	3873S
TRBP Monoclonal Antibody (46D1)	thermo	LF-MA0209
Monoclonal Anti-p53 antibody produced in mouse	Sigma	P8999
UBTF Antibody	Novus biologicals	NBP1-82545
HSF1 Antibody #4356	Cell signaling technol.	4356T
Recombinant Anti-SAM68 antibody [EPR3232]	Abcam	ab109197
Anti-IRE1 (phospho S724) antibody (ab48187)	Abcam	ab48187
Anti-DCP1A antibody produced in rabbit	Sigma / atlas	HPA013202
Anti-Argonaute-2 Antibody	Sino biological	108621-T02
Anti-Argonaute-1 Antibody	MBL	RN028P
G3BP1 Polyclonal Antibody	Invitrogen	PA5-29455
RCAS1 (D2B6N) XP® Rabbit mAb #12290	Cell signaling technol.	12290P
Rab5 (C8B1) Rabbit mAb #3547	Cell signaling technol.	3547P
Caveolin-1 (D46G3) XP® Rabbit mAb #3267	Cell signaling technol.	3267P
Clathrin Heavy Chain (D3C6) XP® Rabbit mAb #4796	Cell signaling technol.	4796P
EEA1 (C45B10) Rabbit mAb #3288	Cell signaling technol.	3288P
Rab7 (D95F2) XP® Rabbit mAb #9367	Cell signaling technol.	9367P
Rab11 (D4F5) XP® Rabbit mAb #5589	Cell signaling technol.	5589P
Syntaxin 6 (C34B2) Rabbit mAb #2869	Cell signaling technol.	2869P
Calnexin (C5C9) Rabbit mAb #2679	Cell signaling technol.	2679P
ERp72 (D70D12) XP® Rabbit mAb #5033	Cell signaling technol.	5033P
PDI (C81H6) Rabbit mAb #3501	Cell signaling technol.	3501P
COX IV (3E11) Rabbit mAb #4850	Cell signaling technol.	4850S
Anti-HLA-DMB Antibody (HPA012298)	Sigma / atlas	HPA012298
CDK9 (C12F7) Rabbit mAb #2316	Cell signaling technol.	2316S
Recombinant Anti-Cyclin B1 antibody [Y106] (ab32053)	Abcam	ab32053
Androgen Receptor (D6F11) XP® Rabbit mAb #5153	Cell signaling technol.	5153S
Anti-NRG2 antibody	Abcam	ab220615
DDX6 Antibody, A300-460A	Bethyl	A300-460A
DCP1A Antibody, A303-591A	Bethyl	A303-591A
XRN1 Antibody, A300-443A	Bethyl	A300-443A
FUS Antibody	Novus biologicals	NB100-565
53BP1 Antibody	Novus biologicals	NB100-304
(sc-899) Pol II (N-20)	Santa Cruz	SC-899
Anti-phospho-Histone H2A.X (Ser139) Antibody, clone JBW301	Millipore	05-636
Anti-DNA-RNA Hybrid Antibody, clone S9.6	Sigma	MABE1095
Anti-TRF1 Antibody, clone BED5 57-6	Millipore	04-638
dc4 Antibody (F-1): sc-374211	Santa Cruz	SC-374211
NOSTRIN Antibody (F-10): sc-365031	Santa Cruz	SC-365031
Anti-Poly ADP-ribose Antibody, clone 10H	EMD-Sigma	MABC547
ERG (A7L1G) Rabbit mAb	Cell signaling technol.	97249S
rRNA Antibody (Y10b)	Novus biologicals	NB100-662SS
GW182 Antibody (4B6): sc-56314	Santa Cruz	SC-56314
Anti-v-H-Ras (Ab-1) Rat mAb (Y13-259)	CalboChem	OP01
Goat-anti-rabbit-Cy5	Jackson Immunolabs	111-175-144
Goat-anti-mouse-Cy5	Jackson Immunolabs	115-175-146

Table 3-2 List of plasmids used in Chapter 3.

REAGENT or RESOURCE	SOURCE	IDENTIFIER
pEGFP-C1	Clontech	Discontinued
pIRES2-EGFP-p53 WT	Lab of Dylan Taatjes	Addgene # 49242
pEGFP-hAgo2		
pPAICS-EGFP	Lab of Stephen Benkovic	Addgene # 99108
pcDNA3.2 TDP-43 YFP	Lab of Aaron Gitler	Addgene # 84911
pT7-EGFP-C1-HsDCP2	Lab of Elisa Izaurralde	Addgene # 25031
pEGFP-N1-FUS/TLS-FLAGC	Lab of Patrick Calsou	Addgene # 60362
pSICO-CPSF6-358-eGFP	Lab of Zandrea Ambrose	Addgene # 110693
FLHKIII-pGFPN3	Lab of Hossein Ardehali	Addgene # 21920
RNT1-GFP	Lab of Hal Dietz	Addgene # 17708
pmyc-GFP-TNRC6A	Lab of Kumiko Ui-Tei	Addgene # 41999
pEGFP-C1-PKM2	Lab of Axel Ulrich	Addgene # 64698
pEGFP-Nck1	Lab of Louise Larose	Addgene # 45903
pT7-EGFP-C1-HsNot1	Lab of Elisa Izaurralde	Addgene # 37370
pIRES2-EGFP-Rac2	Lab of Gary Johnson	Addgene # 12193
pLPS-hAKT1-GFP	Lab of Randall McKinnon	Addgene # 49388
IRE1 alpha-pcDNA3.EGFP	Lab of Fumihiko Urano	Addgene # 13009
HSF1-GFPN3	Lab of Stuart Calderwood	Addgene # 32538
EGFP-Actin-7	Lab of Michael Davidson	Addgene # 56421
GFP-UB	Lab of Nico Dantuma	Addgene # 11928
pEGFP-C1-Dcp1a	Pitchiaya et al. 2019	N/A
pmRFP1-Dcp1a	Nancy Kedersha	N/A
pcDNA5/FRT/TO/FLGA-tGFP-HuR.WT	Lab of Sandra Martha Gomes Dias	Addgene # 110376
pcDH-Halo-DCP1a	This study	
pcDH-CLIP-DCP1a	This study	
pcDH-mCherry-DCP1a	This study	
pcDH-SNAP-DCP1a	This study	
pcDH-GFP-DCP1a	This study	
pEGFP-DCP1a (1-380)	Aizer et al. 2012	N/A
pEGFP-DCP1a (380-582)	Aizer et al. 2012	N/A

Table 3-3 Reagents referenced in Chapter 3.

REAGENT or RESOURCE	SOURCE	IDENTIFIER
Antibodies		
Information about 112 antibodies used in this study are listed in Table S1		
Chemicals, Peptides, and Recombinant Proteins		
MAP Kinase Inhibitor SP100025	Invivogen	tlrl-sp60
Okadaic acid, sodium salt	EMD Millipore	459620-25UG
DiI stain	Thermo-Fisher	D3911
Sodium (meta) Arsenite	Sigma	S7400-100G
JaneliaFluor 549 HaloTag ligand	Promega	GA1110
CLIP-Cell 505 ligand	NEB	S9217S
SNAP-Cell 647-SiR	NEB	S9102S
Crystal Violet (Certified Biological Stain)	Thermo-Fisher	C581-100
Critical Commercial Assays		
Fugene HD	Promega	E2311
Lipofectamine 2000	Thermo-Fisher	11668027
CellTiter-Glo® Luminescent Cell Viability Assay	Promega	G7570
Deposited Data		
Raw and analyzed data	This work	N/A
Experimental Models: Cell Lines		
Human: U2-OS	ATCC	HTB-96
Human: HK-2	ATCC	CRL-2190
Human: Caki-1	ATCC	HTB-46
Human: MCF7	ATCC	CRL-5803
Human: H1299	ATCC	HTB-22
Human: U2-OS stably expressing GFP-Dcp1a (UGD)	Pitchiaya *et al*, 2019	N/A
Oligonucleotides		
Ambion negative control siRNA 1	Thermo-Fisher	AM4611
siRNA targeting EDC4 SMARTPool (siEDC4)	Dharmacon	M-016635-00-0005
Recombinant DNA		
Information about 30 plasmids used in this study are listed in Table S2		
Software and Algorithms		
MATLAB 8.3	The Mathworks Inc.	R2014a
Prizm 7.04	GraphPad	Prizm 7.04
Origin 2018	OriginLab	Origin 2018
Imaris 9.1.0	Bitplane AG	Imaris 9.1.0
Fiji	ImageJ/NIH	Fiji
Custom MATLAB routines	This work	N/A
Custom Image J macros	This work	N/A
Bacterial and viral strains		
XL10-Gold Ultracompetent Cells	Agilent	200315

3.5. References

Aizer, A., Brody, Y., Ler, L.W., Sonenberg, N., Singer, R.H., and Shav-Tal, Y. (2008). The dynamics of mammalian P body transport, assembly, and disassembly in vivo. Mol. Biol. Cell *19*, 4154-4166.

Aizer, A., Kafri, P., Kalo, A., and Shav-Tal, Y. (2013). The P body protein Dcp1a is hyper-phosphorylated during mitosis. PlOS One *8*, e49783.

Alberti, S. (2017). Phase separation in biology. Curr. Biol. *27*, R1097-R1102.

Alberti, S., Gladfelter, A., and Mittag, T. (2019). Considerations and Challenges in Studying Liquid-Liquid Phase Separation and Biomolecular Condensates. Cell *176*, 419-434.

Anderson, P., and Kedersha, N. (2009). RNA granules: post-transcriptional and epigenetic modulators of gene expression. Nat. Rev. Mol. Cell Biol. *10*, 430-436.

Ball, P. (2017). Water is an active matrix of life for cell and molecular biology. Proc. Natl. Acad. Sci. U.S.A. *114*, 13327-13335.

Banani, S.F., Lee, H.O., Hyman, A.A., and Rosen, M.K. (2017). Biomolecular condensates: organizers of cellular biochemistry. Nat. Rev. Mol. Cell Biol. *18*, 285-298.

Berchtold, D., Battich, N., and Pelkmans, L. (2018). A Systems-Level Study Reveals Regulators of Membrane-less Organelles in Human Cells. Mol. Cell *72*, 1035-1049 e1035.

Boeynaems, S., Alberti, S., Fawzi, N.L., Mittag, T., Polymenidou, M., Rousseau, F., Schymkowitz, J., Shorter, J., Wolozin, B., Van Den Bosch, L.*, et al.* (2018). Protein Phase Separation: A New Phase in Cell Biology. Trends Cell Biol. *28*, 420-435.

Bounedjah, O., Hamon, L., Savarin, P., Desforges, B., Curmi, P.A., and Pastre, D. (2012). Macromolecular crowding regulates assembly of mRNA stress granules after osmotic stress: new role for compatible osmolytes. J. Biol. Chem. *287*, 2446-2458.

Boyd-Shiwarski, C.R., Shiwarski, D.J., Roy, A., Namboodiri, H.N., Nkashama, L.J., Xie, J., McClain, K.L., Marciszyn, A., Kleyman, T.R., Tan, R.J.*, et al.* (2018). Potassium-regulated distal tubule WNK bodies are kidney-specific WNK1 dependent. Mol. Biol. Cell *29*, 499-509.

Brocker, C., Thompson, D.C., and Vasiliou, V. (2012). The role of hyperosmotic stress in inflammation and disease. Biomol. Concepts *3*, 345-364.

Cai, D., Sukenik, S., Feliciano, D., Gruebele, M., and Lippincott-Schwartz, J. (2018). Phase Separation of YAP reorganizes genome topology for long-term YAP target gene expression. Nat. Cell Biol. 21, 1578–1589.

Cardiello, J.F., Goodrich, J.A., and Kugel, J.F. (2018). Heat Shock Causes a Reversible Increase in RNA Polymerase II Occupancy Downstream of mRNA Genes, Consistent with a Global Loss in Transcriptional Termination. Mol. Cell Biol. *38*, e00181-00118.

Daher, M., Widom, J.R., Tay, W., and Walter, N.G. (2018). Soft Interactions with Model Crowders and Non-canonical Interactions with Cellular Proteins Stabilize RNA Folding. J. Mol. Biol. *430*, 509-523.

Delarue, M., Brittingham, G.P., Pfeffer, S., Surovtsev, I.V., Pinglay, S., Kennedy, K.J., Schaffer, M., Gutierrez, J.I., Sang, D., Poterewicz, G.*, et al.* (2018). mTORC1 Controls Phase Separation and the Biophysical Properties of the Cytoplasm by Tuning Crowding. Cell *174*, 338-349.e320.

Elkon, R., Ugalde, A.P., and Agami, R. (2013). Alternative cleavage and polyadenylation: extent, regulation and function. Nat. Rev. Genet. *14*, 496-506.

Guo, L., and Shorter, J. (2015). It's Raining Liquids: RNA Tunes Viscoelasticity and Dynamics of Membraneless Organelles. Mol. Cell *60*, 189-192.

Guo, M., Pegoraro, A.F., Mao, A., Zhou, E.H., Arany, P.R., Han, Y., Burnette, D.T., Jensen, M.H., Kasza, K.E., Moore, J.R.*, et al.* (2017). Cell volume change through water efflux impacts cell stiffness and stem cell fate. Proc. Natl. Acad. Sci. U. S. A. *114*, E8618-E8627.

Hancock, R. (2004). A role for macromolecular crowding effects in the assembly and function of compartments in the nucleus. J. Struct. Biol. *146*, 281-290.

Hersen, P., McClean, M.N., Mahadevan, L., and Ramanathan, S. (2008). Signal processing by the HOG MAP kinase pathway. Proc. Natl. Acad. Sci. U. S. A. *105*, 7165-7170.

Hubstenberger, A., Courel, M., Benard, M., Souquere, S., Ernoult-Lange, M., Chouaib, R., Yi, Z., Morlot, J.B., Munier, A., Fradet, M.*, et al.* (2017). P-Body Purification Reveals the Condensation of Repressed mRNA Regulons. Mol. Cell *68*, 144-157 e145.

Huch, S., and Nissan, T. (2017). An mRNA decapping mutant deficient in P body assembly limits mRNA stabilization in response to osmotic stress. Sci. Rep *7*, 44395.

Hyman, A.A., Weber, C.A., and Julicher, F. (2014). Liquid-liquid phase separation in biology. Ann Rev Cell Dev Biol *30*, 39-58.

Jain, S., Wheeler, J.R., Walters, R.W., Agrawal, A., Barsic, A., and Parker, R. (2016). ATPase-Modulated Stress Granules Contain a Diverse Proteome and Substructure. Cell *164*, 487-498.

Jensen, T.R., Ostergaard Jensen, M., Reitzel, N., Balashev, K., Peters, G.H., Kjaer, K., and Bjornholm, T. (2003). Water in contact with extended hydrophobic surfaces: direct evidence of weak dewetting. Phys. Rev. Lett. *90*, 086101.

Kedersha, N., Stoecklin, G., Ayodele, M., Yacono, P., Lykke-Andersen, J., Fritzler, M.J., Scheuner, D., Kaufman, R.J., Golan, D.E., and Anderson, P. (2005). Stress granules and processing bodies are dynamically linked sites of mRNP remodeling. J. Cell Biol. *169*, 871-884.

Khong, A., Matheny, T., Jain, S., Mitchell, S.F., Wheeler, J.R., and Parker, R. (2017). The Stress Granule Transcriptome Reveals Principles of mRNA Accumulation in Stress Granules. Mol. Cell *68*, 808-820 e805.

Lang, F., Busch, G.L., Ritter, M., Volkl, H., Waldegger, S., Gulbins, E., and Haussinger, D. (1998). Functional significance of cell volume regulatory mechanisms. Physiol. Rev. *78*, 247-306.

Liu, P., Huang, X., Zhou, R., and Berne, B.J. (2005). Observation of a dewetting transition in the collapse of the melittin tetramer. Nature *437*, 159-162.

Marenduzzo, D., Finan, K., and Cook, P.R. (2006). The depletion attraction: an underappreciated force driving cellular organization. J. Cell Biol. *175*, 681-686.

Miermont, A., Waharte, F., Hu, S., McClean, M.N., Bottani, S., Leon, S., and Hersen, P. (2013). Severe osmotic compression triggers a slowdown of intracellular signaling, which can be explained by molecular crowding. Proc. Natl. Acad. Sci. U. S. A. *110*, 5725-5730.

Minton, A.P. (2001). The influence of macromolecular crowding and macromolecular confinement on biochemical reactions in physiological media. J. Biol. Chem. *276*, 10577-10580.

Muschol, M., and Rosenberger, F. (1997). Liquid-liquid phase separation in supersaturated lysozyme solutions and associated precipitate formation/crystallization. J. Chem. Phys. *107*, 1953-1962.

Nilsson, D., and Sunnerhagen, P. (2011). Cellular stress induces cytoplasmic RNA granules in fission yeast. RNA (New York, NY) *17*, 120-133.

Nott, T.J., Petsalaki, E., Farber, P., Jervis, D., Fussner, E., Plochowietz, A., Craggs, T.D., Bazett-Jones, D.P., Pawson, T., Forman-Kay, J.D.*, et al.* (2015). Phase transition of a disordered nuage protein generates environmentally responsive membraneless organelles. Mol. Cell *57*, 936-947.

Patel, A., Lee, H.O., Jawerth, L., Maharana, S., Jahnel, M., Hein, M.Y., Stoynov, S., Mahamid, J., Saha, S., Franzmann, T.M.*, et al.* (2015). A Liquid-to-Solid Phase Transition of the ALS Protein FUS Accelerated by Disease Mutation. Cell *162*, 1066-1077.

Paulsen, M.T., Veloso, A., Prasad, J., Bedi, K., Ljungman, E.A., Magnuson, B., Wilson, T.E., and Ljungman, M. (2014). Use of Bru-Seq and BruChase-Seq for genome-wide assessment of the synthesis and stability of RNA. Methods *67*, 45-54.

Perez-Bercoff, A., Makino, T., and McLysaght, A. (2010). Duplicability of self-interacting human genes. BMC Evol. Biol. *10*, 160.

Pitchiaya, S., Mourao, M.D.A., Jalihal, A.P., Xiao, L., Jiang, X., Chinnaiyan, A.M., Schnell, S., and Walter, N.G. (2019). Dynamic Recruitment of Single RNAs to Processing Bodies Depends on RNA Functionality. Mol. Cell *74*, 521-533 e526.

Shin, Y., and Brangwynne, C.P. (2017). Liquid phase condensation in cell physiology and disease. Science (New York, NY) *357*, 1253.

Spector, D.L. (2006). SnapShot: Cellular bodies. Cell *127*, 1071.

Sukenik, S., Salam, M., Wang, Y., and Gruebele, M. (2018). In-Cell Titration of Small Solutes Controls Protein Stability and Aggregation. J. Am. Chem. Soc. *140*, 10497-10503.

Toretsky, J.A., and Wright, P.E. (2014). Assemblages: functional units formed by cellular phase separation. J. Cell Biol. *206*, 579-588.

Tzur, A., Kafri, R., LeBleu, V.S., Lahav, G., and Kirschner, M.W. (2009). Cell growth and size homeostasis in proliferating animal cells. Science (New York, NY) *325*, 167-171.

Van Treeck, B., and Parker, R. (2018). Emerging Roles for Intermolecular RNA-RNA Interactions in RNP Assemblies. Cell *174*, 791-802.

Vilborg, A., Passarelli, M.C., Yario, T.A., Tycowski, K.T., and Steitz, J.A. (2015). Widespread Inducible Transcription Downstream of Human Genes. Mol. Cell *59*, 449-461.

Walter, H., and Brooks, D.E. (1995). Phase separation in cytoplasm, due to macromolecular crowding, is the basis for microcompartmentation. FEBS Lett. *361*, 135-139.

Walter, N.G. (2019). Biological Pathway Specificity in the Cell-Does Molecular Diversity Matter? BioEssays *41*, e1800244.

Wang, J., Choi, J.M., Holehouse, A.S., Lee, H.O., Zhang, X., Jahnel, M., Maharana, S., Lemaitre, R., Pozniakovsky, A., Drechsel, D.*, et al.* (2018). A Molecular Grammar Governing the Driving Forces for Phase Separation of Prion-like RNA Binding Proteins. Cell *174*, 688-699 e616.

Watkins, S., and Sontheimer, H. (2011). Hydrodynamic cellular volume changes enable glioma cell invasion. J. Neurosci. *31*, 17250-17259.

Wheeler, J.R., Matheny, T., Jain, S., Abrisch, R., and Parker, R. (2016). Distinct stages in stress granule assembly and disassembly. eLife *5*, e18413.

Wilson, E.B. (1899). The structure of protoplasm. Science *10*, 33-45.

Wu, C.C., Zinshteyn, B., Wehner, K.A., and Green, R. (2019). High-Resolution Ribosome Profiling Defines Discrete Ribosome Elongation States and Translational Regulation during Cellular Stress. Mol. Cell *73*, 959-970 e955.

Zlotek-Zlotkiewicz, E., Monnier, S., Cappello, G., Le Berre, M., and Piel, M. (2015). Optical volume and mass measurements show that mammalian cells swell during mitosis. J. Cell Biol. *211*, 765-774.

Chapter 4. Higher-Order Assembly Facilitates 3D mRNA Target Search by microRNAs in Cells[4]

4.1. Abstract

The ability of mammalian microRNAs to regulate mRNA translation and stability is dependent on recognition of and binding to partially complementary microRNA response elements (MREs). Conserved microRNA targets are known to contain multiple MRE copies for the same microRNA. While the relationship between MRE number and mRNA repression has been studied, the extent and role of stoichiometric microRNA-mRNA binding and competition during microRNA target search remains unresolved. Here we present a live cell, single-molecule tracking approach to study microRNA-mRNA binding interactions in real-time. We observe that microRNAs predominantly use three-dimensional diffusion to search for and interrogate mRNAs, probing each mRNA many times but only rarely associating stably. We also observe MRE-number and AGO2-dependent higher-order assembly of mRNAs, suggesting a mechanism by which microRNAs can enhance the efficiency of target repression by reducing the target search space. Taken together, these observations suggest that the RISC machinery uses multivalent protein-RNA interactions to facilitate rapid search and resource-efficient repression of target mRNAs bearing multiple MREs.

[4] This work was done with Dr. Hui Li who performed all injection experiments. A.P.J. was involved in experimental design and performed all data analysis.

4.2. Introduction

MicroRNAs regulate protein translation by tuning the stability and translation of eukaryotic mRNAs (Bartel, 2018; Bushati and Cohen, 2007; Pasquinelli and Ruvkun, 2002). To carry out these tasks, microRNAs recruit RNA-induced silencing complexes (RISC) to sites of partial complementarity to microRNAs in the mRNA 3' UTR referred to as microRNA response elements (MREs).

The first step in the process of regulation is the process of target search. In vitro work has revealed a detailed paradigm of target search, which is now understood to occur in two phases. Upon diffusion-limited encounter of an mRNA, the miRNA first non-specifically probes the sequence to find sites of complementarity to the first three nucleotides of the microRNA, using a combination of 1-dimensional ("sliding") search and 3-dimenional ("hopping") search, involving rapid dissociation and re-association (Cui and Joo, 2019). The second phase involves stabilization of AGO2 binding to the mRNA upon encountering an MRE (Flores-Jasso et al., 2013; Salomon et al., 2015; Wee et al., 2012). Since any given target mRNA species can contain multiple MREs, it remains unclear what the role of multiple, often highly conserved, MREs is in this target search process (Arvey et al., 2010; Denzler et al., 2014b; Denzler et al., 2016; Smillie et al., 2018). While the number of MREs has been demonstrated to impact the overall level of repression of such transcripts, and the spacing between MREs has been shown to influence cooperative RISC binding, the role of MRE number in target miRNA occupancy remains unclear (Denzler et al., 2016). Additionally, the evidence for this search paradigm is primarily supported by data from in vitro experiments. It is unclear how these search modes play out inside the cell, whose interior is characterized by an abundance of diverse RNA-binding proteins and molecular crowding (Daher

et al., 2018b; Gehring et al., 2017; Gerstberger et al., 2014; Hafner et al., 2010; Matsuda et al., 2014; Schnell and Turner, 2004; Zhou et al., 2008).

The miRNA target search process in the cell is expected to be confounded by the small numbers of target MREs relative to the large sequence search space, consisting of all accessible RNAs in the cytosol, for any given microRNA (Arvey et al., 2010; Bosson et al., 2014b; Denzler et al., 2016). Additionally, it has been shown that artificially increasing the number of MREs in a cell to very high levels can lead to sponging effects, where microRNAs will bind to the most abundant transcripts, and transcripts of lower abundance will experience decreased repression. This has been coined the competitive endogenous RNA (ceRNA) hypothesis, which posits that endogenous RNAs compete for a limiting pool of functional RISC complexes, and the level of expression of individual competitor transcripts can impact repression of other transcripts (Broderick and Zamore, 2014; Thomson and Dinger, 2016).

Recent work on intracellular macromolecular condensation is starting to unravel the widespread and dynamic relationship between subcellular spatial organization and RNA/protein sequence features (Langdon and Gladfelter, 2018b; Ma and Mayr, 2018). Emerging evidence suggests that RISC components are capable of forming higher-order assemblies by phase-separation (Sheu-Gruttadauria and MacRae, 2018). Additionally, miRNA-interactions impact the localization of target transcripts to membraneless-organelles such as P-bodies (Pitchiaya et al., 2019b). However, the mechanistic relevance of such assembly to miRNA target search and target repression in vivo remains unclear.

Here we introduce a live cell two-color RNA imaging approach to study miRNA-mRNA interactions in living cells. Using this assay, we observe dynamic, MRE-dependent colocalizations

between fluorescently labeled mRNAs and microRNAs. We observe an MRE-number dependent increase in both the degree and stability of colocalization and an MRE-number dependent clustering of mRNAs that is AGO2-dependent. We next investigate the hypothesis that clustering promotes RISC function by using a computational approach to compare the mRNA occupancy predicated by different modes of miRNA binding. We find that such clustering enhances target binding while allowing transcripts to be sub-stoichiometrically occupied by RISC. We conclude that microRNAs primarily use 3D diffusion to probe for MREs and exploit multivalent interactions to facilitate target clustering that preserves silencing under high binding competition.

4.3. Results

4.3.1. Intracellular tethering aids visualization of mRNA-microRNA interactions

To visualize intracellular microRNA-mRNA interactions we modified previously described chemical RNA labeling and microinjection-based single-molecule live cell imaging assays (Custer and Walter, 2017; Pitchiaya et al., 2012; Pitchiaya et al., 2014; Pitchiaya et al., 2017b). Labeled double-stranded miR-21 (m21-Cy5/m21*) was co-injected with in vitro transcribed, fluorescently labeled firefly luciferase mRNA with 11 seed matched miR-21 MREs (FL-11x-m21) (Figure 4-1A). Injected RNAs appeared as bright diffraction-limited spots that could be tracked yielding trajectories that were 0.1 to > 10 s. These tracks showed widespread and dynamic colocalizations 2-3 hours after injection (Figure 4-1B).

We explored the possibility of using molecular tethers to slow down mRNA diffusion and therefore prolong mRNA tracking via 3’ biotinylation of mRNAs downstream of the polyA tail (Figure 4-1A). Previous studies have reported mRNA tethering to the plasma membrane and ER

membrane for live cell single mRNA tracking (Wu et al., 2016; Yan et al., 2016). We investigated the possibility of tethering mRNAs to actin filaments based on evidence that both translating and translationally-silenced mRNAs have been reported to localize to actin (Eberhardt et al., 2016; Stebbings, 2001; Wu et al., 2016). To facilitate mRNA localization to actin, biotinylated Phalloidin (bPh), a mycotoxin known to bind and stabilize filamentous actin filaments was added to the injectate with the aim of tethering mRNAs to intracellular actin (Wu et al., 2016). The presence of the SA-bPh tether significantly extended mRNAs track lengths (Figure 4-1C). The mean track length of mRNA spots showed an increase from 1.6s (11,784 trajectories, 9 cells) without the tethering components to 2.2 s (17,289 trajectories, 9 cells) with streptavidin and biotin-phalloidin. We also observed that track length increased in the presence of streptavidin and biotin, suggesting that streptavidin-mediated mRNA crosslinking may partially contribute to this increase in tracking length. The tethering reagents showed a smaller effect on microRNA track length distribution (Figure 4-2A). Further, cells injected with the tethering mixture showed significantly more colocalization (29%) compared to cells without streptavidin (18%) (Figure 4-1D). Finally, the distribution of diffusion rates, calculated using mean squared displacement analysis and spot intensities of mRNA and miRNA spots, were not significantly different in the presence of the tethering mixture for either microRNA or mRNA spots (Figure 4-2C-D). Finally, a 5-pixel shift in one channel relative to the other (Mellis et al., 2017) decreased colocalization from >15% to ≤5% in all the cases suggesting that even the non-specific interactions represented biological events rather than chance, density-dependent colocalizations (Figure 4-2B).

Because the presence of tethering components significantly increased our ability to visualize colocalization events along with an increase in mRNA track length, we continued to use the SA-bPh tether in all subsequent experiments.

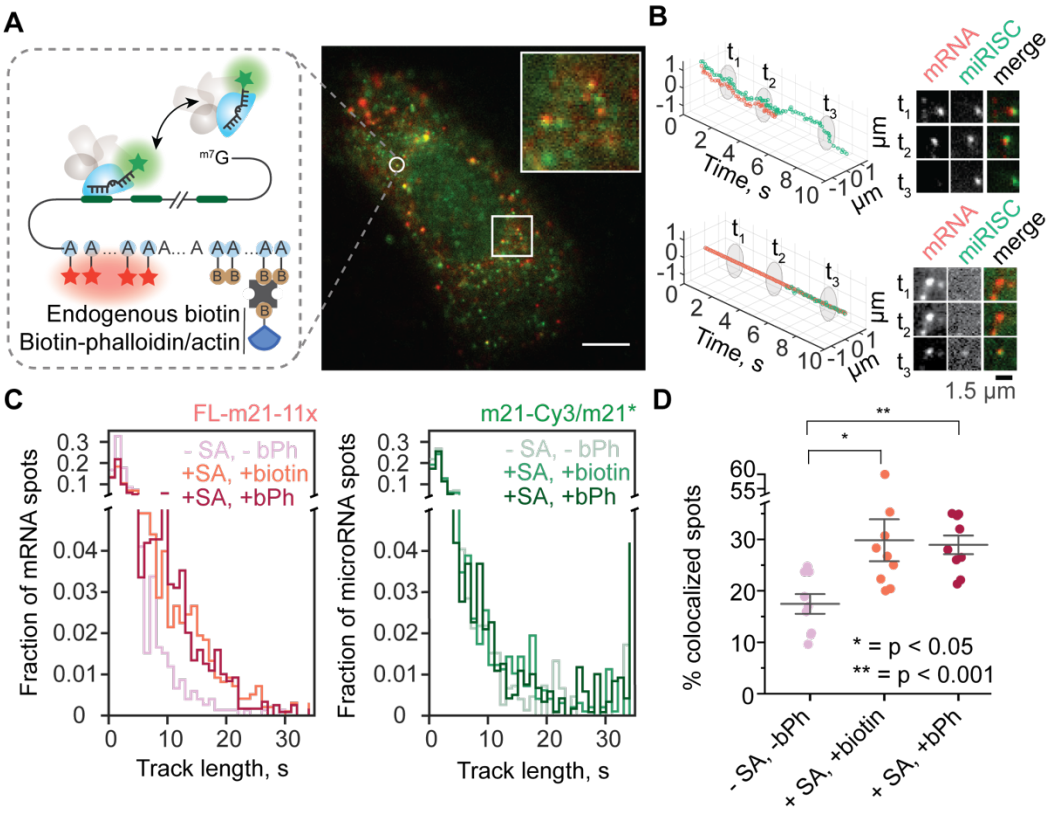

Figure 4-1 Intracellular tethering extends visualization of dynamic mRNA:miRISC interactions. (**A**) Schematic (left) depicting the mRNA labeling strategy and the use of the streptavidin+biotin/biotin-phalloidin tethering mixture to immobilize labeled, injected mRNA co-injected with double-stranded microRNA 3' labeled on the guide strand. Pseudocolored composite image (right) of U2OS cell showing mRNA spots (red) and microRNA spots (green). Inset shows colocalized spots. Scale bar represents 10 µm. (**B**) Two representative trajectories of colocalized microRNA (green) and a rapidly diffusing (top) and slowly diffusing mRNAs (red), showing three arbitrarily chosen frames, labeled t_1, t_2, t_3. Insets (right) show spot images at the selected frames. (**C**) Histogram of track lengths of mRNA bearing 11 miR21 binding sites and miR21 without tethering components, with SA and biotin, and with SA and biotin-phalloidin. (**D**) Percentage of total tracked spots that were found to be colocalized under different tethering conditions depicted in (C). * $p < 0.05$, ** $p < 0.001$ by unpaired Student's t test.

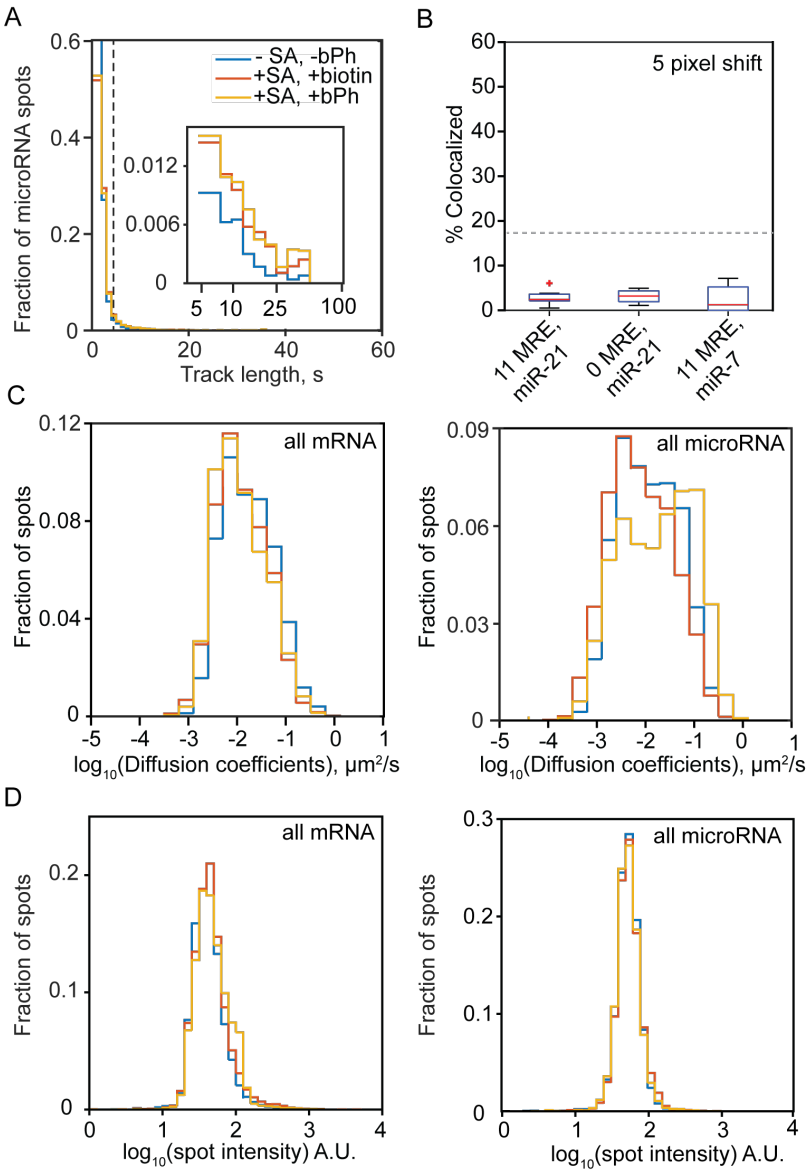

Figure 4-2 Tethering mixture does not influence microRNA tracks or other mRNA observables. (**A**) microRNA track length distribution (**B**) mRNA-microRNA inter-spot distance is slightly stabilized in the presence of streptavidin. (**C**) Diffusion coefficients of spots derived from MSD analysis. (**D**) Spot intensities of mRNA(left) and microRNA (right)

4.3.2. miRNA-mRNA interactions are stabilized by MRE number

Having established that the presence of the tethering mixture allowed us to observe long term, dynamic miRNA-mRNA colocalizations, we applied this method to detect differences in specific and non-specific miRNA-mRNA interactions (Chandradoss et al., 2015). mRNAs bearing 11 seed-matched MREs for miR-21 (FL-11x-m21) or no MREs (FL) were co-injected with labeled

miR-21. Non-specific interactions are expected to be proportional to the length of the transcript. To control for the length of the mRNA, the colocalizations obtained in these two conditions were compared with colocalizations between 11 MRE and a non-specific microRNA miR-7 that is not endogenously expressed in U2OS cells. We observed miRNA-mRNA colocalizations across all three combinations, although there were significantly more total colocalizations per cell between 11 MRE and miR-21 (Figure 4-3A).

The inter-spot distance amongst such spot pairs showed dynamic changes over time and high variability between pairs of spots in all these conditions. A histogram of inter-spot distance of proximal mRNA-microRNA spots (spot centers <5 px away) showed a single peak < 1.2 pixels (~150 nm) and a thick tail. Based on the position of the peak, we classified the inter-spot distance traces of proximal spots into regions of "colocalized" and "non-colocalized" states to include only those that showed an inter-spot center distance of <1.2 pixels (Figure 4-3B, 4-4). With this definition, we determined the fraction of total mRNA spots colocalized with a microRNA spot for at least one frame (0.1 s).

For each pair of proximal mRNA-microRNA spots, inter-spot distance traces were classified into "colocalized" and "non-colocalized" states by imposing the colocalization threshold of 1.2 pixels derived from distance histograms (Figure 4-3C). Dwell times in the colocalized and non-colocalized state from all spot-pairs from a condition were pooled and cumulative dwell time distributions were fit to exponentials to mean time to dissociation (t_{bound}) and association ($t_{unbound}$) (Figure 4-3D, 4-5). A comparison of the dwell times of the microRNAs with the respective mRNA constructs showed similar t_{bound} in all three cases, the $t_{unbound}$ for the 11 MRE transcript was

significantly higher than those for the 0 MRE or control microRNA miR-7, suggesting that specific interactions lasted longer than non-specific colocalizations (Figure 4-3D).

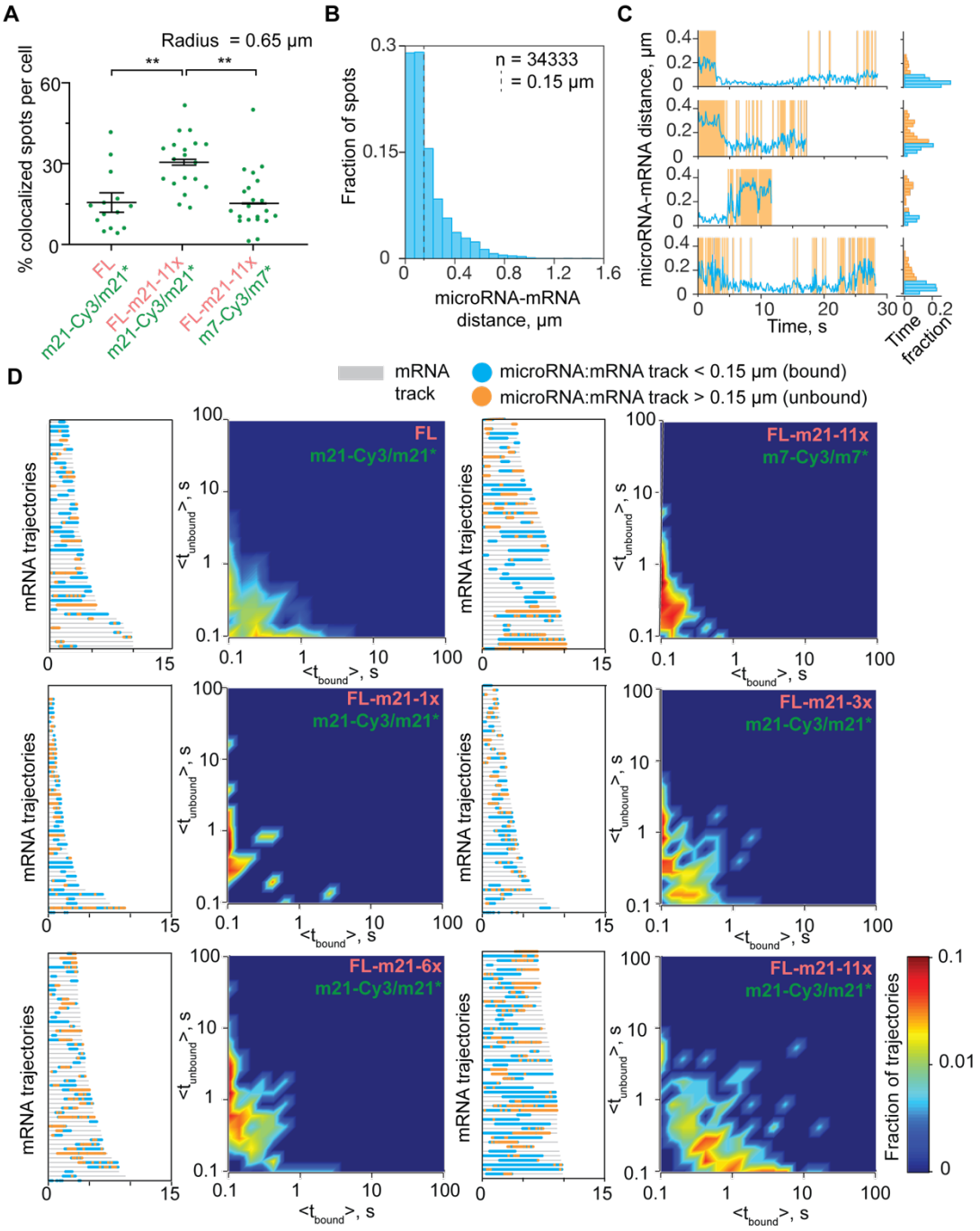

Figure 4-3 miRISC:mRNA colocalization and interaction stability increases with MRE number (**A**) Fraction of spots colocalized (d < 5 px ~ 0.65 μm) between FL and miR-21, FL with 11 miR-21 MREs and miR-21 and FL with 11x miR-21 MREs and miR-7. ** represents p value < 0.01 by unpaired Student's t test. (**B**) Histogram of aggregate

pairwise inter-spot distances of traces found to be colocalized (d < 0.65 μm) for at least one frame. Dotted line represents d = 0.15 μm. (**C**) Representative microRNA-mRNA inter-spot distance traces and corresponding distance histograms. Orange bars represent d > 0.15 μm (unbound, orange bars), white regions represent d ≤ 0.15 μm (bound, blue bars). (**D**) Fifty longest idealized distance traces, colored by bound or unbound states and corresponding aggregate dwell time histograms for 6 miRNA/mRNA pairs with increasing MRE numbers: FL with miR-21, 11xmiR-21 with miR-7 (n = 107 spots), 1x (n = 59 spots), 3x (n = 266 spots), 6x (n = 490 spots) and 11x (n = 764 spots) miR-21 MREs with miR-21. Data was obtained from > 10 cells for each condition.

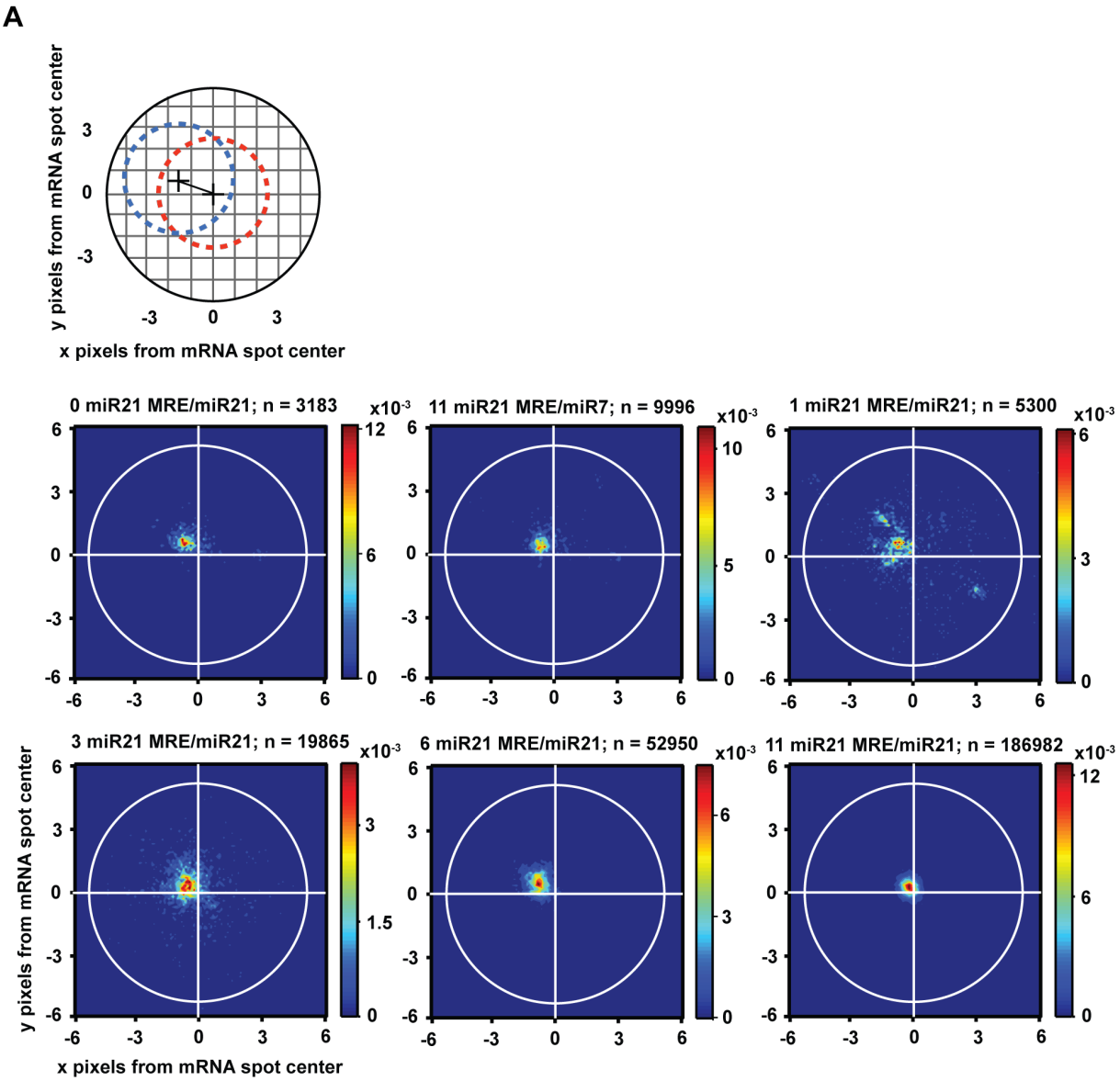

Figure 4-4 Colocalized miRNAs are stabilized close to the mRNA by MRE number. A schematic representation of the spatial distribution of the miRNA, denoted by "+" around a mRNA spot center on a 10x10 pixel grid (top). Increasing MRE numbers (0 and 11 m21 with miR7, 1, 3, 6, 11) decreases the spread of miRNA localization around the mRNA spot center.

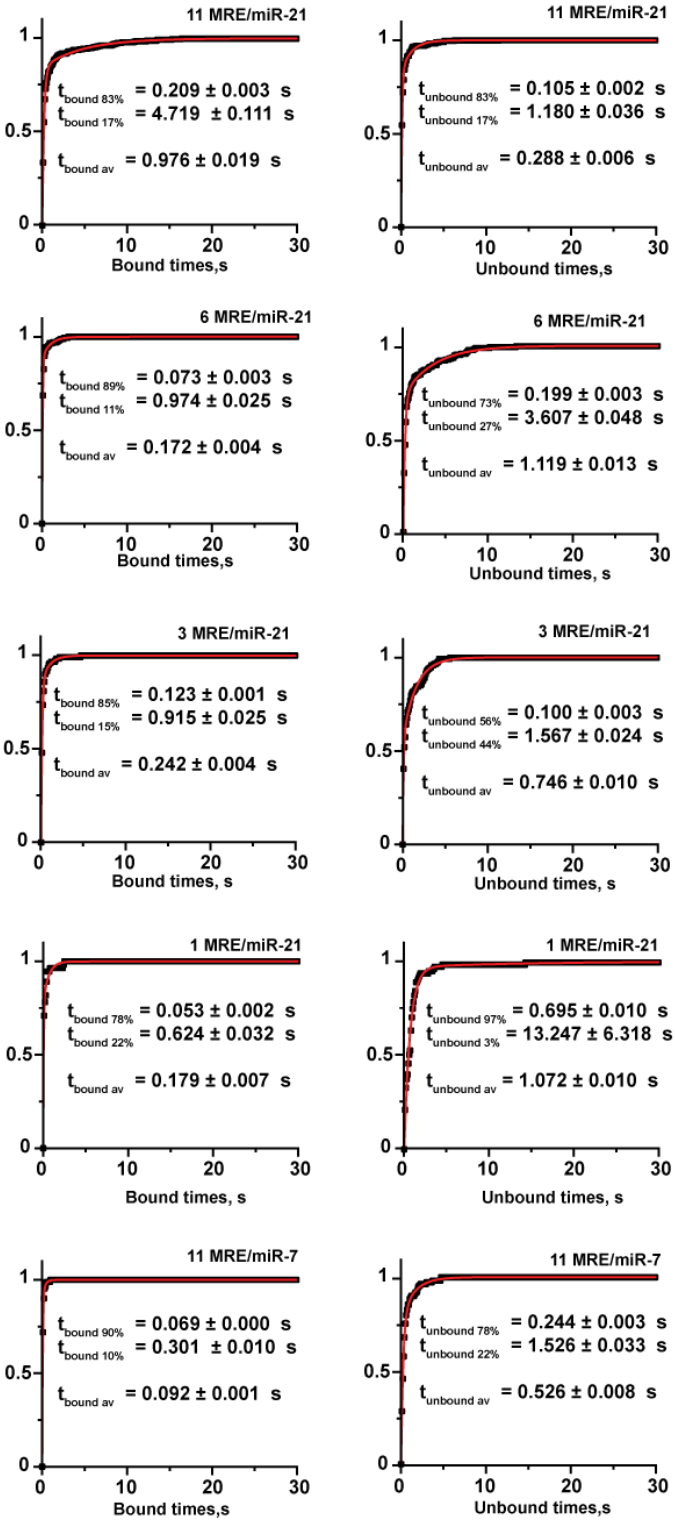

Figure 4-5 Bound and unbound dwell time cumulative histograms. Histograms were fit to double exponentials to extract mean dwell times.

We next investigated the relationship between MRE number and the stability of microRNA colocalization. Labeled mRNA constructs bearing 1, 3 and 6 MREs were co-injected with labeled miR-21. We observed a concomitant increase in the number and duration of close colocalizations of miR-21 with increasing MRE numbers (Figure 4-3D, 4-4). The dwell times increased as from non-specific miR-7 interactions lasting ~0.1 s as 0.18, 0.24, 0.17 to 0.98 s with 1, 3, 6 and 11 MREs with miR-21 respectively (Figure 4-4). The MREs in these mRNAs were spaced in tandem cassettes, with the seed sequences spaced 20 bases apart. Prior work has suggested the possibility of cooperative increase in binding times when MREs are spaced up to 40 bases apart (Chandradoss et al., 2015). However, while we did observe increasing dwell times with MRE number, the increase in dwell time was not commensurate with changes in MRE number.

We noted that the distribution of microRNA spot distance relative to the center of the mRNA spot showed decreased variance with increasing MRE number, suggesting that MRE number helped stabilize microRNA binding (Figure 4-5). These findings together suggest that the number of binding sites promotes stable microRNA binding.

4.3.3. mRNAs show AGO2- and MRE-dependent clustering

We observed that mRNA spots with low MRE numbers tended to show shorter tracks than the 11 MRE spots (Figure 4-3D). Further, the transcripts bearing different MRE numbers showed apparent differences in mRNA spot intensity that appeared to systematically increase with MRE number (Figure 4-6C). Ensemble fluorescence measurements indicated that the labeling efficiency between the different constructs was similar, suggesting that the systematic variation in spot intensities might have a biochemical origin that was not an artefact of our experimental setup. Recent work in the field of intracellular phase separation has revealed the importance of

multivalent RNA-protein interactions in the assembly of structures such as RNA granules (Sheu-Gruttadauria and MacRae, 2018). We tested the hypothesis that a component of the RISC machinery was involved in the MRE-dependent mRNA clustering, which could explain the increased spot intensities.

The human Argonaute protein AGO2 is the major effector protein responsible for microRNA function and is the limiting factor in microRNA pathway. To test the effect of varying AGO2 levels we used two different Mouse Embryonic Fibroblast (MEF) cell lines, one in which the endogenous AGO2 was knocked out (MEF AGO2 KO) and another in which the human AGO2 gene was overexpressed in the same background (MEF AGO2 KO AGO2+) (O'Carroll et al., 2007). The spot intensities of 11 MRE transcripts co-injected with miR-21 were compared between the two cell lines. The intensity distribution showed a significant shift to lower intensity in cells lacking AGO2 compared to those that overexpressed AGO2 in cells injected with miR-21 (Figure 4-6B). In contrast, non-specific interactions between miR7 and FL-m21-11x were not impacted by AGO2 levels (4-7A). Consistent with the trends of spot intensity shifts, only miR-21 showed significant, long colocalizations in the presence of AGO2. We thus concluded that the high-MRE number-dependent clustering requires the presence of both the specific microRNA and functional AGO2 (Figure 4-6B).

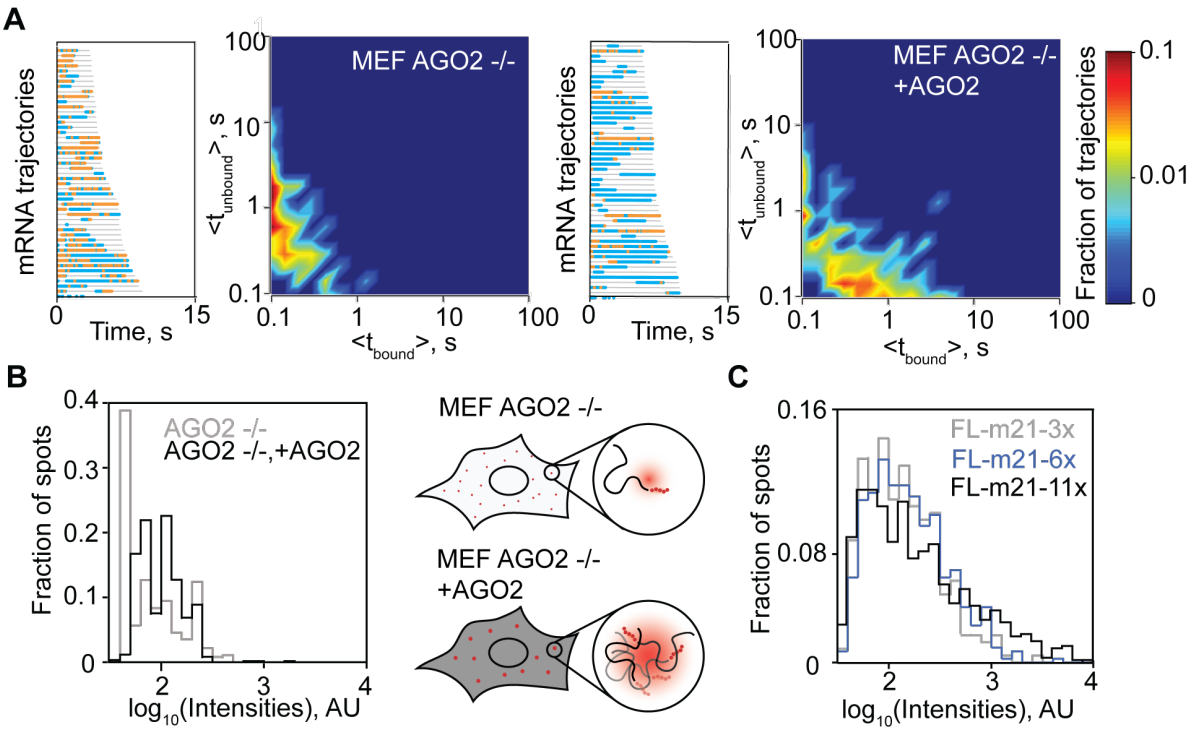

Figure 4-6 mRNAs show miRNA and AGO2-dependent clustering (A) 50 longest idealized distance traces and dwell time histograms from MEF AGO KO cells and MEF AGO2 KO overexpressing AGO2 injected with FL-11x-m21 and miR-21. (B) FL-11x-m21 mRNA spot intensity histograms from AGO2 KO and overexpression cells. Schematic showing mRNA clustering in AGO overexpressing cells. (C) mRNA spot intensity histogram of FL-m21-3x, FL-m21-6x and FL-m21-11x from Figure 2D.

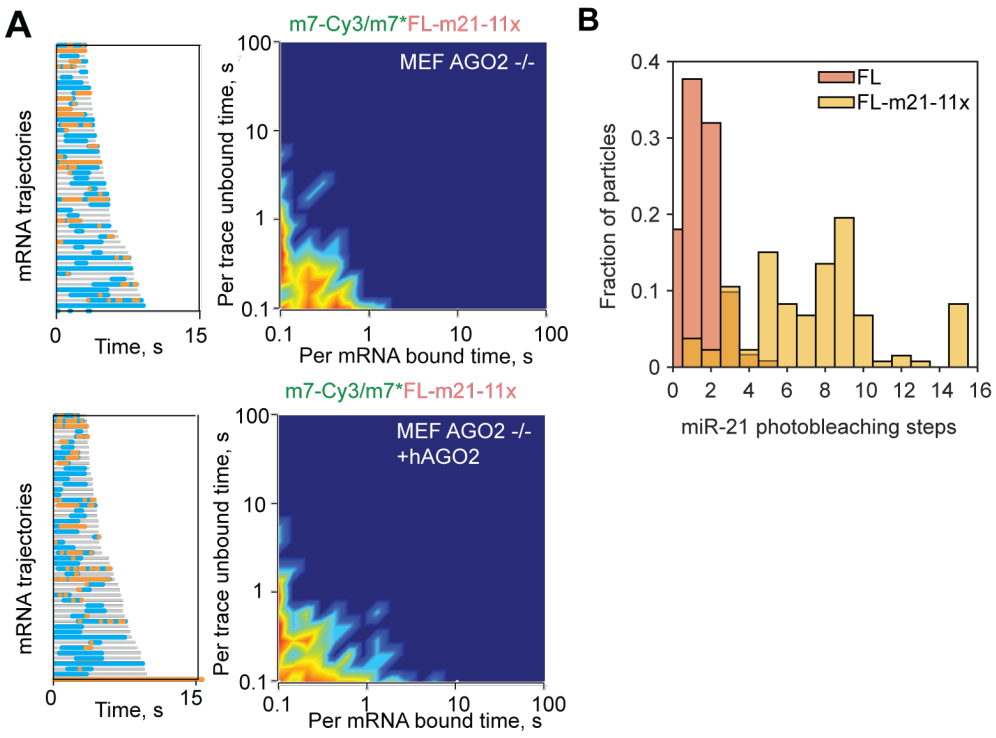

Figure 4-7 MRE-specific and number-dependent miRNA interactions promote higher-order assembly of mRNAs. (**A**) Colocalization tracks and dwell time histograms of miR7 with FL-m21-11x mRNA in MEF AGO2 KO and MEF AGO2 KO +AGO2 cells. (**B**) The number of photobleaching steps from populations of FL-m21-11x and FL mRNAs in fixed U2OC cells injected with miR21.

While we consistently observed MRE- and miRNA-specificity-dependent shifts in mRNA spot brightness, we did not detect dramatic differences in microRNA spot intensities with increased MRE number, which suggests that even in a regime of excess microRNA, stoichiometric MRE occupancy may be rare in the cell. To further investigate binding stoichiometry, the number of miRNA spots colocalized with an mRNA spot in fixed cells was determined by stepwise photobleaching analysis. Cells were injected with FL or FL-m21-11x and miR-21. Cells injected with FL-m21-11x showed significantly more miRNA colocalizations per spot, but the mRNA spot intensities in these cells were also significantly higher (Figure 4-6C, 4-7B). Correcting for mRNA spot intensities, which were ~10 times greater than those of 0MRE suggested that these spots represented aggregates of mRNAs that were sub-stoichiometrically bound.

4.3.4. miRISC-dependent mRNA clustering and sub-stoichiometric target binding enhance target occupancy

We tested the hypothesis that miRISC-dependent target clustering promoted overall target occupancy by comparing the theoretically predicted target occupancy of different miRNA-mRNA binding models. We compared the steady-state mRNA bound fraction as a function of the number of MREs and relative microRNA concentration across ODE mass-action kinetic models that varied in the reversibility of miRNA binding and maximum allowable stoichiometry of binding. The four idealized models of miRNA-mRNA interactions that result from the permutations of these factors are 1. irreversible and stoichiometric binding where it is possible for all MREs to be simultaneously occupied 2. irreversible and sub-stoichiometric, where only one MRE can be bound irrespective of the number of MREs, 3. completely reversible binding and 4. reversible binding but with mRNA "clustering", so that a completely unbound mRNA can enter a bound state by encountering a pre-existing cluster. A comparison of the mRNA bound fractions suggest that while stable (irreversible binding models) binding achieves greater mRNA binding at low MRE numbers, at high MRE numbers mRNA clustering significantly decreases the microRNA concentration required to achieve the same level of occupancy at higher MRE numbers (Figure 4-8A, B). We attribute this effect to a decreased competition among mRNAs of the same species for a limited pool of microRNA, or "self-competition" (Figure 4-8B).

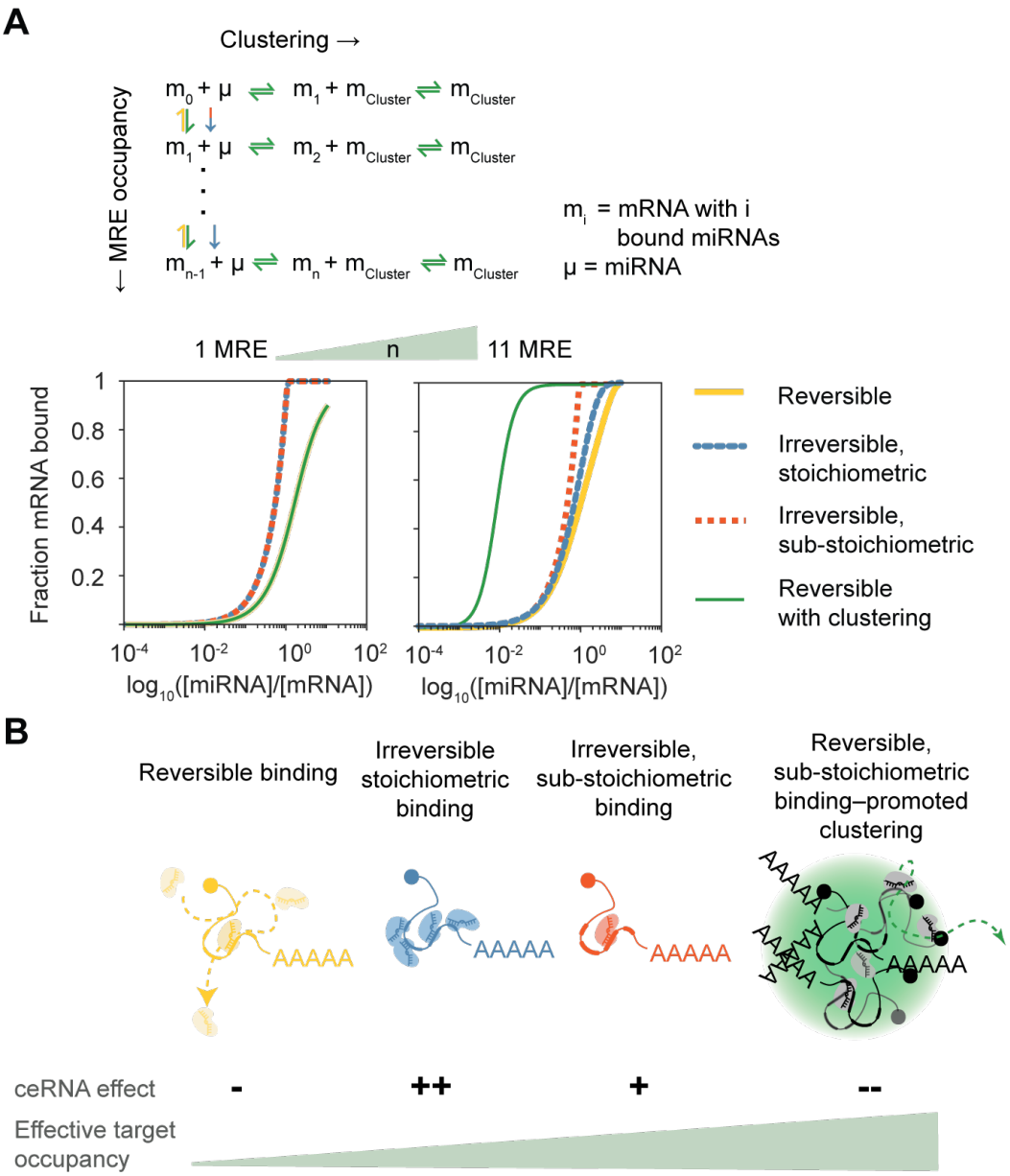

Figure 4-8 A model for MRE-dependent clustering. (**A**) steady-state mRNA occupancy as a function of miRNA concentration under different models of microRNA-mRNA interactions. At low MRE number per mRNA (1 MRE, left) irreversible miRNA binding favors greater occupancy than sub-stoichiometric reversible binding or clustering. However, at high MRE numbers (11 MREs, right) miRNA-binding-dependent clustering enhances mRNA occupancy even under highly sub-stoichiometric conditions. Transcripts bearing high MRE numbers require lower microRNA concentration to achieve significant occupancy (**B**) Schematic depicting the different models of microRNA-mRNA binding. Clustering provides a rapid mechanism by which mRNAs bearing a large number of MREs can be effectively bound by microRNAs without leading to self-competition.

4.4. Discussion

A duplex RNA generated by 6-8 base pairs between the microRNA seed sequence and an MRE is not expected to be sufficiently thermodynamically stable, and consequently the lifetime of such a complex is expected insufficient to stably recruit other elements of the RISC complex in the cell. However, AGO2 drastically alters the binding properties of the hybrid and stabilizes this duplex interaction so that its lifetime is on the order of 5 minutes in vitro (Salomon et al., 2015). It is unknown what the binding times of AGO2 are inside the cell, and how MRE number influences its residence time. Here we have used an intracellular single-molecule miRNA-mRNA visualization approach to demonstrate that both specific and non-specific miRISC-mRNA interactions last on the order of 0.1 s in the cell, and that MRE number stabilizes these interactions in duration and space.

Our single molecule mRNA-microRNA visualization assay allows us to observe dynamic interactions between intracellular microRNA and mRNA molecules in real time. A majority of microRNAs showed transient co-localizations with mRNAs, and only a small fraction colocalized stably, suggesting that transient binding may play a dominant role in target search as the microRNA engages with non-target regions. In vitro analysis of transcript translation repression in lysate suggests that AGO2 clusters support effective repression. Finally, our intracellular observations also hint at an AGO2-dependent, microRNA-mediated mRNA clustering that is dependent on MRE number.

Intracellular target search has been previously studied in the context of transcription factor binding to specific genomic control regions. Early work on transcription factors postulated “facilitated” diffusion to explain the rapid search for specific, high affinity binding sites in the

genome (Riggs et al., 1970; Tafvizi et al., 2011). Over the last four decades, successive refinements of molecular search models have led to the consensus that a mix of "1D" or linear diffusion and "3D" diffusion, by hopping and intersegmental transfer can explain the rapid search mechanism of transcription factors for specific binding sites (Halford, 2009; Halford and Marko, 2004; Tafvizi et al., 2011). Target search by miRISC is expected to be slower in comparison to transcription factors by virtue of the decreased density of cytosolic RNA compared to DNA in the nucleus, which excludes inter-segmental hopping, or highly processive 1D search. Recent in vitro single molecule experiments have suggested that both 3D and 1D search may contribute to microRNA target search (Cui and Joo, 2019; Klein et al., 2017).

It is unclear under the ceRNA hypothesis how to explain repression of highly abundant target mRNAs, especially if they contain multiple copies of the same MRE. In this case the model predicts a high level of self-competition amongst such transcripts, resulting in low overall levels of translation repression despite experimental evidence that high MRE number ought to promote target repression (Mayr et al., 2007). Further, conflicting reports of whether the ceRNA effect does in fact significantly alter target occupancy in vivo has remained controversial (Bosson et al., 2014b; Liu et al., 2019). Thus, under this paradigm it is unclear what the advantage of having multiple MREs is if self-competition is predicted to inhibit repression.

Recent work has demonstrated that RISC proteins can undergo phase separation via multivalent RNA-protein and protein-protein interactions. Sheu-Gruttadauria et al reported the formation of in vitro condensates of GW182 protein in the presence of AGO2. Since GW182 acts downstream of AGO2, and serves as a scaffold for the RISC machinery, condensation of this protein may potentially form the basis for mRNA clustering downstream of target binding.

Clustering may be particularly valuable in order for mRNAs with a large number of MREs to achieve significant repression. Under an mRNA-clustering driven model of target search where sub-stoichiometric levels of microRNAs can efficiently recruit a network of RISC proteins to transcripts bearing multiple binding sites, it is possible for unbound transcripts to enter a RISC-bound state without stoichiometric microRNA binding. Thus, clustering can enhance microRNA activity when the regulated transcripts possess multiple binding sites.

MREs spaced 8-40 nucleotides apart have been shown to show cooperative microRNA binding and translation repression (Chandradoss et al., 2015). Our observations suggest that microRNAs are only bound at sub-stoichiometric levels to transcripts even with closely spaced MREs. We conclude that tandem MREs may serve to increase the dwell time of microRNAs rather than to recruit multiple RISC complexes cooperatively. Taken together, we propose that multiple MREs may form networks of mRNAs bridged by multivalent RISC complexes. This may allow multiple mRNAs, rather than multiple MREs on the same mRNA, to be bound by a searching microRNA, by a mechanism akin to inter-segmental transfer of transcription factors on DNA. Further, while this work has focused on the role of tandem MRE repeats, these results can be extended to long 3'UTRs containing multiple MREs of different specificities, adding another layer of complexity and cross-talk to miRNA-mRNA networks. Our work therefore highlights the role that spatial organization may play in target search by RNA-protein machines, adding a new dimension to the discussion of the ceRNA effect. Future work may clarify the role of phase-separation and dynamic target search in mRNA translation regulation and define the molecular interactions that underlie this phenomenon.

4.5. Methods

RNA preparation and labeling All RNA constructs were cloned into pcDNA™ 3.1 (-) Mammalian Expression Vector backbones. Plasmids were linearized by restriction digestion using AFl II. Firefly luciferase (FL) RNA, bearing 0, 1, 3, 6, or 11 tandem miR21 MREs, was transcribed from linearized plasmids, which were further purified by QIAquick PCR Purification Kit. FL RNA are first transcribed from 0.5 μg of linearized plasmid using MEGAscript® T7 Transcription Kit (Thermo Fisher Scientific, Cat# AM1333), incubated at 37 ℃ for 4 h. RNA was precipitated using 5 M Ammonium Acetate for this and following enzymatic reactions. Precipitated RNA was capped using ScriptCap™ m7G Capping System (CellScript™, Cat# C-SCCE0610). Capped RNA was yPAP treated with the total pool of ATP replaced with 2'-Azido-2'-deoxyadenosine-5'-Triphosphate (Trilink Biotechnologies, Cat# N-1045), 1μL polymerase was used for tailing 30 μg mRNA. 5 M Ammonium Acetate was used twice here to remove extra 2'-Azido-2'-deoxyadenosine-5'-Triphosphate. A-Plus™ Poly(A) Polymerase Tailing Kit (Cellscript, C-PAP5104H) was used to form the poly(A) tail per their instructions. After purification, RNAs were fluorescently labeled using Click-IT® Alexa Fluor® 647/555 DIBO Alkyne (Invitrogen, Cat# C10408). Click-iT® Alexa Fluor® 647 DIBO Alkyne was dissolved in anhydrous DMSO to a stock concentration of 1 mM. 60 μg of azide-ATP modified RNA is mixed with Click-iT® AlexaFluor® 647/555 DIBO Alkyne (1 mM, 10 μL) in 1X PBS for 45 min at 37 ℃. Then the RNA was yPAP treated again with the total pool of ATP replaced with 2'-Azido-2'-deoxyadenosine-5'-Triphosphate (Trilink Biotechnologies, Cat# N-1045), 0.5 μL polymerase was used for tailing 30 μg mRNA. Finally Click-iT® DIBO-biotin (Invitrogen, Cat# C10412) was used to label the tailed RNA. 5 M Ammonium Acetate was used twice for purification.

Precipitated RNA was dissolved and stored in water. RNA integrity was analyzed via 1.2% agarose gel electrophoresis. The number of Alexa647 on one mRNA was calculated by the concentration ratio of mRNA and Alexa647. The extent of biotinylation was determined by measuring the amount of RNA bound by Streptavidin MagneSphere® Paramagnetic Particles (Promega, Z5481) or Dynabeads® MyOne™ Streptavidin C1 beads (Invitrogen, Cat# 65001).

Microscopy and microinjection Streptavidin (SA) was dissolved to a final concentration of 1 mg/mL in ddH2O and stored frozen until use. In the instance that miR-21 was co-injected, both 15 μM passenger and 10 μM guide strands were heat annealed from 90ºC to room temperature in 1X PBS. Injection mixture consisting of 1 μL of 10 mg/mL Cascade Blue Dextran (Thermo Fisher Cat# D1976), double stranded microRNA (10μM, 1.5μL), SA (1 mg/mL, 0.38 μL), RNA (final concentration: 50 nM, 35 nM or 20 nM), glycerol (7.5 μL, 20%), 3 μL 10X PBS was made up to a final volume of 30μL with water. The solution was mixed at room temperature for 7 min, following which 1.5μL of 20 μM Biotin-XX Phalloidin (Thermo Fisher Scientific Cat# B7474) solution was added to it and incubated at 37 ℃ for 5 min. The samples were then spin filtered using a 0.22 μm PVDF filter before microinjection. Injection mixtures were microinjected into U2OS, MEF-AGO2 KO and MEF-AGO2 KO+AGO2 cells as previously described (Pitchiaya et al., 2012; Pitchiaya et al., 2013). Prior to injection, cells were washed three times and immersed with BSS imaging media. Injected cells were imaged 2-4 h post-injection. Cells were identified by their Cascade Blue 10 kDa Dextran injection marker signature.

For photo-bleaching experiments, the injection mixtures were injected into MEF-AGO2 KO + AGO2. After 3h of microinjection, the cells were washed three times with 1X PBS and fixed using 4% para formaldehyde for 20min. After washing with PBS, OSS (2 mM trolox, 50 μM

protocatechiuc acid, and 50 nM protocatechuate dehydrogenase in 1X PBS) were added before imaging.

Imaging was performed using highly inclined and laminated optical sheet (HILO) microscopy based on an Olympus IX81 microscope equipped with a 60x 1.49 NA oil-immersion objective (Olympus) as well as 405 nm (200 μW for imaging Cascade Blue Dextran), 532 nm (8 mW for imaging Cy3) and 640 nm (4 mW for imaging Alexa Fluor 647) solid-state lasers. Quad-band filter cubes consisting of z405/488/532/640rp dichroic filters (Chroma) and z405/488/532/640m emission filters (Chroma) were used to filter fluorescence of the appropriate fluorophores from incident light. Emission from fluorophores was detected simultaneously on two EMCCD cameras (Andor IXon Ultra). The exposure time is usually 100ms.

Cell culture U2OS (HTB-96, ATCC), were propagated in McCoy's 5A (GIBCO, # 16600) supplemented with 10% FBS (GIBCO, # 16000) and 100 U/mL Penicillin-Streptomycin (ThermoFisher Scientific, Cat# 15140122). MEF cells were propagated in DMEM (GIBCO, #11995) supplemented with 10% FBS and 100 U/mL Penicillin-Streptomycin. For live cell imaging, cells were imaged in phenol-red free medium containing 1% FBS.

Live cell particle tracking Colocalization analysis was performed in two steps. Raw, beads-registered images were used for particle tracking using Imaris. The obtained particle trajectories were then analyzed using custom Matlab scripts. Spots were first determined to be colocalized if the spot center coordinates were < 5 px away for at least one frame. Inter-spot distances from pairs of trajectories that satisfied this criterion were then further analyzed by imposing an empirically determined radius cutoff (150 nm) to classify frames into "bound" and "unbound" classes based on proximity. The cumulative sum of successive frames in either of these

states was taken to be the dwell time in that respective state, and these dwell times were used to populate dwell time histograms. Only trajectories that were longer than 5 frames (0.5 s) were used for colocalization and diffusion analyses. Diffusion rates were obtained by obtaining the slope of mean squared displacement (MSD) vs interval plots assuming 2-D Brownian diffusion.

Photobleaching analysis was performed using the method described in Tsekouras et al. 2016. Briefly, injected cells were fixed using 4% PFA. A custom LabView script was used to localize spots and extract fluorescence traces. The obtained traces were analyzed using the JuPyter notebook implementation of the algorithm described in (Tsekouras et al.).

Quantification and statistical analysis Origin were used for statistical analysis and plotting. For pairwise comparisons, p-values were calculated based on non-parametric unpaired t-tests with a Kolmogorov-Smirnov test. For comparisons involving more than 2 samples, one-way-ANOVA tests were used with a Geisser-Greenhouse correction.

Table 4-1 List of reagents and other resources referenced in Chapter 4.

REAGENT or RESOURCE	SOURCE	IDENTIFIER
Chemicals, Peptides, and Recombinant Proteins		
2'-Azido-2'-deoxyadenosine-5'-Triphosphate	Trilink Biotechnologies	N-1045
Click-iT® Alexa Fluor® 647/555 DIBO Alkyne	Invitrogen	C10408
Click-iT® DIBO-biotin	Invitrogen	C10412
Biotin-XX Phalloidin	Thermo-Fisher	B7474
Critical Commercial Assays		
MEGAscript® T7 Transcription Kit	Thermo-Fisher	AM1333
ScriptCap™ m 7 G Capping System	CellScript	C-SCCE0610
A-Plus™ Poly(A) Polymerase Tailing Kit	CellScript	C-PAP5104H
Deposited Data		
Raw and analyzed data	This work	N/A
Experimental Models: Cell Lines		
Human: U2-OS	ATCC	HTB-96
Human: MEF AGO2 KO		
Human: MEF AGO2 +AGO2		
Oligonucleotides		
hsa-miR21-5p: pUAGCUUAUCAGACUGAUGUUGA-Cy3	IDT	Custom
hsa-miR21-3p: pCAACACCAGUCGAUGGGCUGU	IDT	Custom
hsa-miR7-1-5p: pUGGAAGACUAGUGAUUUUGUUGUU-Cy3	IDT	Custom
hsa-miR7-1-3p: pCAACAAAUCACAGUCUGCCAUA	IDT	Custom
Recombinant DNA		
pcDNA3.1-FL	Custer and Walter 2017	
pcDNA3.1-FL-1x-m21	Custer and Walter 2017	
pcDNA3.1-FL-3x-m21	Custer and Walter 2017	
pcDNA3.1-FL-6x-m21	Custer and Walter 2017	
pcDNA3.1-FL-11x-m21	Custer and Walter 2017	
Software and Algorithms		
MATLAB	The Mathworks Inc.	R2018a
Origin 2018	OriginLab	Origin 2018
Imaris 9.1.0	Bitplane AG	Imaris 9.1.0
Fiji	ImageJ/NIH	Fiji
Custom MATLAB routines	This work	N/A
Bacterial and viral strains		
XL10-Gold Ultracompetent Cells	Agilent	200315

4.6. References

Arvey, A., Larsson, E., Sander, C., Leslie, C.S., and Marks, D.S. (2010). Target mRNA abundance dilutes microRNA and siRNA activity. Mol. Syst. Biol. *6*, 363.

Bartel, D.P. (2018). Metazoan MicroRNAs. Cell *173*, 20-51.

Bosson, A.D., Zamudio, J.R., and Sharp, P.A. (2014). Endogenous miRNA and target concentrations determine susceptibility to potential ceRNA competition. Mol. Cell *56*, 347-359.

Broderick, J.A., and Zamore, P.D. (2014). Competitive endogenous RNAs cannot alter microRNA function in vivo. Mol. Cell *54*, 711-713.

Bushati, N., and Cohen, S.M. (2007). microRNA functions. Annu. Rev. Cell Dev. Biol *23*, 175-205.

Chandradoss, S.D., Schirle, N.T., Szczepaniak, M., MacRae, I.J., and Joo, C. (2015). A Dynamic Search Process Underlies MicroRNA Targeting. Cell *162*, 96-107.

Cui, T.J., and Joo, C. (2019). Facilitated diffusion of Argonaute-mediated target search. RNA Biol. *16*, 1093-1107.

Custer, T.C., and Walter, N.G. (2017). In vitro labeling strategies for in cellulo fluorescence microscopy of single ribonucleoprotein machines. Protein Sci. *26*, 1363-1379.

Daher, M., Widom, J.R., Tay, W., and Walter, N.G. (2018). Soft Interactions with Model Crowders and Non-canonical Interactions with Cellular Proteins Stabilize RNA Folding. J. Mol. Biol. *430*, 509-523.

Denzler, R., Agarwal, V., Stefano, J., Bartel, D.P., and Stoffel, M. (2014). Assessing the ceRNA hypothesis with quantitative measurements of miRNA and target abundance. Mol. Cell *54*, 766-776.

Denzler, R., McGeary, S.E., Title, A.C., Agarwal, V., Bartel, D.P., and Stoffel, M. (2016). Impact of MicroRNA Levels, Target-Site Complementarity, and Cooperativity on Competing Endogenous RNA-Regulated Gene Expression. Mol Cell *64*, 565-579.

Eberhardt, W., Badawi, A., Biyanee, A., and Pfeilschifter, J. (2016). Cytoskeleton-Dependent Transport as a Potential Target for Interfering with Post-transcriptional HuR mRNA Regulons. Front. Pharmacol. *7*, 251.

Flores-Jasso, C.F., Salomon, W.E., and Zamore, P.D. (2013). Rapid and specific purification of Argonaute-small RNA complexes from crude cell lysates. RNA *19*, 271-279.

Gehring, N.H., Wahle, E., and Fischer, U. (2017). Deciphering the mRNP Code: RNA-Bound Determinants of Post-Transcriptional Gene Regulation. Trends in Biochemical Science *42*, 369-382.

Gerstberger, S., Hafner, M., and Tuschl, T. (2014). A census of human RNA-binding proteins. Nat. Rev. Genet. *15*, 829-845.

Hafner, M., Landthaler, M., Burger, L., Khorshid, M., Hausser, J., Berninger, P., Rothballer, A., Ascano, M., Jr., Jungkamp, A.C., Munschauer, M.*, et al.* (2010). Transcriptome-wide identification of RNA-binding protein and microRNA target sites by PAR-CLIP. Cell *141*, 129-141.

Halford, S.E. (2009). An end to 40 years of mistakes in DNA-protein association kinetics? Biochem. Soc. Trans *37*, 343-348.

Halford, S.E., and Marko, J.F. (2004). How do site-specific DNA-binding proteins find their targets? Nucleic Acids Res *32*, 3040-3052.

Klein, M., Chandradoss, S.D., Depken, M., and Joo, C. (2017). Why Argonaute is needed to make microRNA target search fast and reliable. Semin. Cell Dev. Biol. *65*, 20-28.

Langdon, E.M., and Gladfelter, A.S. (2018). A New Lens for RNA Localization: Liquid-Liquid Phase Separation. Annu. Rev. Microbiol *72*, 255-271.

Liu, Y., Xue, M., Du, S., Feng, W., Zhang, K., Zhang, L., Liu, H., Jia, G., Wu, L., Hu, X.*, et al.* (2019). Competitive endogenous RNA is an intrinsic component of EMT regulatory circuits and modulates EMT. Nat. Commun. *10*, 1637.

Ma, W., and Mayr, C. (2018). A Membraneless Organelle Associated with the Endoplasmic Reticulum Enables 3'UTR-Mediated Protein-Protein Interactions. Cell *175*, 1492-1506.e1419.

Matsuda, H., Putzel, G.G., Backman, V., and Szleifer, I. (2014). Macromolecular crowding as a regulator of gene transcription. Biophys. J. *106*, 1801-1810.

Mayr, C., Hemann, M.T., and Bartel, D.P. (2007). Disrupting the pairing between let-7 and Hmga2 enhances oncogenic transformation. Science *315*, 1576-1579.

Mellis, I.A., Gupte, R., Raj, A., and Rouhanifard, S.H. (2017). Visualizing adenosine-to-inosine RNA editing in single mammalian cells. Nat. Methods *14*, 801-804.

O'Carroll, D., Mecklenbrauker, I., Das, P.P., Santana, A., Koenig, U., Enright, A.J., Miska, E.A., and Tarakhovsky, A. (2007). A Slicer-independent role for Argonaute 2 in hematopoiesis and the microRNA pathway. Genes Dev *21*, 1999-2004.

Pasquinelli, A.E., and Ruvkun, G. (2002). Control of developmental timing by micrornas and their targets. Annu. Rev. Cell Dev. Biol *18*, 495-513.

Pitchiaya, S., Androsavich, J.R., and Walter, N.G. (2012). Intracellular single molecule microscopy reveals two kinetically distinct pathways for microRNA assembly. EMBO Rep *13*, 709-715.

Pitchiaya, S., Heinicke, L.A., Custer, T.C., and Walter, N.G. (2014). Single molecule fluorescence approaches shed light on intracellular RNAs. Chem. Rev. *114*, 3224-3265.

Pitchiaya, S., Heinicke, L.A., Park, J.I., Cameron, E.L., and Walter, N.G. (2017). Resolving Subcellular miRNA Trafficking and Turnover at Single-Molecule Resolution. Cell Rep. *19*, 630-642.

Pitchiaya, S., Krishnan, V., Custer, T.C., and Walter, N.G. (2013). Dissecting non-coding RNA mechanisms in cellulo by Single-molecule High-Resolution Localization and Counting. Methods *63*, 188-199.

Pitchiaya, S., Mourao, M.D.A., Jalihal, A.P., Xiao, L., Jiang, X., Chinnaiyan, A.M., Schnell, S., and Walter, N.G. (2019). Dynamic Recruitment of Single RNAs to Processing Bodies Depends on RNA Functionality. Mol. Cell *74*, 521-533.e526.

Riggs, A.D., Newby, R.F., and Bourgeois, S. (1970). lac repressor--operator interaction. II. Effect of galactosides and other ligands. J. Mol. Biol. *51*, 303-314.

Salomon, W.E., Jolly, S.M., Moore, M.J., Zamore, P.D., and Serebrov, V. (2015). Single-Molecule Imaging Reveals that Argonaute Reshapes the Binding Properties of Its Nucleic Acid Guides. Cell *162*, 84-95.

Schnell, S., and Turner, T.E. (2004). Reaction kinetics in intracellular environments with macromolecular crowding: simulations and rate laws. Prog. Biophys. Mol. Biol. *85*, 235-260.

Sheu-Gruttadauria, J., and MacRae, I.J. (2018). Phase Transitions in the Assembly and Function of Human miRISC. Cell *173*, 946-957.e916.

Smillie, C.L., Sirey, T., and Ponting, C.P. (2018). Complexities of post-transcriptional regulation and the modeling of ceRNA crosstalk. Crit. Rev. Biochem. Mol. Biol. *53*, 231-245.

Stebbings, H. (2001). Cytoskeleton-dependent transport and localization of mRNA. Int. Rev. Cytol. *211*, 1-31.

Tafvizi, A., Mirny, L.A., and van Oijen, A.M. (2011). Dancing on DNA: kinetic aspects of search processes on DNA. ChemPhysChem *12*, 1481-1489.

Thomson, D.W., and Dinger, M.E. (2016). Endogenous microRNA sponges: evidence and controversy. Nat. Rev. Genet. *17*, 272-283.

Tsekouras, K., Custer, T.C., Jashnsaz, H., Walter, N.G., and Pressé, S. (2016). A novel method to accurately locate and count large numbers of steps by photobleaching. Mol. Biol. Cell *27*, 3601-3615.

Wee, L.M., Flores-Jasso, C.F., Salomon, W.E., and Zamore, P.D. (2012). Argonaute divides its RNA guide into domains with distinct functions and RNA-binding properties. Cell *151*, 1055-1067.

Wu, B., Eliscovich, C., Yoon, Y.J., and Singer, R.H. (2016). Translation dynamics of single mRNAs in live cells and neurons. Science *352*, 1430-1435.

Yan, X., Hoek, T.A., Vale, R.D., and Tanenbaum, M.E. (2016). Dynamics of Translation of Single mRNA Molecules In Vivo. Cell *165*, 976-989.

Zhou, H.X., Rivas, G., and Minton, A.P. (2008). Macromolecular crowding and confinement: biochemical, biophysical, and potential physiological consequences. Annu. Rev. Biophys *37*, 375-397.

Chapter 5. Outlook and Future Directions[5]

5.1. Beyond HOPS

In Chapter 3 we provide evidence for a proteome-wide phase separation phenotype in response to rapid changes in molecular crowding induced by hyperosmotic shock, termed hyperosmotic phase separation (HOPS). We first characterized HOPS of DCP1A, a component of P-bodies, and demonstrated that its trimerization domain was necessary and sufficient for HOPS. We then probed the proteome using a low-throughput live-cell screen and a high-throughput screen immunofluorescence screen and found that homomultimeric proteins in general showed a tendency to undergo HOPS.

This work opens up new questions related to the biochemical bases and modulation of HOPS, protein evolution and regulation of crowding inside cells. Additionally, HOPS forces us to rethink the internal organization of the cell. By suggesting that macromolecules are situated close to a phase boundary, HOPS suggests a picture of the dynamic internal organization of cells sensitive to external perturbations. These ideas, directions and possible experimental approaches are briefly explored here.

---

[5] Section 5.1.2 has been published as:

Jalihal, A.P., Schmidt A.S., Gao G., Little S., Pitchiaya S. and Walter, N.G. Hyperosmotic phase separation: Condensates beyond inclusions, granules and organelles. (2020) JBC. 10.1074/bc.REV120.010899

All authors contributed to writing and editing.

5.1.1. Regulation of HOPS at the level of solutes and cells

Chapter 3 explores the biochemical basis of HOPS and identifies homomultimerization as the dominant driver of this ubiquitous reorganization. However, many of the tested proteins also possess RNA-binding and heteromultimeric interactions, both of which are known to be drivers of phase separation (Langdon and Gladfelter, 2018a). It will be important to further investigate the contributions of RNA-interactions and charge contributions of RNA both for the assembly and disassembly of HOPS condensates. Computational and in vitro methods will be useful to tease apart these contributions to crowding-dependent phase separation.

Various synthetic crowders have been used to investigate the effects of crowding of protein folding and phase separation in vitro, and these have revealed the complex and multiple influences crowders have on solutes (Kuznetsova et al., 2015; Roden and Gladfelter, 2020; Zhang et al., 2015). However, in general, the use of artificial crowders are associated with important caveats. The most important consideration is to account for physical and biochemical interactions the crowders may have with molecules of interest (Feig and Sugita, 2012; Jiao et al., 2010; Miklos et al., 2010; Minton, 2005; Zhou, 2013). Also notable is that while crowders are capable of recapitulating in vivo protein folding and other behaviors, the composition of crowders in cells is highly heterogeneous in size and other properties. A detailed analysis of the combined effects of heterogeneous crowder mixture on any given solute is restricted by current technologies which are best suited at probing the effects of individual crowding species (Courtenay et al., 2000; Sarkar et al., 2013).

In addition to exploring the effects of changes in crowding on phase separation, studies into cellular mechanisms that regulate crowding and phase separation responses to crowding is a

major outstanding question. In this regard, peioneering work by Delarue and colleagues has shown that mTORC activity can alter the polysome load in yeast, thereby altering the overall state of crowding by dispersing ribosomes into monosomes (Delarue et al., 2018). Additionally, we and several others have examined the role of post-translational modifications on phase separation. These results hint at a coupling between mechanisms that sense changes in molecular crowding in various contexts, including cell division, and mechanisms that modulate phase-separation potential via post-translational modifications during crowding changes. Further exploration of the relationship between cell cycle regulators and these mechanisms are required to uncover such coupling.

While the role of HOPS in modulating individual biochemical pathways is now becoming apparent (Boyd-Shiwarski et al., 2018b; Cai et al., 2019; Jalihal et al., 2020a), the global role of HOPS in conferring protection against osmotic stress remains unclear. One potential avenue to investigate this would be a candidate or systematic genome-wide deletion of HOPS domains. It would be interesting to see if the distinct pathways affected by HOPS represent redundant mechanisms, or their coordinated action is required to confer a sufficiently protective phenotype. Alternatively, inducible multimerization systems can be used to probe whether enhanced HOPS propensity confers an additional resistance to stress. The question of the global protective role, however, remains open and important to address.

5.1.2. Reconceptualizing intracellular organization

The term “condensate” has been used in the literature alongside some everyday metaphors for liquid-liquid phase separation, such as the formation of immiscible droplets in vinaigrette or lava lamps (Hyman et al., 2014c). These examples capture the thermodynamics of demixing,

where the energy of the vinaigrette system is minimized when oil and vinegar undergo phase separation. However, this analogy is limited because it suggests that the two components of the mixture exist in stable, mutually exclusive phases. In biological contexts, phase separation more typically leads to an enrichment of components in one or the other phase, and the degree of partitioning is relevant to understanding the gain or loss of activity in the more concentrated phase. Furthermore, while LLPS appears to be widespread, maturation of liquid-like droplets into gel- and solid-like states is a pervasive phenomenon not captured by the oil-water analogy. As the study of MLOs in physiological and disease contexts becomes more widespread, an additional analogy, serving as a model for biologists may be beneficial.

The study of phase separation has extensively used cloud-related terminology in the more distant past. In the study of protein precipitation, for example, the temperature at which a protein solution turns opaque due to phase-separation of the protein is denoted as $T_{cloud,}$ or the cloud point, above which the solution is constituted of a single phase (Taratuta et al., 1990a). The cloud point therefore represents the optimal conditions of concentration and other physicochemical factors that allow a protein to traverse the phase boundary from a vapor-like state to a condensed state. Here we reintroduce the analogy of cloud formation, that has previously been alluded to in the context of biological LLPS (Courchaine et al., 2016a; Hyman and Simons, 2012; Sehgal et al., 2020; Taratuta et al., 1990b). This metaphor emphasizes the rapid, highly reversible transition from a dispersed to a more condensed phase characteristic of phase separation responses to stress.

The cloud-formation metaphor takes us beyond merely the assembly of droplets. It intuitively allows us to make specific predictions related to the impact of physical variables such as temperature (kinetic motion) and “humidity” (relative component concentration) to

condensation. It also renders intuitive predictions about possibilities for intracellular condensates that are not currently reported, such as the potential for "smog", where a condensate of one type is nucleated or otherwise influenced by components that do not otherwise constitute it. It provides a rich language to describe condensates based on a continuum of physical properties – "vapor/mist" versus "droplets" versus frozen/hardened "hail". Finally, it provides a new conceptual model of mesoscale organization biology that draws from a physical system that is intrinsically emergent and possesses fractal properties.

Consider the highly studied case of TDP43 fibrillization in ALS. TDP-43 under physiological conditions has been found to condense into dynamic, liquid-like droplets in the nucleus and shows condensation behavior in the cytosol upon exposure to preexisting TDP-43 fibrils. Cytosolic TDP-43 droplets formed upon deletion of the protein's nuclear localization signal were found to mature into less dynamic, gel-like structures upon arsenite stress (Afroz et al., 2017; Gasset-Rosa et al., 2019). Similarly, FUS protein, also associated with ALS pathologies, condenses under normal conditions, but these condensates show liquid-to-solid transitions, and this tendency is enhanced by disease mutations (Patel et al., 2015; Qamar et al., 2018). These examples highlight how vapor-liquid-solid transitions may represent a universal, intrinsic tendency of multivalent biopolymers under physiological conditions. The resulting condensates can undergo maturation/solidification upon exposure to specific environmental or biochemical perturbations, resulting in both altered material properties of the condensates and consequences for cellular homeostasis, including pathologies.

The emerging picture is therefore one of a pervasive potential for multivalent molecules to be either within the two-phase regime or poised on the phase boundary between a "vapor"-like

dispersed state and a more condensed phase. This allows such molecules to rapidly transition to more condensed phases in response to intrinsic- and extrinsic perturbations, albeit in a highly regulated and carefully tuned manner. This hypothesis is consistent with the existence of dedicated cellular mechanisms that serve to promote the dissolution of condensates (Gomes and Shorter, 2019b; Jalihal et al., 2020a; Rai et al., 2018). Moreover, the resulting condensates can protect the cell by suspending vital cellular functions until the perturbations cease, but alternatively are then susceptible to pathogenic maturation into gel-like or solid states that can result in toxicity.

As our insights into intracellular organization by phase separation expand, laying the foundation for understanding how phase-separation pervasively regulates cellular function and survival, we also learn about the selection pressures that shape our proteome. It is our hope that the additional metaphor proposed here of phase separation as a kind of intracellular "cloud formation" may facilitate the intuition needed to appreciate the associated range of phenomena as readily reversible, highly adaptive cell reorganization responses to internal and external cues.

5.2. Binding and localizing RNAs inside the cell

Chapters 2 and 4 explored intracellular molecular interactions and the relationship between molecular sequence and localization. In chapter 2, RNA length, miRNA binding and translation potential were explored as contributors to PB interactions. We found that RISC and IGFBP1 interactions mediate the dynamics and specificity of PB localization of RNAs. In chapter 4, we explored the mechanisms that promote miRNA target search and observed that multiple MREs both promote stable miRNA binding but also promote clustering of targets. These mechanisms promote not just target repression, but also minimize the consequences of the ceRNA effect, in

which self-competition between highly expressed targets is expected to decrease overall repression.

One significant insight from this body of work is that the primary sequence influences RNA localization to condensates, and therefore has a major role to play in structuring the intracellular space. This theme is echoed in other recent work that explores the close connection between RNA sequence and localization (Ma and Mayr, 2018; Zhang et al., 2015). Additionally, these results raise important questions about the nature of RNA-miRNA regulatory networks in cell, such as the direction of regulation and the value of non-specific interactions. The following sections examine these ideas.

5.2.1. Spatial regulation in miRNA networks

The major objection raised against the possibility of exogenously modulating miRNA activity on the basis of the ceRNA hypothesis is that de-repression of miRNA targets requires a vast excess of the competitor RNAs, which in the context of highly expressed miRNAs can amount to unphysiologically high RNA concentrations (Salmena et al., 2011; Tay et al., 2014). Indeed, this claim about the unlikelihood of de-repression by overexpression has been experimentally verified (Denzler et al., 2014a). However, there is a second claim that ceRNA makes, that highly abundant targets, especially those with multiple MREs, can show self-competition, and thereby reduce the overall bound mRNA fraction, while also buffering gene expression fluctuations (Martirosyan et al., 2017). This notion is in line with other emerging evidence that the direction of regulatory arrows in ceRNA networks may not be trivial to assign, and inasmuch as miRNAs can act to destabilize targets, the target transcripts themselves can act as sponges to modulate miRNA activity levels.

Differential localization of translationally-repressed mRNAs and other RNAs within PBs as discussed in Chapter 2 raises the important question of how spatial organization of granules, specifically the core-shell structure of PBs contributes to differences in biochemical effects on these RNAs, if any. While there is accumulating evidence that mRNAs in PBs are intact and not fragments of degradation products, it remains to be investigated if the interior of PBs is incapable of supporting translation because they lack ribosomes or are simply devoid of ribosomes by virtue of being enriched for non-translating mRNAs. High-resolution imaging and live-cell single-molecule translation visualization experiments show promise in investigating these questions.

Evidence in Chapter 4 suggests that cells possess mechanisms to combat the effects of self-competition, by allowing mRNA targets possessing multiple MREs to assemble into higher-order structures downstream of AGO2 activity. This then suggests that in addition to a level of spatial complexity, miRNA-mRNA interactions can redistribute and re-localize these reactants themselves. The possibility of such interactions giving rise to more pervasive and regular sub-cellular organization, as predicted by reaction-diffusion theory, requires further exploration (Vanag and Epstein, 2007).

5.2.2. Specific and non-specific interactions

Having focused for several decades on highly specific macromolecular interactions, the field of biomolecular interactions has started revisiting "non-specific" interactions both as a source of regulation and as a way to understand intracellular biochemistry. It is becoming increasingly apparent that most molecular interactions inside the cell are short lived, and indeed highly transient

and dynamic molecular encounters predominate in the cell's crowded and dense interior. Recent studies on low-affinity protein interactions have focused both on high specificity interactions, such as receptor-ligand interactions (Parker et al., 2019) and low specificity interactions, also called quinary interactions (Ribeiro et al., 2018; Walter, 2019). Our work in Chapter 4 reveals that miRNAs in RISC complexes are ubiquitously engaged in short, probing interactions on non-target transcripts, lasting 100s of milliseconds. It remains to be explored if such pervasive non-productive, low-affinity interactions by both proteins and RNA-protein complexes can themselves come under selection. One way to test this possibility would be to investigate the detailed RNA composition in cells of different related species or cell types to evaluate the distribution of specific seed sequences of miRNAs in cells in which they are highly expressed. This also suggests another role for the coupling of transcription factors and miRNA networks, as de novo transcription may potentially also contribute to changes in the non-specific interactome.

5.3. Spatiotemporal gene regulation in vivo

Across its chapters, this thesis has made a case for subcellular spatial and localization information encoded in genetic and protein sequences. Thus, strategies for efficient molecular search, as in the case of miRNA target binding are closely related to strategies to form structures. High resolution single molecule fluorescence tools have allowed these nano- to micro-scale domains in cells to be dissected and their formation via phase separation-like mechanisms to be studied in living cells. The next frontier is to extend these tools and observations in living tissues and organisms, where cellular phenotypes ultimately translate to organismal phenotypes and behaviors. Thus the major next step in investigation, for which this work sets the stage both

scientifically and methodologically, is inquiry into the hierarchical spatiotemporal gene-regulatory mechanisms that cross spatial and temporal scales.

5.4. References

Afroz, T., Hock, E.M., Ernst, P., Foglieni, C., Jambeau, M., Gilhespy, L.A.B., Laferriere, F., Maniecka, Z., Plückthun, A., Mittl, P.*, et al.* (2017). Functional and dynamic polymerization of the ALS-linked protein TDP-43 antagonizes its pathologic aggregation. Nat. Commun. *8*, 45.

Boyd-Shiwarski, C.R., Shiwarski, D.J., Roy, A., Namboodiri, H.N., Nkashama, L.J., Xie, J., McClain, K.L., Marciszyn, A., Kleyman, T.R., Tan, R.J.*, et al.* (2018). Potassium-regulated distal tubule WNK bodies are kidney-specific WNK1 dependent. Mol. Biol. Cell *29*, 499-509.

Cai, D., Feliciano, D., Dong, P., Flores, E., Gruebele, M., Porat-Shliom, N., Sukenik, S., Liu, Z., and Lippincott-Schwartz, J. (2019). Phase separation of YAP reorganizes genome topology for long-term YAP target gene expression. Nat. Cell Biol. *21*, 1578-1589.

Courchaine, E.M., Lu, A., and Neugebauer, K.M. (2016). Droplet organelles? EMBO J. *35*, 1603-1612.

Courtenay, E.S., Capp, M.W., Anderson, C.F., and Record, M.T., Jr. (2000). Vapor pressure osmometry studies of osmolyte-protein interactions: implications for the action of osmoprotectants in vivo and for the interpretation of "osmotic stress" experiments in vitro. Biochemistry *39*, 4455-4471.

Delarue, M., Brittingham, G.P., Pfeffer, S., Surovtsev, I.V., Pinglay, S., Kennedy, K.J., Schaffer, M., Gutierrez, J.I., Sang, D., Poterewicz, G.*, et al.* (2018). mTORC1 Controls Phase Separation and the Biophysical Properties of the Cytoplasm by Tuning Crowding. Cell *174*, 338-349.e320.

Denzler, R., Agarwal, V., Stefano, J., Bartel, D.P., and Stoffel, M. (2014). Assessing the ceRNA hypothesis with quantitative measurements of miRNA and target abundance. Mol Cell *54*, 766-776.

Feig, M., and Sugita, Y. (2012). Variable interactions between protein crowders and biomolecular solutes are important in understanding cellular crowding. J. Phys. Chem. B *116*, 599-605.

Gasset-Rosa, F., Lu, S., Yu, H., Chen, C., Melamed, Z., Guo, L., Shorter, J., Da Cruz, S., and Cleveland, D.W. (2019). Cytoplasmic TDP-43 De-mixing Independent of Stress Granules Drives Inhibition of Nuclear Import, Loss of Nuclear TDP-43, and Cell Death. Neuron *102*, 339-357.e337.

Gomes, E., and Shorter, J. (2019). The molecular language of membraneless organelles. J. Biol. Chem. *294*, 7115-7127.

Hyman, A.A., and Simons, K. (2012). Cell biology. Beyond oil and water--phase transitions in cells. Science *337*, 1047-1049.

Hyman, A.A., Weber, C.A., and Jülicher, F. (2014). Liquid-liquid phase separation in biology. Annu. Rev. Cell Dev. Biol. *30*, 39-58.

Jalihal, A.P., Pitchiaya, S., Xiao, L., Bawa, P., Jiang, X., Bedi, K., Parolia, A., Cieslik, M., Ljungman, M., Chinnaiyan, A.M.*, et al.* (2020). Multivalent Proteins Rapidly and Reversibly Phase-Separate upon Osmotic Cell Volume Change. Mol. Cell *79*, 978-990.e975.

Jiao, M., Li, H.T., Chen, J., Minton, A.P., and Liang, Y. (2010). Attractive protein-polymer interactions markedly alter the effect of macromolecular crowding on protein association equilibria. Biophys. J. *99*, 914-923.

Kuznetsova, I.M., Zaslavsky, B.Y., Breydo, L., Turoverov, K.K., and Uversky, V.N. (2015). Beyond the excluded volume effects: mechanistic complexity of the crowded milieu. Molecules *20*, 1377-1409.

Langdon, E.M., and Gladfelter, A.S. (2018). A New Lens for RNA Localization: Liquid-Liquid Phase Separation. Annu.Rev. Microbiol. *72*, 255-271.

Ma, W., and Mayr, C. (2018). A Membraneless Organelle Associated with the Endoplasmic Reticulum Enables 3'UTR-Mediated Protein-Protein Interactions. Cell *175*, 1492-1506.e1419.

Martirosyan, A., De Martino, A., Pagnani, A., and Marinari, E. (2017). ceRNA crosstalk stabilizes protein expression and affects the correlation pattern of interacting proteins. Sci. Rep. *7*, 43673.

Miklos, A.C., Li, C., Sharaf, N.G., and Pielak, G.J. (2010). Volume exclusion and soft interaction effects on protein stability under crowded conditions. Biochemistry *49*, 6984-6991.

Minton, A.P. (2005). Models for excluded volume interaction between an unfolded protein and rigid macromolecular cosolutes: macromolecular crowding and protein stability revisited. Biophys. J. *88*, 971-985.

Parker, B.W., Goncz, E.J., Krist, D.T., Statsyuk, A.V., Nesvizhskii, A.I., and Weiss, E.L. (2019). Mapping low-affinity/high-specificity peptide-protein interactions using ligand-footprinting mass spectrometry. Proc. Natl. Acad. Sci. U.S.A. *116*, 21001-21011.

Patel, A., Lee, H.O., Jawerth, L., Maharana, S., Jahnel, M., Hein, M.Y., Stoynov, S., Mahamid, J., Saha, S., Franzmann, T.M.*, et al.* (2015). A Liquid-to-Solid Phase Transition of the ALS Protein FUS Accelerated by Disease Mutation. Cell *162*, 1066-1077.

Qamar, S., Wang, G., Randle, S.J., Ruggeri, F.S., Varela, J.A., Lin, J.Q., Phillips, E.C., Miyashita, A., Williams, D., Ströhl, F.*, et al.* (2018). FUS Phase Separation Is Modulated by a Molecular Chaperone and Methylation of Arginine Cation-π Interactions. Cell *173*, 720-734.e715.

Rai, A.K., Chen, J.X., Selbach, M., and Pelkmans, L. (2018). Kinase-controlled phase transition of membraneless organelles in mitosis. Nature *559*, 211-216.

Ribeiro, S., Ebbinghaus, S., and Marcos, J.C. (2018). Protein folding and quinary interactions: creating cellular organisation through functional disorder. FEBS Lett. *592*, 3040-3053.

Roden, C., and Gladfelter, A.S. (2020). RNA contributions to the form and function of biomolecular condensates. Nat. Rev. Mol. Cell Biol.

Salmena, L., Poliseno, L., Tay, Y., Kats, L., and Pandolfi, P.P. (2011). A ceRNA hypothesis: the Rosetta Stone of a hidden RNA language? Cell *146*, 353-358.

Sarkar, M., Smith, A.E., and Pielak, G.J. (2013). Impact of reconstituted cytosol on protein stability. Proc. Natl. Acad. Sci. U.S.A. *110*, 19342-19347.

Sehgal, P.B., Westley, J., Lerea, K.M., DiSenso-Browne, S., and Etlinger, J.D. (2020). Biomolecular condensates in cell biology and virology: Phase-separated membraneless organelles (MLOs). Anal. Biochem. *597*, 113691.

Taratuta, V.G., Holschbach, A., Thurston, G.M., Blankschtein, D., and Benedek, G.B. (1990a). Liquid-liquid phase separation of aqueous lysozyme solutions: effects of pH and salt identity. J. Phys. Chem. *94*, 2140-2144.

Taratuta, V.G., Holschbach, A., Thurston, G.M., Blankschtein, D., and Benedek, G.B. (1990b). Liquid-liquid phase separation of aqueous lysozyme solutions: effects of pH and salt identity. Journal of Physical Chemistry *94*, 2140-2144.

Tay, Y., Rinn, J., and Pandolfi, P.P. (2014). The multilayered complexity of ceRNA crosstalk and competition. Nature *505*, 344-352.

Vanag, V.K., and Epstein, I.R. (2007). Localized patterns in reaction-diffusion systems. Chaos: An Interdisciplinary Journal of Nonlinear Science *17*, 037110.

Walter, N.G. (2019). Biological Pathway Specificity in the Cell-Does Molecular Diversity Matter? Bioessays *41*, e1800244.

Zhang, H., Elbaum-Garfinkle, S., Langdon, E.M., Taylor, N., Occhipinti, P., Bridges, A.A., Brangwynne, C.P., and Gladfelter, A.S. (2015). RNA Controls PolyQ Protein Phase Transitions. Mol Cell *60*, 220-230.

Zhou, H.X. (2013). Polymer crowders and protein crowders act similarly on protein folding stability. FEBS Lett. *587*, 394-397.

Appendix A. Temperature Effects on HOPS

A1. Background

Organisms, both unicellular and multicellular are known to adapt to narrow ambient temperature ranges (Angilletta and Angilletta, 2009; Berry and Foegeding, 1997; Pörtner et al., 2006). Low temperatures influence the kinetics of reactions whereas high temperatures affect macromolecular structure and assembly. Additionally, high heat causes nucleic acids and proteins to denature, and many organisms possess chaperones and other mechanisms to respond to damage induced by heat stress (Somero, 1995, 2020).

Temperature also influences phase separation. Polymer mixtures show characteristic phase behaviors, either showing phase-separation at low temperature (in which case the phase boundary has an upper critical saturation temperature), or at high temperature (in which case the phase boundary has a lower critical saturation temperature), or both (Jalihal et al., 2020c). Having investigated hyperosmotic phase separation (HOPS, Chapter 3), it is of interest to study the effects of temperature on the condensation of multimeric proteins in general, and during HOPS in particular.

Our characterization of HOPS suggests that it may be largely driven by changes in molecular crowding and presumably reduced diffusion of monomers. Based on this, we can make the prediction that temperature would primarily impact condensation via its impact on diffusion: lower temperatures decrease diffusion, and thus limit the size and number of condensates.

Alternatively, lower temperatures might stabilize condensates by preventing dissociation of monomers and might lead to more or larger condensates. We investigated these possibilities using our established model of HOPS using UGD cells.

A2. Method

Hypertonic DMEM media were prepared by adding the appropriate volume of 10X PBS to Phenol Red-free DMEM medium supplemented with 1% FBS. The 5 mL of the media was aliquoted into 15 mL falcon tubes which were then prewarmed for 15 minutes at the appropriate test temperature after the temperature reading on the water-bath had stabilized. Delta T dishes seeded with UGD cells were equilibrated at the test temperature for 5 minutes on the stage before imaging. Cells were imaged in isotonic medium and 1 minute after addition of the hypertonic medium. Imaris was used for spot detection and tracking and the number of foci per cell in each condition measured was plotted in Origin.

A3. Results

GFP-DCP1A's HOPS response and recovery (see Chapter 3) was measured at 27, 32 and 42 ºC. A clear trend of increasing foci number with temperature was observed in all three conditions: isotonic, 230 mM Na^+ and recovery. Additionally, at a higher salt concentration (300 mM Na^+) this trend was disrupted. Overall, these data provide two conclusions regarding the effects of temperature of DCP1A condensation: firstly, under moderate hypertonic shock and isotonic conditions, DCP1A foci number are sensitive to temperature. Secondly, this temperature sensitivity is weaker than the strong compression-dependence of HOPS, and temperature effects are overcome at higher salt concentrations (Figure A-1).

Lower temperatures show decreased number of DCP1A foci. Tentatively, this then suggests that DCP1A diffusion and accessibility might be sensitive to temperature fluctuations. However, it is also important to rule out effects that temperature may have on macromolecular crowding.

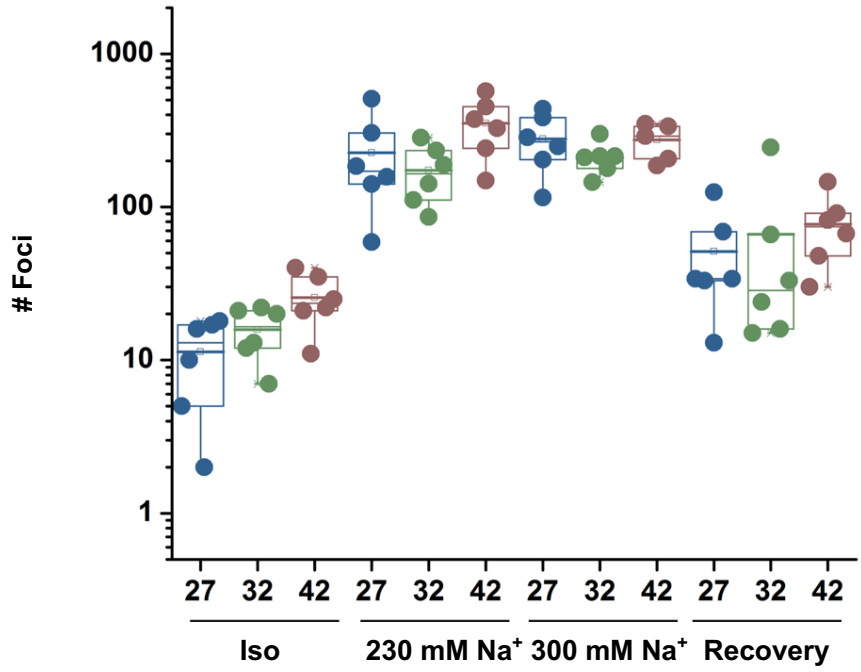

Figure A-1 Effect of temperature on DCP1A HOPS. Boxplots represent foci numbers per cell measured under isotonic, 230 mM Na^+, 300 mM Na^+, and 1-minute recovery in isotonic medium, at three different temperature conditions.

A4. Future Directions

These results raise important questions regarding temperature-sensitive phase separation in vivo and temperature sensing mechanisms in general. While several protein-structure-based mechanisms have been described in the search for temperature sensors (Sengupta and Garrity, 2013), one possibility that the field of condensates opens up is a system-wide sensor, rather than an individual molecule. In this way, the entire proteome and its spatial organization serve as the

sensor of temperature, and thresholds imposed on the degree of condensation can be used to read out and initiate responses to high and low temperature stresses.

In this regard it is of interest to generalize this observation of HOPS proteins' sensitivity to temperature. While our work has revealed the importance of hydrophobic multivalent domains in HOPS, it remains to be explored what interactions sensitize these proteins to temperature.

These preliminary results can be followed up by evaluating what interactions and structural features influence this temperature sensitivity. To evaluate the hypothesis that diffusion plays a role, it might be important to modulate diffusion using an orthogonal approach, such as by fusing DCP1A to a larger protein. Independently, measuring the state of molecular crowding as a function of temperature will also clarify the factors that influence temperature sensitivity.

Appendix B. Methylated mRNAs and P-Body Localization

B1. Background

RNAs are known to be abundantly chemically modified, and these modifications impact RNA-protein interactions and consequently RNA function (Lewis et al., 2017; Saletore et al., 2012). Among the various known modifications adenosine N^6 methylation (m^6A) has come into the limelight after the discovery of the complement of metazoan m^6A writer (METTL3/14), reader (YTHD proteins) and putative erasers (FTO/ALKBH5), suggesting that this modification may be dynamic and subject to regulation (Meyer and Jaffrey, 2014; Yang et al., 2018). Further, work over the past decade has shown that m^6A can regulate splicing and mRNA stability and even RNA phase separation (Lee et al., 2020; Ries et al., 2019).

Recent work on RNA methylation suggests that methylation serves as a signal to promote RNA turnover by recruitment of YTH proteins.

B2. Methods

UGD cells were plated on Delta T dishes 24-48 hours before injection. Injection solutions containing 2 µL of 10 mg/mL Cascade Blue-Dextran, containing labeled and methylated or unmethylated Sox2 mRNA at a final dilution of 500 pg/µL- 10 ng/µL were made up to 20 µL using 1X PBS. Cells were washed thrice with HBS just before the start of injection. Cells were injected in the cytosol and imaged directly following injection or 1 hours after injection. In the second case,

cells were washed twice with DMEM medium containing 1% FBS and were incubated in a 37ºC CO2 incubator until imaging.

Cells were imaged with one camera using HILO illumination and 100 ms acquisition time. The samples were excited for 10 frames with 405 nm, 10 frames with 488 nm and 80 frames with 640 nm to image the cascade blue, to examine cytosolic localization, GFP-DCP1A and Alexa-647 labeled mRNA respectively. Cells were imaged using the 60x oil objective lens, with a 2x magnification insert, to obtain a net image magnification of 120x.

Particle tracking was performed using TrackMate plugin in FiJi. The obtained tracks were then subjected to colocalization and diffusion analyses. P-bodies (GFP-DCP1A foci) were found to be largely immobile, and their positions were fixed at the spot center obtained by spatially averaging the positions of the individual GFP-DCP1A foci spots over 10 frames. Representative images were convolved with a LoG filter (5x5 Gaussian filter followed by 3x3 Laplacian) in FiJi to enhance spots in both channels.

B3. Results

Two color representative images with insets, boxplots showing the extents of mRNA-PB colocalization 5 minutes after injection (Figure B-1). While the methylated mRNA sample shows colocalization comparable to the background, density-dependent level, the non-methylated sample shows statistically significant increase in the degree of colocalization both over background and the methylated sample. The background level of density-dependent colocalization for each cell was derived using a 10-pixel shift of the mRNA channel relative to the P-body channel. The extents

of colocalization per cell were normalized to the number of P-bodies so as to control for the variability in cell sizes and P-body numbers.

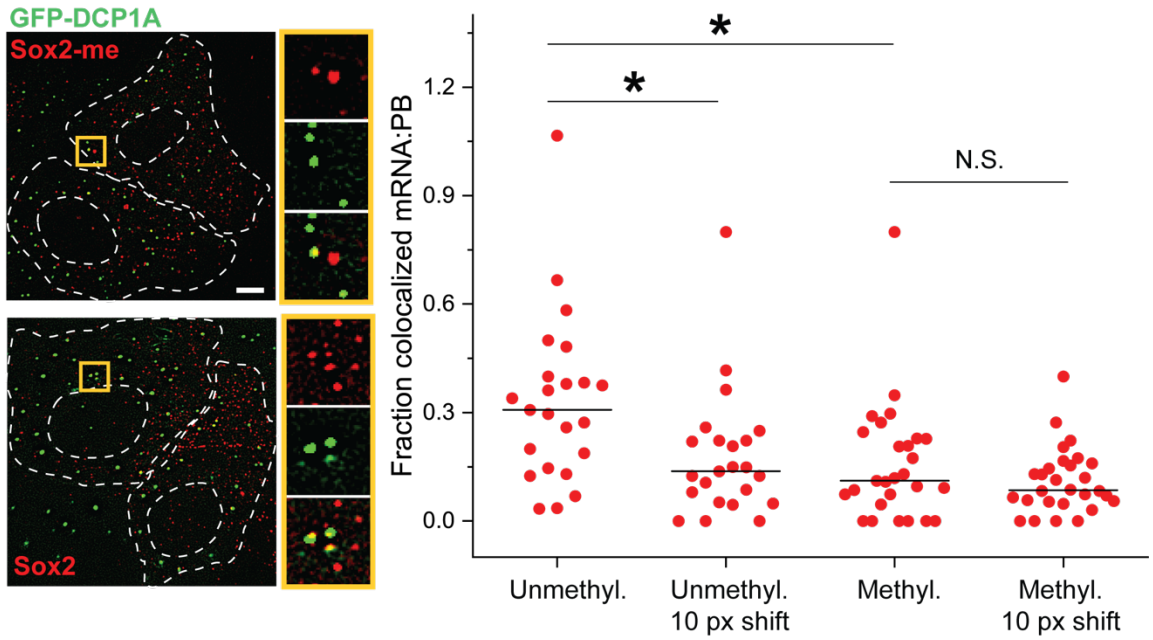

Figure B-1 Methylated mRNAs show differential colocalization with P-bodies. Representative images of UGD cells injected with methylated (top) or unmethylated (bottom) mRNA (right). The insets show magnified images of the indicated boxes. Green represents GFP-DCP1A and red represents Cy5-labeled injected RNAs. The boxplot on the right depicts the degree of mRNA:P-body colocalization per cell expressed as a fraction of total P-body number. Number of cells = 26 for unmethylated mRNA, 28 for methylated mRNA. The colocalization fraction from each condition is compared to internal density control measurements denoted as 10 px shift. * denotes statistical significance under unpaired two-sample Student's t-test at a significance level of $p < 0.05$.

B4. Future directions

This preliminary data indicates that methylation at early time-points hinders mRNA localization to P-bodies. It will be of interest to track the degree of colocalization at various time points after injection. Another experiment in which endogenous YTHD proteins are depleted will shed light on the mechanism of this difference and will clarify the role of YTHD binding in regulating this localization.

Appendix C. HILO Characterization

C1. Background

A major source of poor signal characteristics in fluorescence microscopy of biological samples is out-of-focus fluorescence that can increase the background signal. One common solution is the use of confocal illumination to image thick biological samples, which also provides higher XY resolution than epifluorescence illumination. However, in these set-ups the pinhole has to be scanned in a raster over the sample, and this process typically imposes a limit on the time of imaging, where rapid processes that occur on the similar time scales as the raster speed will be inaccessible. A wide-field illumination mode called highly inclined and laminated optical sheet illumination (HILO) provides an elegant solution to both problems. Its principle is similar to total internal reflection (TIRF), in that it provides a narrow band of illumination that minimizes fluorophore excitation outside the focal plane. However, unlike TIRF in which the evanescent field is limited to ~100 nm, HILO can be used to illuminate several 10s of microns within the sample by changing the angle of incidence of specific excitation wavelengths.

Here we present a general method to characterize the HILO beam thickness using suspended fluorescent beads. The spatial characterization of the beam is useful to determine the true beam width and to determine the extent of inhomogeneities across the illuminated region. It also provides a simple and reproducible strategy of analysis and beam reconstruction using two spot-detection and a scatter plot readout.

C2. Methods

Glass slides (Fisher Scientific, 125443) and coverslips (24x30 mm VWR 48393-092) were rinsed with 70% ethanol and wiped with Kimwipes to remove debris from the surface. Two 3 mm x 10 mm strips of parafilm were placed 2 cm apart in the center of the slide and gently pressed down using the flat edge of a razor blade. This prepared glass slide and clean coverslips were kept at 37ºC while the agarose-beads mixture was prepared. 5% agarose solution in water was prepared by dissolving 0.5 g Ultrapure electrophoresis grade agarose (ThermoFisher 16500500) in 10 mL deionised water. The solution was microwaved for one minute and was intermittently shaken to ensure uniform dissolution and mixing. 10 µL of vortexed and centrifuged TetraSpeck beads solution (0.1 µm, ThermoFisher Scientific T7279) was placed between the two parafilm strips on the glass slide and 90µL of in the hot, freshly prepared agarose solution was pipetted directly onto the drop. The two solutions were quickly mixed by pipetting up and down without introducing bubbles and a clean coverslip was placed on the two strips of parafilm to wedge the agarose-beads solution before it solidified. The gel was allowed to polymerize at room temperature for 5 minutes before the edges of the coverslip were then sealed using epoxy. The beads were imaged by placing the slide assembly so the coverslip made contact with the oil objective. 50 Z-stacks, were images at every 200 nm with 100 ms acquisition time per slice using 532 and 640 nm illumination.

The centers of the 3D PSFs were obtained using the spots function from Imaris. The beam profile f(x,y,z) at any given plane was calculated by projecting a 5x5 pixel window centered at the x-y coordinate of the center of every detected PSF onto the plane of interest (z) and integrating the pixel intensities over the window.

C3. Results

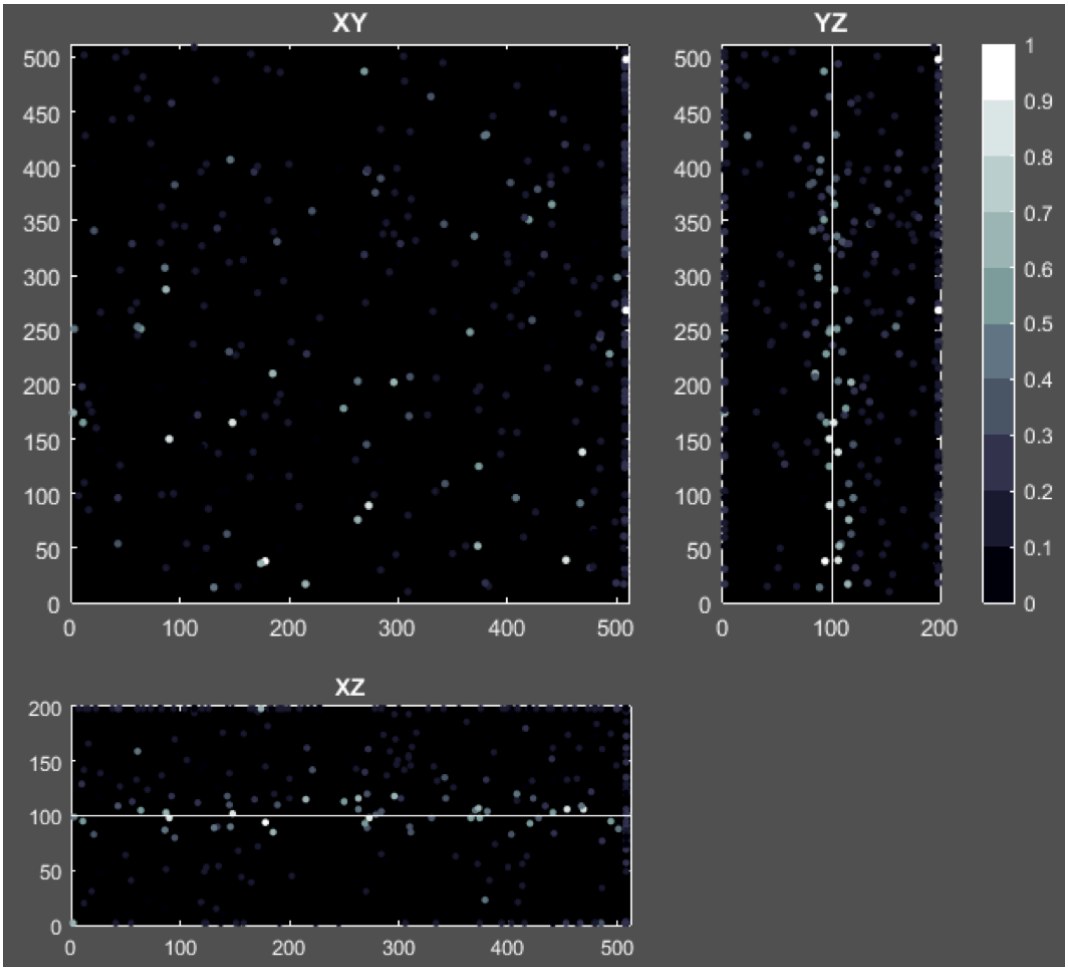

Figure C-1 Reconstruction of the HILO bead profile. XY, XZ and YZ intensity projections of beads positions illuminated at a single plane corresponding to plane 100. The color bar indicates relative brightness of beads illuminated at this Z-height. Scale:XY 1 px = 65 nm. Z 10 px = 200 nm, total range = 10 μm.

C4. Outlook

This straightforward protocol for determining the HILO illumination volume it enables quantitative volume illumination experiments of fluorophores is solution, while providing a more accurate estimate of Z-illumination for cell imaging applications.

C5. References

Angilletta, M.J., and Angilletta, M.J. (2009). Thermal Adaptation: A Theoretical and Empirical Synthesis (OUP Oxford).

Berry, E.D., and Foegeding, P.M. (1997). Cold Temperature Adaptation and Growth of Microorganisms (†). J. Food Prot. *60*, 1583-1594.

Jalihal, A.P., Schmidt, A., Gao, G., Little, S., Pitchiaya, S., and Walter, N.G. (2020). Hyperosmotic phase separation: Condensates beyond inclusions, granules and organelles. J. Biol. Chem.

Lee, Y., Choe, J., Park, O.H., and Kim, Y.K. (2020). Molecular Mechanisms Driving mRNA Degradation by m(6)A Modification. Trends Genet. *36*, 177-188.

Lewis, C.J., Pan, T., and Kalsotra, A. (2017). RNA modifications and structures cooperate to guide RNA-protein interactions. Nat. Rev. Mol. Cell Biol. *18*, 202-210.

Meyer, K.D., and Jaffrey, S.R. (2014). The dynamic epitranscriptome: N6-methyladenosine and gene expression control. Nat. Rev. Mol. Cell Biol. *15*, 313-326.

Pörtner, H.O., Bennett, A.F., Bozinovic, F., Clarke, A., Lardies, M.A., Lucassen, M., Pelster, B., Schiemer, F., and Stillman, J.H. (2006). Trade-offs in thermal adaptation: the need for a molecular to ecological integration. Physiol. Biochem. Zool. *79*, 295-313.

Ries, R.J., Zaccara, S., Klein, P., Olarerin-George, A., Namkoong, S., Pickering, B.F., Patil, D.P., Kwak, H., Lee, J.H., and Jaffrey, S.R. (2019). m(6)A enhances the phase separation potential of mRNA. Nature *571*, 424-428.

Saletore, Y., Meyer, K., Korlach, J., Vilfan, I.D., Jaffrey, S., and Mason, C.E. (2012). The birth of the Epitranscriptome: deciphering the function of RNA modifications. Genome Biol. *13*, 175.

Sengupta, P., and Garrity, P. (2013). Sensing temperature. Curr. Biol. *23*, R304-307.

Somero, G.N. (1995). Proteins and temperature. Annu. Rev. Physiol. *57*, 43-68.

Somero, G.N. (2020). The cellular stress response and temperature: Function, regulation, and evolution. J. Exp. Zool. A Ecol. Integr. Physiol. *333*, 379-397.

Yang, Y., Chen, Y.S., Sun, B.F., and Yang, Y.G. (2018). [RNA methylation: regulations and mechanisms]. Yi Chuan *40*, 964-976.